

**Fluid dynamic behaviour of dilute  
*Dunaliella Salina* suspensions  
in contraction-expansion microfluidic  
devices: potential implications for  
tubular photobioreactors**

Vincenzo Infante

**Thesis submitted to the University of Strathclyde for  
the degree of Doctor of Philosophy**

Departments of Chemical and Process Engineering and  
Mechanical and Aerospace Engineering

University of Strathclyde

2018

# Declaration

This thesis is the result of the author's original research. It has been composed by the author and has not been previously submitted for examination which has led to the award of a degree.

The copyright of this thesis belongs to the author under the terms of the United Kingdom Copyright Acts as qualified by University of Strathclyde Regulation 3.50.

Due acknowledgement must always be made of the use of any material contained in, or derived from, this thesis.

Signed:

Date:

*“We shall not cease from exploration. And the end of all our exploring will be to arrive where we started and know the place for the first time.” [Thomas Stearns Eliot]*

*“Non smetteremo di esplorare. E alla fine di tutto il nostro esplorare ritorneremo da dove siamo partiti e conosceremo il luogo per la prima volta.” [Thomas Stearns Eliot]*

# Acknowledgments

Firstly, I would like to express my sincere gratitude to my supervisors, Doctor Mónica Oliveira and Doctor Mark Haw, who provided me the opportunity to undertake this research project. I am deeply thankful for your help, patience, guidance and encouragement, through every stage of my research.

I would also like to show my appreciation to everyone who helped me throughout my project, thanks to all of you for your support, suggestions, fruitful discussions and all the help in the lab.

I also wish to thank the many friends I have made during this experience, thanks for making the office environment more colourful, for being always there for a chat, thanks to those who have listened to me, supported me, celebrated with me, mourned with me, laughed with me and cried with me. You have been a rock for me during this testing journey and I will always have great memories thanks to all of you.

I would want to extend my wholehearted thanks to members of the Chemical and Process Engineering Department and the Mechanical and Aerospace Engineering Department, for making my time in these Departments a pleasure and memorable experience.

I also show my gratitude to the secretarial and technical staff of Strathclyde University for the support and guidance given to me during these years.

Finally and most importantly, I am especially grateful to my family and friends for their undying support and dedication. I am overwhelmingly appreciative of the continued encouragement you all have provided me throughout the PhD.

# The author

## Presentations

- British Society of Rheology Winter Meeting, Durham University (UK), December 2014, Poster Presentation – “Behaviours of *Dunaliella Salina* in microfluidic contraction devices”.
- 10<sup>th</sup> Annual European Rheology Conference, Nantes (France), April 2015, Oral Presentation – “Effect of flow conditions on the swimming efficiency of *Dunaliella Salina* in microfluidic contraction devices”.
- Rheologists in Scotland Meeting II, Strathclyde University (UK), May 2015, Oral Presentation – “Microswimmers in Microfluidics: Enhancing the Engineering of Nano and Micro-Scale Driven Transport Applications”.
- The 5<sup>th</sup> UK Algae Conference, Glasgow University (UK), July 2015, Poster Presentation – “Behaviours of *Dunaliella Salina* in Contraction-Expansion Microfluidic Devices”.
- British Society Rheology Mid-Winter Meeting, Glasgow University (UK), December 2015, Poster Presentation – “Fluid dynamic responses of diluted *Dunaliella Salina* suspensions in microfluidic contraction devices”.
- Chemical Process Engineering Research Presentation Event, Strathclyde University (UK), April 2016, Oral Presentation – “Microswimmers in Microfluidics: Enhancing the Engineering of Nano and Micro-Scale Driven Transport Applications”.
- 29<sup>th</sup> Scottish Fluid Mechanics Meeting, Edinburgh Centre for Carbon Innovation (ECCI), Edinburgh University (UK), May 2016, Oral Presentation – “Fluid Dynamic Behaviour of *Dunaliella Salina* Cells In Microfluidic Devices When Subjected To Different Flow Rates”.
- The 6<sup>th</sup> Algae Conference UK, Sheffield University (UK), July 2016, Poster Presentation – “Effects of flow conditions on the fluid dynamic responses of diluted *Dunaliella Salina* suspensions in microfluidic devices”.

## **Awarded grants**

- British Society Rheology poster award and a grant of £350 for attending any suitable European/International Rheology Conference, Glasgow University (UK), December 2015.

## List of abbreviations

2D	Two dimensional
3D	Three dimensional
ACDP	Algal cells distribution percentage
ADE	Advection-diffusion equation
AR	Aspect Ratio
ATP	Adenosine triphosphate
AVR	Area to volume ratio of a photobioreactor
C	The centre of buoyancy of a bottom-heavy cell
CAD	Computer-aided design software
CCAP	Culture collection of algae and protozoa
CCAP 19/18	The specific strain of <i>Dunaliella Salina</i> cells
CCD	Charge-coupled device
CCW	Counterclockwise
CEG	Contraction-expansion geometry
CFD	Computational fluid dynamic
CFRA	Cells free regions area
Chl.	Chlorophyll
CP	Cultivation process
CR	<i>Chlamydomonas Reinhardtii</i>
Crt	Contraction ratio
CW	Clockwise
DDC	Dead <i>Dunaliella</i> cell
DIC	Differential interference contrast
DLC	Dark/light cycle
DNA	Deoxyribonucleic acid
DO	Dissolved Oxygen
DOF	Depth of field
DP	Design process
DS	<i>Dunaliella Salina</i>
DSP	Downstream process
<i>E. Coli</i>	<i>Escherichia Coli</i>
ECR	Expansion/contraction ratio
<i>e.g.</i>	<i>Exempli gratia</i> (meaning for example)
Em	Emission wavelength
eq.	Equation
ER	Expansion ratio
<i>etc.</i>	<i>Etcetera</i>
Ex	Excitation wavelength
FPR	Flat plate reactor
FTR	Fermenter-type reactor
G	The centre of mass of a bottom-heavy cell
GRAS	Generally recognised as safe

HEPA	High efficiency particulate air
HLID	Homogeneous light intensity distribution
HTPBR	Horizontal tubular photobioreactor
HWMCM	Hejazi and Wijffels modified culture medium
<i>i.e.</i>	<i>Id est</i> (meaning that is, precisely)
IAP	Image analysis process
ID	Inner diameter
LAC	Low algal concentration
LDC	Live <i>Dunaliella</i> cell
LUCA	Last universal common ancestor
OD	Outer diameter
OMT	Optical microscopy techniques
NA	Numerical aperture
NADPH	Nicotinamide adenine dinucleotide phosphate
NAPA	Net algal plume area
NUP	Nutrient uptake process
PAR	Photosynthetically active radiation
PBR	Photobioreactor
PCE	Photosynthetic conversion efficiency
PDMS	Polydimethylsiloxane
<i>Pe</i>	Péclet
QC	Quality control
RAM	Random access memory
RBRM	Rolling ball radius method
<i>Re</i>	Reynolds
rpm	Rotation per minute
SD	Standard deviation
SE	Standard error
<i>Sh</i>	Sherwood
SM	Static mixer
<i>Sr</i>	Strouhal
SR	Straight region of the channel
SSA	Segrè's and Silberberg's annulus
SVR	Surface to Volume Ratio of the cell
TA	Total area of a channel
TADT	Taylor-Aris dispersion theory
THAM	Tris(hydroxymethyl)aminomethane
TKP	Thermal killing procedure
UK	United Kingdom
UV	Ultraviolet
VC	Vena contracta
zi	A given horizontal zone of the microgrid

## List of symbols

$a$	Radius of a spherical microorganism
$A_c$	Cellular surface area
$\overline{ACDP}$	Average algal cells dispersion percentage
$A_{Ch}$	Cross-section area of a microchannel
$a_e$	Major axis of a given ellipse
$A_G$	Aperture (ground) area of a photobioreactor
$A_R$	Total surface area of a photobioreactor
$AVR$	Ratio between the surface area and the volume of a reactor
$B$	Timescale for reorientation by gravity
$b_e$	Minor axis of a given ellipse
$\mathbf{B}_F$	Buoyant force also known as Archimedes' force
$B_N$	Buoyancy number
$C$	Concentration of a given solute in a flow
$\bar{C}$	Average concentration of a given solute in a flow
$\tilde{C}$	Nondimensional concentration
$C_A$	Concentration of the algal cells within a given photobioreactor
$C_{A,max}$	Maximum algal concentration that can be tracked in a given microfluidic device
$C_{A,min}$	Minimum algal concentration that can be tracked in a given microfluidic device
$C_b$	Concentration of the biomass in the PBR
$C_c$	Characteristic concentration
$c_e$	Distance of the focal point of a given ellipse from its centre
$C_f$	Fanning friction factor
$C_{O_2,IN}$	Oxygen concentration at the aeration port of the PBR
$C_{O_2,OUT}$	Maximum oxygen concentration that does not inhibit photosynthesis
$C_0$	Concentration of a given nutrient on the surface of the absorbing cell
$C_\infty$	Concentration of a given nutrient far away from the absorbing cell
$D$	Diffusion coefficient of a solute in a flow
$\mathbf{D}_C$	Cell diffusivity tensor
$D_{Eff}$	Effective diffusivity coefficient
$D_{H,C}$	Hydraulic diameter of the contraction region
$D_{H,E}$	Hydraulic diameter of the expansion region
$d_p$	Particle diameter
$d_s$	Microswimmer's characteristic size

$d_t$	Diameter of the PBR tube
$e$	Smallest resolvable feature size of an optical system
$E$	Rate of energy dissipation of the turbulence field per unit mass of fluid
$\mathbf{E}$	Rate of strain
$E_{crit}$	The critical value of $E$
$e_e$	Eccentricity of a given ellipse
$\mathbf{f}$	Body of forces
$\tilde{\mathbf{f}}$	Nondimensional body forces
$\mathbf{F}$	Point force acting on a fluid
$\mathbf{F}_b$	External body of force per unit mass acting on a swimming cell
$\mathbf{F}_d$	Drag force
$\mathbf{F}_{d  }$	Flagellar drag force in the parallel direction
$\mathbf{F}_{d\perp}$	Flagellar drag force in the normal direction
$F_e$	Focal point of a given ellipse
$\vec{\mathbf{F}}_{LS}$	Shear gradient lift force
$\vec{\mathbf{F}}_{LW}$	Wall-induced lift force
$\mathbf{F}_{prop}$	Propulsive force of the organism
$f_s$	Scale factor
$\vec{\mathbf{F}}_S$	Saffman force
$\mathbf{g}$	Gravitational acceleration
$\mathbf{G}_F$	Gravitational force
$h$	Distance between the centre of mass and the centre of buoyancy of an algal cell
$H$	Height of a rectangular channel
$H_{Ch}$	Microchannel depth
$H_{Cr}$	Critical dimension of a microchannel
$\mathbf{I}_A$	Areal diffusive current of a given solute
$I_{AV}$	Average irradiance within the PBR
$I_C$	Compensation intensity
$I_k$	Experimental constant dependent on algal species and culture conditions used for estimating the algal biomass growth rate (see eq. 5.3)
$I_L$	Punctual light intensity within the PBR
$I_P$	Photoinhibition intensity
$I_S$	Saturation intensity
$\mathbf{i, j, k}$	Fixed-space axes
$I_0$	Incident solar radiation
$\mathbf{J}(\mathbf{r})$	Flux of the diffusing molecule
$\mathbf{k}$	Preferential swimming direction
$K_a$	Algal extinction coefficient
$k_d$	Biomass decay coefficient

$l$	Kolmogoroff microeddy length scale
$L$	Characteristic length scale
$L_c$	External couple acting on a cell
$L_C$	Contraction length
$L_{Ch}$	Length of a given microchannel measured between its inlet and outlet holes
$L_E$	Effective external torque acting on a cell
$L_{EN}$	Hydrodynamic entrance length
$L_{EX}$	Hydrodynamic exit length
$L_t$	Length of the PBR tube
$L_{t,max}$	Maximum achievable length of the PBR tube
$L_v$	Viscous torque exerted by the fluid on a cell
$Ma$	Objective magnification
$m_p$	Mass of a particle
$m_s$	Mass of the swimming organism
$\mathbf{n}$	Normal vector
$n$	Local concentration of algal cells in a suspension
$N$	Number of instantaneous velocity values found in the $j$ -th subinterval by the code
$n_A$	Empirically-established exponent used for estimating the algal biomass growth rate (see eq. 5.6)
$NA_{obj}$	Numerical aperture of the objective
$NA_{cond}$	Numerical aperture of the condenser
$p$	Pressure
$\mathbf{p}$	Swimming direction of a cell
$\tilde{p}$	Nondimensional pressure
$p_{Biomass}$	Biomass productivity
$PCE_{PAR}$	Photosynthetic conversion efficiency (PCE) evaluated at the photosynthetically active radiation (PAR)
$Pe$	Péclet number
$P_G$	Biomass areal productivity
$p_L$	Path length travelled by the light within the PBR
$P_R$	Biomass volumetric productivity
$P_W$	Channel wetted perimeter
$\mathbf{p, q, r}$	Body axes
$Q$	Volumetric flow rate
$r$	Ratio of the major to the minor axis of the cell
$R$	Radius of a particle
$Re$	Reynolds number
$Re_c$	Channel Reynolds number
$Re_p$	Particle Reynolds number
$r_F$	Distance from the location where a force is applied
$ri$	Refractive index of the imaging medium
$R_{O_2}$	Volumetric rate of oxygen generation in the tube

$R_p$	Radius of a pipe
$r_p$	Resolving power of an objective
$r_{pl}$	Radial position in the rheometer plate
$R_{pl}$	Radius of the upper rheometer plate
$SD_j$	Standard deviation of the j-th subinterval
$SE_j$	Standard error of the j-th subinterval
$Sh$	Sherwood number
$Sr$	Strouhal number
$t$	Time
$\tilde{t}$	Nondimensional time
$tbf$	Time interval between two frames
$t_c$	Characteristic time scale
$T_f$	Flagellar beat period
$T_1$	Lower threshold value
$T_2$	Upper threshold value
$U$	Flow speed
$\bar{U}$	Mean flow velocity
$\tilde{\mathbf{u}}$	Nondimensional flow velocity
$\mathbf{u}_{  }$	Transversal component of the flagellar velocity
$\mathbf{u}_{\perp}$	Normal component of the flagellar velocity
$U_c$	Characteristic velocity scale
$\mathbf{u}_f$	Velocity of the flagella
$\mathbf{u}_{fl}$	A velocity which is representative of the of the local instantaneous fluid velocity field
$U_{L,L}$	Linear culture velocity at larger scale
$U_{L,max}$	Maximum permissible culture velocity
$U_{L,S}$	Linear culture velocity at smaller scale
$U_M$	Maximum flow velocity
$\mathbf{u}_p$	The instantaneous particle centre of mass velocity
$\mathbf{u}_s$	The slip velocity of a particle
$\mathbf{U}(\mathbf{u}, \mathbf{v}, \mathbf{w}, t)$	Flow velocity field
$(\mathbf{u}, \mathbf{v}, \mathbf{w})$	The velocity component in the x, y and z directions
$V_c$	Average volume of a cell
$V_{ins}$	Instantaneous velocity
$\bar{V}_j$	Average velocity of the j-th subinterval
$V_p$	Volume of a particle
$V_R$	Total working volume of a photobioreactor
$V_s$	Microswimmer's swimming speed
$V_{SW}$	Algal swimming velocity magnitude
$\mathbf{V}_T$	Sedimentation velocity of a particle
$V_{T,DDC}$	Sedimentation velocity of a dead <i>Dunaliella</i> cell
$V_{T,LDC}$	Sedimentation velocity of a living <i>Dunaliella</i> cell
$V_x$	Algal velocity in the x direction between two frames

$V_y$	Algal velocity in the y direction between two consecutive frames
$X, Y$	Algal spatial positions within the microchannels
$x_0$	Generic fixed point of the fluid where the force is applied
$W$	Width of a rectangular channel
$W_C$	Width of the contraction region
$W_E$	Width of the expansion region
$\alpha$	Dimensionless resistance to rotation
$\alpha_L$	One-half angle of the inverted light captured by an objective.
$\alpha_0$	Cell eccentricity
$\dot{\gamma}$	Shear rate
$\gamma_{crit}$	Critical shear rate threshold value
$\dot{\gamma}_W$	Wall shear rate in a fully-developed laminar flow
$\Delta P$	Pressure gradient
$\theta$	The angle between the dipole direction.
$\theta_f$	Angle between the flagella and the local tangent
$\lambda$	Wavelength of the illuminating light
$\mu$	Dynamic viscosity of the surrounding fluid
$\mu_A$	Algal growth rate
$\mu_m$	Dynamic viscosity of the algal medium
$\mu_{A, MAX}$	Maximum algal biomass growth rate
$\nu$	Kinematic viscosity of the surrounding fluid
$\nu_m$	Kinematic viscosity of the algal medium
$\xi_{\perp}$	Flagellar drag coefficient in the normal direction
$\xi_{\parallel}$	Flagellar drag coefficient in the parallel direction
$\rho_c$	Average density of a cell
$\rho_{DDC}$	Density of a dead <i>Dunaliella</i> cell
$\rho_f$	Density of the surrounding fluid
$\rho_{LDC}$	Density of a living <i>Dunaliella</i> cell
$\rho_m$	Density of the algal medium
$\rho_p$	Density of a particle
$\tau$	Shear Stress
$\tau_{max}$	The maximum shear stress at the edge of the rheometer plate
$\tau_W$	Wall shear stress in a fully-developed laminar flow
$\omega$	Vorticity vector
$\%_{CFRA}$	The cells depleted regions areas expressed as the percentage of the channel surface.

## Abstract

In the last decades, microalgal biotechnology has been triggering increasing attention and several species have been cultivated industrially in photobioreactors (PBRs) of various designs. However, operational costs are currently too high since, in order to guarantee proper mixing levels and prevent algal accumulations, the cells are turbulently pumped and treated as passive particles. Whereas, PBRs should be adapted to the intrinsic features of the cultured organisms; hence, it is paramount to devise a new procedure that would permit experimental data to be acquired directly from the microalgae and use the data for optimising all the phases of the PBR design and utilisation.

Therefore, the main objective of this PhD was to investigate experimentally the possibility of exploiting microfluidic devices as complementary tools for PBRs optimisation processes, focusing particular attention on horizontal PBRs equipped with static mixers. The experiments were mainly aimed at exploring the fluid dynamic behaviours of a specific microalga, *Dunaliella Salina* (DS), considering both living and dead cells while flowing within microchannels characterised by different abrupt expansion-contraction ratios (ECR) geometries (ECR 2-1, ECR 4-1 and ECR 7-1), assuming the employed microchannels as “simplified PBRs” and their microgeometries as static mixers.

Initially, the experiments explored the algal behaviours subject to different flow rates in the channels, in order to assess whether better processing conditions may be achieved by optimising the PBR geometrical configuration and therefore addressing the exploitation of microfluidic devices for design purposes. The microgeometries were found to cause the developments of algal plumes that inhibited the wall interactions of the living cells but increased those of the dead ones. These opposite behaviours were due to different spatial distributions of the cells in the plumes. Moreover, the algal plumes also caused the formation of cell free zones which led to more homogeneous irradiance profiles.

The second set of experiments investigated the potential use of microchannels for quality control purposes, studying the fluid dynamic experiences of the cells in crucial regions of the channels through targeted image analysis processes and assessing sizes and shapes of the DS cells studied. The results demonstrated that microfluidic devices can be used to detect early shear-induced damage to the cells and the variations of their size and shape distributions during the cultivation process.

# Contents

## Chapter 1: Microswimmers and low Reynolds numbers world

1.1 Chapter layout.....	20
1.2 Introduction to microorganisms .....	20
1.2.1 Taxonomy of microorganisms.....	21
1.2.1.1 Prokaryotic organisms .....	22
1.2.1.2 Eukaryotic organisms.....	23
1.2.2 Morphology and shape.....	23
1.2.3 Autotrophic, heterotrophic and mixotrophic organisms.....	24
1.3 Planktonic microorganisms.....	24
1.3.1 The photosynthetic process.....	24
1.4 Microswimmers .....	26
1.4.1 Prokaryotic flagella.....	26
1.4.2 Eukaryotic flagella .....	27
1.5 Comparison between microswimmers and passive particles.....	28
1.5.1 Feeding .....	28
1.5.2 Settling rate.....	29
1.5.3 Sensing: the taxis effects .....	29
1.5.3.1 Chemotactic behaviour.....	29
1.5.3.2 Phototactic behaviour .....	29
1.6 Algal accumulations.....	30
1.6.1 Rayleigh-Bénard-type instabilities.....	30
1.6.2 Overturning instabilities .....	31
1.6.3 Controlling the cell's fluid dynamic behaviours .....	31
1.7 Why should microswimmers' fluid dynamic behaviours be studied?.....	32
1.8 Low Reynolds numbers world.....	32
1.8.1 Creeping flows.....	33
1.8.2 The Stokes equation .....	34
1.8.3 Main properties of Stokes flows .....	36
1.9 Overcoming the Stokesian constraints: the drag anisotropy and the most important swimming strategies .....	38
1.10 Hydrodynamic interactions.....	40

1.10.1 Swimming as a singularity.....	41
1.10.2 Sedimenting cells versus swimming organisms .....	42
1.10.3 Pushers versus pullers .....	43
1.10.4 Cells-boundaries interactions .....	45
1.11 Locomotion in flows .....	47
1.11.1 Gravitactic and gyrotactic behaviours .....	48
1.12 Transport phenomena at low Reynolds numbers.....	51
1.12.1 The advection-diffusion equation .....	51
1.12.2 Diffusive nutrient uptake process .....	52
1.12.3 Advective nutrient uptake process.....	54
1.13 Chapter summary.....	55
<b>Chapter 2: The microalga <i>Dunaliella Salina</i>, the algal biofuels and the photobioreactors</b>	
2.1 Chapter layout.....	56
2.2 General considerations about the algae.....	56
2.2.1 Macroalgae and microalgae.....	57
2.2.2 Green, red and brown algae .....	58
2.2.3 Diatoms.....	59
2.2.4 Dinoflagellates.....	59
2.2.5 Algal industrial applications.....	60
2.3 The microalga <i>Dunaliella Salina</i> .....	61
2.3.1 The <i>Dunaliella</i> Genus.....	61
2.3.2 The <i>Dunaliella Salina</i> cell .....	62
2.3.3 <i>Dunaliella Salina</i> reproduction.....	64
2.3.4 How does <i>Dunaliella Salina</i> swim?.....	64
2.3.5 <i>Dunaliella Salina</i> and its taxis effects .....	65
2.3.6 <i>Dunaliella Salina</i> applications .....	66
2.3.6.1 $\beta$ -carotene production.....	66
2.3.6.2 Polluted effluents treatment .....	66
2.3.6.3 <i>Dunaliella Salina</i> used as a bio-indicator .....	67
2.4 The production of algal biofuels .....	67
2.4.1 Why the algal biofuels? .....	67
2.4.2 Processing the microalgae .....	69
2.5 The algal cultivation .....	70

2.6 Different types of reactors and main technical features.....	72
2.6.1 Open photobioreactors .....	73
2.6.2 Closed photobioreactors .....	74
2.6.2.1 Flat plate reactors (FPR).....	75
2.6.2.2 Fermenter-type reactors (FTR).....	76
2.6.2.3 Biological and engineering challenges of tubular photobioreactors.....	78
2.7 An energetic analysis of the photosynthetic conversion process.....	79
2.7.1 The role of the local weather .....	80
2.7.2 The photosynthetically active radiation and the photosynthetic conversion efficiency.....	80
2.7.3 The photoinhibition process and the dark/light cycles .....	81
2.8 Gas, pH and temperature gradients.....	82
2.9 Optimal fluid dynamic conditions .....	83
2.10 Exploiting the microalgal swimming properties for photobioreactors .....	84
2.10.1 The continuum model for dilute algal suspensions within a flow field.....	86
2.10.2 Potential advantages for downstream processes .....	88
2.11 Alternative approaches for enhancing the microalgal applications.....	89
2.12 Chapter summary.....	90
<b>Chapter 3: Experimental apparatus and procedures</b>	
3.1 Chapter layout.....	91
3.2 Optimal cultivation of <i>Dunaliella Salina</i> cells.....	91
3.2.1 <i>Dunaliella Salina</i> physiology .....	92
3.2.2 The Hejazi and Wijffels modified medium.....	93
3.2.3 Preparation of <i>Dunaliella Salina</i> suspensions.....	94
3.3 Technical properties of microfluidic devices .....	96
3.3.1 The microfabrication process.....	99
3.4 Why did we employ the brightfield illumination technique and microfluidic devices?.....	104
3.4.1 Photobioreactors optimisation: a new approach .....	105
3.4.2 Olympus IX71 inverted microscope.....	105
3.4.3 Main technical features of the used objectives .....	107
3.4.4 The lateral resolution and the depth of field.....	109
3.5 The experimental setups .....	110

3.6 The flow visualisation .....	114
3.6.1 The optimal exposure time .....	116
3.6.2 The most relevant experimental issues.....	117
3.7 The image analysis process.....	118
3.7.1 Pre-processing the experimental videos .....	119
3.7.1.1 Removing the fixed parts from experimental videos .....	119
3.7.1.2 Background subtraction.....	120
3.7.1.3 Thresholding and binary conversion processes .....	121
3.7.2 Filtering the desired features of the algal cells.....	122
3.7.3 The tracking process and the analysis of the results.....	124
3.7.4 Limits of the image analysis process .....	124
3.8 Chapter summary.....	125
<b>Chapter 4: From microfluidic devices to photobioreactors: the study of living <i>Dunaliella Salina</i> cells</b>	
4.1 Chapter layout.....	126
4.2 The current procedure for the design of PBRs.....	127
4.3 The exploitation of static mixers in photobioreactors .....	130
4.4 Intrinsic features of different microalgal strains and their effects on photobioreactors.....	131
4.5 Why should microfluidic devices and the image analysis be employed for optimising PBRs? .....	133
4.6 Experimental results regarding living <i>Dunaliella</i> cells.....	134
4.6.1 Terminal sinking velocity of a <i>Dunaliella</i> cell .....	134
4.7 <i>Dunaliella</i> cells at stagnant flow conditions .....	136
4.7.1 Effects of microfluidic geometries on algal behaviours at stagnant conditions .....	137
4.7.2 The study of freely swimming microalgae: potential benefits for photobioreactors .	141
4.8 Effect of fluid flow on algal cell behaviours: straight geometry .....	143
4.8.1 The governing equations .....	143
4.8.1.1 Fully-developed laminar flow within a rectangular channel.....	144
4.8.1.2 The continuum model for dilute algal suspensions and the advection-diffusion equation .....	145
4.8.2 Algal behaviours in the straight channel .....	146

4.8.2.1 The most significant algal responses and the microgrid employed for the straight channel.....	148
4.8.3 Quantification of dispersion and walls interactions of <i>Dunaliella</i> cells within a straight channel.....	151
4.9 <i>Dunaliella</i> cells and static mixers .....	155
4.9.1 General effects of contraction and expansion geometries on flows of different fluids .....	155
4.9.2 Fluid dynamic effects induced by an abrupt contraction on a laminar flow .....	157
4.9.3 Qualitative effects of the contraction-expansion geometries on the algal behaviours.....	160
4.9.4 Quantification of the effects due to microgeometries on living algal cells .....	164
4.10 Chapter Summary.....	176
<b>Chapter 5: Dead <i>Dunaliella Salina</i> cells: implications for PBR and static mixers</b>	
5.1 Chapter layout.....	178
5.2 From optimal culturing conditions to algal demise.....	178
5.2.1 Light effects on the algal cells .....	180
5.2.2 Temperature effects on algal cultures.....	182
5.2.3 Effects of parasitic organisms on algal cultures .....	183
5.2.4 Effects of dead cells accumulations on algal cultures .....	184
5.3 Dead <i>Dunaliella</i> cells: the killing procedure and experimental setup.....	185
5.3.1 The development of the killing procedure .....	185
5.3.2 The development of the experimental setup .....	188
5.4 Fluid dynamic behaviours of passive particles in flow .....	190
5.4.1 Particle Reynolds number.....	191
5.4.2 The tubular pinch effect for spherical and non-spherical particles .....	192
5.4.3 The governing lift forces .....	194
5.4.4 Potential implications for photobioreactors.....	197
5.5 Exploring dead cell behaviour: objectives and procedures .....	198
5.6 Quantification of the microgeometries effects on dead <i>Dunaliella</i> cells .....	199
5.7 Effects of the geometrical configuration on the photobioreactor productivity .....	214
5.7.1 Area of the cell free region: a potential indicator for the improvement of light distribution within PBRs .....	216
5.7.2 Effects of homogeneous irradiance levels on biomass productivity .....	221

5.8 Chapter Summary.....	223
<b>Chapter 6: Effects of cell fragility on algal cultures: exploiting microfluidic devices for quality controls purposes</b>	
6.1 Chapter layout.....	225
6.2 Effects of shear-induced damage on cultured cells .....	226
6.2.1 Sensitivity of cultured cells to shear.....	226
6.2.2 The critical shear threshold value for <i>Dunaliella</i> cells.....	228
6.2.3 Preventing cells from being damaged: the case of photobioreactors equipped with static mixers.....	229
6.3 Exploitation of targeted image analysis for quality controls purposes: a practical example .....	232
6.3.1 Experimental study of the 7-1 ECR channel centreline .....	232
6.3.2 Instantaneous and average velocities of the cells .....	235
6.3.3 Quantification of the inertial-induced effects on the algal behaviours .....	236
6.3.4 Sensitivity to shear: implications for photobioreactors .....	241
6.4 Size and shape distribution of used <i>Dunaliella</i> cells .....	242
6.4.1 The role of size and shape in the cultivation process.....	243
6.4.2 Experimental procedure for assessing size and shape distributions.....	244
6.4.3 Assessing size and shape distributions: data analysis and results discussion .....	246
6.5 The scaling-up of tubular photobioreactors .....	252
6.6 Chapter Summary.....	255
<b>Chapter 7: Studying photobioreactors through microfluidic devices: main limitations and future work</b>	
7.1 Chapter layout.....	257
7.2 The most important results achieved during this research work: a recap .....	258
7.3 Limitations of the suggested approach and main implications for the results.....	260
7.3.1 Employing the research approach in parallel with other procedures: two practical examples .....	265
7.4 Further suggestions for future research work .....	267
7.5 Final conclusions .....	269
Appendix 3.1: Preparation of the culture medium and its physical properties .....	270
Appendix 3.2: Preparation of <i>Dunaliella Salina</i> suspensions .....	276
Appendix 5.1: Dead <i>Dunaliella Salina</i> cells: the killing procedure and their density.....	278
References.....	280

## – Chapter 1 –

# Microswimmers and low Reynolds numbers world

## 1.1 Chapter layout

The first part of the chapter is concerned with some general features about microorganisms, such as their ecological and industrial importance, their taxonomy, the distinction between prokaryotes and eukaryotes, *etc.*, focusing special attention on the puzzling properties of microswimmers (*i.e.* that particular variety of microorganisms able to propel themselves), which will be introduced by analysing the main differences between them and passive particles.

Next, particular emphasis will be given to those varieties of different environmental stimuli (*i.e.* the taxis effects) which can be used for controlling and engineering the cells' behaviours and may lead to algal accumulation phenomena in aqueous environments. Furthermore, the main characteristics and constraints of the microscale world will be explored through the Stokes equation, discussing also how microswimmers manage to overcome them.

Moreover, the main hydrodynamic interactions between cells and other cells and between cells and boundaries are physically described, considering also the effects of gravitational and viscous torques acting on bottom-heavy swimming algal cells, at different fluid dynamic conditions. Finally, the last part of the chapter addresses the transport of dissolved chemicals at low Reynolds numbers and the resulting biological implications.

## 1.2 Introduction to microorganisms

This section introduces microorganisms, considering some of their characteristics and applications, describing the main differences between prokaryotic and eukaryotic cells and also classifying them according to the sources of energy they use. The effects of size and morphology on microorganismal behaviours have also been mentioned briefly, as they will be discussed in details in other sections of the thesis.

The importance of microorganisms (from the Greek μικρός, *mikros*, "small" and ὄργανισμός, *organismós*, "organism") and their fundamental functions in different contexts is well-documented. [1] Microorganisms constitute the major part of the world's biomass and have a wide range of fundamental biological functions in ecosystems [2, 3]; in fact, they play a vital role in all the biogeochemical cycles and help to regulate the climate by fixing the atmospheric carbon. [3]

Microorganisms represent the lowest level of the food chain [4], helping to transfer dissolved organic compounds to larger organisms that feed on them. [5] They can be found in almost every part of the biosphere, such as aqueous environments, deserts and glaciers. What's more, some of them can survive under extreme conditions (extremophiles), as they have been found living in deep seas, acidic and alkaline environments, *etc.* [6, 7]

Microorganisms are utilised in a wide range of applications that encompass food and beverage preparation, genetic engineering, renewable energy and so on. For instance, fermentation involves the use of yeast (that is an eukaryotic microorganism) [8], while some bacteria (*e.g.* Lactic acid bacteria) are used for the production of milk derivatives. [9] Furthermore, photosynthetic microalgae have been exploited for the production of bio-hydrogen and biodiesel. [10] Both larger organisms and microorganisms may have mutual symbiotic interactions; some of them can be harmful (*e.g.* parasites, viruses that carry diseases, *etc.*) and some of them can be useful (*e.g.* digestive bacteria, reproductive fluids, *etc.*). [3, 11]

### **1.2.1 Taxonomy of microorganisms**

The classification of the living world has been achieved by the definition of two kingdoms, the animal kingdom and the plant kingdom. Nevertheless, botanists and biologists had been experiencing many problems with the microorganisms' classification, since many of them have certain features that give equal reason for placing them in both kingdoms (*e.g.* certain microalgae exhibit both photosynthesis and motility). Hence, for microorganisms, a further subdivision had been adopted between organisms without a cell nucleus (*i.e.* prokaryotes) and those with it (*i.e.* eukaryotes). [8]

Later, this scheme has been superseded by a three-domain system (*i.e.* the phylogenetic tree of life) (see **Figure 1.1**), which classified organisms as bacteria, archaea and eukaryota, because it was noticed that prokaryotic bacteria have different biological characteristics from the archaea (*e.g.* cell wall composition, protein synthesis, *etc.*). [12, 13]

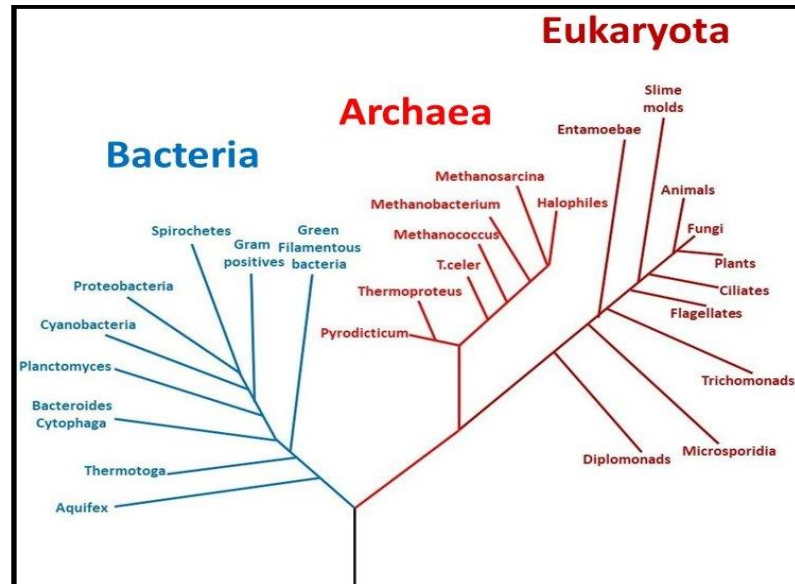


**Figure 1.1 – The phylogenetic tree of life represents the three life domains: Bacteria, Archaea and Eukaryota. The three domains are implied to have descended from a common ancestor and this explains why the three branches are linked to the last universal common ancestor (LUCA), indicated by the black trunk at the bottom of the tree. The tree was suggested by Carl Woese *et al.* [14]. Adapted from [14].**

To provide context for the study of swimming algae, some of the main differences between the domains will be discussed in the next sections, introducing also prokaryotic and eukaryotic cells.

### 1.2.1.1 Prokaryotic organisms

Prokaryotic organisms can be unicellular or multicellular. Compared with the eukaryotes, they do not have a nucleus, which is the organelle containing the genetic information (*i.e.* the Deoxyribonucleic acid [DNA]). Furthermore, they lack of all the membrane-bound organelles (*e.g.* mitochondria, endoplasmic reticulum, *etc.*). [1] There are three major shapes that prokaryotes can have, cocci (round), bacilli (rod-like shape) and spirilla (helical shape). [13, 15] Prokaryotic organisms include bacteria and archaea. Bacteria prefer to live in damp environments and can obtain food through parasitism (*i.e.* exploiting other living organisms), saprophytism (*i.e.* from decomposing organisms) or photosynthesis.

They reproduce asexually by either binary fission, in suitable environments, or spore formation, in relative harsh environments. [16] Archaea live in hostile environments (*e.g.* very high temperatures, salty environments, *etc.*) and they represent the descendants of some of the oldest forms of life on the planet. [17]

### 1.2.1.2 Eukaryotic organisms

Eukaryotes include animals, plants, protozoans and fungi. Unlike prokaryotes, their cells contain many different organelles, like the nucleus, which houses the genetic information, the endoplasmic reticulum, responsible for synthesizing proteins, chloroplasts, used for photosynthesis, *etc.* (see **Section 2.3.2**). [1, 18]

More differences between prokaryotes and eukaryotes can be seen in **Table 1.1**. [1, 18]

**Table 1.1 – Major differences between eukaryotic and prokaryotic organisms.**

Properties	Prokaryotes	Eukaryotes
Nucleus	absent Nucleus	Nucleus present
Cell wall	All have cell wall	Some have cell wall
Ribosomes	30S and 50S ribosomes	40S and 60S ribosomes
Plasmid	Common	Rare
Number of cells	Mostly unicellular	Mostly multicellular
Cell diameter	Body length less than 2 $\mu\text{m}$	Body length greater than 2 $\mu\text{m}$
Nutrition	Parasitism, saprophytism	Parasitism, saprophytism, autotrophic
Reproduction	Asexual	Sexual

### 1.2.2 Morphology and shape

Morphologically, microorganisms can be elongated, spherical or round and their size ranges from  $\sim 0.1$  to  $1,000 \mu\text{m}$ . [19, 20] On average, small organisms are spherical while elongation tends to increase with size, albeit the adaptive significance of their morphology is often unknown. [20, 21] Both dimensions and shapes influence their biological behaviours and interactions with the surrounding fluid, *i.e.* their metabolisms, their motility, their tendency for clustering or living as single cells, *etc.* [21, 22] For example, small cells, characterised by large surface-to-volume ratios (SVR), can better uptake dissolved nutrients by osmosis and are strongly affected by the random Brownian motion. [21, 23] More examples about morphology and shape effects can be found in the **Sections 1.10** and **1.12**, concerning the hydrodynamic interactions and the nutrient uptake of dissolved nutrients.

### 1.2.3 Autotrophic, heterotrophic and mixotrophic organisms

Depending on the utilised source of energy, organisms can be classified as autotrophic or heterotrophic. Autotrophic organisms can produce complex organic compounds from simple substances, using energy from either light (photosynthesis) (*e.g.* the biflagellated microalga *Dunaliella Salina* [DS]) or inorganic chemical reactions (chemosynthesis) (*e.g.* the bacterium *Venenivibrio stagnispumantis* obtains its energy by oxidizing hydrogen). [1, 24]

Heterotrophs need organic carbon for growth but cannot fix it from inorganic sources. If they obtain energy from light are termed as photoheterotroph (*e.g.* *heliobacteria* [1]), while if they use chemical energy, then are considered chemoheterotroph (*e.g.* some microorganisms that belong to the archaea domain, like *Sulfolobus solfataricus* [25]).

Nevertheless, some microorganisms, known as mixotrophic, can take advantage of both mechanisms, surviving in various environmental conditions by using different sources of energy and carbon. [26]

As better explained in the next section, plants, algae or more in general planktonic microorganisms (*e.g.* DS cells) exploit the photosynthesis for converting solar light energy into chemical energy, which is employed to fuel their biological activities. [27]

## 1.3 Planktonic microorganisms

Planktonic microorganisms have been triggering growing attention owing to their utilisation for the production of biofuels. This kind of microorganisms can be found in photic zones of aqueous environments, which extend from the surface down to a depth where the solar light intensity falls to one percent of that at the surface. [5, 27]

### 1.3.1 The photosynthetic process

Planktonic microorganisms produce nearly half of the world's oxygen via photosynthesis, a naturally-occurring process where sun light, water and carbon dioxide are utilised to produce carbohydrates and oxygen (see **Figure 1.2**). [1, 28]

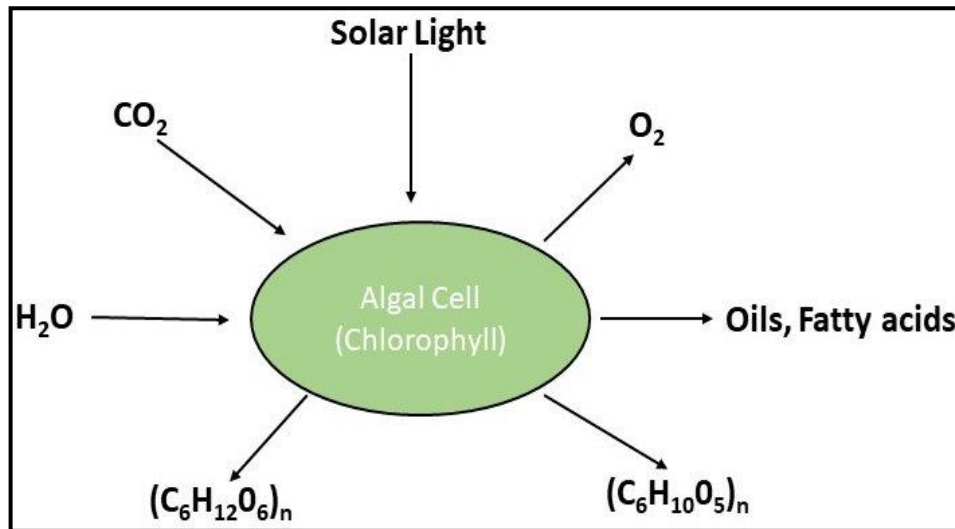


Figure 1.2 – Schematic of the photosynthetic process in a microalgal cell. Fundamentally, photosynthesis converts sunlight into chemical energy, leading to the production of oxygen and fixes carbon dioxide into sugar. Adapted from [29].

The general photosynthetic reaction can be represented as: [1, 28]



More specifically, the photosynthetic process occurs in some cellular organelles, termed chloroplasts, and can be divided into two phases: the light reactions and the Calvin cycle.

During the light-dependent reactions, water and light are exploited to produce energy in the form of Adenosine triphosphate (ATP), Nicotinamide adenine dinucleotide phosphate (NADPH) and oxygen molecules as a by-product:



ATP and NADPH will be used in the Calvin cycle, along with carbon dioxide, to synthesize sugar:



The obtained glucose is transported as soluble sugar within the cell and is used in the respiration process to obtain energy. Moreover, it is also converted into insoluble substances (*i.e.* oils, fat and starch) and stored within the cell. [1, 28]

## 1.4 Microswimmers

This section introduces the definition of microswimmers, providing also a biological description of the appendages employed by these organisms to swim (*i.e.* cilia and flagella).

Generally, microorganisms can also be classified as motile and non-motile; this research work is concerned with motile unicellular microorganisms, also known as microswimmers, which can swim and propel themselves by exploiting some contractile appendages or deforming their own body. This definition includes bacteria, spermatozoa, unicellular algae and protozoans. [2, 30]

Microswimmers can have two types of appendages: cilia and flagella. Flagella are usually employed for locomotion and can be distinguished as prokaryotic and eukaryotic, whereas cilia can be further classified as motile and non-motile (or primary cilia); therefore they have many functions (*e.g.* cleaning, filtering, *etc.*) and can also be found in human sensory organs, such as eyes and nose. [31] Motile cilia and eukaryotic flagella are biologically comparable but fluid dynamically different, since cilia are more numerous, flexible and may occur throughout the cellular surface. Furthermore, flagella are longer (up to 150  $\mu\text{m}$ ), while cilia are shorter (from 5 to 10  $\mu\text{m}$ ). [31]

As better explained in the next sections, prokaryotic and eukaryotic flagella are characterised by different structures, sources of energy, types of motion, compositions and working mechanisms (see **Table 1.2**). [32, 33]

**Table 1.2 – The main differences between prokaryotic and eukaryotic flagella.**

	<b>Prokaryotic Flagella</b>	<b>Eukaryotic Flagella</b>
Motion	Rotation	Bending
Energy	Proton Pump	ATP Pump
Structure	Helical Hollow	9+2 arrangements
Protein	Flagellin	Microtubule

### 1.4.1 Prokaryotic flagella

As shown in **Figure 1.3**, a prokaryotic flagellum comprises a basal body (the two protein rings, the rod and the sleeve structure) that anchors the flagellum in the cell membrane, a hook and a filament. The filament is  $\approx 20$  nm in diameter and is made of a singular globular protein, known as flagellin, which wraps around in a helical fashion to create

a rigid hollow cylinder. [34] The hook connects the basal body to the filament. The protein rings act as proton pumps that allow the movement of hydrogen ions across the cell membrane down their electrochemical gradients. This movement of ions rotates the rings at 100-1000 Hz, which in turn rotates the basal body creating the anti-clockwise rotation of the flagella. If the prokaryotic cell wants to change the swimming direction, the flagellum must rotate clockwise, changing the entire direction of motion of the cell. [20, 30, 35]

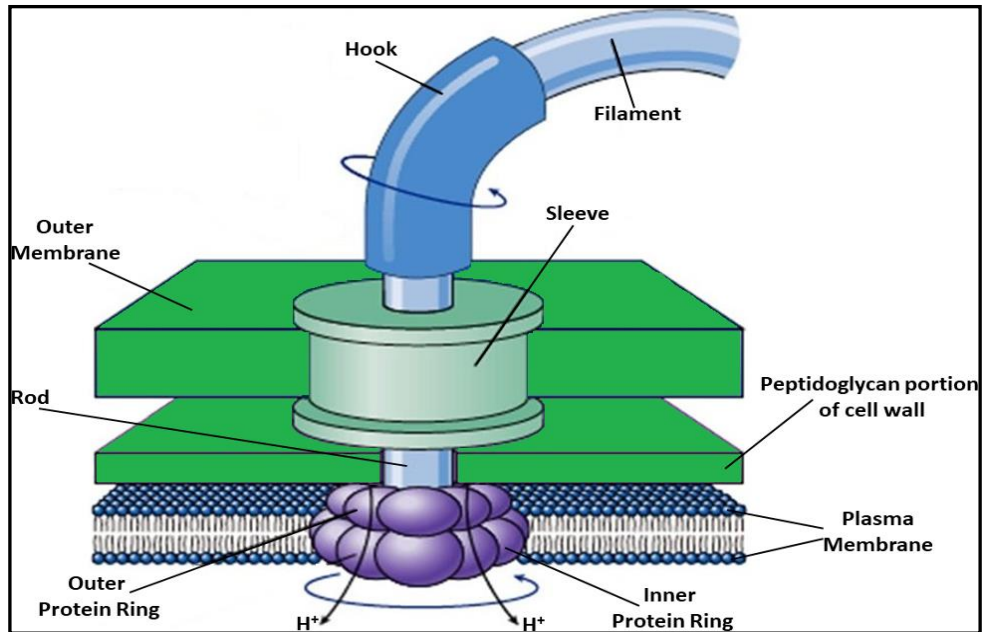


Figure 1.3 – Structure of a prokaryotic flagellum. These flagella are powered by a motor present in the cytoplasmic membrane and uses proton ions for the movement of the propeller. Adapted from [35].

## 1.4.2 Eukaryotic flagella

Eukaryotic flagella are 200-400 nm in diameter, 10-150  $\mu\text{m}$  long, contain more than 250 types of proteins and are enclosed inside the plasma membrane, anchored to the cell through a basal body and sometimes can be beset by hairs or scales. [36] The inner core of its external part consists of a cytoskeletal called the axomene that contains 9 doublet pairs of protein filaments, termed as microtubules, which create a circular arrangement surrounding two central microtubules, known as “9+2” structure (see **Figure 1.4**). [37] The outer pairs of microtubules are connected to the axomene by a protein called Nexin. Each doublet microtubule has an “A” tubule and “B” tubule. A tubules are connected to numerous molecules of a protein called dynein, which are motor proteins that utilise ATP to create a motion of the microtubules, forcing them to slide one another, generating an internal shear that is converted into a whip-like motion, propelling the cell forward. [8, 30]

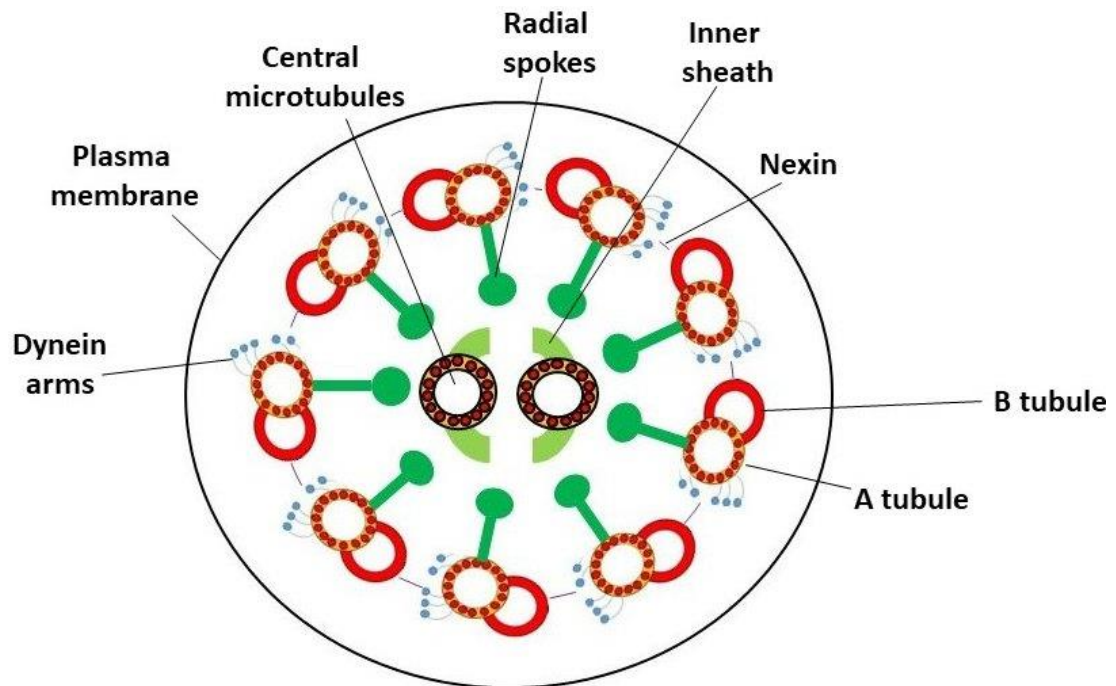


Figure 1.4 – Structure of the axoneme, *i.e.* the cross section of a eukaryotic flagellum. Eukaryotic flagella are microtubule-based structures that resemble cilia and may have a common origin [38]. Adapted from [38].

## 1.5 Comparison between microswimmers and passive particles

In order to better understand microswimmers' behaviours, this section provides a description of their most important features, specifically feeding, the ability of regulating their settling rate and sensing (*i.e.* taxis-biased behaviours) which, along with motility, distinguish them from lifeless particles. [20]

### 1.5.1 Feeding

Microorganisms need to feed through the uptake of dissolved compounds (*e.g.* nitrate, phosphate, iron, *etc.*) [20] and this plays a crucial ecological role in all the biogeochemical cycles (such as nitrogen and carbon cycles). [5] Moreover, nutrient transport, diffusion and the resulting uptake can influence microswimmers' motility and behaviours (see **Section 1.12**). [20]

## 1.5.2 Settling rate

Being denser than the fluid where they live [2], microswimmers must be able to control their settling rates in order to stay afloat at suitable altitudes. This can be achieved by exploiting either dynamic solutions (*e.g.* obtaining lift by swimming) or static solutions (*e.g.* regulating their form resistance or buoyancy) [20, 39], *e.g.* many diatoms and dinoflagellates can decrease their drag and control their form resistance by using their cellular spines, whereas the buoyancy can be controlled using techniques such as carbohydrate ballasting or ion replacement. [40, 41]

## 1.5.3 Sensing: the taxis effects

As we shall see in the next sections, some microorganisms can use their sensing, responding positively or negatively to a variety of different environmental stimuli, termed as taxis effects, and consequently both their motion and their behaviours can be influenced, therefore different microorganisms exhibit distinct forms of taxes. [3, 42]

### 1.5.3.1 Chemotactic behaviour

Chemotactic organisms can sense chemical gradients in their environment and move towards higher concentrations of a favourable chemical or away from a poisonous one. One of the most studied chemotactic organisms is the prokaryotic bacterium *Escherichia Coli* (*E. Coli*) that tends to swim towards higher oxygen concentrations. [3, 43] Some eukaryotic microorganisms also exhibit chemotactic behaviours (*e.g.* spermatozoa swim towards chemoattractants released by an egg [44]). Chemotaxis is fundamental in a wide range of fields, *e.g.* the bacteria *Pseudomonas putida* tends to swim towards harmful organic compounds, facilitating the bioremediation of contaminated sites [45] or, in oceans, chemotaxis increases the rate at which some limiting elements are recycled. [46]

### 1.5.3.2 Phototactic behaviour

Phototactic organisms are sensitive to light and can swim towards to or away from a light source, depending on its intensity. For example, photosynthetic algae (*e.g.* the algal genus *Chlamydomonas Reinhardtii* [CR]) need to swim up to the surface of aquatic environments in order to exploit the light for the photosynthesis. [3]

Phototaxis plays an important role in cells motion as their responses cause flagella to behave in different ways; for example, when a sharp increase in the light intensity occurs, CR cells stop swimming for a short period, align their flagella, adjust their swimming stroke and swim in the reverse direction (negative phototaxis). [47] In the particular case of chemotactic microalgae, a receptor-membrane is located across the eye-spot (see **Section 2.3.2**). [8]

Other taxis effects include magnetotaxis (sensitivity to an external magnetic field) [48], thermotaxis (sensitivity to heat) rheotaxis (sensitivity to shear) [49], gravitaxis (biased swimming against gravity) and gyrotaxis that occurs when bottom-heavy organisms undergo particular flow fields (*e.g.* simple shear flows) and the balance between gravitational and viscous torques may orientate their locomotion, leading to cell focusing in downwelling regions of the fluid [2, 42]; a detailed analysis of both the algal gravitactic and gyrotactic behaviours will be provided in the **Section 1.11**.

Nevertheless, as better described in the next section, the taxis-biased swimming behaviours may be responsible for the formation of complex patterns and plumes of highly concentrated microorganismal aggregations, termed as bioconvection, which can result in algal accumulations. [2, 3, 50]

## **1.6 Algal accumulations**

In aquatic environments, bioconvections may lead to the formation of those potentially dangerous algal accumulations, entailing environmental consequences, such as the horizontally-uniform distributions that absorb and scatter the solar light, creating non-uniform distributions of light intensity. Moreover, algal aggregations are generally nonlinear dynamical systems that may lead to overturning and Rayleigh-Bénard-type instabilities which affect surrounding fluids. [3, 10]

### **1.6.1 Rayleigh-Bénard-type instabilities**

Swimming cells are usually about 5% denser than their surrounding fluids [2], hence their accumulations may imply that certain regions of the fluid become denser than their neighbouring ones, resulting in fluid dynamic instabilities.

For instance, gravitactic and phototactic cells tend to accumulate on upper surfaces of aquatic environments, therefore the flux of up-swimming cells is balanced to the one of down-swimming organisms, leading to instabilities that resemble the ones due to Rayleigh-Bénard convection. [51]

### **1.6.2 Overtuning instabilities**

In shear flows, bottom-heavy cells tend to swim towards downwelling regions of the fluid, owing to the gyrotactic behaviour (see **Section 1.11**), hence the resulting added mass causes the fluid to sink quicker, increasing its average density, generating gyrotactic instabilities and leading to cell transport phenomena that occur much faster than the ones involving swimming alone. [47]

### **1.6.3 Controlling the cell's fluid dynamic behaviours**

Taxis effects have also been exploited to study and model the microswimmers' fluid dynamic behaviours and enhance the viability of their industrial applications. [10, 43] For example, Garcia and co-workers managed to control CR cells, taking advantage of both their gyrotactic and phototactic behaviours. In their experiments, they forced the microalgae to self-concentrate at the centre of a channel by using the right combination of light stimuli and flow vorticity; this has the potential to reduce algal accumulations at pipe walls and prevent fouling of surfaces due to adhesion processes (See **Section 2.4.2.1**). [43, 52]

Moreover, Croze *et al.* studied the macroscopic rings generated by the chemotactic bacterium *E. Coli* in Petri dishes filled with low-concentration agar solutions, observing that bacteria can be modelled as gases in a porous medium, albeit the same model was ineffective in describing bacterial behaviours at higher-concentration agar solutions. [3]

## 1.7 Why should microswimmers' fluid dynamic behaviours be studied?

The above-mentioned examples emphasise the importance of studying fluid dynamic behaviours of microswimmers residing within fluids that may undergo flows. Specifically, understanding the manner in which they swim and orientate relative to the main flow direction and the effects on their behaviours have acquired a new layer of ecological and industrial significance. [53]

For example, organisms naturally occur in large populations (*e.g.* planktonic blooms and biofilms) (see **Section 1.6**), therefore studying their fluid dynamic behaviours can help to control and prevent these potentially-toxic accumulations. [3, 54] Furthermore, analysing the behaviours of individual microswimmers has led to develop some mathematical models that have been used to simulate the dynamics of living microorganismal suspensions as continuum systems. These models have been particularly successful in describing algal pattern formations [2, 55] and transport of living cells suspensions in laminar and turbulent flows in photobioreactors (PBRs) (see **Section 2.10.1**). [10, 56]

As we shall see in the **2<sup>nd</sup> Chapter**, controlling and engineering the swimming cells' behaviours would also be beneficial for the design of PBRs and the viability of the algal biofuel production. [43, 52]

Nevertheless, the fully understanding of microswimmers' behaviours requires to outline the main features of the micro-scale world, creeping flows and their governing Stokes equation, which will be addressed in the next sections.

## 1.8 Low Reynolds numbers world

Microswimmers live in a world dominated by viscous forces and governed by counterintuitive physical rules that mediate crucial processes, including motility, nutrient uptake and hydrodynamic interactions. [20] Hence, the next sections introduce the main properties of viscous flows, their implications for swimming organisms and the Stokes equation, which governs the micro-scale world. [20, 30]

## 1.8.1 Creeping flows

In fluid mechanics, a fundamental dimensionless number is the Reynolds number ( $Re$ ) (named after the physicist Osborne Reynolds), which is the ratio of inertial to viscous forces:

$$Re = \frac{\text{Inertial forces}}{\text{Viscous forces}} = \frac{\rho_f \cdot U \cdot L}{\mu} \quad (\text{eq. 1.1})$$

where  $\rho_f$  and  $\mu$  are the density and the dynamic viscosity of the surrounding fluid,  $U$  is the flow speed and  $L$  is a characteristic length.

We can also define the kinematic viscosity  $\nu$  as the ratio of the dynamic viscosity to the density of the fluid:

$$\nu = \frac{\mu}{\rho_f} \quad (\text{eq. 1.2})$$

For a water-like medium,  $\rho_f = 10^3 \text{ kg}\cdot\text{m}^{-3}$ ,  $\mu = 10^{-3} \text{ Pa}\cdot\text{s}$ , hence  $\nu = 10^{-6} \text{ m}^2\cdot\text{s}^{-1}$ . Combining *eq. 1.1* and *eq. 1.2*,  $Re$  number can be rewritten as:

$$Re = \frac{U \cdot L}{\nu} \quad (\text{eq. 1.3})$$

There is a particular variety of flows, called Stoke flows or creeping flows, characterised by relatively low  $Re$  numbers and therefore where viscosity dominates over inertia or, in other words, inertia can be neglected. [20, 57]

Creeping flows can be due to: [58]

- Small  $L$ : *e.g.* swimming of microorganisms in body fluids;
- Small  $U$ : the motion of glaciers, the earth mantle or flows in rocks;
- Large  $\nu$ : due to either massless fluids or viscous fluids (*e.g.* molten lava [59]).

For a swimming organism,  $Re$  number can be defined as:

$$Re = \frac{V_s \cdot d_s}{\nu} \quad (\text{eq. 1.4})$$

where  $d_s$  is the microswimmer's characteristic size and  $V_s$  is the microswimmer's swimming speed.

In particular, considering a typical microswimmer with a size of 10  $\mu\text{m}$ , swimming at 80  $\mu\text{m s}^{-1}$  in a water-like medium, it can easily be worked out that its  $Re$  number is  $8 \times 10^{-4}$ . Thus, for motile organisms swimming in aqueous mediums,  $Re$  numbers range customarily between  $10^{-5}$  to  $10^{-3}$  or, that is to say, the majority of microswimmers live and thrive at low  $Re$  numbers (See **Table 1.3**). [20]

**Table 1.3 – The body lengths, speeds and  $Re$  for some swimming microorganisms. [60]**

Reynolds Number of different Organisms			
Organism	Body Length [ $\mu\text{m}$ ]	Speed [ $\mu\text{m s}^{-1}$ ]	$Re$
<i>Escherichia Coli</i> (Bacterium)	3	30	$9 \times 10^{-5}$
<i>Lytechinus</i> (Sea urchin)	5.1	160	$8.16 \times 10^{-4}$
<i>Chlamydomonas</i> (Flagellated)	13	60	$7.8 \times 10^{-4}$
<i>Euglena</i> (Flagellated)	50	80	$4 \times 10^{-3}$
<i>Tetrahymena</i> (Ciliate)	70	480	$3.36 \times 10^{-2}$
<i>Paramecium</i> (Ciliate)	210	1000	$2.1 \times 10^{-1}$
<i>Convoluta</i> (Ciliated flatworm)	2000	600	1.2

Physically, the effects of the absence of inertia on the microswimmers' behaviour can be shown by observing what would happen to the previously considered swimming organism, if it suddenly stops rotating its flagella and propelling itself; under the effects of its own drag, the forward movement of the cell would cease instantaneously and the microswimmer would come to rest within a breaking distance of about 1.8 nm. [20]

Generally, creeping flows can be modelled using a linearized form of the Navier-Stokes equation (*i.e.* the Stokes equation) that will be discussed in the next section and will also be employed in the **Section 1.8.3** to describe the main physical properties of Stokes flows and their implications for swimming organisms.

## 1.8.2 The Stokes equation

In fluid mechanics, the fundamental constitutive equations are the conservation of mass, momentum and energy. If temperature effects can be neglected, it must only be considered the continuity equation, which represents the differential form of the conservation of mass principle:

$$\frac{\partial \rho_f}{\partial t} + \nabla \cdot (\rho_f \mathbf{U}) = 0 \quad (\text{eq. 1.5})$$

and the Navier-Stokes equation that expresses the conservation of momentum:

$$\rho_f \left( \frac{\partial \mathbf{U}}{\partial t} + \mathbf{U} \cdot \nabla \mathbf{U} \right) = -\nabla p + \mu \nabla^2 \mathbf{U} + \mathbf{f} \quad (\text{eq. 1.6})$$

where  $\mathbf{U}(\mathbf{u}, \mathbf{v}, \mathbf{w}, t)$  is the flow velocity ( $\mathbf{u}, \mathbf{v}, \mathbf{w}$  are the velocity components in the  $x, y$  and  $z$  directions) and  $\mathbf{f}$  represents some other body forces (e.g. the gravitational components). Moreover, the term  $\frac{\partial \mathbf{U}}{\partial t}$  refers to the unsteady acceleration,  $\mathbf{U} \cdot \nabla \mathbf{U}$  to the convective acceleration,  $\nabla p$  to the pressure gradient and  $\mu \nabla^2 \mathbf{U}$  is the viscous dissipation term, represented by the vector Laplacian of the velocity field. [61]

For swimming microorganisms, the surrounding fluid is an incompressible Newtonian liquid (i.e. its density is constant), and therefore eq. 1.5 becomes:

$$\nabla \cdot \mathbf{U} = 0 \quad (\text{eq. 1.7})$$

The  $Re$  number can be introduced into the Navier-Stokes equation by making it dimensionless through the definition of appropriate length, time and velocity scales ( $L, t_c$  and  $U_c$  respectively), so that  $\tilde{\mathbf{u}} = \frac{\mathbf{U}}{U_c}$  and  $\tilde{t} = \frac{t}{t_c}$ , while the nondimensional pressure and body forces can be defined as  $\tilde{p} = \frac{p \cdot L}{\mu \cdot U_c}$  and  $\tilde{\mathbf{f}} = \frac{\mathbf{f} \cdot L^2}{\mu \cdot U_c}$ . [20]

Consequently, eq. 1.6 and 1.7 become:

$$\tilde{\nabla} \cdot \tilde{\mathbf{u}} = 0 \quad (\text{eq. 1.8})$$

$$\frac{Re}{Sr} \frac{\partial \tilde{\mathbf{u}}}{\partial \tilde{t}} + Re \tilde{\mathbf{u}} \cdot \tilde{\nabla} \tilde{\mathbf{u}} = \tilde{\nabla}^2 \tilde{\mathbf{u}} - \tilde{\nabla} \tilde{p} + \tilde{\mathbf{f}} \quad (\text{eq. 1.9})$$

where  $Sr = \frac{t_c \cdot U_c}{L}$  is the Strouhal number, which compares a forcing timescale to the flow timescale, while tildes denote nondimensional variables. [20]

As discussed in the **Section 1.8.1**, microorganisms live at low  $Re$  numbers, thus the Navier-Stokes equation reduces to the Stokes equation:

$$\nabla p = \mu \nabla^2 \mathbf{U} + \mathbf{f} \quad (\text{eq. 1.10})$$

provided also that  $\frac{Re}{Sr} \ll 1$ , which is the required condition for neglecting the unsteady term. [20] Specifically, for microswimmers,  $Sr$  is calculated taking into account the flagellar beat period  $T_f$ :

$$Sr = \frac{T_f \cdot V_s}{d_s} \quad (\text{eq. 1.11})$$

Thus, for a typical microswimmer with a size of  $10 \mu\text{m}$ , swimming at  $80 \mu\text{m s}^{-1}$  in a water-like medium, with a flagellar beat period  $T_f$  of  $1/100 \text{ s}$ ,  $Re = 8 \times 10^{-4}$  (see **Section 1.8.1**),  $Sr = 8 \times 10^{-2}$  and therefore  $\frac{Re}{Sr} = 10^{-2} \ll 1$ , meaning that the unsteady term can be disregarded [20]. However,  $Re$  numbers of motion are never zero, therefore the Stokes equation never describes the fluid flow rigorously, albeit, in most cases relevant to microswimming, it turns out to be conveniently accurate. [8]

As explained in the next section, Stokes equation can be further exploited for outlining the main characteristics and constraints of creeping flows; in particular, the equation is independent of time and linear (see *eq. 1.10*) and these properties lead to kinematic reversibility, an important and well-known symmetry property associated with the motion of any body at zero  $Re$  numbers. [20, 30]

### 1.8.3 Main properties of Stokes flows

The Stokes equation has several proprieties that can be employed to describe the main features of the micro-scale world and how they affect the microswimmers locomotion. [20]

Its first property is the pseudo-steadiness, owing to the fact that the equation does not have any time-derivative of the velocity field, *i.e.* time has no influence. This implies that the fluid is able to perfectly respond instantaneously to any forces exerted anywhere within its domain and therefore the rate of applying forces in the fluid is immaterial. Consequently, when a microswimmer propels itself moving its appendages and exerts instantaneous forces on the surrounding environment, the fluid will respond immediately and therefore its net motion is independent of how fast it deforms its body. [20]

Its second property is linearity, due to the fact that all the variables of the Stokes equation (*i.e.*  $p$  and  $\mathbf{U}$ ) appear only linearly or, in other words, there are no products between the variables or their gradients; this is not true for the Navier-Stokes equation (*i.e.* at high  $Re$  numbers), where the non-linear advection term must be taken into account. As a result, the linear combination of two solutions of the Stokes equation is also a solution and this has a practical importance as complex flow fields can be solved and assembled by taking advantage of the superposition principle. [20]

The two above-mentioned properties imply a third one: kinematic reversibility; specifically, if the applied forces within a Stokes flow are reversed over time, the fluid will reverse perfectly too or analogously, a time-reversed Stokes flow would be the same as the original one (*e.g.* reversing the flow direction, the exerted drag would be the same). [20]

This has also biological consequences for the motion of organisms in the Stokes regime, as can be better understood considering the Purcell's scallop theorem. [57] At the macroscopic scale, a swimmer like a scallop, which can be thought as constituted of two rigid flaps connected by a hinge, can simply move by exploiting a symmetrical mechanism which consists of opening and closing its flaps in order to, respectively, send water in and out (see **Figure 1.5**). [62]

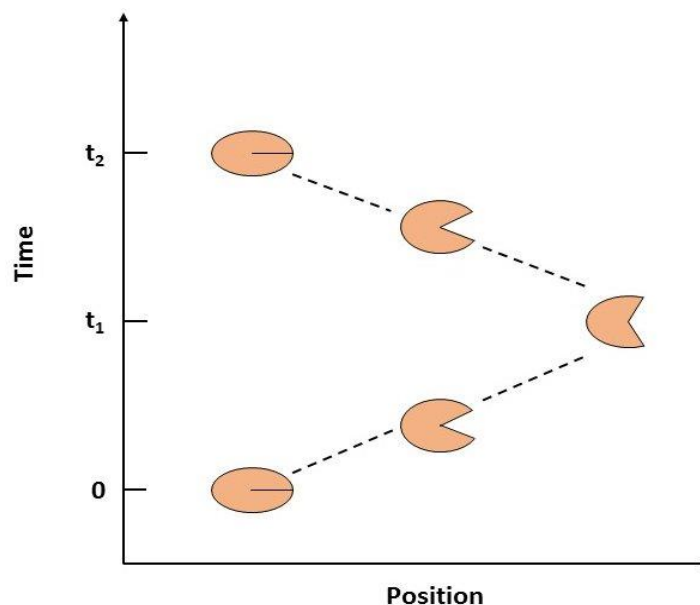


**Figure 1.5** – According to the scallop theorem, a swimmer must deform in a way that is not invariant under time-reversal. In particular, opening and closing its flaps, a scallop will not produce any net motion as the distance covered in the first half-cycle is cancelled by the negative distance covered in the second half-cycle. Adapted from [63].

Nonetheless, at low  $Re$  numbers, this symmetric mechanism does not produce propulsion, as it results in a reciprocal motion, which is obtained when a motile organism swims deforming its body and following a certain sequence that is reversible in time. [20, 57] In other words, in the viscosity-dominated world, any symmetrical swimming mechanisms do not produce any motion. [57]

Hence, as we shall see better in the next section, kinematic reversibility requires that, when a microswimmer propels itself, the periodic movement of its appendages must not be reversible in time so as to generate a net propulsive force and overcome the constraints of the micro-scale world. [20, 30, 57]

## 1.9 Overcoming the Stokesian constraints: the drag anisotropy and the most important swimming strategies

This section will introduce a fundamental property for the locomotion at low  $Re$  numbers, *i.e.* the flagellar drag anisotropy, deriving from the fact that, while a flagellum beats and generates a wave, its normal drag coefficient is larger than the transversal one, resulting in a net propulsive force that permits an organism to swim. [30] Moreover, few non-time-reversible swimming strategies will also be mentioned, focusing particular attention to the run and tumble mechanism, which allows bacteria like *E. Coli* to swim and bypass the Stokesian constraints. [57, 64]

Commonly, while swimming, microswimmers exploit a fundamental feature of their slender appendages, *i.e.* the flagellar drag anisotropy. As shown in **Figure 1.6**, the velocity  $\mathbf{u}_f$  of a straight beating flagellar filament section, moving at an angle  $\theta_f$  with the local tangent, will have a transversal component  $\mathbf{u}_{||} = \mathbf{u}_f \cdot \cos\theta_f$  and a normal component  $\mathbf{u}_{\perp} = \mathbf{u}_f \cdot \sin\theta_f$ , leading to both a parallel and a perpendicular drag force: [30]

$$\mathbf{F}_{d||} = -\xi_{||} \cdot \mathbf{u}_{||} = -\xi_{||} \cdot \mathbf{u}_f \cdot \cos\theta_f \quad (\text{eq. 1. 12})$$

$$\mathbf{F}_{d\perp} = -\xi_{\perp} \cdot \mathbf{u}_{\perp} = -\xi_{\perp} \cdot \mathbf{u}_f \cdot \sin\theta_f \quad (\text{eq. 1. 13})$$

being  $\xi_{\perp}$  and  $\xi_{||}$  the normal and transversal flagellar drag coefficients. [30]

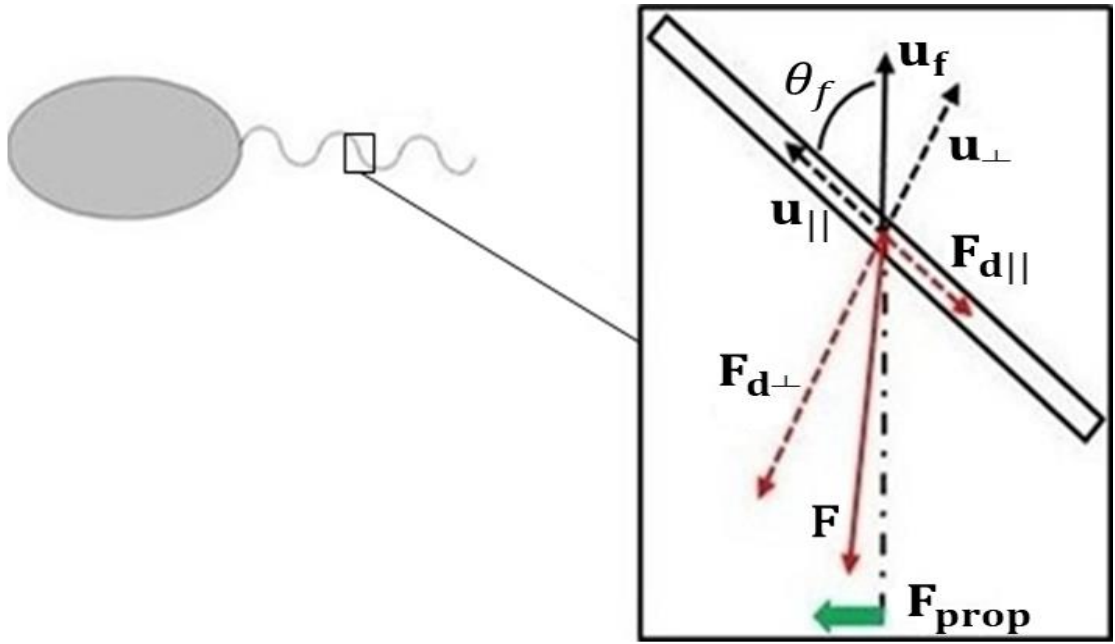


Figure 1.6 – For a slender filament moving in an unbounded Newtonian fluid, the normal Stokes drag coefficient is almost twice than the one in the parallel direction, resulting in a drag anisotropy which is a fundamental property for the propulsion at low  $Re$  number flows. [30] Adapted from [30].

Nevertheless,  $\xi_{\perp}$  is larger than  $\xi_{\parallel}$  (typically  $\xi_{\perp} \sim 2 \xi_{\parallel}$ ) leading to a flagellar drag anisotropy which results in a propulsive force  $\mathbf{F}_{\text{prop}}$ , given by: [30, 65]

$$\mathbf{F}_{\text{prop}} = (\xi_{\parallel} - \xi_{\perp}) \mathbf{u}_f \cdot \sin\theta_f \cdot \cos\theta_f \quad (\text{eq. 1.14})$$

The drag anisotropy is fundamental for the microswimmers' locomotion because it allows propulsive forces to be created, since this kind of propulsion would not be possible under isotropic drag. [30, 66]

Thus, in order to bypass the constraints of reversibility, microorganisms must swim using drag-based propulsive thrusts, produced by exploiting different asymmetric non-time-reversible swimming strategies. The most important are the corkscrew technique (*i.e.* the helical rotation of rigid appendages by prokaryotes, *e.g.* *E. Coli*), and the flexible oar technique (*i.e.* the nonreciprocal motion of slender flagella by eukaryotes, *e.g.* DS). However, biological methods of propulsion are varied and range from mechanisms involving a single appendage (*e.g.* spermatozoa and monotrichous bacteria) to biflagellated locomotion for algae (*e.g.* CR and DS cells). [42, 57]

Nevertheless, one of the most well-known asymmetric swimming strategy is the run and tumble pattern exhibited by bacteria. [64]

Specifically, during the run phase, due to geometric and hydrodynamic interactions, the flagella of peritrichous bacteria (meaning that they have appendages distributed all over their surface, like *E. coli*, *Salmonella typhimurium*, and *Bacillus subtilis*) tend to bundle together into twisting corkscrews that rotate anticlockwisely, propelling the bacteria in a nearly straight run. [64] After a short time, one or more flagella dissociate from the bundle, reversing the rotating direction, causing the bacterium to tumble and reorienting it by a nearly random angle, before a new run begins. [67] At long times, this swimming strategy results in a random walk that has a diffusivity comparable with that of small molecules. [64] While they are swimming, bacteria can be affected by the presence of favourable conditions (*e.g.* higher food concentrations), that cause runs to become longer, biasing the chemotactic cells' random walks and orientating their swimming directions. [64]

**Section 2.3.4** provides a description of another swimming strategy employed by the microalga *Dunaliella Salina*, which propels itself by moving asymmetrically two anterior whip-like eukaryotic flagella. [68]

Once the main constraints of the micro-scale world have been analysed, the final part of this chapter addresses cell-cell and cell-boundary hydrodynamic interactions, mainly giving a physical overview without providing mathematically comprehensive treatments, which can be found elsewhere: [30, 69, 70]. Moreover, the effects of gravitational and viscous torques acting on bottom-heavy algal cells at different fluid dynamic conditions will also be discussed, giving particular emphasis to their gravitactic and gyrotactic behaviours. Finally, transport processes of dissolved components at the microscope scale, their governing equation (*i.e.* the advection-diffusion equation) and some biological resulting implications will be analysed.

## 1.10 Hydrodynamic interactions

Cell-cell and cell-boundary interactions play crucial roles in a wide range of biological and industrial processes, (*e.g.* wood mouse's spermatozoa tend to aggregate in order to swim faster [30], swimming microorganisms involved in human functions and diseases [71], microalgal biofilm formations in photobioreactors [10], *etc.*) and their dynamics are governed by fluid mechanics in concert with the cells' behaviours. [30]

Generally, when microorganisms swim or move (*e.g.* sedimenting particles, swimming organisms, *etc.*), they generate flow fields that can affect nearby cells' dynamics and, as further explained in the next section, can be approximated through singularities of the Stokes equation, which can be used for inferring the forces and torques exerted on the flow by moving organisms, modelling their resulting streamlines and velocity fields and studying their hydrodynamic interactions with other cells and boundaries. [20, 30, 70]

### **1.10.1 Swimming as a singularity**

Several important velocity fields obtained by solving the Stokes equation (also known as singularities of the Stokes equation [30]) can be employed for studying the ways swimming organisms or non-motile ones affect the surrounding fluid and influence the cells interactions, since they approximate the resulting flow fields. [20, 30, 42]

The simplest singularity of the Stokes equation is called Stokeslet, represents the flow field associated with a single force  $\mathbf{F}$  exerted on the fluid at a fixed point  $x_0$  and is exploited to describe the motion due to translation; as a Stokeslet decays with  $r_F^{-1}$ , being  $r_F$  the distance from the location where the force is applied, it involves a relative big region of the fluid. [70] Another important singularity is the force dipole, *i.e.* the velocity field due to the application of two forces acting in opposite directions at a certain distance and that are not generally aligned with the vector joining them. Nevertheless, two simple cases are usually considered, *i.e.* a Stresslet due to two aligned forces and which velocity field has pure radial components and a Rotlet due to two forces acting perpendicularly and that is pure rotational. The Stresslet does not produce any net force, since the two forces are acting in opposite directions, while the Rotlet generates a torque. [70]

The most used singularities and their related velocity fields can be seen in **Table 1.4**. More fundamental Stokesian singularities have been discussed in details by Visser [70].

**Tab 1.4 – The most important singularities of the Stokes equation, their main features and spatial decay; when a flow field is described using different flow singularities, the one with the slowest spatial decay dominates in the far field. In the mentioned formulas,  $\mu$  refers to the fluid viscosity and  $\theta$  is the angle between the dipole direction. [20, 70]**

Singularity	Velocity Field	Feature	Spatial decay
Stokeslet	$\mathbf{U} = \frac{1}{8\pi\mu} \left\{ \frac{\mathbf{F}}{r_F} + \frac{(\mathbf{F} \cdot (\mathbf{x} - \mathbf{x}_0)) \cdot (\mathbf{x} - \mathbf{x}_0)}{r_F^3} \right\}$	Net Force	$\mathbf{U} \sim r_F^{-1}$
Stresslet	$\mathbf{U} = \frac{\mathbf{F}}{8\pi\mu r_F^3} [3 \cdot (\cos^2 \theta) - 1] r_F$	No Net Force	$\mathbf{U} \sim r_F^{-2}$
Rotlet	$\mathbf{U} = -\frac{ \mathbf{F}  \mathbf{b} }{8\pi\mu r_F^2} \hat{\boldsymbol{\theta}}$	Net Torque	$\mathbf{U} \sim r_F^{-2}$

Employing the Stokesian singularities described above, the next sections analyse some well-known biological examples of cell-cell and cell-boundary hydrodynamic interactions, *i.e.* the comparison between a sedimenting and a swimming organism and the reciprocal interactions between pullers and pushers. In fact, from a general point of view, studying the cell-cell and cell-boundary hydrodynamic interactions would also help to achieve a better comprehension of the phenomena occurring in algal cultivation devices (*e.g.* algal biofouling, prey-predator interactions, *etc.*), which will be described in details in the **2<sup>nd</sup>** and **5<sup>th</sup>** Chapters.

## 1.10.2 Sedimenting cells versus swimming organisms

Singularities of the Stokes equation and their spatial decays (see **Table 1.4**) can be used for modelling the different hydromechanical signals generated by planktonic microorganisms through different motile behaviours (*e.g.* swimming, settling, rotation, *etc.*), simply considering the net forces and torques exerted by a given organism on the fluid. [70] These signals can be sensed through mechanodetection mechanisms by nearby organisms (*e.g.* predators, prey, conspecifics, *etc.*) that will react accordingly; for instance, ambush-feeding copepods (*e.g.* *Oithona similis*) are predators able to locate their preys by sensing differences in velocities and shear through their mechanoreceptive antennas. Hence, mechanodetection has important ecological consequences, since is responsible for microorganismal interactions and encounters. [30, 70]

For example, a settling microorganism and a downwards swimming cell with the same shape and dimension that are moving at the same velocity, will generate two very diversified scenarios for mechanodetecting organisms; the sinking cell exerts only the drag force on the fluid and therefore can be modelled as a Stokeslet (that decays with  $r_F^{-1}$ ), whereas, a motile organism swims by generating a propulsive force that is balanced by the drag force (*i.e.* no net forces or torques are applied to the fluid) and the small separation between the centre of the drag and thrust implies that the flow field due to a swimming cell can be modelled as a symmetric force dipole (that decays with  $r_F^{-2}$ ). [70]

As we shall see better in the 5<sup>th</sup> Chapter, these significantly different kinds of flow disturbances have also implications in algal cultivation devices since demonstrate that a sedimenting dead microalga and a live swimming one will be felt differently by potential predators and opportunistic species, leading to different biological behaviours.

### 1.10.3 Pushers versus pullers

In a still fluid, when a generic cell A is moving, its resulting far-field flow will lead to two types of hydrodynamic stimuli for a given neighbouring cell B, which will be able to feel both the velocity field and the gradient of the velocity field created by the cell A. [30]

Nevertheless, microswimmers can be classified as pushers (*e.g.* *E. Coli*) and pullers (*e.g.* CR or DS cells). As shown in **Figure 1.7**, pushers swim by repelling the fluid away from the body, drawing fluid in to the sides and therefore the induced flow field can be modelled as a positive Stresslet (*i.e.*  $\mathbf{F} > 0$ , see **Table 1.4**); in contrast, pullers draw fluid in along the elongated direction, push fluid out from the sides and consequently they can be approximated as a negative Stresslet (*i.e.*  $\mathbf{F} < 0$ , see **Table 1.4**). [30]

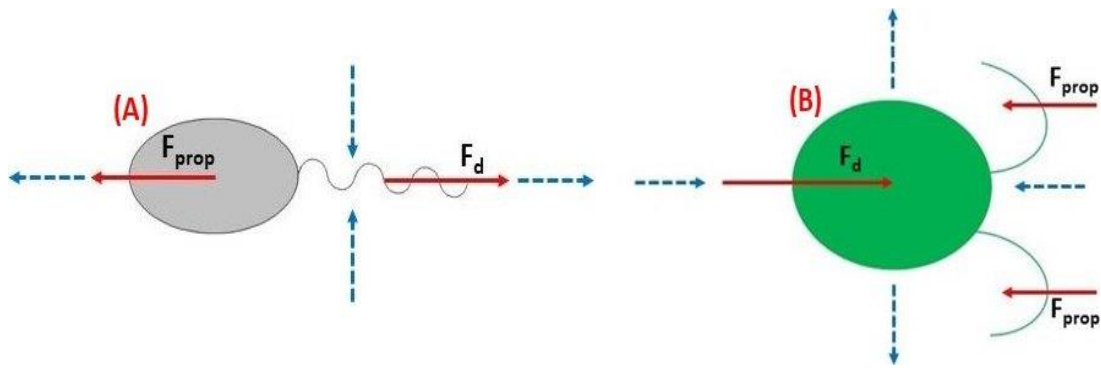


Figure 1.7 – Microswimmers can be classified as pushers (A) which thrust comes from the posterior part of the body and pullers (B), characterised by an anterior propulsive force. While swimming, microswimmers also experience a drag force  $F_d$ , that is a resistive force acting opposite to the relative motion of any object moving with respect to a surrounding fluid. [72] In particular, the red arrows indicate the local propulsion and drag forces while the blue arrows represent the flow direction in the fluid [30, 72]. Adapted from [30, 73].

Therefore, pushers and pullers generate velocity fields with opposite signs, resulting in different hydrodynamic interactions that mostly depend on cell-cell reciprocal swimming positions (see **Table 1.5**). [30]

**Tab 1.5 – The main hydrodynamic interactions between pusher-type and puller-type cells due to their induced velocity fields.** [30]

Swimming-cell type	Reciprocal swimming position	Resulting hydrodynamic interaction
Pusher-pusher	Side-by-side	Mutual attraction
Puller-puller	Side-by-side	Mutual repulsion
Pusher-pusher	Aligned along their swimming directions	Mutual repulsion
Puller-puller	Aligned along their swimming directions	Mutual attraction

Moreover, the resulting velocity gradients lead to qualitatively different rotational behaviours that are dependent on the swimming-cell type (*i.e.* pushers or pullers), their shape, the induced vorticity field and the symmetric part of the rate of strain  $\mathbf{E}$ . Practically these effects cause cells reorientations, *e.g.* nearby pushers on a converging course reorient one another in the side-by-side configuration while nearby pullers reorient themselves in the elongated direction. [30] More examples of cell-cell interactions and their theoretical explanation can be found in Lauga’s and Powers’ paper: [30].

## 1.10.4 Cell-boundary interactions

Interactions between swimming organisms and solid surfaces have important implications in many biological and industrial processes, where the cells live in geometrically-confined environments, *e.g.* microalgal and bacterial accumulations near boundaries and biofilm formations [10, 74], the locomotion of spermatozoa in mammalian cervical mucus, *etc.* [75]

In particular, the presence of boundaries influences the cells locomotion in different ways, mainly leading to a change of their near-wall swimming velocity, reorienting their swimming directions and causing scattering phenomena; the cell-surface interactions are governed by long-range hydrodynamic forces, which orient microswimmers toward to or away from a given surface, and short-range or steric interactions, which induce the cells to scatter from solid boundaries. [30, 71, 76]

As explained in the **Section 1.9**, for a given flagellar waveform, the propulsive force is an increasing function of the ratio between the flagellar drag coefficient in the normal direction  $\xi_{\perp}$  and the one in the transversal direction  $\xi_{\parallel}$  (see **Figure 1.6**), usually  $\xi_{\perp} \sim 2 \xi_{\parallel}$ . [30] These two coefficients are both found to increase near walls but  $\xi_{\perp}$  increases more than  $\xi_{\parallel}$ , leading to an increase of the resulting propulsive force and therefore swimming organisms should be expected to speed up when approaching solid surfaces. Nevertheless, compared to unbounded flows, the viscous drag also increases when a body comes closer to a boundary [72] therefore, associated with the increase in speed, there will also be an increase of the required working rate that the microswimmer must provide to maintain the same waveform. Thus, if an organism swims with constant power, the presence of walls implies a decreasing of the swimming speed. [20, 30]

Moreover, as can be seen in the **Figure 1.8**, another important effect of boundaries on swimming cells resembles the previously-explained cell-cell attraction and reorientation phenomena (see **Section 1.10.3**).

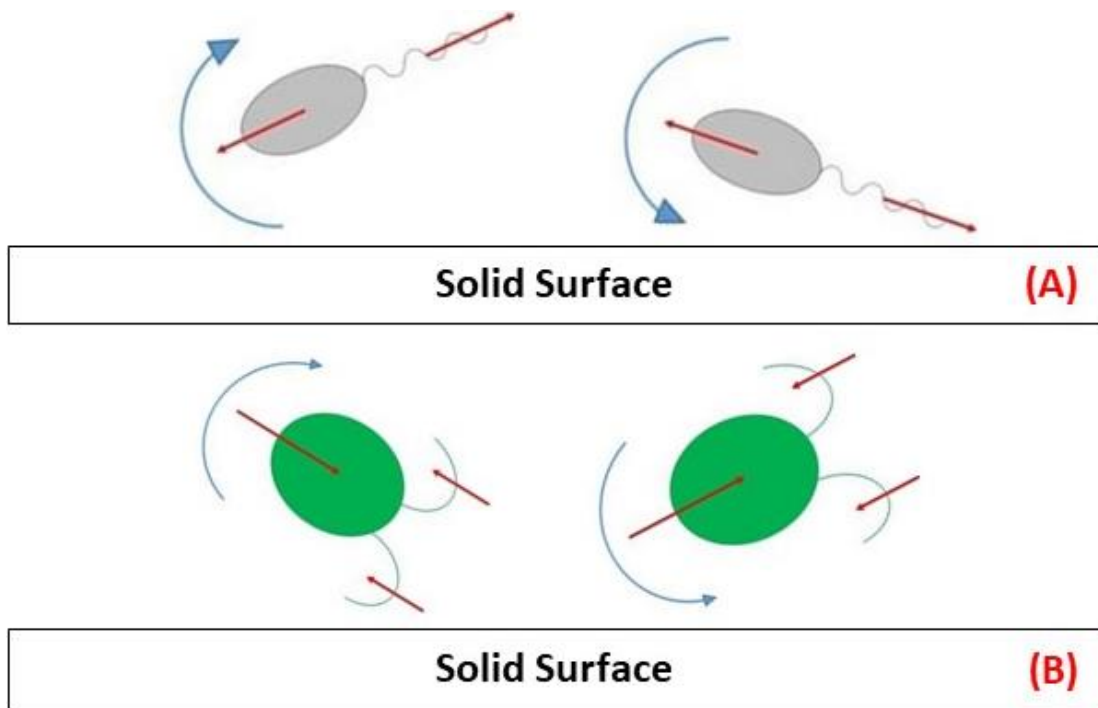


Figure 1.8 – Wall-induced rotation of a pusher cell (A) and a puller cell (B). Mathematically, the presence of solid boundaries requires to modify or implement flow singularities, since their original set does not fulfil the no-slip boundary condition along the walls. As a result, the flow in presence of the walls is modelled through the linear superposition of the infinite-fluid flow singularities plus a sequence of image flow fields located on the other side of the surface which must be arranged to satisfy the correct boundary condition along the wall, *e.g.* a stokeslet near the wall is represented by the unbounded fluid flow stokeslet along with a force dipole, a source quadrupole and a force quadrupole on the other side of the surface. [30, 71]. Adapted from [30].

Another important effect of boundaries on swimming cells resembles the previously-explained cell-cell attraction and reorientation phenomena (see **Section 1.10.3**).

Specifically, if the swimming organism is a pusher, wall-induced rotations occur as if the cell is interacting with a mirror-image one located on the other side of the surface, resulting in a side-by-side configuration. In addition, wall-induced rotations tend also to align the swimming organism in the direction parallel to the surface, leading to hydrodynamic attraction towards the surface which, combined with the counter-rotation of cell body and flagella, cause the cells to swim in circle and accumulate close to boundaries (see **Figure 1.8 A**). [30, 76] In contrast, pullers are reoriented perpendicularly and therefore these cells are always swimming toward a given surface (see **Figure 1.8 B**). [30, 71]

Furthermore, Kantsler and co-workers investigated experimentally the scatterings from corned-shaped boundaries of bull spermatozoa (*i.e.* a pusher swimmer) and three different strains of CR algal cells (*i.e.* puller swimmers) with different flagellar length, observing that for all these swimmers the scattering phenomena were mainly determined by direct contact interactions between their flagella and the surface. [76]

In particular, during a typical scattering event, a sperm cell were seen following the boundary, reaching the corner and departing from it at negative scattering angles, which tended to turn the spermatozoa towards the boundary. [76] Concerning the three pullers, their flagella were observed to prevent the cell body from touching the surface and their typical scattering angles were found to be positive, to increase with the flagella length and to depend also on the diameter of the cell and its distance from the surface at the moment of the departure. [76]

However, apart from the cell-cell and cell-boundary interactions, microswimmers are also subject to both physical and physiological orienting mechanisms [2], which can determine their swimming directions. In particular, in the next sections will be considered the specific case of bottom-heavy microalgae cells (*e.g.* DS or CR cells [42]), describing their gravitactic-biased and gyrotactic-biased behaviours, their dependence from the fluid dynamic conditions and also mentioning some related biological consequences.

## 1.11 Locomotion in flows

A given cell in a body of fluid translates and rotates itself as a result of an external body of force  $\mathbf{F}_B$ , an external torque  $\mathbf{L}_c$  and intrinsic swimming motion. [2]

Generally,  $\mathbf{F}_B$  is due to gravity and is given by  $\mathbf{F}_B = \frac{\rho_c - \rho_f}{\rho_f} \cdot \mathbf{g}$ , being  $\mathbf{g}$  the gravitational acceleration,  $\rho_c$  the average density of the cell and  $\rho_f$  the density of the ambient fluid. Since microorganisms are usually denser than their surrounding fluids [2], the effect of the gravitational force will result in a sedimentation velocity  $\mathbf{V}_T$  that can usually be neglected for swimming organisms, since its magnitude is much smaller than that of typical swimming velocities (see **Section 4.6.1**). [2]

The external torque is also commonly due to gravity, while on the cell will also be acting a further viscous torque  $\mathbf{L}_V$  exerted by the ambient fluid, which can be expressed as a linear combination of the velocity, angular velocity of the cell relative to the fluid and the strain rate [2, 77]; more theoretical details and the mathematical definition of  $\mathbf{L}_V$  can be found in Pedley's and Kessler's papers [2, 77].

The swimming behaviour and direction  $\mathbf{p}$  in which the cell will swim are determined by the balance of the viscous torque  $\mathbf{L}_V$  and the total effective external torque  $\mathbf{L}_E$ , with the latter due to the actual external torques (*i.e.* physical orienting processes) and the responses of the cell to its characteristic taxis effects (*i.e.* physiological orienting processes) (see **Section 1.5.3**), which can be assumed as equivalent to an external torque. [2]

Specifically, in the absence of inertia:  $\mathbf{L}_E + \mathbf{L}_V = 0$ . [2, 77]; as further explained in the next section, this torque balance implies interesting taxis-biased behaviours for anisotropic cells.

### **1.11.1 Gravitactic and gyrotactic behaviours**

Generally, in a still fluid, many microorganisms tend to swim towards a preferential direction  $\mathbf{k}$  and therefore if their actual swimming direction  $\mathbf{p}$  is not parallel to  $\mathbf{k}$ , the effective external torque  $\mathbf{L}_E$  will tend to reduce the angle between them. [2, 77]

In the specific case of bottom-heavy algal cells  $\mathbf{k}$  is directed vertically upward, since their centre of mass  $G$  is offset from the centre of buoyancy  $C$  and consequently their behaviour will be affected by the gravitational torque which tends to keep  $G$  below  $C$  (see **Figure 1.9**), leading the algal cells to swim upwards and exhibiting the gravitaxis behaviour. [2, 77] Thus, gravitaxis is the reaction to gravity that, in a stagnant body of water, causes organisms to swim at the upper boundaries of the fluid and is often used in conjunction with phototaxis. [42]

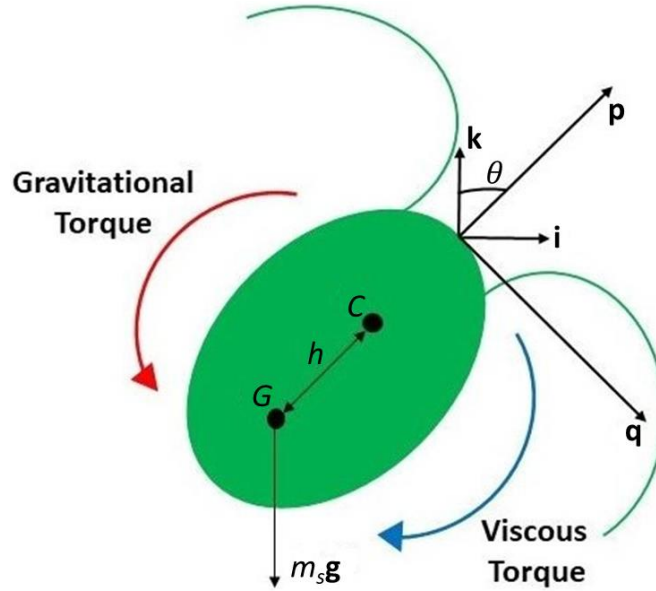


Figure 1.9 – For anisotropic biflagellated microalgal cells, the gravitactic behaviour is due to an asymmetric mass distribution of the cell, being its centre of buoyancy  $C$  offset by a distance  $h$  from the centre of mass  $G$ . In the schematic representation,  $p, q, r$  refer to the body axes while  $i, j, k$  are the fixed-space axes, with  $j$  pointing into the page and  $m_s$  is the mass of the cell. [42]. Adapted from [42].

Nonetheless, when anisotropic algal cells undergo a given flow rate, the interactions between swimming, gravitational torque and hydrodynamic torque may lead to directed locomotion, termed gyrotaxis which may orientate the microalgae, leading to cell focusing in downwelling regions of the flow.

In particular, assuming the swimming algal cells as rigid prolate spheroids and neglecting the flagellar effects on the viscous torque, the orientation  $\mathbf{p}$  of a gyrotactic alga is given by: [2, 77]

$$\dot{\mathbf{p}} = \frac{1}{2B} [\mathbf{k} - (\mathbf{k} \cdot \mathbf{p})\mathbf{p}] + \frac{1}{2} \boldsymbol{\omega} \times \mathbf{p} + \alpha_0 \mathbf{p} \cdot \mathbf{E} \cdot (\mathbf{I} - \mathbf{p}\mathbf{p}) \quad (\text{eq. 1.15})$$

where  $\boldsymbol{\omega}$  and  $\mathbf{E}$  refer respectively to the fluid flow vorticity and strain rate,  $\alpha_0 = \frac{(r^2-1)}{(r^2+1)}$  is the cell eccentricity,  $r$  is the ratio of the major to the minor axis of the cell.

$B$  represents a timescale for reorientation by gravity and is defined as:

$$B = \frac{\mu\alpha}{2g\rho_c h} \quad (\text{eq. 1.16})$$

$\mu$  is the fluid viscosity,  $\alpha$  a dimensionless resistance to rotation and  $h$  the displacement of  $G$  (see Figure 1.9). [2, 20, 42] In case of spherical particles,  $\alpha_0=0$  and  $\mathbf{E}$  has no effect on  $\mathbf{p}$ . [2]

Hence, eq. 1.15 describes the effects of the viscous and gravitational torques acting on a rigid spheroid and can be used to determine potential equilibrium orientations of a swimming cell for any set of initial conditions. For example, Pedley and Kessler [2, 77] showed that a stable equilibrium orientation exists for bottom-heavy algal cells within a unidirectional flow in a vertical pipe (*i.e.* a flow whose vorticity is entirely horizontal), as long as  $B\omega < 1$ . When this condition is fulfilled, bottom-heavy algal cells within a Poiseuille flow in a vertical circular pipe will swim upwards at an angle  $\theta$  to the vertical (*i.e.*  $\sin \theta = B\omega$ ), showing also an accumulative gyrotactic behaviour, meaning that the cells will be concentrating in the pipe axis in downwelling flows or at the walls in upwelling flows. [2, 77] On the contrary, when  $\omega$  exceeds the critical value  $B^{-1}$ , no equilibrium is possible and the cells will tumble. [2, 20, 77]

Pedley and Kessler [77] investigated also the equilibrium orientations of nonspherical cells for flows conditions in which vorticity and strain rate are comparable (*e.g.* vertical pipe flows or simple shear flows), finding that a stable swimming direction exists providing  $B\omega$  is less than a certain critical value, which depends on  $\alpha_0$  and the orientation of the flow. [77]

Moreover, Kessler [78] considered the equilibrium orientations for both spherical and spheroidal cells within a simple shear flow in a vertical plane, finding that for both types of cells a gyrotactic angle can be obtained, as long as  $B\dot{\gamma}$  is less than a critical value depending on  $\alpha_0$  and the orientation of the flow, being  $\dot{\gamma}$  the imposed shear rate. When  $\dot{\gamma} > B^{-1}$  the gravitational torque cannot compensate the viscous spin and the cells will tumble.

Interestingly, the gyrotactic behaviours described above were not observed both during experimental investigations involving dead gyrotactic cells and during experiments involving living non-swimming algal cells, such as *Chlorella*. [50]

From a biological point of view, gravitaxis and gyrotaxis can drive patchiness in phytoplankton distributions, *e.g.* in spatially-varying shear conditions, gyrotaxis can trap cells at specific depths (*i.e.* in regions where  $\dot{\gamma}$  surpasses  $B^{-1}$ ), leading to the formation of phytoplankton layers, which have been observed for the microalgal strains *Chlamydomonas nivalis* and *Heterosigma akashiwo*. [20, 79] Moreover, cell accumulations can also induce Rayleigh-Bénard-type and overturning instabilities (see **Section 1.6**).

Generally, concentrated populations of cells can have detrimental effects in aquatic environments by shading and scattering the solar light, consuming nutrients, attracting toxic predators, *etc.*; furthermore, as explained in the **2<sup>nd</sup> Chapter**, these dangerous accumulation phenomena must also be avoided in photobioreactors. [3, 10]

Encounters and interactions between microorganisms can also be facilitate and influenced by the transport of dissolved chemicals (*e.g.* pheromones can attract conspecifics for reproduction, released waste products may be used as a signal by other chemotactic organisms to locate and prey the exuding cell, *etc.*) [20, 70]; therefore they will be explored in the next sections.

## **1.12 Transport phenomena at low Reynolds numbers**

This section addresses the main mechanisms which regulate the transport of dissolved components at the microscopic scale (*e.g.* nutrients, waste products, *etc.*) and that can be exploited for describing some biological phenomena, such as the nutrient uptake by an osmotroph (*i.e.* an organism that feeds by osmosis), the release of waste products or pheromones in the fluid, *etc.* [80] In particular, these transport phenomena are governed by the advection-diffusion equation, which will be employed for analysing the diffusion-governed nutrient uptake of a non-motile spherical cell and the advection-induced nutrient uptake enhancement.

### **1.12.1 The advection-diffusion equation**

The concentration  $C$  of a given solute in a flow field  $\mathbf{U}$  is governed by the advection-diffusion equation (ADE),

$$\frac{\partial C}{\partial t} = \nabla \cdot (D \cdot \nabla C) - \nabla \cdot (\mathbf{U} \cdot C) \quad (\text{eq. 1.17})$$

$D$  is the solute's diffusivity, whose value depends on the characteristics of the diffusing molecules (*e.g.* light molecules can diffuse faster and have higher  $D$  values). [81]

The right-hand side of the *eq. 1.17* is formed by two terms:  $\nabla \cdot (D \cdot \nabla C)$  that considers the diffusion effects and  $\nabla \cdot (\mathbf{U} \cdot C)$  that takes into account the advection effects, while

$\frac{\partial C}{\partial t}$  is the unsteady concentration. [20]

ADE can be adimensionalised through the definition of a characteristic concentration  $C_c$ , so that  $\tilde{C} = \frac{C}{C_c}$  and therefore *eq. 1.17* becomes:

$$\frac{Pe}{Sr} \cdot \frac{\partial \tilde{C}}{\partial \tilde{t}} + Pe \tilde{\mathbf{u}} \cdot \tilde{\nabla} \tilde{C} = \tilde{\nabla}^2 \tilde{C} \quad (\text{eq. 1.18})$$

$\tilde{\mathbf{u}}$  is the dimensionless velocity and  $Sr$  the Strouhal number (see **Section 1.8.2**). [20]

$Pe$  refers to the dimensionless Péclet number which can be defined as:

$$Pe = \frac{\text{Nutrient uptake due to advection}}{\text{Nutrient uptake due to diffusion}} = \frac{U \cdot L}{D} \quad (\text{eq. 1.19})$$

$Pe$  depends on the characteristic velocity scale  $U$ , the characteristic physical length  $L$  and the solute's diffusivity  $D$  and it is used to evaluate whether the nutrient uptake process (NUP) is dominated by either diffusion or advection; in particular, when  $Pe \ll 1$ , NUP is governed by diffusion. [20, 72]

Practically, ADE can be employed to obtain the nutrient uptake rate by solving for  $C$ , computing the flux  $-D\nabla C$  at the cell surface area  $A_c$  and consequently obtain the areal diffusive current as:

$$I_A = -D \int_{A_c} \nabla C \cdot \mathbf{n} \cdot dA \quad (\text{eq. 1.20})$$

Physically,  $I_A$  indicates the total rate of a given nutrient diffusing into the cell through its surface area.

A typical application of the ADE regards the diffusion-governed nutrient uptake by a spherical osmotroph in a quiescent aquatic environment (*i.e.*  $U = Pe = 0$ ) [20], which will be addressed in the next section.

## 1.12.2 Diffusive nutrient uptake process

The stationary nutrient uptake process (NUP) of a given solute by a non-motile spherical osmotroph in a quiescent aquatic environment can be modelled employing the advection-diffusion equation (ADE) which, at the conditions considered and assuming that the diffusion coefficient is constant, reduces to:

$$D\nabla^2 C = 0 \quad (\text{eq. 1.21})$$

Eq. 1.21 describes the nutrient concentration profile around the cell (see **Figure 1.10**) and shows that the diffusion-governed NUP depends on the solute's diffusivity and the concentration gradient, (in addition to the cellular ability to shuttle nutrients molecules across its membrane). [20, 82]

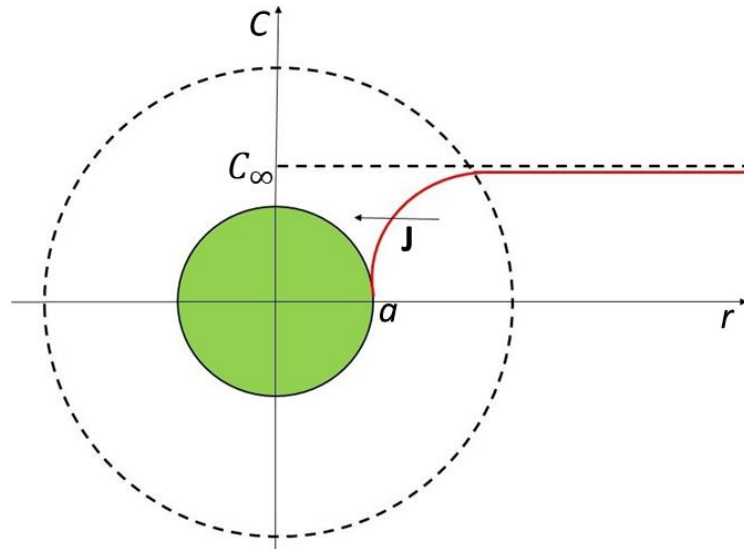


**Figure 1.10** –  $C_\infty$  and  $C_0$  refer to the nutrient concentrations respectively far away from the absorber and at the cellular surface,  $a$  is the radius of the cell,  $r$  the radial distance from the centre of the particle and  $J$  the negative nutrient flux towards the osmotroph. In a pure diffusive case, the nutrient concentration (red solid line) increases away from the spherical absorber, which will be surrounded by a limiting diffusing boundary layer (*i.e.* the region where the nutrient concentration goes from  $C_\infty$  to  $C_0$ ). Adapted from [82].

The diffusive NUP is affected by the cellular dimensions; for a given osmotroph, if its volume is too large, relative to the surface area, diffusing nutrients cannot reach all parts of the cell quickly and the diffusion process does not occur at sufficiently high rates. This can be quantified defining the surface to volume ratio (SVR):

$$SVR = \frac{\text{Surface area of the cell}}{\text{Volume of the cell}} \quad (\text{eq. 1.22})$$

Hence, from a diffusive point of view, the smaller the cell is, the larger  $SVR$  will be and the faster substances can diffuse in and out of the cellular membrane. Nevertheless, if the cell is too small, there are also other affecting biological phenomena that must be taken into account, *e.g.* the Brownian translational and rotational diffusions [83, 84]; typically, microorganisms larger than  $0.6 \mu\text{m}$  can compete with Brownian motion, in line with the observation that smaller organisms are not motile. [21]

As discussed in the next section, the NUP can also be enhanced by advection, meaning that, instead of being non-motile and in a quiescent environment, the absorbing organism may be sinking, swimming or generally be within a flow field. [21]

### 1.12.3 Advective nutrient uptake process

Biologically, when an absorbing organism starts moving and advection plays a part, the shape of the previously-defined limiting diffusive boundary layer changes, leading to a concentration wake that will be thicker on one side of the cell and thinner on the other side, depending on the direction of the motion. The thinner front layer reduces the actual time required by the diffusing molecules to penetrate the boundary layer and reach the surface of the absorber, leading to an increase of the concentration gradient and consequently of the nutrient current. [85] In other words, advection increases the uptake rate by transporting fresh solute into the vicinity of the cell, leading to a steepening of the concentration gradient at the cell surface. [20]

Customarily, the advection-induced uptake enhancement is estimated through the dimensionless Sherwood number  $Sh$ , defined as the ratio of uptake in the presence of flow to uptake due solely to diffusion. For a spherical cell it is given by: [20]

$$Sh = \frac{\text{Transport due to advection and diffusion}}{\text{Transport due to diffusion}} = \frac{-D \int_{A_c} \nabla C \cdot \mathbf{n} \cdot dA}{4\pi Da(C_\infty - C_0)} \quad (\text{eq. 1.23})$$

hence, the higher  $Sh$  is, the more the nutrient uptake is improved by advection and therefore  $Sh \geq 1$ ; when  $Sh = 1$ , the uptake process is governed by diffusion. [20]

Specifically, the uptake enhancement due to advection is usually calculated exploiting empirical equations where  $Sh$  is expressed as a function of  $Pe$ , for a given flow and cell shape. [85, 86]

Therefore, from a biological point of view, in order to overcome the limits due to diffusion, microorganisms must increase their  $Pe$  number and this can be achieved by either swimming (*i.e.* increasing  $U$ ) or aggregating in colonies (*i.e.* increasing  $L$ ), see eq. 1.19. [82]

Various empirical equations can be found in the literature, which predict the nutrient uptake improvements due to different fluid dynamic conditions; for example, Brenner *et al.* have studied the effects of different cellular shapes [87], while Guasto *et al.* have analysed the uptake enhancements due to shear flows and turbulent flows in oceans. [20]

As we shall see in the **2<sup>nd</sup> Chapter**, the advection-diffusion equation, along with the continuity equation, the Navier-Stokes equation (see **Section 1.8.2**) and the continuum model for dilute algal suspensions (see **Section 2.10.1**), is one of the governing equations that can be utilised for describing the effects of the fluid flow on the algal cells behaviours.

### **1.13 Chapter summary**

In this chapter, some fundamental biological and fluid dynamical features of microswimmers have been introduced, which will be reconsidered in different parts of this thesis and will also be employed to address the technical limits and optimisation processes required for algal cultivation devices. For example, as addressed in the **2<sup>nd</sup> Chapter**, the light harvesting in tubular PBRs must be maximised (*i.e.* the algal cells convert the sun light into chemical energy, through the photosynthetic process); PBRs can be contaminated by predatory species which feed on the algal cells (*i.e.* cell-cell hydrodynamic interactions); the PBRs performance can be compromised by algal biofouling processes (taxi-biased behaviours and cell-boundary interactions), *etc.*

Moreover, the concepts discussed in this chapter will also help to explain the assumptions made and the results obtained in this research (see the **4<sup>th</sup> Chapter**).

## – Chapter 2 –

# The microalga *Dunaliella Salina*, the algal biofuels and the photobioreactors

## 2.1 Chapter layout

In the first part of this chapter, the most important aspects about microalgae are analysed, focusing special attention on their main biological characteristics and the engineering applications of the most industrially-grown microalgal species.

Next, a detailed biological description of the microalga *Dunaliella Salina* is provided, considering also the circumstances of its classification, its main swimming features (*e.g.* the way DS cells swim, their taxis behaviours, *etc.*) and industrial applications (*e.g.*  $\beta$ -carotene production, the treatment of polluted effluents, *etc.*).

Moreover, the most important engineering, biological and fluid dynamic benefits and limits of the algal biofuels production and the related cultivation devices will also be discussed, placing particular emphasis on closed tubular photobioreactors (PBRs), performing a technical analysis and showing that cost-reducing self-concentration algal mechanisms must be exploited in order to increase the overall viability of algal applications.

Finally, the existing literature on alternative approaches for enhancing the algal biomass production is also briefly explored.

## 2.2 General considerations about the algae

In order to provide context for the study of microalgae, in this section the main algal biological features are discussed, considering their adaptability (*i.e.* the various habitats where they can be found) and the main differences between multicellular and unicellular algae. Moreover, the most important microalgal species are briefly described, mentioning also some of their industrial applications.

## 2.2.1 Macroalgae and microalgae

The word algae identifies a diverse group of chlorophyll-containing organisms, which belong to the domain Eukaryota and the kingdom Protista. The study of algae is termed as phycology or algology. Although there are almost 100,000 different known species, algae can be distinguished depending upon their main characteristics, such as being unicellular or multicellular, macroscopic or microscopic, their cell composition, their pigments, *etc.* [88]

Algae can predominantly be found in aquatic habitats, like freshwater (*e.g.* lakes and rivers), marine (*e.g.* oceans) and terrestrial habitats (*e.g.* damp soils and rocks), albeit they can live and thrive in various environments, *e.g.* epiphytic algae can grow harmlessly upon plants (*e.g.* *Bulbochaete* growing on *Cladophora* [89]) or epizoic algae can grow on animals (*e.g.* *Protoderma* on the back of tortoises [90]). Furthermore, some algal species are extremophile and grow in very harsh environments; for instance, thermophilic algae survive at relative high temperatures (*e.g.* *Cyanidium caldarium* that can resist at temperatures as high as 74°C [91]), cryophilic algae can be found at very low temperatures (*e.g.* *Chlamydomonas nivalis* that causes the watermelon snow [92]) and halophilic algae in salty environments (*e.g.* DS [93]).

Multicellular algae or macroalgae (*e.g.* seaweed) lack roots, stems, leaves, vascular tissues and have very simple reproductive structures, even though they may grow well over 20 metres in size, such as the giant Kelp. Their plant body is composed of a thallus, which can be unbranched (*e.g.* *Spyrogyra*) or branched (*e.g.* *Sargassum*); unbranched thalli consist of a straight row of cells, while branched thalli show lateral outgrowth. [94, 95] Similarly to plants, algae possess chlorophyll A as their primary pigment, therefore employ solar light to produce their own food through photosynthesis (see **Section 1.3.1**). [96]

Nevertheless, the majority of algae are microscopic and unicellular and represent the main contribution to the global primary biomass productivity. [4] Their sizes vary from a few micrometres to a few hundred micrometres and their shapes range from spherical to large irregular-shaped cells, aiming to increase the surface to volume ratio of the cells. Some of them are non-motile (*e.g.* *Chlorella* [97]) others are motile, (*e.g.* CR genus [98]). In order to enhance the nutrient uptake process (see **Section 1.12.3**) and for reproduction purposes, microalgae may also occur in colonies, which typically exist as clumps (*e.g.* the microalga *Volvox* [94]).

The main algal groups and phyla have been summarized in the **Table 2.1** and described in the next sections. [88]

**Table 2.1 – The main algal groups and phyla. [88]**

Group	Phyla
Green algae	Chlorophyta
Brown algae	Phaeophyta
Red algae	Rhodophyta
Dinoflagellates	Dinoflagellata
Diatoms	Bacillariophyta

## 2.2.2 Green, red and brown algae

Green, brown and red algae are subject to increasing attention industrially and ecologically. Apart from the chlorophyll, these algae contain various pigments and absorb the solar light at different wavelengths; therefore, they can grow at different depths in aquatic environments (see **Figure 2.1**). [27, 88]

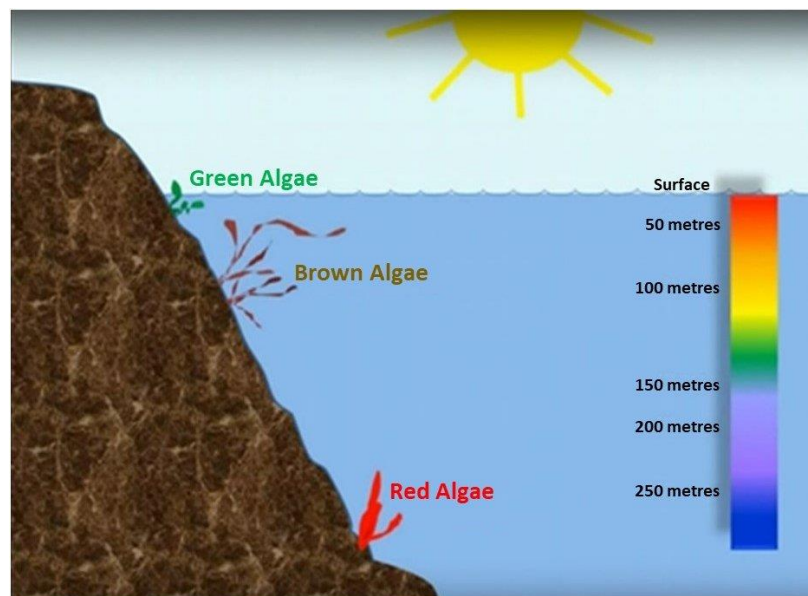


**Figure 2.1 – Biologically, the different pigments affect the algal colouring, also determine the wavelengths that can be absorbed and limit the depths at which the algae can survive. They also lead to different levels of algal toxicity and may provide opportunities to create different industrial products. Adapted from [27, 88].**

When solar light hits the surface of the water, the red wavelengths are absorbed first, so the green algae live close to the surface (*i.e.* in the photic zone), whereas the red algae have pigments which are able to absorb light in the blue wavelengths, so that they are able to survive at greater depths. [27, 88]

More details concerning these kinds of algae are shown in the **Table 2.2**. [27, 88]

**Table 2.2 – The main characteristics of green, brown and red algae. [27, 88]**

<b>Phyta</b>	<b>Chlorophyta</b>	<b>Phaeophyta</b>	<b>Rhodophyta</b>
Common name	Green algae	Brown algae	Red algae
Major Pigments	Chl. A, Chl. B	Chl. A, Chl. C, Fucoxanthin	Chl. A, Chl. B, Phycoerythrin
Habitats	Fresh water, salt water, brackish water	Fresh water, salt water, brackish water	Fresh water, salt water, brackish water
Major component of the cell wall	Cellulose	Cellulose and Algin	Cellulose
Cellular Energy Source	Starch	Mannitol, Luminarin Starch	Floridean Starch
Flagella	2-8, equal	2, unequal	absent
Flagella Position	Apical	Lateral	absent

### 2.2.3 Diatoms

Diatoms are the dominant life form in the phytoplankton family and probably represent the largest group of biomass producers on earth. The cell walls of diatoms, known as frustule, contain polymerised silica (hydrated silicon dioxide), which is the main component of glass. They can grow as single cells or form filaments and simple colonies. Despite being predominantly microscopic cells, some species of diatoms can reach up to 2 mm in length and most of them are non-motile. Furthermore, diatoms contain the pigments fucoxanthin and  $\beta$ -carotene, which give them a characteristic golden colour. [99]

### 2.2.4 Dinoflagellates

Dinoflagellates are unicellular organisms; most of them are photosynthetic, whereas a few forms are parasitic and predators. The photosynthetic ones are second only to diatoms as primary biomass producers in coastal waters. Some species are endosymbionts of marine animals and play an important role in the biology of coral reefs.

Nevertheless, dinoflagellates may have a big impact on aquatic environments, owing to the toxic blooms that they form during the warm summery months, leading to a visible red coloration of the water, colloquially called red tide. When this happens, they also release various poisoning neurotoxins affecting many kinds of marine life. [100]

## 2.2.5 Algal industrial applications

Over recent decades, algal biotechnological potential has gained attention and several microalgal species have been cultivated on an industrial scale, in photobioreactors of various designs, for the production of proteins, pharmaceutical formulations, glycerol, carotenoids and valuable chemicals. [52] Moreover, photosynthetic algae are able to store energy due to the photosynthesis in the form of starch and lipids (fats in the form of oil), therefore they have also been exploited as a source of bioenergy, mainly as biodiesel. [10]

Due to food safety regulations and commercial factors, the microalgal market is currently dominated by the following species: *Botryococcus*, *Chlorella*, *Dunaliella*, *Haematococcus* and *Spirulina*. [101] In particular, *Chlorella* and *Spirulina* are grown because of their high protein content and the presence of other essential nutrients, *Haematococcus* is cultivated for its high content of astaxanthin (a strong antioxidant used as a dietary supplement [102]) and *Botryococcus* for its ability to produce large amounts of hydrocarbons. [103] *Dunaliella* species are cultivated for the production of  $\beta$ -carotene, vitamin A and biofuels. [93]

Further details about the main industrially-grown microalgae can be found in the **Table 2.3**.

**Table 2.3 – The main industrially-cultivated microalgae, their most important products and application areas. Modified from [104].**

Producing Organism	Products	Application Areas
<i>Dunaliella Species</i> <i>Halobacteriaceae</i>	Carotenoids, fatty acids	Antioxidant, Food colouring agent, cosmetic industry
<i>Spirulina</i>	Phycocyanin biomass	Food and cosmetic industries
<i>Haematococcus</i>	Carotenoids, Astaxanthin	Pharmaceuticals and food industries
<i>Odontella Aurita</i>	Fatty acids	Pharmaceuticals and food industries
<i>Porphyridium cruentum</i>	Polysaccharides	Cosmetic and Pharmaceuticals industries
<i>Isochrysis galbana</i>	Fatty acids	Animal nutrition
<i>Phaedactylum tricornutum</i>	Lipids, fatty acids	Biofuel production
<i>Lyngbya majuscula</i>	Immune modulators	Pharmaceuticals and food industries
<i>Muriellopsis sp.</i>	Lutein, Carotenoids	Pharmaceuticals and food industries
<i>Botryococcus</i>	Lipids, fatty acids	Biofuel production

Nevertheless, considering the enormous biodiversity of microalgae and the recent developments in genetic engineering, algal exploitation is continuously extended into new areas, enabling new products and applications. [104]

## 2.3 The microalga *Dunaliella Salina*

This research work is primarily concerned with a specific microalgal species, called *Dunaliella Salina* (DS) and, in this section, the DS cell will be explored in detail, considering the historical circumstances that had led to its discovery and classification, the biological description and its main characteristics: the absence of a cell wall and its high adaptability. Moreover, its swimming behaviour is also analysed, providing a comprehensive description of the flagella beat sequence and the exhibited taxis effects.

In the final part of the section, the main DS industrial applications are discussed, highlighting how the DS features are exploited and contribute to making DS one of the most industrially-used microalgal species.

### 2.3.1 The *Dunaliella* Genus

The *Dunaliella* Genus was first discovered and described by Michael Felix Dunal (1838), in Montpellier (France), during an investigation commissioned by the Académie des Sciences (Paris, France), aimed to verify the causes of the red coloration of saltern brines, which had been assumed to be caused by chemical and physical factors. Dunal had reported occurrence of two unicellular biflagellated red-coloured microalgae, naming them as *Haematococcus salinus* and *Protococcus*. [105]

Later, in 1905, two papers were published by Emaniol C. Teodorescu that had described a new genus called *Dunaliella*, in honour of its first discoverer. Teodorescu characterised two species that belong to *Dunaliella* genus: *Dunaliella Salina* and *Dunaliella Viridis*. [105]

Today, it is known that the *Dunaliella* genus encompasses 22 species that are subdivided as marine, halophilic and freshwater species and belong to the phylum Chlorophyta, order Volvocales and family *Polyblepharidaceae*. [106, 107]

Halophilic species (*i.e.* those that prefer to live in media with high salt concentrations) can be found all over the world in a wide range of aqueous hypersaline habitats, such as oceans, inland salt lakes, salt marshes, *etc.* All these environments must contain high magnesium and salt concentrations, up to saturation [93], as salinity, temperature and nutrients are limiting factors on the growth of halophilic *Dunaliella* species (See **Section 3.2.1**). [108]

### 2.3.2 The *Dunaliella Salina* cell

As shown in the **Figure 2.2**, DS cell is enclosed within a semi-permeable cytoplasmic membrane that is responsible for the cell transport (*e.g.* allowing nutrients in and out the cell), communication and protection against sources of harm.

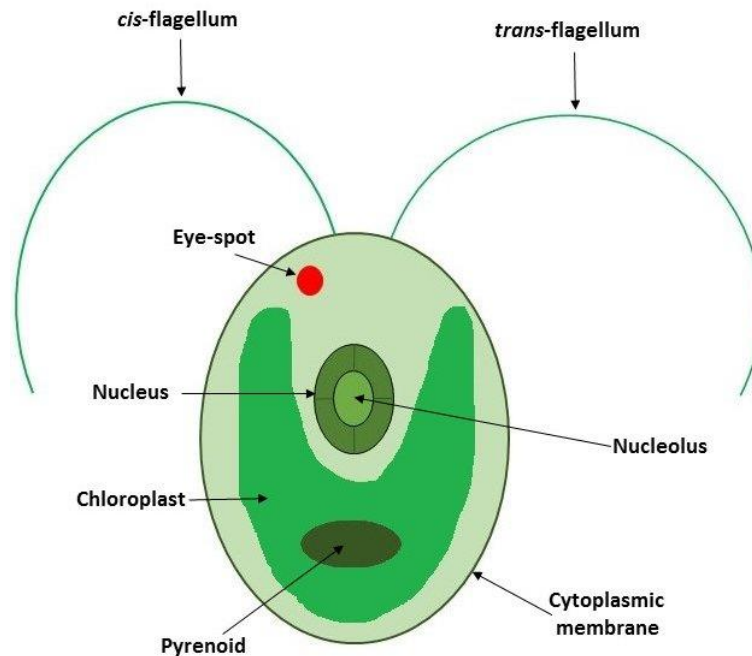


**Figure 2.2** - The internal cellular structure of the Eukaryotic microalga *Dunaliella Salina*. DS cell shares many common features with CR, the main differences are that DS lacks of a rigid cell wall, their body size and the location, number and size of the eye-spots differ between species. Being a motile cell, in its anterior part, DS has two flagella: the flagellum close to the eye-spot is known as the *cis*-flagellum, while the other is referred as the *trans*-flagellum. [8] Adapted from [8, 109].

Despite lacking a polysaccharide cell wall, the cellular membrane is surrounded by an external amorphous mucilaginous coating of variable thickness, known as glycocalyx, which mainly acts as a cellular barrier and also takes part in the adhesion processes. [107, 110]

Being a eukaryotic organism, within the membrane, the cell contains a nucleus, which houses the DNA and has its own membrane, known as the nuclear envelope. At the centre of the nucleus there is a special region, called the nucleolus, where incomplete ribosomes are synthesised. These ribosomes will end up either in the endoplasmic reticulum or as free ribosomes inside the cell membrane and are responsible for synthesising proteins. [111]

The cells also contain a single cup-shaped chloroplast where large amounts of  $\beta$ -carotene are accumulated [105] and that plays a key role during the photosynthetic process. [93, 107] The photosynthetic-formed carbohydrates are converted into starch that is stored in a structure called pyrenoid, located within the chloroplast, and converted into energy for the cell through the respiration process that occurs in the mitochondria. [93, 107] Other organelles are the vacuoles, which have a variety of functions including food and water storage and the Golgi apparatus, which packages, sorts and modifies proteins before they either remain within the cell or will be exuded. [13]

Located at the anterior part of the cell, there is a carotenoid-filled structure called eye-spot, also known as stigma, which plays an important role in phototaxis. In particular, when the cell is exposed to a source of light with a suitable intensity, the beating of the *cis*-flagellum (*i.e.* the one close to the eyespot) is hindered, whereas the beating of the *trans*-flagellum is facilitated, orienting the cell toward the light. [42]

The length of a DS cell ranges from 5 to 25  $\mu\text{m}$ , its width from 3 to 13  $\mu\text{m}$  and it can have different shapes, *i.e.* ovoid, spherical, pyriform, fusiform or ellipsoid. [112] Since DS lacks a rigid cell wall, its morphology depends strongly on the specific stage of growth and environmental conditions; *i.e.* the cells can modify their shape, often becoming spherical under unfavourable conditions. [113] In particular, osmotic changes can strongly affect the cells' shape which can adapt to hypertonic and hypotonic conditions, shrinking or swelling by changing their internal glycerol concentrations. [107, 112] Moreover, DS can survive under stress conditions, *i.e.* high salinity, high light intensities and oligotrophic environments, by producing and accumulating carotenoids to maintain the enzymatic activity and prevent chlorophyll photo-damage. [114] Furthermore, DS has also a very high tolerance to fuel oil contaminations, compared with other planktonic algae, therefore it is one of the most environmentally well-known eukaryotic organisms and has been used as a model in molecular biology to study the adaptation of cells to salt. [112, 115]

### 2.3.3 *Dunaliella Salina* reproduction

DS undergoes complex life cycles that encompass both longitudinal division of the motile cell (vegetative reproduction) and fusion of two cells to form a zygote through sexual reproduction. [96] During the latter, the algal flagella touch one another, the equally-sized gametes form a cytoplasmic bridge and fuse. The formed zygotes have a thick outer layer, can survive prolonged periods of dryness and, after a resting stage, germinate releasing up to 32 haploid daughter cells. [96, 116] It has been observed that the zygotic formation was induced by a reduction in salt concentration from 10 to 3%. [105] Nevertheless, DS primarily reproduces vegetatively, since sexual reproduction is rarely observed in cultures, but more often in the field. [113]

### 2.3.4 How does *Dunaliella Salina* swim?

As shown in **Figure 2.3**, DS has two eukaryotic flagella (12  $\mu\text{m}$  long) which can be moved synchronously, in a back and forth movement, at a frequency of 40-60 Hz, allowing DS to swim at a velocity of 60 - 100  $\mu\text{m}\cdot\text{s}^{-1}$ , in a water-like medium. [39, 43] In particular, the DS flagellar beat sequence consists of two parts, an effective or power stroke and a recovery stroke and they strongly influence the swimming characteristics of the cells. [68] During the effective stroke, the flagella maximise the propulsive force by moving toward the posterior part of the cell and remaining perpendicular to the swimming direction whereas, during the recovery stroke, the flagella return to their original position. [20]

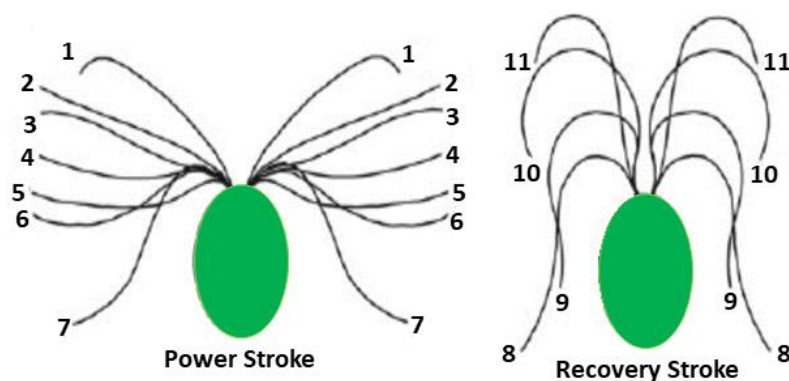


**Figure 2.3** – The swimming pattern of DS. The positions from 1 to 7 are the power stroke, while from 8 to 11 are the recovery stroke. During the power stroke the flagella produce a positive displacement whereas, during the recovery stroke, they return to their original position, moving closer to the cell body and leading to a negative displacement. [68] Adapted from [68].

As a result, the effective stroke induces a net forward motion since the quantity of surrounding fluid that is pushed backwards by the flagella, during the power stroke, is more than the one that adheres to them during the recovery stroke. [20] Nevertheless, the two strokes are not entirely distinct and they overlap one another, as the power stroke starts before the recovery stroke has completed and *vice versa*. [117] Moreover, the cells are also able to swim backward, by performing a flagellar undulatory movement. [39]

The complete algal flagellar beat sequence must also be asymmetric in time in order to overcome the constraints of the low *Re* numbers world (see **Section 1.8.4**) and this results in a small rotation of the cells. For example, some experimental observations on the microalgae *Dunaliella bioculata* and CR have highlighted that their flagella do not usually beat at the same frequency and therefore one flagellum becomes inactive while the other continues its beat, causing the algal cells to rotate. Similarly, DS cells tend to rotate counterclockwise around their longitudinal axis at a frequency of 2 Hz and trace out a helical path, while swimming. [39, 43]

### **2.3.5 *Dunaliella Salina* and its taxis effects**

DS cells exhibit a variety of interesting responses since its fluid dynamic behaviours can be affected by taxis effects (see **Section 1.5.3**). Specifically, similarly to other bottom-heavy organisms, DS can show both gravitactic and gyrotactic behaviours, leading to potential algal aggregations and their related instabilities (see **Section 1.6.1 and 1.11.1**). [3, 10] DS cells can also exhibit phototactic behaviour and positive chemotaxis towards dissolved nutrients they feed upon. [52]

These taxi effects cause the cells to bias their movements in certain preferential directions and this has consequences in designing PBRs (see **Section 2.10**); for example, microalgae have a tendency to swim towards surfaces in search of light, biofouling them and creating non-uniform distributions of light intensities within the reactors. [118]

## 2.3.6 *Dunaliella Salina* applications

*Dunaliella* species are grown for the production of carotenes, vitamin A and biofuels, since they can be cultivated in a simple medium of high salinity that helps to inhibit the growing of predatory and opportunistic organisms. [93] Moreover, DS can also be used for the production of foreign proteins (*e.g.* vaccines, antibiotics, *etc.*) as, due to the lacking of a cell wall, the introduction of vectors into the cell can easily be accomplished. [112]

### 2.3.6.1 $\beta$ -carotene production

DS is the main commercial source of natural  $\beta$ -carotene because, when being stressed, cells turn red producing and accumulating protective carotenoids up to a concentration of 14% of their dry weight. [93, 119]  $\beta$ -carotene is a high-value compound that has been used as colorant and additive in food, cosmetic and pharmaceutical industries. [120] It is also well-known for its cancer-preventing, high nutritional and antioxidant properties. Although some carotenoids (*e.g.* carotene and zeaxanthin) are available in synthetic forms, the demand for natural  $\beta$ -carotene has been increasing, owing to new findings concerning the carcinogenic effects of synthetic  $\beta$ -carotenes. [112] In addition, algal  $\beta$ -carotene production allows several useful by-products to be obtained since, after removing carotenoids from the cells, the remaining dried algal meal contains about 40% of proteins and other healthy compounds, which can be utilised as animal feed for aquatic species. [121, 122]

### 2.3.6.2 Polluted effluent treatment

DS (among other *Dunaliella* species) is also used to treat polluted effluents from municipalities and industries. In fact, during a wastewater treatment, organic pollutants are decomposed into simpler compounds (*i.e.* nitrogen, phosphorous, carbon dioxide, *etc.*) by microbes, while algae can both consume these chemicals and support microbes symbiotically, through the photosynthetic oxygen. [112, 123]

Moreover, algae can also be exploited to absorb and accumulate residual inorganic pollutants and heavy metals from wastewater and effluents. [112, 123] For example, some *Dunaliella* species have been employed for taking up inorganic arsenic [124], nitrogen, phosphorus and chromium ions. [125]

### **2.3.6.3 *Dunaliella Salina* used as a bio-indicator**

Along with other microalgae, DS can be also used as an environmental bio-indicator of anthropogenic compounds, due to its sensitivity and adaptability to thrive in difficult environments and the lack of a rigid cell wall that prevents toxic substances from not being permeated and assessed. The integration of algal bioassays with environmental monitoring of polluted effluents can lead to pollution prevention and environmental protection. [105] For instance, *D. primolecta* has been used as a biosensor of herbicidal-polluted effluents [126] and *D. Salina* to assay the toxicity of typical mutagenic phenols. [127, 128]

## **2.4 The production of algal biofuels**

In the next three sections, the current main advantages and constraints of algal biofuels will be introduced, focusing particular attention to algal biodiesel and describing the different phases required for its production (*i.e.* cultivation, harvesting, concentration, dewatering and drying of the algal cells and finally the final transesterification reaction, which permits the transformation of algal biomass into biodiesel and glycerol [129]). The algal cultivation process and its critical requirements will also be analysed in detail, carrying out a technical analysis regarding the main biological and engineering challenges concerning algal PBRs.

The main aim of the following sections is to provide an overview about the context of this research work which looks at improving the algal cultivation conditions in PBRs and enhance the viability of the whole biomass production process.

### **2.4.1 Why the algal biofuels?**

Fossil fuels have been our main energy source for centuries, although they are known to be a limited resource and harmful to the environment. [107] In 2005, Hirsch *et al.* [130] reported that the global energy demand for transportation is due to increase by 45% by the year 2045, owing to the increasing of the population and expanding economies, while the remaining global reserves of crude oil are continuously declining. Moreover, greenhouse gases concentrations have been increasing in the atmosphere, causing climate change and global warming. [36, 130]

All these factors are driving the need to explore and develop new sustainable alternatives to address the World's energy requirement, without affecting the technological and economic growth and further compromising the environmental balance.

Amongst other solutions, unicellular microalgae represent a very attractive alternative, being the most effective photosynthetic organisms for generating chemical energy from sunlight without any intermediate required chemical feedstock and accumulating high quantities of lipids and fatty acids (more than 80% by weight of dry biomass) that can be converted into biofuels, like biodiesel. [10, 118, 131]

What is more, being aquatic organisms, microalgae offer many advantages over terrestrial crops (*e.g.* Soybean, Palm, Jatropha, *etc.*) because they do not require to be cultivated on fertile lands, treated with costly and potential harmful fertilizers, and irrigated with natural freshwater resources, and therefore having much lower impacts on the World's food supply. Microalgae grow rapidly and can be harvested continuously, while terrestrial plants have relative long growing seasons. [129] Furthermore, algal biofuels, compared to the terrestrial-plant-produced ones, have higher calorific values, low kinematic viscosities and can be utilised in different climatic conditions. [132]

Additionally, since microalgae need carbon dioxide for the photosynthesis (see **Section 1.3.1**) and have large surface to volume ratios (*i.e.* high rates of absorption), they can be used to reduce the atmospheric carbon dioxide impact. [95, 112]

Nonetheless, as we shall discuss in the next sections, despite all the advantages mentioned, some critical aspects must still be overcome in order to make microalgal biofuels economically and technologically competitive against fossil fuels. [129]

Specifically, three fundamental issues remain critical to the economic and technical implementation of the algal biodiesel production: *i.e.* the optimisation of the biological productivity through species selection and the enhancement of the culture conditions, the development of both low-costs PBRs and more inexpensive downstream processes techniques, in particular the harvesting and the extraction phases. [129]

Nevertheless, this research work has mostly been focused upon the enhancement of the culture conditions and the reduction of the operational costs related to PBRs, as will be addressed in the results discussion.

## 2.4.2 Processing the microalgae

Regardless the desired final product(s), processing the algae involves the following phases (see **Figure 2.4**):

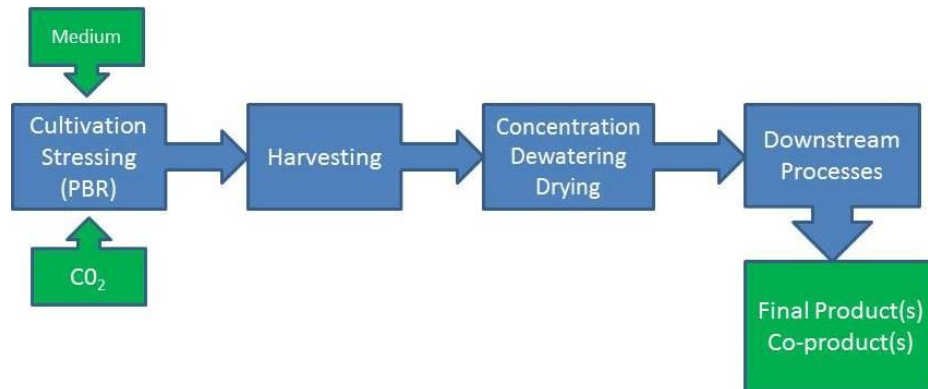


**Figure 2.4 - General block diagram of the whole biomass production. The major inputs required are the culture medium, carbon dioxide, the chemicals and the energy required by each production phase. Adapted from [129].**

- The algal cultivation (in open or closed PBRs) and stressing (to trigger the cellular accumulation of a particular substrate that will be treated in the downstream processes).
- The harvesting process (to remove physically the algae from the cultivation site). Mainly, the harvesting technique depends on the growth species and the desired final products, albeit this is usually achieved through centrifugation or filtration. [112]
- The concentration, dewatering and drying processes (to extract from the cells the desired substrate for the downstream processes);
- The downstream processes (to obtain the final product(s) and co-product(s)). [10, 129]

In the case of algal biodiesel production, oily algae are cultivated in closed PBRs and stressed (through a nitrogen deficiency in the medium [131]) to maximise the cellular lipids concentrations, *i.e.* predominantly C16-C18 chain products that are the substrates used for the biodiesel production. [133]

Once the cells have been harvested and concentrated, the lipids are extracted and reacted with alcohols to produce glycerol and biodiesel, through the transesterification reaction (see **Figure 2.5**): [10]

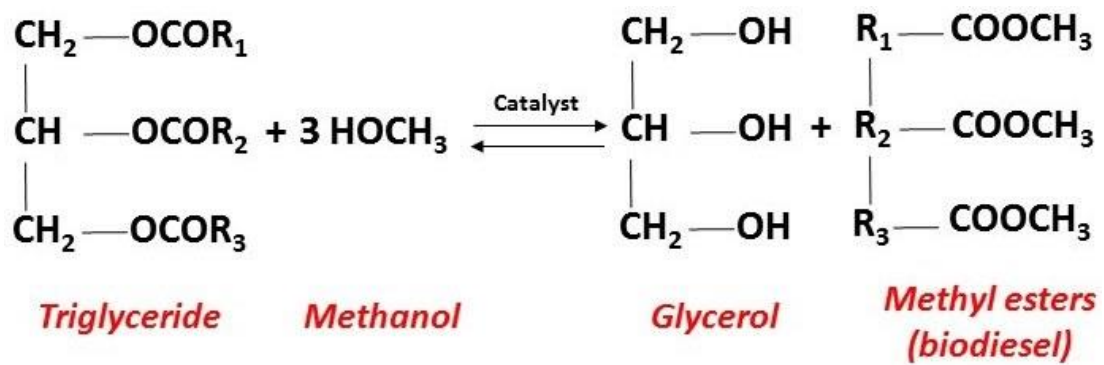


Figure 2.5 - During the transesterification reaction, also known as alcoholysis, triglycerides are reacted with methanol producing glycerol and methyl esters of fatty acids. Stoichiometrically, the reaction would require three moles of alcohol for each mole of triglyceride, while industrially six moles of alcohol are always used in order to ensure that the reaction is driven towards the methyl ester production (*i.e.* towards the biodiesel), which yield can exceed 98% on weight basis. [134] Transesterification is catalysed through alkalis, such as sodium or potassium hydroxide, at a concentration of about 1% by weight of oil. [135] Adapted from [136].

## 2.5 The algal cultivation

A phototrophic algal culture is composed of a growth medium, containing some key nutrients (*e.g.* nitrogen, phosphorous, trace elements) that must be optimised, depending upon the requirements of each species. Moreover, the microalgae also need a source of inorganic carbon (*e.g.* carbon dioxide) and light, required for the photosynthetic process. [118]

Thus, in an algal culture, three phases can be distinguished: liquid (*i.e.* the medium) solid (*i.e.* the microalgae) and gas (*i.e.* usually carbon dioxide-enriched air). Nevertheless, the gas phase must also include the oxygen that is released by the algae, due to the photosynthesis (see **Section 1.3.1**). [118]

After fulfilment of the proper light and nutritional growth needs, the culture requires optimal mixing levels, in order to produce a uniform algal dispersion and to eliminate gradients of light, nutrients, gases and temperatures that may lead to irreversible biological damage for the algae. Inadequate mixing can also promote the formations of algal patchiness and aggregations (see **Section 1.6**). [137]

Hence, the design of an algal culture device implies the optimisation of its fluid dynamical, biochemical and light harvesting conditions (see **Figure 2.6**). [118]

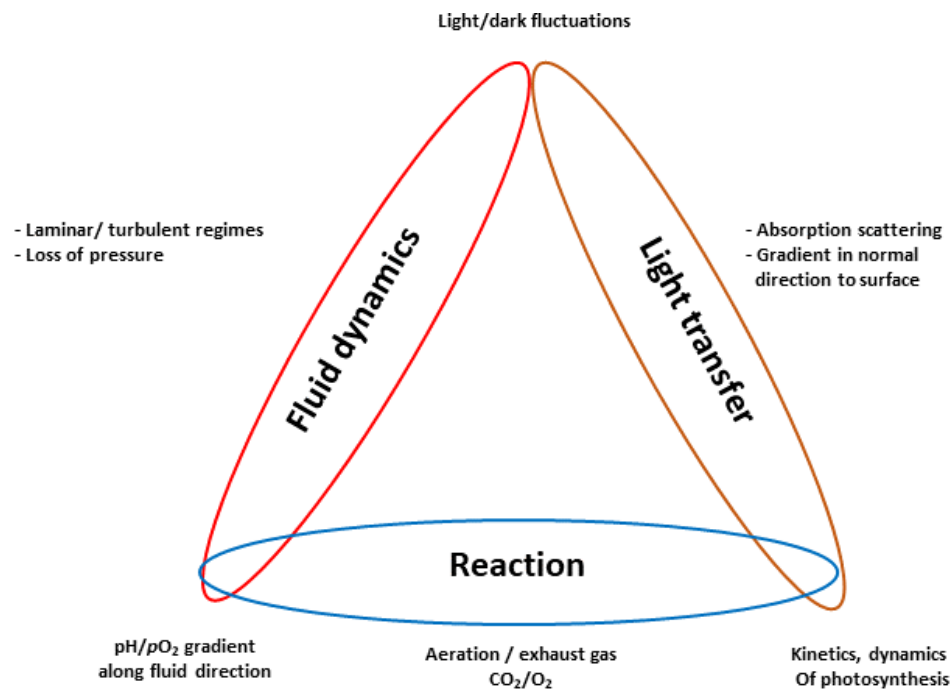


Figure 2.6 – The design of an algal cultivation device requires understanding of the interactions between its fluid dynamic conditions, the biochemical reactions and the light distribution within the culture. These technical aspects must be optimised and interconnected, in order to reduce the operational costs. Adapted from [118].

Furthermore, ideally, algal cultures should be axenic (*i.e.* they must contain only one predominant species) and both chemical and biological contaminations should be avoided. Chemical contaminations may include some pollutants that may be absorbed by the culture medium or to some chemical flocculants, used for creating algal self-aggregations (see **Section 2.10.2**), which may compromise both the algae and the final products; while biological contaminations are caused by other eukaryotes and prokaryotes opportunistic species that may compete for food against the cultured algal species and even predate them, leading to their extinction. [138]

Industrially, microalgae are cultured in artificial devices termed as PBRs, which theoretically should recreate algae's natural environments, however, many differences are often deliberately imposed through the stressing procedures. [138]

## 2.6 Different types of reactors and main technical features

This section is focused on the different industrial PBRs and some of their distinctive technical characteristics which allow evaluation of their performance, to compare different configurations and will be employed in the next chapters to understand the results. The main industrially-used PBR configurations will also be discussed, providing some examples of other research work involving them, which illustrate different technical solutions and some of the most important aspects that are taken into account, when PBRs are researched.

The high number of economic, biological and engineering variables that affects the design of PBRs has led to the development of a huge variety of geometries and configurations, hence it is fundamental to define some technical parameters that can be used for assessing and comparing the performance of different PBRs (see **Figure 2.7**): [118]

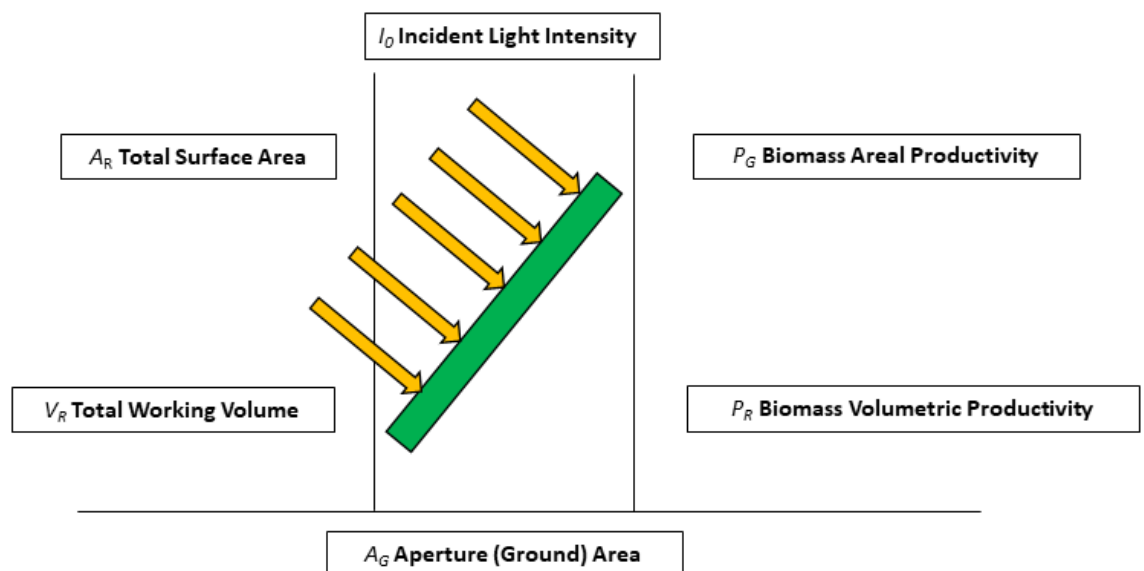


**Figure 2.7** – The technical parameters that characterise PBRs are vitally important as they make a serious contribution to the reactor costs and can be used for evaluating different configurations, albeit their values strongly depend on the purpose of the reactor and even on the research discipline, making the comparison process daunting. [118] Adapted from [118].

The most important are:

- The total working volume  $V_R$  [l or  $m^3$ ] of a reactor is the volume where the algae are actually cultured.

- The total surface area  $A_R$  [m<sup>2</sup>] of the transparent parts of the reactor determines the amount of light that hits the reactor surfaces.
- The area-to-volume ratio  $AVR$  [m<sup>-1</sup>] is the ratio between  $A_R$  and  $V_R$ .
- The aperture (ground) area  $A_G$  [m<sup>2</sup>] measures the area from which the light is collected.
- The biomass volumetric productivity [g l<sup>-1</sup> d<sup>-1</sup>] can be defined as:

$$P_R = \frac{p_{Biomass}}{V_R \cdot day} \quad (eq. 2.1)$$

where  $p_{Biomass}$  is the biomass productivity. The volumetric productivity is often used for measuring the productivity in lab-scale experiments.

- The biomass areal productivity [g m<sup>-2</sup> d<sup>-1</sup>] can be defined as:

$$P_G = \frac{p_{Biomass}}{A_G \cdot day} \quad (eq. 2.2)$$

$P_G$  allows to assess the productivity of larger PBRs plants, measuring the conversion efficiency of the incident light in chemical energy.

Moreover, industrially and at lab-scale, PBRs can be classified as open or closed. [118, 139]

### 2.6.1 Open photobioreactors

Open PBRs consist of outdoor ponds that can be quiescent or paddlewheel stirred, they are relative cheap to operate, strongly dependent upon the local weather and eventual sources of pollution (*i.e.* chemical contamination). [140]

Moreover, they can easily be contaminated by opportunistic species (*i.e.* biological contamination), and the light penetration may be hindered by spontaneous algal accumulations within the reactor; therefore, they can just be used for cultivating organisms that can grow in prohibitive conditions, such as DS. [129, 140]

An example of a stirred open pond is the raceway pond, where the required levels of mixing and aeration are achieved through paddlewheels and guiding baffles (see **Figure 2.8**).

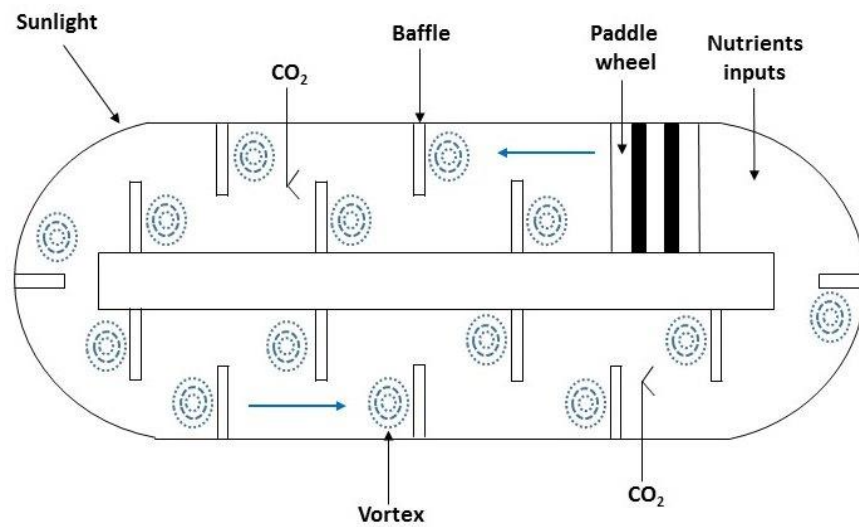


Figure 2.8 – The top view of a raceway pond, showing the paddlewheel and its guiding baffles. Usually the technical parameters that must be monitored and regulated properly are the pH, the medium level and temperature. The typical depths of open PBRs are in the range of 10-30 cm to ensure an optimal light penetration within the culture. [141] Adapted from [141].

## 2.6.2 Closed photobioreactors

Closed bioreactors can be thought as sealed containers, used for culturing fast-growing microalgae in monoseptic environments, under a great variety of growth conditions and are usually manufactured with common transparent materials (*e.g.* polyethylene, glass, *etc.*) to be inexpensive and ensure an optimal light penetration.

Compared to open ponds, closed PBRs are characterised by higher biomass productivities and less medium evaporation.

The optimal aeration and mixing levels within the reactor can be achieved by either pumping the suspensions or bubbling them with rising bubbles at both laminar and turbulent conditions. [142]

Despite the high number of technical solutions, only three standard designs have mostly been used: the flat plate reactors, the fermenter-type reactors and the tubular PBRs. [118]

### 2.6.2.1 Flat plate reactors (FPR)

FPRs are made of narrow panels in order to maximise the area-to-volume ratio and the harvesting efficiency of the solar light (see **Figure 2.9**). Their light path length ranges from a few mm up to 70 mm. The required carbon dioxide is usually bubbled through a perforated plastic tube and these reactors may be equipped with baffles to evoke eddy formation and enhance the mixing. [118] FPRs allow high biomass productivity, a uniform distribution of light and they do not need a gas transfer unit to remove the oxygen from the culture. Nevertheless, they can easily be affected by contaminants, the culture temperature may be difficult to control and the photosynthetic-released oxygen can reach critical concentrations. [142]

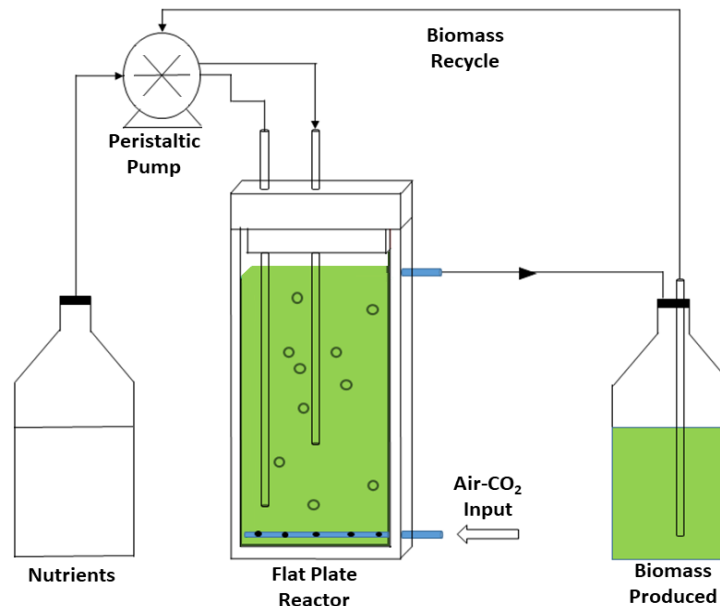


**Figure 2.9 – Schematic of a continuous FPR, where the carbon dioxide is bubbled from the bottom of the reactor, while the medium and the biomass recycle are sent to the reactor through a pump. This reactor can be also used for batch operations; in this case both the inoculum and the nutrients are loaded into the reactor at the beginning and, during the run, no inlet and outlet streams are operated, apart from the carbon dioxide-enriched air flow. [143] Adapted from [143].**

FPRs have been studied intensively, for example Richmond *et al.* exploited a vertical FPR for outdoor cultivations of the microalgae *Nannochloropsis sp.*, employing a reactor with an overall volume of 1000 l, the carbon dioxide-enriched air bubbled at the bottom through a perforated plastic tube and a closed system of water spraying for controlling the temperature. They considered different light paths (from 1.3 cm to 17 cm), finding out that the shorter the light path, the higher the attained volumetric productivity. [144, 145]

Some more interesting engineering features have been described by Iqbal *et al.* who studied a V-shaped FPR apparatus for the cultivation of *Porphyridium cruentum* [146] and Sun and co-workers, which have cultivated the microalga *Chlorella vulgaris* in a vertical FPR, increasing the productivity by about 23% by embedding hollow light guides within the reactor. [147]

### 2.6.2.2 Fermenter-type reactors (FTR)

FTRs can be thought as wrapped flat plate reactors and are frequently used for lab scale experiments. They are also known as bubble columns and consist of either one single cylinder or two cylinders placed one inside the other, forming an annular chamber (see Figure 2.10).

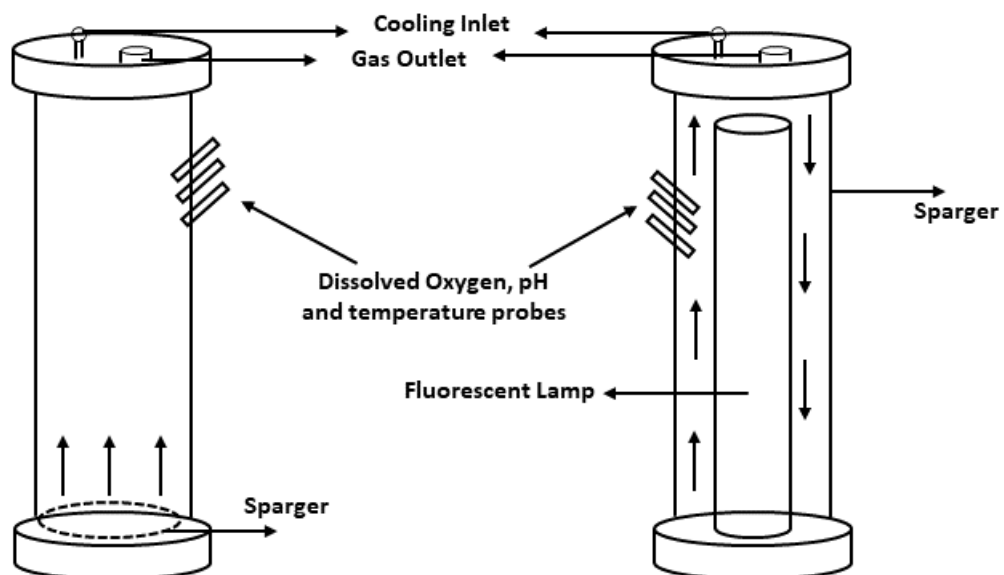


Figure 2.10 – The layout of a cylindrical FTR (a) and an annular chamber FTR (b). For the cylindrical FTR, the carbon dioxide-enriched air flow is usually supplied from the bottom part of the reactor and allowed to flow throughout it, while in the case of the annular chamber FTR, the gas is provided from the top of the riser section and then is allowed to flow in an anti-clockwise direction. However, the annular chamber FTR is preferred because the internal draft tube ensures a more homogenous light paths and higher biomass productivities. [148] Adapted from [148].

Nevertheless, cylindrical FTRs must have relative high diameters to provide enough culture volume, hence they are characterised by low area-to-volume ratios and therefore their light harvesting efficiency is quite low, creating heterogeneous light distributions within the reactor and compromising their performances.

For this reason, annular chamber FTRs are more widely used, since their internal cylinder can be equipped with internal artificial lights, reducing the dark fractions. FTRs allow to culture axenic suspensions under well-controlled conditions; however, their biomass productivities are relatively low and they are difficult to scale up, due to their high operational costs. [118, 142]

Many attempts have been made to overcome the FTRs limitations, for instance Ogbonna *et al.* developed a FTR that can utilise both artificial and sun light, which can be collected using optical fibres and a light tracking sensor that orientates the lens towards the position of the sun. The reactor had a working volume of 3.5 l and the mixing was achieved by an impeller. In particular, they considered *Chlorella sorokiniana* cultures (a freshwater green microalga used for the biodiesel production [149]), comparing the attainable biomass productions at different conditions: using only the solar light collection device, alternating autotrophic-heterotrophic cycles and cultivating the microalgae with the integrated solar and artificial light illumination system, achieving higher cell growth rates in the last case. [150]

Furthermore, Dong Ding *et al.* studied the effects of the carbon dioxide bubbles on the growth and distribution of the microalga *Chlorella pyrenoidosa*, used for the production of bio-hydrogen, in a bubble column reactor, characterised by a working volume of 400 ml, an inner diameter of 0.045 m and a height of 0.3 m. The reactor was equipped with a gas supply and a data acquisition system. In particular, they had taken into account different inlet carbon dioxide concentrations, blast orifice sizes and gas flow rates, finding that, depending on the experimental conditions considered, the bubbles tended to drag the algae to the top of the suspension, creating heterogeneous algal distribution within the reactor. The optimal operational conditions were obtained bubbling a 5% (v/v) carbon dioxide-enriched air flow, at a flow rate of 20 mL·min<sup>-1</sup>, through 20-µm-diameter orifices. [151]

### 2.6.2.3 Biological and engineering challenges of tubular photobioreactors

Tubular PBRs are transparent tubes that can be assembled in different arrangements (e.g. horizontally, vertically, helically, etc.). Nevertheless, horizontal tubular PBRs (HTPBRs) are the most widely used ones as they guarantee optimal homogenous incident light conditions, being characterised by relative high area-to-volume ratios (see **Figure 2.11**). [152]

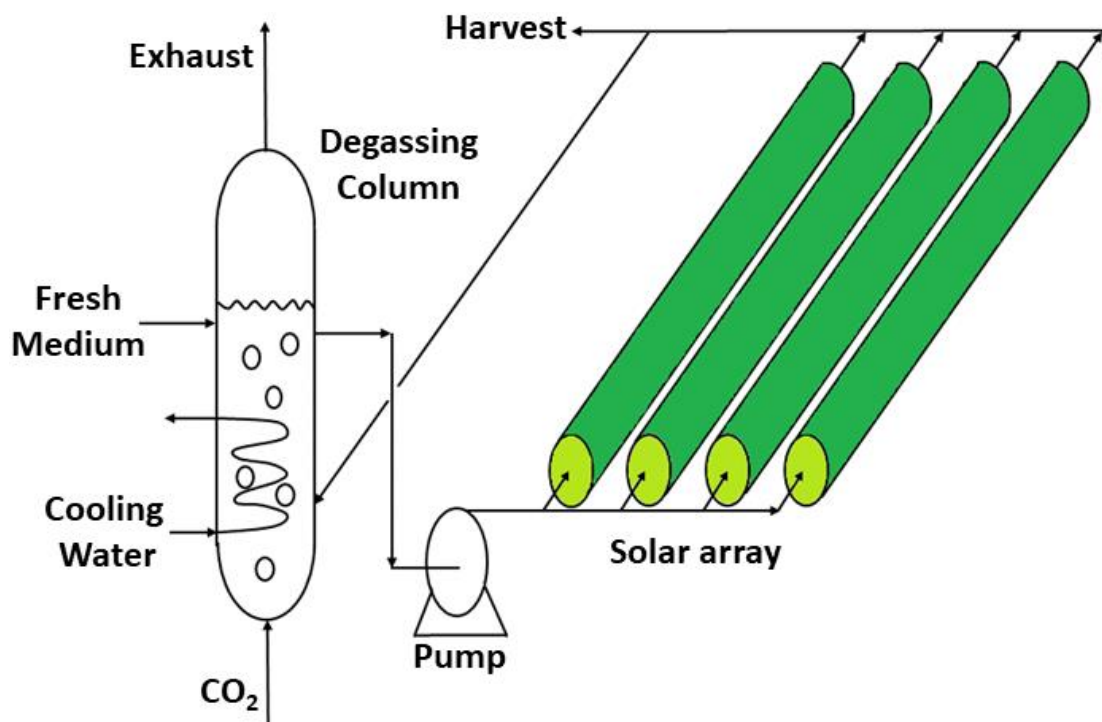


Figure 2.11 – A HTPBR is composed of two main parts: the plastic tubes, where the algae are cultivated and the gas exchange section, where the carbon dioxide is injected in the medium and the oxygen is removed from it. HTPBR can be illuminated both by sunlight or fluorescent lights and they must optimally be assembled in order to maximise the area-to-volume ratio. [139] Adapted from [153].

HTPBRs diameters usually range between 10 to 60 cm and must not exceed the light path length in order to prevent algal demise [154, 155]; amongst their advantages, HTPBRs can handle large working volumes, guarantying high biomass areal productions under a high degree of control of the algal culturing conditions. [156]

However, in order to achieve optimal overall mixing levels, enhance gaseous exchanges and prevent algal biofouling, the flow within tubular PBRs is usually kept turbulent, sometimes also using plastic beads (see **Section 2.9**) [156], leading to high operational costs.

Moreover, a considerable amount of heat may be generated inside these systems, attaining temperature gradients of up to 20°C within a single day and therefore HTPBRs must be equipped with a heat exchange system, increasing their operational complexity (see **Section 2.8**) [157]

Consequently, as explained in detail in the following sections, the biological and engineering parameters of PBRs (*e.g.* the temperature control, the incident light distribution, fluid dynamic conditions, *etc.*), must be optimised so as to improve the viability of the whole microalgal biofuel production process and make it economically and technologically more competitive against fossil fuels.

## **2.7 An energetic analysis of the photosynthetic conversion process**

In the following sections, a technical energetic analysis of horizontal PRBs (*i.e.* the ones which have been investigated through the experimental observations) is reported, in order to understand the main biological and engineering challenges involved in the algal cultivation process. In particular, some key concepts (*e.g.* dark/light cycles, photosynthetic conversion efficiency, *etc.*) are analysed in order to justify the need for turbulent flow conditions within the reactors and the resulting high operational costs.

Moreover, the main theoretical reasons behind the experimental investigations of this PhD will be outlined, showing why swimming microalgae should not be treated as passive particles during the PBR design and demonstrating that through concrete examples (*i.e.* the generalised Taylor-Aris dispersion theory, the comparison between the dispersion of microalgae and passive particles in downwelling and upwelling pipe flows, *etc.*).

In the last part of the chapter, a brief introduction is also given regarding different approaches for overcoming some of the PBR limiting factors; they mainly consist of growing parallel cultures of different microalgae in order to exploit their symbiotic interactions and to genetic engineering the cells.

## 2.7.1 The role of the local weather

When a solar radiation travels towards the Earth's surface, its first impediment is represented by the local weather of the actual PBR location (*e.g.* it can dramatically be compromised by cloudy skies [129]); generally, the incident intensity tends to diminish as one travels away from the equator latitude. Thus, a preliminary detailed meteorological analysis, regarding the actual location of the algal cultivation facilities is required; as it will also affect their design (*e.g.* high solar irradiance means high evaporative water loss in open ponds or more complicated cooling systems in closed PBRs, *etc.*) (see **Section 4.2**). [158]

## 2.7.2 The photosynthetically active radiation and the photosynthetic conversion efficiency

When the incident solar light hits the algal cultivation facilities and travels through the liquid medium, it will be absorbed by millions of algal cells. Nonetheless, plants and algae have adapted to utilise only a limited spectrum of light (*i.e.* the photosynthetically active radiation PAR), which is included between 400 to 700 nm and represents only the 45% of the total energy in the visible light spectrum (see **Figure 2.12**).

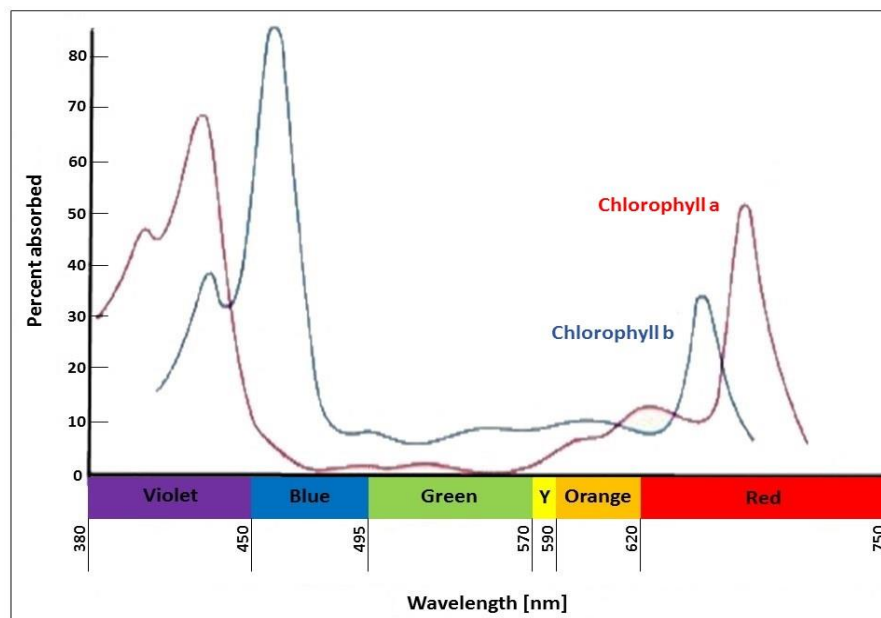


**Figure 2.12** – The absorption spectra of chlorophyll a and b, against the spectrum of visible light. Chlorophyll is the most abundant pigment in plants and green algae, it absorbs efficiently red and blue light, while green wavelengths are reflected. Therefore, PAR represents the spectral range of the solar radiation that photosynthetic organisms can employ for the photosynthesis. Adapted from [159].

The incident PAR is absorbed by the cellular photosynthetic apparatus, located in the chloroplast membrane, that acts as light-harvesting antennae, collecting the photons required for the photosynthetic reaction, which has an energy conversion efficiency of roughly 25% [158], implying a photosynthetic conversion efficiency (PCE) of:

$$PCE_{PAR} = 45\% \cdot 25\% \cong 11\% \quad (\text{eq. 2.3})$$

However, *PCE* is a theoretical upper limit since its values are normally below 6.5%, because nearly 40% of the converted solar energy is employed for cellular biological functions and growth, leaving an estimated 60% available for the biomass accumulation. [118, 142]

### 2.7.3 The photoinhibition process and the dark/light cycles

An additional drawback of the cultivation process is that cellular photosystems can just handle limited capacities of energy and be easily saturated by high light intensities, leading to photoinhibition phenomena that may cause cellular damage and premature population demise (see **Section 5.2.1**) [160, 161] Hence, the incident light transmission within PBRs must be optimised, ensuring high surface-to-volume ratios. [162]

Moreover, light penetration may also be inhibited by cell accumulations and shading phenomena (*i.e.* biofouling), since the algae tend to absorb and scatter the solar light, creating heterogeneous radiation fields, and therefore, within the reactor, there will be high-radiance zones (*e.g.* close to the walls) and low-radiance zones (*e.g.* in the depth of the culture). [162]

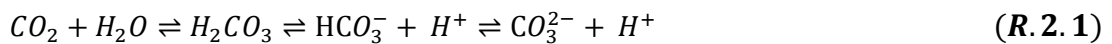
This can be overcome by periodically recirculating the shaded cells from the dark regions to the surface, ensuring suitable dark/light cycles (DLCs) that must also prevent the cells from dying due to photoinhibition (see **Section 5.2.1**). [161]

Nevertheless, DLCs frequency must be optimised since, slow DLCs would lead to low algal growth rates while, during fast DLCs, the algae can collect and store some solar light, when they are in the bright zones, which will be used in the dark zones (this phenomenon is called the flashing light effect), leading to beneficial effects. However, the flash light effect is usually achieved by turbulently pumping the algal suspensions and it implies both high operational costs and potential shear-induced damages for the cultured organisms; thus a compromise for the DLCs frequency must be found. [118]

## 2.8 Gas, pH and temperature gradients

Compared to other PBRs configurations, the complexity of horizontal tubular PBRs is further increased by the fact that phototropic microalgae need an inorganic carbon source to synthesise the microalgal biomass [163]; usually the carbon requirement is fulfilled by injecting in the system carbon dioxide-enriched air, since carbon dioxide is present in the atmosphere at very low concentrations (about 0.03 % v/v). [142] For a given algal strain, the required carbon dioxide transfer rate can be calculated stoichiometrically and depends on the cellular carbon content and its growth rate. [118]

When carbon dioxide dissolves in water, it will form carbonic acid and consequently bicarbonate and carbonate ions, according to the following reaction, which is the natural equilibrium between carbon dioxide and protons: [164]



Nevertheless, when algae perform photosynthesis and consume carbon dioxide, the equilibrium is shifted toward the left and the pH increases, whereas algal respiration produces carbon dioxide, decreasing the pH and shifting the equilibrium to the right. Moreover, during the algal growth, the pH and alkalinity of the culture medium can also change due to fluxes of organic and inorganic compounds in and out the cells, for example hydrogen ions, bicarbonate ions, hydroxide ions, *etc.* [112, 165]

Beyond a given threshold, this may cause the precipitations of phosphorous, calcium and carbon salts, leading to a chemical deterioration of the medium and flocculation of the algal cells. [142] Hence, the pH must be maintained within an optimal range (usually between 7-8) and this can be achieved employing different control systems, amongst which the most common one is an on-off arrangement, that supplies carbon dioxide into the culture, when the pH exceeds a desired set point, halting the injection once the pH has been regulated. [164]

The photosynthetic process implies also that the algae release significant amounts of oxygen within the reactor, creating potential oxygen gradients that may inhibit the cellular growth and therefore must be avoided by periodically purging the PBR. [160]

Furthermore, when a PBR is exposed to natural light, a large amount of heat is generated and absorbed, leading to a considerable increase in the culture temperature, which can reach up to 45°C in warm climates, and therefore PBRs must be equipped with both a temperature control system and a cooling system, in order to maintain ideal thermic profiles. [157]

Further operational costs are due to the fact that the reactor must also be protected from inclement weather and some materials of construction tend to degrade quickly under the sunlight. [142]

## 2.9 Optimal fluid dynamic conditions

In PBRs, in order to guarantee proper nutrients mixing levels, to prevent algal biofouling, to obtain the most favourable dark/light cycles and to avoid gas concentration gradients, optimal fluid dynamic conditions must be ensured. This is currently achieved by turbulently pumping the algal suspensions, using either airlift circulators or pumps. [10, 118] When airlifts are utilised, the circulation does not involve moving parts and both the aeration and degassing of the suspensions are achieved in the airlift component. On the contrary, when pumps are employed, horizontal PBRs must be equipped with a separate gas exchanger and the mechanical parts of the pump may damage the cells. [152, 154] The mixing within PBRs can be also enhanced adding plastic beads in order to inhibit algal adhesions and accumulations. [166]

Nevertheless, turbulent fluid dynamic conditions may lead to potential fluid microeddies, (which dimensions should always be greater than those of the algae, to prevent shear-induced damages on the culture (see **Section 6.2.3**) [167]). These represent a costly solution and, as explained in the next section, do not allow to exploit the microalgal fluid dynamic behaviours.

## 2.10 Exploiting the microalgal swimming properties for photobioreactors

When algal cultures are turbulently pumped in PBRs, the cells are treated like passive particles, neglecting and overlooking their swimming properties and assuming that they will be equally likely to swim in all directions, behaving stochastically. [10] However, the distribution and consequent dispersion of swimming microalgal suspensions in flows are very different from those of passive particles, since the algae can drift faster across the streamlines, disperse less, accumulate in specific regions of the flow and swim towards preferred directions, affecting the flow profile. [10, 56] For instance, in downwelling flows in vertical pipes, passive particles are transported with the mean flow while gyrotactic algal cells tend to focus in the centreline, swimming faster than the mean flow velocity, whereas in upwelling flows, the algae will tend to swim towards the walls (see **Section 1.11**). [10, 56] More examples concerning the different behaviours of living cells and lifeless particles in bounded flows will be provided in the results and discussion sections.

Nonetheless, when operating a given PBR, it is also important to take into account how the cultured organisms behave in comparison with the dissolved nutritional components; in fact, if the cells disperse differently from nutrients they may eventually separate, compromising the cellular survival. [168] In particular, when some fresh medium (*i.e.* with high nutrients concentrations) is loaded in a culture device, it will disperse according to the Taylor-Aris dispersion theory (TADT), *i.e.* similarly to a blob of dye particles that has been injected in a pipe where is flowing a fully-developed Poiseuille flow. [169, 170]

As shown in the **Figure 2.13**, TADT states that the tracer particles will drift along the pipe and also will diffuse with an effective diffusivity coefficient  $D_{Eff}$ , given by:

$$D_{Eff} = D \left( 1 + \frac{Pe^2}{48} \right) = D + \frac{R_p^2 \cdot \bar{U}^2}{48 \cdot D} \quad (eq. 2.4)$$

where  $D$  is the diffusion coefficient of the particles,  $Pe$  is the Péclet number (see *eq. 1.19*),  $R_p$  is the radius of the pipe and  $\bar{U}$  is the mean fluid velocity. *Eq. 2.4* shows that  $D_{Eff}$  increases with  $R_p$  and  $\bar{U}$  (*i.e.* larger pipes or higher speeds, increase  $D_{Eff}$ ) and is a function of the molecular diffusivity plus a term proportional to one over the molecular diffusivity. [10]

Nevertheless, TADT does not concern just passive particles within Poiseuille flows in pipes but it occurs every time there is a velocity gradient; in fact, similar results have been found for turbulent flows in pipes and channels. [171, 172]

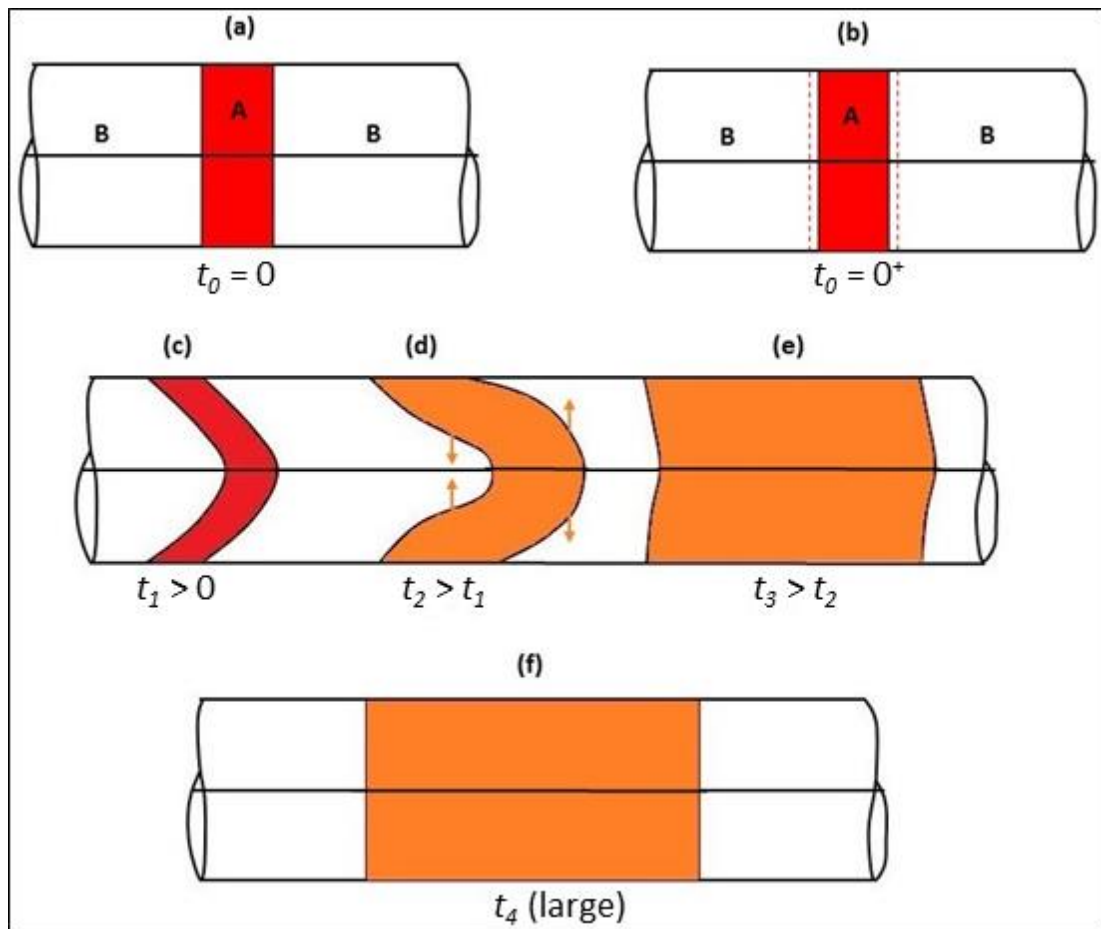


Figure 2.13 – The injection of a slug of solute A (the red compound) into a fully-developed laminar flow of a solvent B (the white compound). (a) During the first instants there is no diffusion. (b) At very short time after the injection A diffuses into B through pure axial molecular diffusion (represented by the two dashed segments), albeit this phenomenon occurs almost instantaneously and therefore it is not of practical interest. (c) The tracer patch is axially advected and stretched out parabolically by the flow. (d) The parabolic shape will give rise to a radial concentration gradient that tends to mix the solute A with the solvent B (generating the orange parts), through the radial molecular diffusion. In particular, the radial diffusion plays a part in the dispersion process as, at the rear of the patch, causes the solute A to move inward, from the low-velocity wall regions towards the high-velocity central regions, speeding up the back of the tracer patch. Similarly, at the front of the slug, the radial molecular diffusion moves the particles outwards, slowing down the tracer patch. (e) The net effect of the axial advection, the radial diffusion and the axial diffusion (*i.e.* the Taylor-Aris dispersion) is to enhance the dispersion, leading to an average concentration  $\bar{C}$  of the tracer, which is the one that would have been obtained if the tracer was diffusing with a diffusion coefficient  $D_{Eff}$  (see eq. 2.4). (f) At longer times, the region occupied by the mixed zone will increase. [173] Adapted from [173].

As a consequence, due to their unique characteristics, in recent years the fluid dynamic behaviours of photic algal cells have been studied and much progress has been made in understanding the physics of microalgal suspensions, employing both numerical and experimental approaches. [10, 56]

Specifically, dilute suspensions of bottom-heavy swimming algae have been modelled as a continuum through the conservation of mass, the conservation of momentum and the conservation of cells equations [2, 10, 55]. As addressed in the next section, the continuum model can be used for describing algal patterns and inferring the transport properties of algal suspensions. [56, 167]

### 2.10.1 The continuum model for dilute algal suspensions within a flow field

A dilute suspension of gyrotactic microalgae with local concentration  $n$ , which is subject to a macroscale fluid flow of velocity  $\mathbf{U}$ , can be modelled as a continuum employing the conservation of mass, the conservation of momentum and the conservation of cells equations. In fact, since in dilute suspensions the algal volume fraction is small, the fluid velocity fields satisfies both the continuity equation and the Navier-Stokes equation which takes into account the algal cells through a negative buoyancy term: [2, 10, 55]

$$\nabla \mathbf{U} = 0 \tag{eq. 2.5}$$

$$\rho_f \left( \frac{\partial \mathbf{U}}{\partial t} + \mathbf{U} \cdot \nabla \mathbf{U} \right) = -\nabla p + \mu \nabla^2 \mathbf{U} + n V_c \cdot \rho_c \mathbf{g} \tag{eq. 2.6}$$

$V_c$  and  $\rho_c$  are respectively the average volume and density of an algal cell; the other terms of eq. 2.6 have already been defined in the **Section 1.8.2**.

Eq 2.6 is subject to the Boussinesq approximation, meaning that the variation of  $\rho_c$  with  $n$  is negligible, except in the gravitational buoyancy term. [10, 55]

The other key equation for the model describes the conservation of the cells:

$$\frac{\partial n}{\partial t} = -\nabla \cdot [n \cdot \mathbf{U} + n \cdot \mathbf{V}_s - \mathbf{D}_c \cdot \nabla n] \quad (\text{eq. 2. 7})$$

$\mathbf{V}_s$  is the average swimming velocity and  $\mathbf{D}_c$  is the cell diffusivity tensor.

$\frac{\partial n}{\partial t}$  is the rate-of-change of cell concentration while the terms on the right-hand side refer to cell fluxes due to flow advection, mean cell swimming (due to the taxis effects) and random swimming motions, modelled as a diffusive process through  $\mathbf{D}_c$ . [2, 10, 55, 174]

Nevertheless, the continuum model requires knowledge of the mean swimming velocity  $\mathbf{V}_s$  and the cell swimming diffusion tensor  $\mathbf{D}_c$  as a function of the flow field; these functions can be computed from either the Fokker-Plank equation or an improved generalised Taylor dispersion theory. [56, 167]

The continuum model, along with its boundary conditions (*i.e.* stress-free conditions at free surfaces or no-slip conditions at solid boundaries, as well as no cell-flux at each boundary [10, 174]) has been exploited for modelling bioconvection in dilute suspensions [2] and obtaining analytical predictions of transport properties of algal suspensions in channel and pipe flows at both laminar and turbulent conditions. [56, 167]

As a consequence, these potential cost-reducing algal fluid dynamical features should be harnessed in PBRs design and processing, in order to reduce operational and capital costs; for instance, the downwelling parts of horizontal tubular PBRs would represent an ideal location for the harvesting, since there will be little biofouling at the walls. [168]

Moreover, the exploitation of the algal swimming properties can also result in a reduction of the costs related to the energy-intensive harvesting and concentration processes [129], since these production phases are more difficult and expensive for DS cells, compared to the ones of other commercial microalgae. [175]

## 2.10.2 Potential advantages for downstream processes

Since DS lacks a rigid cell wall, the traditional algal concentration technologies, that exploit centrifugation, may shear-damage the cells compromising their substrates and also the filtration processes are unreliable, owing to the fact that DS cells are surrounded by an external mucilaginous layer (*i.e.* the glycocalyx) that tends to clog the filter pores rapidly. [175] What is more, DS cultures have a relative low density ( $\sim 1 \text{ kg}\cdot\text{l}^{-1}$ ); hence very large volumes must be treated. [175]

These factors, alongside with the small DS cell size and the high salinity of their medium, contribute to make the algal harvesting, concentration and substrate extraction processes very challenging from an engineering perspective and energy-intensive and therefore any process that facilitates the algal pre-concentration should be evaluated and exploited. [112, 113] In that sense, chemical flocculants (*e.g.* ferric sulfate or aluminium sulfate) have been used to promote the formation of DS aggregates and their sedimentation or floatation but, in most cases, these chemicals are considered as unsafe impurities in the final products. [176]

In conclusion, generally speaking PBRs should ideally be optimised, designed and operated starting from the biological and fluid dynamic characteristics of the cultured microalgae (*e.g.* their shape, their dimension, their taxes effects, *etc.*) while, at the moment, the contrary has been happening, since the algal swimming properties are thrown out as insignificant complications and the cells are treated as passive particles, while being advected and shear-stressed in costly PBRs. [56]

As we shall see better in the next chapters, the facts that different microalgal strains have unique biological and fluid dynamic characteristics and that they should be taken into account and exploited during the design and processing of PBRs, are the two milestones of this research activity.

## 2.11 Alternative approaches for enhancing the microalgal applications

Apart from the fluid dynamic approach, some other solutions have been considered in order to overcome some of the limitations which have been discussed and increase the microalgal productivity.

For instance, some attempts have been made to grow in parallel cultures of different algal and bacterial species that may interact symbiotically; some interesting results have been achieved considering cultures of motile and non-motile algae, where the latter had been mixed by the former, increasing their biological biomass productivity, *e.g.* mixed cultures of the biflagellated microalga *Chlamydomonas* and the microalga *Chlorella vulgaris*. [10]

For example, Berberoğlu *et al.* studied the conversion efficiency of the solar light into bio-hydrogen in mixed cultures containing the microalga CR and the purple bacteria *Rhodobacter sphaeroides*, cultivated in outdoor PBRs with various diameters, finding an average increase of about 23% with respect of that of a axenic culture of CR. [177]

However, some studies on the growth of mixed species in stirred cultures have shown detrimental effects and biological constraints, such as predator-prey interactions, competition for nutrients and negative effects of secreted harmful chemicals; *e.g.*, in mixed cultures of *Hematococcus pluvialis* and CR, it was found that *Hematococcus* cells were suppressed by a fat-like substance released by CR cells; while other results showed a decreasing in growth of 25% when CR and *Chlorella vulgaris* were cultivated together. [178]

Furthermore, there are some research works where algal cell structures have been genetically engineered, in order to enhance the photosynthetic efficiency and their light saturation kinetics. These aspects have been analysed in details by Rosenberg *et al.* [129]

## 2.12 Chapter summary

In this chapter, the microalga *Dunaliella Salina* has been described, considering in detail its biological characteristics (*i.e.* the lack of a cell wall, its high tolerance to hypertonic and hypotonic conditions, *etc.*) and its swimming behaviour (*i.e.* the flagellar beat sequence, the exhibited taxis-effects, *etc.*); these features contribute to make DS one of the most industrially-cultivated microalga, particularly for biodiesel productions.

Moreover, a comprehensive technical analysis regarding horizontal tubular PBRs has been provided, outlining their main advantages, drawbacks and the importance of attaining optimal mixing levels, to guarantee the best possible performance. However, as discussed in this chapter, the current production costs of microalgal biofuels are not competitive against those of fossil fuels, since the ideal fluid dynamic conditions within PBRs are achieved by turbulently pumping the algal suspensions, treating the microalgae as passive particles and overlooking their unique swimming features, which instead should be exploited.

Therefore, these considerations and the discussed limitations of PBRs will be used in the subsequent chapters to justify the assumptions made in this research work, which was aimed to investigate the potential exploitation of microfluidic devices and the image analysis technique as complementary tools for PBRs optimisation processes, since they allow analysis and quantification of the algal cells behaviours under different fluid dynamic conditions.

## – Chapter 3 –

# Experimental apparatus and procedures

### 3.1 Chapter layout

This chapter describes the main experimental setups and procedures employed and developed in this research. In the first part, a comprehensive description of the requirements that must be fulfilled for the cultivation of algal cultures is provided, focusing in particular on the DS physiology and the preparation of both the culture medium and the suspensions.

Next, the microfabrication processes used to produce the devices are described. The microfluidic device set-up as well as the use of microscopy-based techniques for flow characterisation are discussed in detail.

Finally, the experimental setups utilised for both living and dead algae are introduced, analysing the flow visualisation process and the most significant experimental issues, which occurred during the investigations. The image analysis process is also explored, showing how the acquired experimental videos were analysed, the DS cells tracked and the resulting data was then processed.

### 3.2 Optimal cultivation of *Dunaliella Salina* cells

This section analyses in details the DS physiology and the requirements that the used Hejazi and Wijffels modified culture medium (HWMCM) must meet for its cultivation. The procedures for preparing the HWMCM and the DS suspensions are also described.

### 3.2.1 *Dunaliella Salina* physiology

The first controlled experiments to study the physiology and ecology of *Dunaliella* species were reported in 1930s, when Baas-Becking had observed that *Dunaliella viridis* lives optimally at sodium chloride concentrations between 6 – 23% and over a pH range of 6 – 9 whereas, calcium and magnesium ions in high concentrations can inhibit the algal growth. [179] Later, more experiments were reported by Lerche (1937) who had found that some *Dunaliella* species grow excellently at salt concentrations above 15%. [105, 180]

In recent decades, the nutritional requirements of different *Dunaliella* strains have been investigated in detail [181-183], allowing the optimisation of different culture media. In particular, it has been found that the required salt concentrations depend upon the cultivated strains, *e.g.* it has been reported to be around 6% for *D. viridis*, while for DS the salt concentration is around 12%. [105] Interestingly, a general trend observed in all these studies, showed that the actual salinities of natural environments, where the different strains had been isolated, were always much higher than the optimal salt concentrations found in laboratory experiments, demonstrating that the growth of a particular strain in a certain environment does not automatically imply optimal growth conditions, but more likely that the organism is more adaptable than its competitors. [105]

As previously discussed (see **Section 2.3.2**), DS cells live in halophilic environments and have simple growing requisites, due to their adaptability; therefore this makes it feasible to cultivate them in a wide range of culture media (*e.g.* enriched sea water, modified Johnson medium, *etc.* [184]), providing that they are optimised by adding some chemicals and adjusting some limiting physiological factors. [181, 185]

Specifically, the culture media employed must contain an inorganic carbon source for the photosynthesis, such as carbon dioxide or bicarbonate. [184] Moreover, the culture medium must also contain some key nutrients that can easily be uptaken by the microalgae; one of the most important is represented by nitrate ions which are supplied by adding chemicals, such as sodium nitrate or potassium nitrate to the medium. [184]

Monosodium phosphate needs also to be added as a source of phosphorous, essential for the algal survival. [186] The optimal phosphorous content ranges between 0.02 to 0.025 g·l<sup>-1</sup> as, at higher concentrations, can have inhibitory effects since the concomitant presence of phosphate and calcium can lead to algal flocculation. [112]

Other important nutrients that must be provided are chloride ions, sulfate ions, magnesium ions and calcium ions. Specifically, the concentration of chloride ions should be 1.5 times larger than the concentration of sulfate ions [113], while both magnesium ions and calcium ions can be tolerated at concentrations ranging between 0.8 and 20.0 mg·l<sup>-1</sup>. [184] Various trace elements (*i.e.* zinc, cobalt, copper, molybdenum, manganese) have also to be added to the DS growth media, albeit they are not necessary if the medium is composed of technical grade salt (*i.e.* a type of salt less pure than the food grade salt [187]) or seawater. [112]

Low quantities of iron are also essential and its optimal concentration is between 1.25 to 3.75 mg·l<sup>-1</sup>, as higher concentrations may inhibit the algal growth rates. [188] Moreover, the iron should be supplied in a chelated form, such as iron citrate or ferric citrate-EDTA, as it will easily be assimilated by the organisms. [112, 184]

Temperature and pH play also a part; in fact, the optimal growth temperature for DS is between 20 and 40°C as, while DS can tolerate extremely low temperatures, even below freezing [189], whereas temperatures greater than 40°C are usually lethal. [105] Furthermore, the optimum pH for DS and *D. viridis* has been found to be about 9. [112]

### **3.2.2 The Hejazi and Wijffels modified medium (HWMCM)**

In this research work, the DS cells were cultivated using the HWMCM [185], which was prepared adding the following chemicals to a litre of distilled water: sodium chloride (87.6600 g), sodium nitrate (0.4200 g), magnesium sulphate heptahydrate (1.2324 g), potassium chloride (0.0746 g), calcium chloride dihydrate (0.0441 g), sodium bicarbonate (0.8400 g); tris(hydroxymethyl)aminomethane (THAM) (12.1140 g); 2.5 ml of a 0.15 M boric acid solution and 0.1 ml of trace elements, called f/2 medium and purchased from a Scottish company called Culture Collection of Algae and Protozoa (CCAP). [185, 190, 191]

At this point, the pH of the medium had to be adjusted to 7.5 with 1 M hydrochloric acid solution. The medium was then sterilised by autoclaving it at 121°C for 30 minutes to prevent some biological contaminations caused by opportunistic organisms that may compete for light and nutrients against the cultivated cells. [120, 140] In order to avoid precipitation issues [185], 1 ml of a 0.1 M monosodium phosphate solution has to be added to the solution after it has cooled down at room temperature. The medium must be kept in the fridge, where it can maintain its chemical properties for a few months. [185]

As can be seen in **Table 3.1**, the used medium fulfilled the DS physiological needs.

**Table 3.1 – The DS nutritional requirements and how the used medium fulfilled them.**

<b>DS nutritional requirements</b>	<b>How DS nutritional requirements are satisfied</b>
Halophilic environment	All the salts used for preparing the medium
Inorganic carbon source	Adding sodium bicarbonate
Nitrate ions	Adding sodium nitrate
Phosphorous	Adding monosodium phosphate
Chloride ions	Adding potassium chloride, sodium chloride calcium chloride dihydrate
Sulfate ions	Adding magnesium sulfate heptahydrate
Magnesium ions	Adding magnesium sulfate heptahydrate
Iron, zinc, cobalt, copper, molybdenum, manganese	Adding trace elements.

A more detailed procedure for preparing the HWMCM and its physical properties can be found in the **Appendix 3.1**.

### **3.2.3 Preparation of *Dunaliella Salina* suspensions**

The specific strain of DS cell (CCAP 19/18), which was used to create further cultures, had been purchased from the Scottish company CCAP. [190] The algal suspensions were prepared inoculating 2-ml samples of relatively high-concentrated 4-week old cultures in 50-ml of fresh culture medium, inside borosilicate flasks.

During initial inoculations and early algal growth, batch suspensions could easily be compromised due to high nutrients and low algal concentrations, thus particular care must be taken during their preparation (see **Appendix 3.2**). [138] Moreover, in order to avoid any foreign contamination, the flasks were sealed using cotton wool balls and aluminium foil as breathable lids.

DS is relatively simple to cultivate as it is categorised as a Generally Recognised As Safe (GRAS) organism, its cells do not tend to clump, cling or form chains and, being a good swimmer, the cultures do not need to be continuously mixed. [93, 192]

Furthermore, due to the photosynthesis, DS cultures needed to be exposed to a source of light at an intensity of approximately 1600-2000 lux, which ensured a quick algal growth without causing any stress. [52] The light source used was a set of cool white fluorescent tubes, which had been set to provide 12-hour light/dark cycles, guaranteeing the best lighting conditions for the algal suspensions. DS cultures were kept at room temperature in a wooden “algae hut” (see **Figure 3.1**), which prevented the cells from being affected by any other form of luminous pollution.



**Figure 3.1 – The wooden algae hut used to grow batches of DS cultures. The whole set up had been arranged in such a way as to ensure that the only light reaching the cultures came from the fluorescent lights.**

Nevertheless, the batch algal suspensions were characterised by limited resources, consequently new cultures had to be reprepared periodically, in order to be able to use fresh cells for the experiments and also to prevent dead and lysed algae from affecting the cultures or skewing the results.

### 3.3 Technical properties of microfluidic devices

This section is concerned with the microchannels used throughout this PhD, describing their main geometrical characteristics and the microfabrication process.

In recent years, microfluidic devices have triggered growing attention since have been used in a wide range of fields (*e.g.* biophysical research, disease diagnostics, *etc.* [193]), and represent a valuable tool to study the role of flows on the motility of aquatic microorganisms and measuring their responses under different conditions. [194]

Firstly, this is due to the opportunity to carefully control the experimental conditions at the microscopic scale (*e.g.* microgeometries, fluid flows, *etc.*), secondly they are cheap and transparent devices, which microfluidic sizes and geometries can be designed and fabricated with great accuracy and can be sealed with relative ease. [194]

The experimental investigations reported in this PhD were run using a series of microchannels made of polydimethylsiloxane (PDMS) which is one of the most commonly used material in the microfluidic fabrication, since it is inexpensive, rugged, biocompatible and characterised by high optical transparency and easy adaptability, all high desired properties for microscopic applications. [195, 196] PDMS is permeable to gases but may be incompatible with many organic solvents (*e.g.* acetone, isopropyl ether, *etc.* [197]), which might have the potential to cause the PDMS to swell up and be rendered unusable. [195]

Geometrically, the microchannels used had a rectangular cross section with a depth  $H_{Ch}$  of  $\sim 100 \mu\text{m}$  and a width  $W_E$  of  $\sim 400 \mu\text{m}$ . The length  $L_{Ch}$  of the channels, measured between their inlet and outlet holes, was approximately 56 mm.

The experiments were carried out employing a straight geometry and four abrupt contraction/expansions geometries, characterised by three different expansion/contraction ratios (ECRs) of  $\sim 2:1$ ,  $4:1$  and  $7:1$ . Specifically, two different  $7:1$  ECR channels were used: a short one and an elongated one, with the latter about 6.4 times longer than the former (See **Figures 3.2, 3.3, 3.4** and **Table 3.2**).

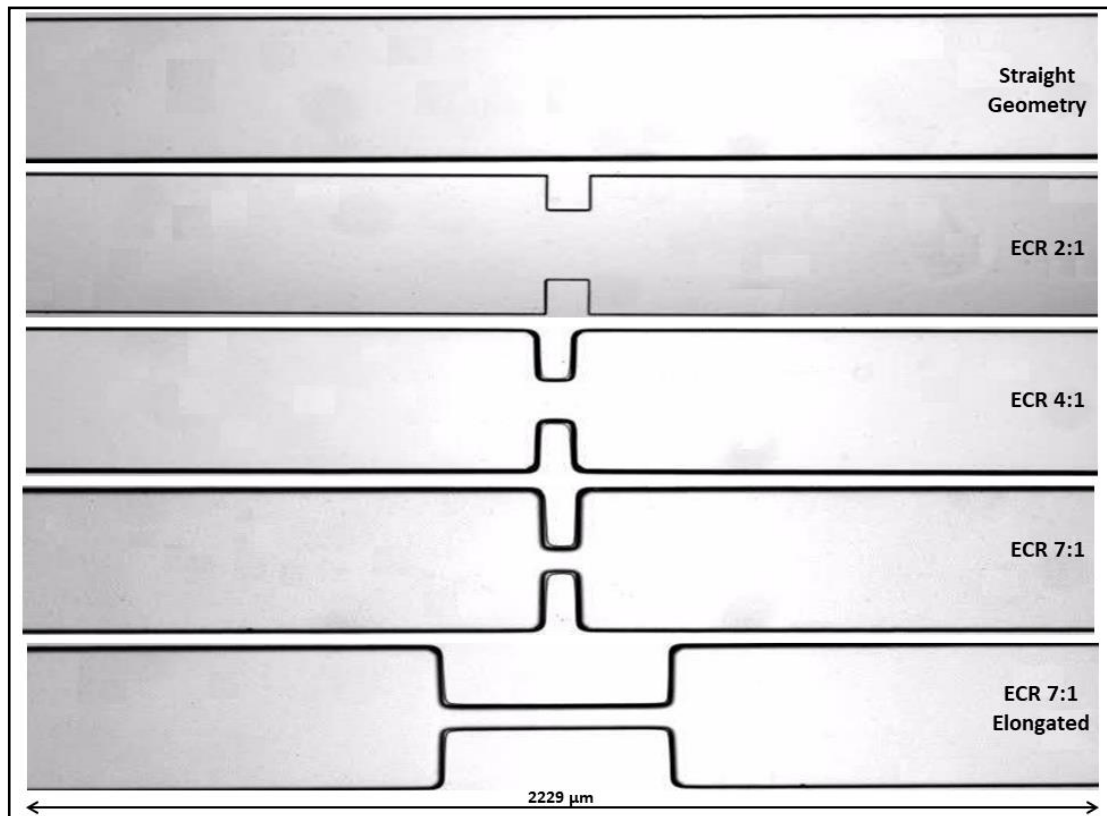


Figure 3.2 – All the microchannels were fabricated using the same mould, apart from the ECR 2-1 one; this explains why its contraction angles were not bevelled like the ones of the other geometries. The shown images were acquired using a 4X microscope objective, which allowed to observe a length of the channels of about 2229  $\mu\text{m}$ .

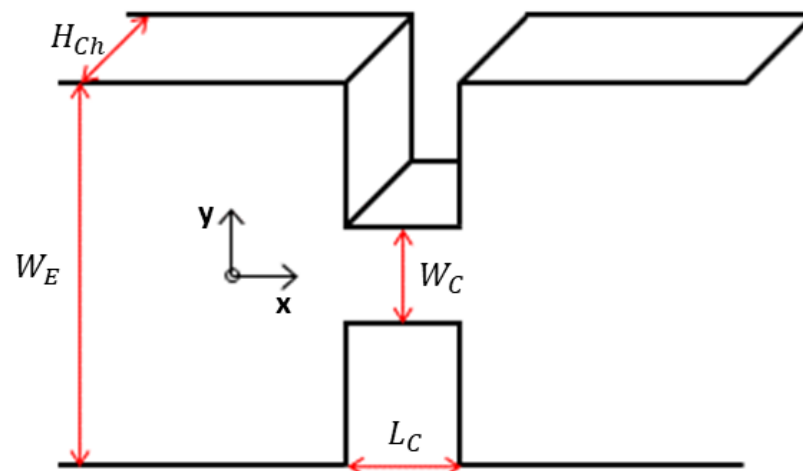
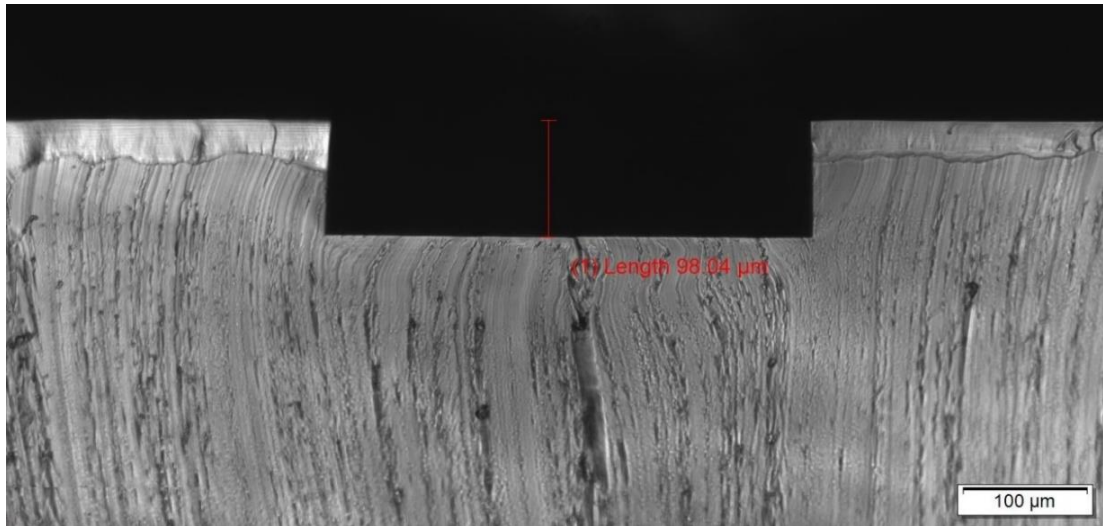


Figure 3.3– Schematic of a contraction/expansion microchannel used in the experiments. Geometrically, a given microchannel is characterised by the definition of its depth  $H_{Ch}$ , the width  $W_E$  of the expansion region, width  $W_C$  and length  $L_C$  of the contraction region and the hydraulic diameters of the expansion  $D_{H,E}$  and the contraction regions  $D_{H,C}$  (see Table 3.2). The width of the upstream and downstream channels were the same.

**Table 3.2 – The main geometrical dimensions of the employed microchannels.**

Geometry	$H_{Ch}$	$W_E$	$W_C$	$L_C$	$D_{H,E}$	$D_{H,C}$
	$\mu\text{m}$	$\mu\text{m}$	$\mu\text{m}$	$\mu\text{m}$	$\mu\text{m}$	$\mu\text{m}$
Straight	102	402	----	----	162.71	----
ECR 2-1	94.86	395	198	90.5	152.98	128.27
ECR 4-1	102	401	112	74	162.63	106.77
ECR 7-1	101.71	401	57	76	162.26	73.06
Elongated	101.53	400	57	486	161.95	73.01



**Figure 3.4** – Once the experimental observations were carried out and the microchannel did not have to be used anymore, its depth  $H_{Ch}$  was measured by cutting it transversally in two close parts, obtaining its cross section (*i.e.* its depth) that could be observed and measured through the microscope. For statistical reasons, usually 5 images were acquired at different focus positions, and the final depth of each channel was the average of the measured values.

As we shall see better in the next sections and in the **4<sup>th</sup> Chapter**, during the experimental investigations, various volumetric flow rates  $Q$  of algal suspensions were pumped through the microchannels, therefore their geometrical characteristics (see **Table 3.2**) were used to calculate the relative  $Re$  numbers, given by

$$Re = \frac{\bar{U} \cdot D_{H,E}}{\nu_m} \quad (\text{eq. 3.1})$$

where  $\nu_m$  is the kinematic viscosity of the culture medium ( $\nu_m = 1.12 \times 10^{-6} \text{ m}^2 \cdot \text{s}^{-1}$ , see **Appendix 3.1**),  $\bar{U} = \frac{Q}{A_{ch}}$  is the cross-sectionally averaged fluid velocity or discharge velocity in the channel,  $D_{H,E} = 4 \frac{A_{ch}}{P_W}$  is the hydraulic diameter,  $A_{Ch} = W_E \cdot H_{Ch}$  is the channel cross-section area perpendicular to the discharge velocity and  $P_W = 2W_E + 2H_{Ch}$  is the channel wetted perimeter. [36]

Moreover, the maximum or wall shear rate in a developed laminar flow of a Newtonian fluid through a rectangular channel is given by: [198]

$$\dot{\gamma}_W = \frac{6 \cdot \bar{U}}{H_{Cr}} \quad (\text{eq. 3.2})$$

Consequently the shear stress at the wall will be:

$$\tau_W = \mu \cdot \frac{6 \cdot \bar{U}}{H_{Cr}} \quad (\text{eq. 3.3})$$

$H_{Cr}$  can be defined as the “critical dimension” of the channel considered, *i.e.* the smallest geometrical dimension of a microchannel which causes the shear stress to be the highest. In particular, concerning the straight geometry, the ERC 2-1 and the ERC 4-1, the critical dimension  $H_{Cr}$  could be considered as the depth of the channel, whereas regarding the ERC 7-1 and the elongated geometries, their critical dimension was the width of their microgeometries, being smaller than the depth (see **Table 3.2**).

### 3.3.1 The microfabrication process

The microfabrication process encompassed three fundamental steps: **a)** the design of the desired microgeometries through computer-aided design (CAD) software and the manufacture of the corresponding masks, **b)** the manufacture of the moulds using the masks and **c)** the fabrication of the PDMS microchannels through the moulds. An overview of the fabrication procedure is shown in **Figure 3.5**.

#### **a) The design of the microgeometries and the manufacture of the related masks**

The microfabrication procedure began by designing and optimising the required system of channels using the CAD software and afterwards having them printed and transferred onto high-resolution image setters by a British company called JD Photo-Tools [199], to create the masks required for the fabrication of the moulds. [53, 195]

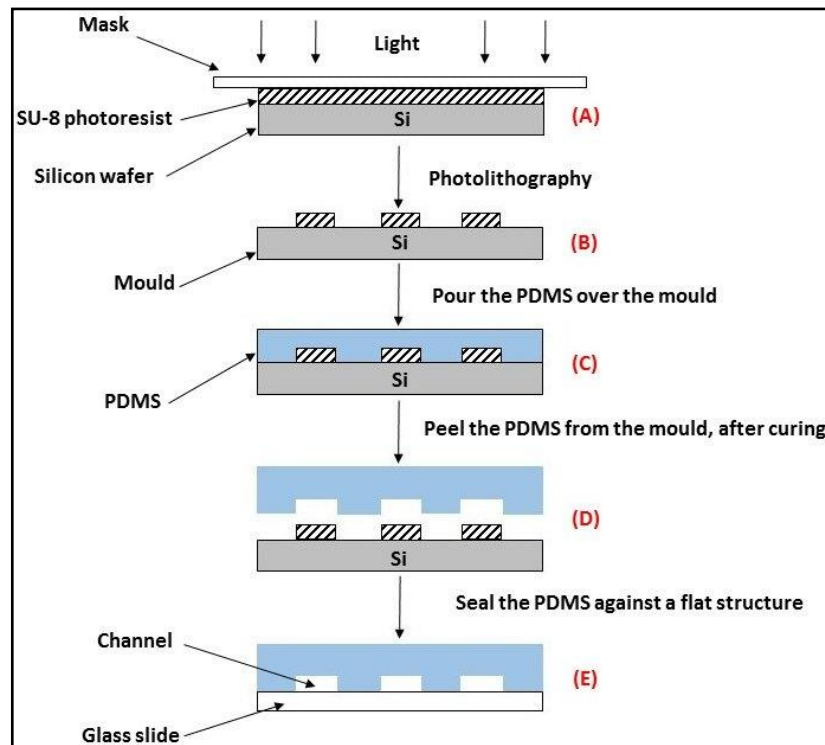


Figure 3.5 – Overview of the PDMS device fabrication procedure. (A) In photolithography, UV light and high-resolution masks are employed to produce a mould. (B) The cross-section of a mould, which consists of a positive relief of the SU-8 photoresist. (C) The mixture of the oligomer PDMS and the curing agent was poured over the mould and cured for 20 minutes at 80°C. (D) After the curing process, the PDMS replica was peeled from the mould and its inlet and outlet holes were created. (E) The PDMS layer was bonded to the coated glass slide and placed back in the oven to further seal the channel. [195, 196] Adapted from [195, 196].

#### a) The manufacture of the moulds

As shown in the **Figure 3.5 A**, each mould was fabricated through photolithography, a technique used normally for the production of microelectronic components, like integrated circuits. [196] Specifically, a silicon wafer was spin-coated with a layer of SU-8 photoresist to create a positive relief, which thickness corresponded to the final depth of the channels [53]. The coated wafer and the mask were then exposed to UV light in order to polymerize the exposed regions of the photoresist, leaving the channels structure on the mould, after dissolving the unpolymerized photoresist. [53] The moulds contained the inverse structures of the microchannels to be fabricated (see **Figure 3.5 B**) and, since they are extremely expensive, they were re-used several times without a significant reduction in their performance. [196]

Nevertheless, our group's microfluidics laboratory did not have the required pieces of equipment for the operations described above, hence we had the moulds kindly manufactured by Dr Michele Zagnoni and his research group from the Electronic and Electrical Engineering Department of Strathclyde University (Glasgow, UK).

**a) The fabrication of the microchannels**

The microfluidic devices were then fabricated using the soft-lithography technique, by casting the PDMS on the mould. PDMS soft-lithography is a well-established process that is less affected by the environmental conditions than the photolithography [196], thus the PDMS microchannels used for experimental investigations were fabricated in house, using the pieces of equipment shown in the **Figure 3.6**.

Nonetheless, before starting the fabrication procedure, all the used apparatus (*e.g.* the mould, the glass microslides, *etc.*) had to be cleaned properly by washing with isopropyl alcohol and dried with compressed air, to prevent potential contaminations from dust and other fine particles. Moreover, the fabrication process had to be carried out in a contained cabinet that filtered the atmospheric air by drawing and then blowing it out at its front, creating a positive pressure which stopped the air-suspended particles from entering the working area (see **Figures 3.6 A and B**).



Figure 3.6 – (A) The air compressor (Apache 50 Wolf Air compressor) used for cleaning purposes. In the image can also be seen the vacuum pump (Vacuum Pump Model 0523-101q-sg588dx, Gast Manufacturing) utilised to create the vacuum in the desiccator. (B) The laminar flow cabinet (M1390 Cabinet, Hepaïre Manufacturing LTD) exploited a high efficiency particulate air (HEPA) filter, in order to remove many of the air-suspended particles. (C) The asymmetric centrifugal laboratory mixer (Centrifugal Mixer ARE-250 CE, Thinky USA) operates without the use of blades or mixing tools, eliminating the air bubbles and ensuring a uniform mixture. (D) The vacuum desiccator (200-mm borosilicate glass tubulated desiccator, Fisher Scientific UK Ltd) was equipped with a stopcock to permit the evacuation while eliminating the air bubbles from the mixture. (E) The oven used (Fed 53 (E2) model drying and heating oven, Binder GmHB) was a variable-speed fan assisted convection oven, heated from all the four sides, to provide even heating. The oven was also employed during the algal killing procedure (see Section 5.3.2). (F) The spin coater (WS-650-23 Spin Coater, Laurell Technologies Corporation) allows spreading the coating mixture evenly over the microslide by rotating it at relatively high rotational velocities. (G) The oxygen plasma system (2.6 litre Zepto Low Cost Plasma Laboratory Unit, Diener Electronic): the oxygen was provided through an oxygen cylinder and exploited to clean the surfaces, prior to bonding, due to its low cost and wide availability. (H) The final PDMS chip which contained various microchannels, characterised by differing microgeometries, which made it possible to exploit various experimental conditions.

For simplicity, the microfabrication procedure of the microchannels has been divided into five steps, explained in details in the following sub-sections:

### **Step 1: Prepare the PDMS mixture**

The PDMS (Sylgard 184, Dow Corning) had been purchased as a prepolymer kit comprising a PDMS oligomer and a crosslinking agent or curing agent, which were mixed at 9:1 PDMS : curing agent ratio (*i.e.* 45 g of PDMS and 5 gr of curing agent) to produce the polymer used in the fabrication process, which chemical formula is  $\text{CH}_3 [(\text{CH}_3)_2\text{SiO}]_n \text{Si}(\text{CH}_3)_3$ ,  $[(\text{CH}_3)_2\text{SiO}]$  being the repeating unit. [195, 196]

The mixture was homogenised through a centrifugal mixer (see **Figure 3.6 C**), employing a mixing cycle composed of two separate phases, *i.e.* a mixing phase (2000 rpm for 5 minutes) and a deaerating phase (1600 rpm for 1 minute), in order to ensure an optimal mixing and reduce the air bubbles content within the mixture. [195]

### **Step 2: Pour the PDMS mixture over the mould, the degassing and curing processes**

The mould was carefully surrounded in aluminium foil, folding it up tightly to create a lip, where the mixture was cast (see **Figure 3.5 C**) and then degassed through a desiccator connected to a vacuum pump, (see **Figure 3.6 D**), before being cured thermally in the oven (see **Figure 3.6 E**) at 80°C for 20 minutes.

### **Step 3: Peel the PDMS geometry from the mould and create the inlet and outlet holes**

Once the thermal curing process was finished, the PDMS layer conformed the features of the mould and contained the microchannel structures. At this point, it had to be peeled delicately from the mould (see **Figure 3.5 D**); the low surface free energy and elasticity of PDMS allowed it to be released without damaging the mould or itself. [195]

Inlet and outlet holes were also created by puncturing accurately the PDMS substrate through a mechanical puncher (Harris Uni-core 1.00 mm puncher). The PDMS residues, created during the punching operations, were removed carefully in order to maintain the microchannels as clean as possible.

### **Step 4: Spin-coat a glass slide**

The spin coater (see **Figure 3.6 F**) was used to create extremely thin and even coating layers of mixture on the surface of some glass microslides, employing a spin speed of 6000 rpm for 1 minute, followed by a 10 s ramping.

### **Step 5: Seal the microchannel and its final curing.**

The last step of the fabrication process was to create a watertight bond between the coated microslide and the PDMS substrate, so as to provide the latter with a structural support and to allow it to be easily viewed in the microscope.

The bonding process was carried out using the oxygen plasma bonder (see **Figure 3.6 G**), which created a surface on both the PDMS geometry and the coated glass slide that were highly active to bond. Specifically, this treatment generated silanol groups on the surface of the PDMS, by the oxidation of its methyl groups. Once the bonding process had finished, the PDMS geometry was carefully removed, placed on the coated microslide and allowed to seal under its own weight; eventually they were placed back into the oven for 12 hours at 80°C, to promote a better adhesion and complete the PDMS cure. The final microfluidic device was formed of four microchannels gathered in a particular structure called a chip (see **Figures 3.5 E and 3.6 H**).

## **3.4 Why did we employ the brightfield illumination technique and microfluidic devices?**

The next sections provide a detailed technical analysis regarding the microscope utilised for the experimental investigations, considering also the main technical features of the objectives used.

Moreover, some applications of the principal optical microscopy techniques (OMTs) are also mentioned, emphasising particularly their current usages concerning photobioreactors, where they are mainly employed for quality controls on the cultures. [166] Nevertheless, as we will see better in the next chapters, we have envisaged that both OMTs and microfluidic devices could also be exploited for PBRs optimisation purposes, allowing to take into account the algal fluid dynamic behaviours (see **Section 4.2.1**).

What is more, in the development of this approach, we also wanted to employ the most versatile and inexpensive techniques: an inverted microscope, which utilised the brightfield observation technique, and the microfluidic devices (see **Section 3.3**).

### 3.4.1 Photobioreactors optimisation: a new approach

The principal optical microscopy techniques (OMTs) encompass brightfield illumination, darkfield illumination, fluorescence, phase contrast and differential interference contrast (DIC), which are exploited in numerous fields (*e.g.* biology, medical science, *etc.*) as they exhibit many advantages over other techniques; *i.e.* they are not invasive, provide real-time data and exhibit great flexibility in design. [200, 201] OMTs have also been used for studying live microorganisms, since they allow to observe them individually, to filter them (*e.g.* ruling out potential contaminants, dead cells, *etc.*) and to obtain results that are not population-averaged. [200, 201]

Nevertheless, regarding the case of microalgal cultivations in PBRs, the usage of OMTs is currently limited to quality controls and prevention purposes, since the cultures must periodically be monitored, to verify the absence of any potential biological or chemical contaminants (see **Section 2.5**) and also for checking the quality and quantity of the produced biomass [166]; (*e.g.* the fluorescent dye Nile red is used to localise and quantify lipids within the cells [166] or DIC can be utilised to identify different species in the cultures [202]).

However, as addressed in the results sections, this research activity aimed to investigate whether OMT, microfluidic devices and their characteristic microgeometries can potentially be utilised as complementary tools in the preliminary phases of PBRs design and optimisation and also for overcoming all those technical and costly constraints discussed in the **2<sup>nd</sup> Chapter**, through the exploitation of culture-specific features of the microalgal cells (see **Section 4.2.1**). What is more, we also wanted to employ the most flexible, versatile and cheapest approach, hence, for our experimental investigations, we exploited mainly an inverted microscope, the brightfield observation technique (*i.e.* the simplest OMT [200]), and various microfluidic devices.

### 3.4.2 Olympus IX71 inverted microscope

The experimental observations were carried out using an Olympus IX71 inverted microscope (see **Figure 3.7 A**), in which the light path includes four key components: the light source, the condenser lens, the objective lens, the eyepiece/camera (**Figure 3.7 B**).

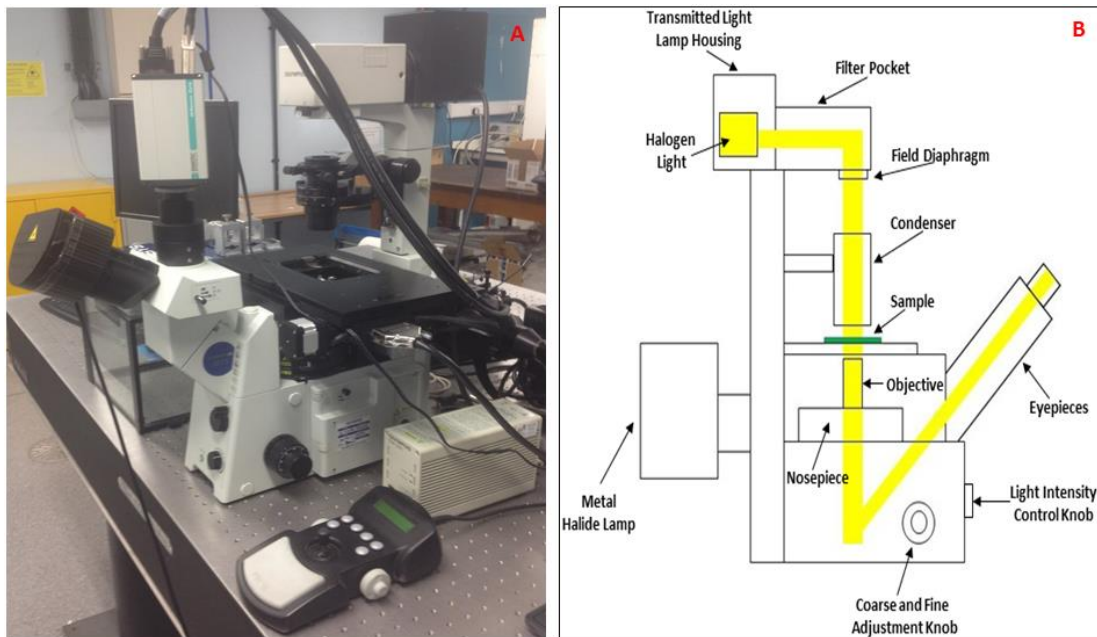


**Figure 3.7 – (A) Olympus XI71 inverted microscope, its power supply unit and the manual joystick for controlling the stage. (B) A simplified scheme of the light path, which source was provided by a halogen light positioned above the stage. The illumination light passed through the filter pocket and the field diaphragm, before entering the condenser front aperture. After being focused by the condenser lens system, the uniform transmitted light was projected into the specimen, which was placed on the stage. The fraction of the light that was not absorbed by the sample continued through the objective, which enhances the specimen details by a factor of magnification, and eventually it was directed either to the eyepiece or the camera. The figure 3.2 B was adapted from [203].**

In particular, the light source was supplied by a halogen light held in a transmitted light lamp housing. Nevertheless, the microscope was also equipped with a metal halide lamp, used for epi-fluorescence observations. [203]

Between the transmitted light lamp housing and the microscope condenser, there were a filter pocket and a collector lens (*i.e.* the field diaphragm) that permitted to filter and regulate the amount of light entering the microscope condenser, which function is to focus the transmitted light through its lens system, before it is projected into the specimen, placed on the microscope stage. Below the stage, there were some objective lenses of different magnification values, fitted to a rotating turret, known as nosepiece. The microscope was also provided with both a Charge-Coupled Device (CCD) monochrome camera and an eyepiece for images visualisations. [203, 204]

### 3.4.3 Main technical features of the used objectives

When a typical sample (*e.g.* some stained particles or swimming microorganisms) is viewed through a microscope, choosing an optimal objective is mandatory to achieve suitably resolved images. Hence, some technical features, related to the microscope objectives, must be defined in order to compare their performance and optimise the observation conditions, *i.e.* the magnification, working distance and the numerical aperture.

Microscope objectives amplify the sample details by a factor of magnification, usually denoted by an X next to a numeric value, which quantifies the magnification. Conventionally, the various magnifications are indicated through different coloured bands engraved around the outer housing of the objectives (see **Figure 3.8**).

Microscope objectives are also characterised by a working distance, the distance between the objective front lens and the surface of the coverslip. Manufacturers strive to find the best compromise between the longest working distance and the highest resolution of an objective. [205]



**Figure 3.8** – Two of the most used objectives, their specifications and identifications characteristics, which are inscribed on the barrel of the objective body. Amongst the different technical characteristics, the objectives usually show their magnification, numerical aperture, the manufacturer and are also labelled with different colour codes indicating the different magnifications, *e.g.* a yellow band indicates a 10X magnification. More technical features and their meanings can be found here in the Olympus webpage [206].

When the incident light is projected into the specimen, it will partially be absorbed, reflected and diffracted, deviating from its original direction and therefore will enter the microscope objective as an inverted cone (see **Figure 3.9**). Generally, the smaller the observed objects, the more the incident light rays will be diffracted. [204]

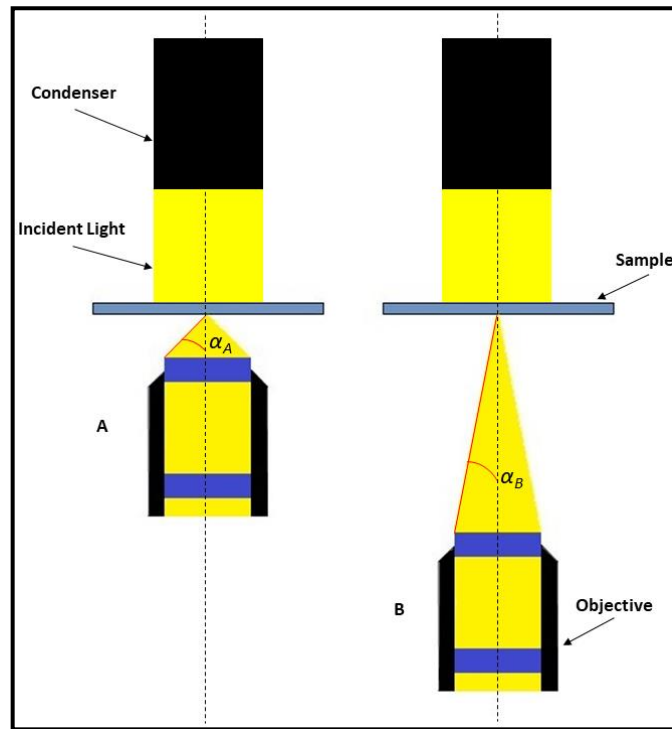


Figure 3.9 – The imaging light waves pass through the observed specimen and enter the two objectives as an inverted cone. The objective A has a larger NA value than B, owing to the inverted light cone increasing which in turn increases the angular aperture, *i.e.*  $\alpha_{L,A} > \alpha_{L,B}$ . Adapted from [205].

The ability of a microscope objective to gather light and resolve fine specimen details, at a fixed object distance, is termed as numerical aperture (NA) and can be expressed as:

$$NA_{obj} = ri \cdot \sin(\alpha_L) \quad (eq. 3.4)$$

where  $\alpha_L$  is the one-half angle of the inverted light cone captured by the objective and  $ri$  is the refractive index of the immersion medium between the objective front lens and the specimen (*i.e.* the imaging medium). [205] Eq. 3.4 shows that  $NA_{obj}$  values can be increased by using objectives designed to function in immersion media characterised by higher  $ri$  values (*e.g.*  $ri$  is 1 for air, 1.33 for water and 1.51 for immersed oil [205]).

In optical microscopy,  $NA_{obj}$  values are also increased by adding a condenser to generate a ray cone on the illumination side of the specimen, enabling the objective to gather light rays at larger diffraction angles. Hence, it can be defined a NA value for the objective and a NA value for the microscope condenser; the sum of the aperture angles of the objective and the condenser is defined as the working aperture. [200, 204] Objectives with high  $NA_{obj}$  values are capable of improved signal collection, but also an increased collection of noise. [200]

### 3.4.4 The lateral resolution and the depth of field

The resolution or resolving power of an objective is defined as the shortest distance between two points on a particular specimen that can still be distinguished as separate entities and it may be compromised by the light diffraction, which tends to increase the actual size of an observed molecule or particle. Thus, when resolving between two close particles, it may become more difficult to tell if there are one or two particles present, due to them appearing inflated in size and warped by diffraction. [200]

The relationship between the lateral resolution  $r_p$  (*i.e.* the one in the plane x-y [200]) of a microscope, the wavelength  $\lambda$  of the illuminating light, the numerical aperture (NA) of the objective  $NA_{obj}$  and the microscope condenser  $NA_{cond}$  can be expressed as [205]:

$$r_p = \frac{1.22 \cdot \lambda}{NA_{obj} + NA_{cond}} \quad (\text{eq. 3.5})$$

As can be seen from *eq. 3.5*, the lateral resolution depends only on the imaging wavelength (shorter wavelengths yield higher resolutions, *i.e.* lower  $r_p$  values), on NA (the higher NA, the better the resolution) but is not directly dependent on the objective magnification. [205]

The depth of field (DOF), *i.e.* the axial resolution of an objective measured parallel to the z or optical axis, must also be taken into account, especially when tracking particles and swimming microorganisms in a liquid sample. [200, 205] DOF can be defined as the distance between the nearest object plane and the farthest object plane of the specimen, that are still simultaneously in acceptable focus, and is given by [205, 207]:

$$DOF = \frac{\lambda \cdot ri}{(NA)^2} + \frac{ri \cdot e}{Ma \cdot (NA)} \quad (\text{eq. 3.6})$$

where  $Ma$  is the objective magnification and  $e$  is the smallest resolvable feature size. [207]

DOF is usually measured in microns and represents one of the main limitation of the cell tracking processes (See **Section 3.7.4**). [194]

### 3.5 The experimental setups

The final part of the chapter analyses the experimental setups and procedures used for the characterisation of the DS cell behaviours in various microfluidic devices and flow rates, *ergo* at different fluid dynamic conditions, considering also the related image analysis procedure.

Specifically, as reported in the subsequent chapters, my investigations involved both living and dead DS cells, in order to emphasise their differences, albeit this required the experimental setups to be modified, mostly owing to sedimentation issues.

As shown in **Figure 3.10**, the experimental setups comprised the Olympus IX71 inverted microscope (see **Section 3.4.2**), equipped with a cooled CCD Olympus XM 10 monochrome camera, a syringe pump (PHD 22/2000 Programmable Syringe Pump, Harvard Apparatus), a square 600 nm long-pass red filter (Cokin A003 [208]) and different microfluidic devices described in **Section 3.3**.

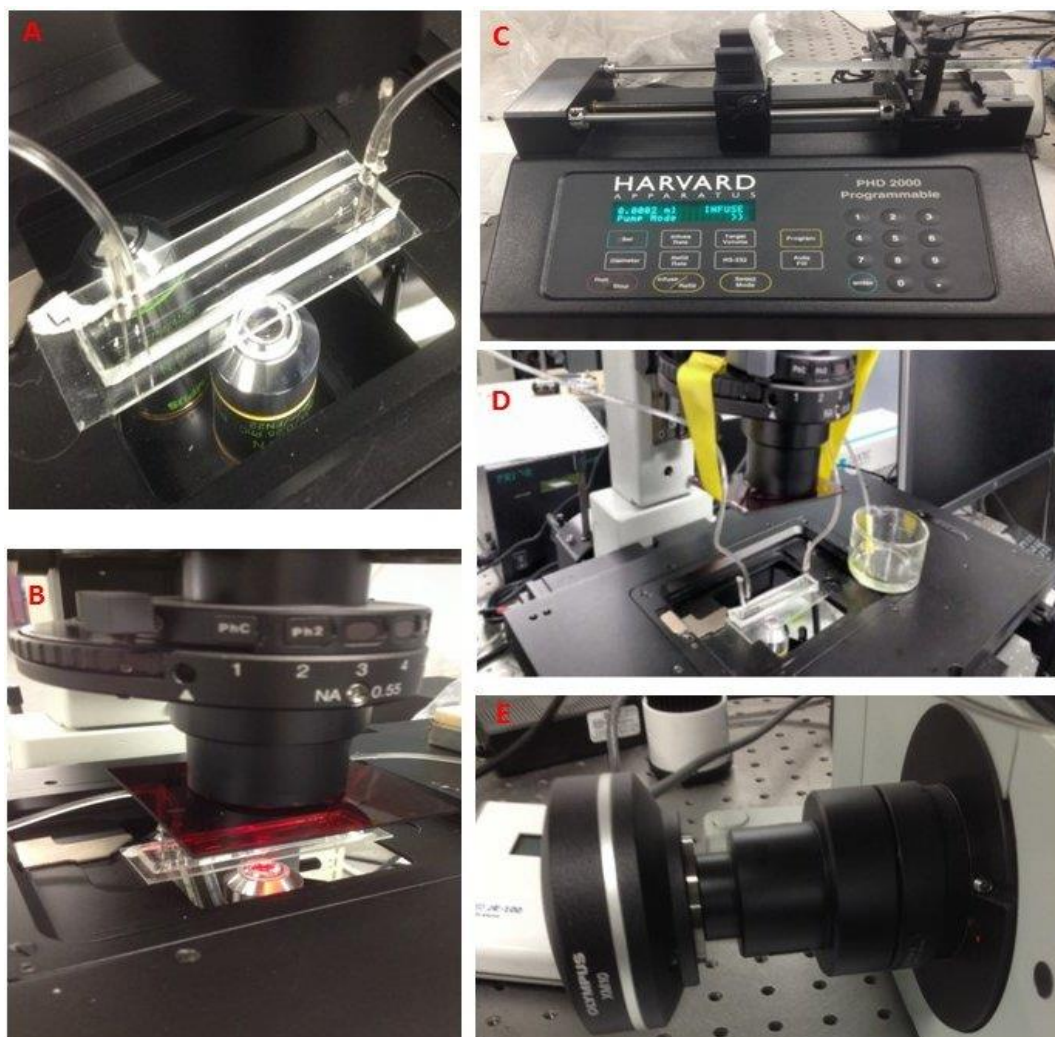


Figure 3.10 – (A) The inlet and outlet of a microchannel, the microbore tubes and the precision tips. (B) The red filter, engaged between the microscope condenser and its stage. It is also possible to see the numerical aperture of the condenser ( $NA_{cond} = 0.55$ ) (C) The syringe pump, its main keyboard and the experimental syringe. (D) A microchannel placed on the microscope stage and connected to its reservoir. (E) The monochrome Olympus XM 10 camera, attached to the microscope port.

After the algae suspensions had pigmented enough (see **Section 3.2.3**), the cells could be harvested for experiments using a syringe (3-ml BD Luer-Lok™), carefully avoiding picking up any air bubbles.

As can be seen in the **Figure 3.11**, the syringe had to be placed in the syringe pump, ensuring to set its diameter data correctly, according to the Harvard Apparatus syringe selection guide [209], to guarantee that the required flow rates would be provided accurately and could be controlled precisely.

Next, the microchannel was placed on the stage of the microscope, where its inlet was connected to the syringe through a piece of flexible microbore tubing (Tygon® Tubing, 0.508 mm ID, 1.524 mm OD) and a blunt precision tip, while its outlet was connected to a reservoir that collected the exiting fluids. Before starting any experimental investigation, the microchannel had to be cleaned by pumping distilled water through it at  $1 \text{ ml}\cdot\text{min}^{-1}$ , in order to dislodge any residual particles left over from previous experiments. This process was repeated before and after any fluid was switched in the microchannels.

Since the experiments were designed to observe the natural algal swimming behaviours, the red filter was placed between the microscope condenser and the microchannel, to attenuate the shorter wavelengths and minimise the phototactic response [43, 210]; the presence of the filter meant that the wavelength  $\lambda$  of the illuminating light 600 nm. The red filter reduced the ambient light, enhancing the contrast between DS cells and the background. [211] However, despite this, the experiments involving living cells were carried out in a dark environment, *i.e.* turning out the lights.

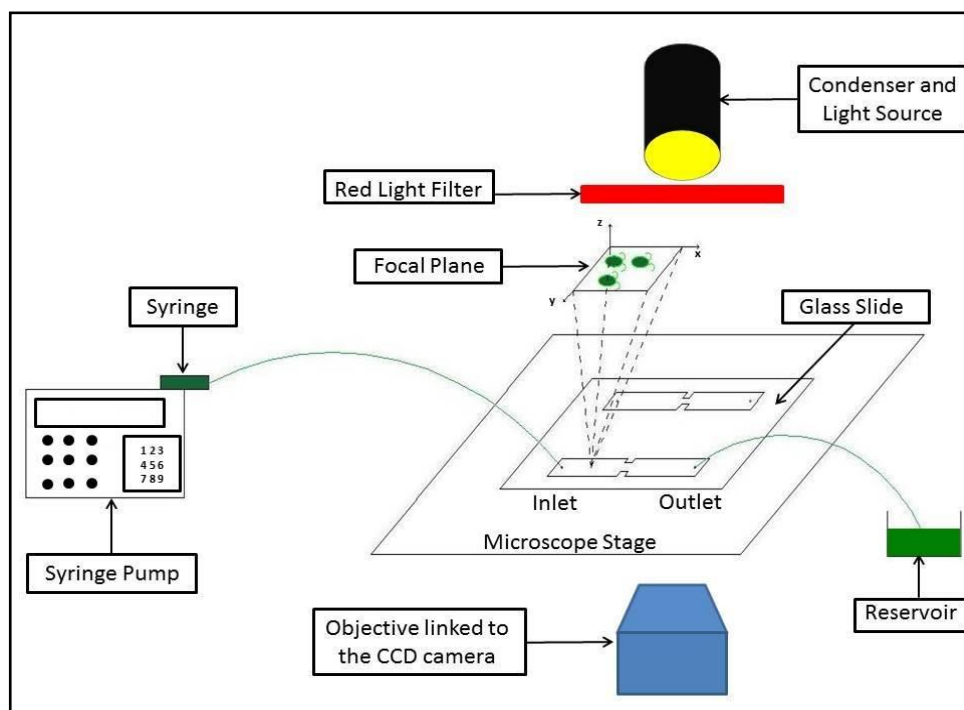


**Figure 3.11** – Schematic of the experimental setup involving living DS cells, showing the microchannel placed on the microscope stage and its input/output fluid tubes. The syringe pump on the left was used to send the algal suspension flows through the microchannel, while the red filter, engaged between the microscope condenser and the its stage, prevented potential algal phototactic behaviours.

For comparison purposes, the killing procedure and the experimental setup used for dead DS cells are also described. The theoretical reasons behind the study of dead cells, their main characteristics and the various experimental issues, which had led the adapted methodology, is explained in detail in the **5<sup>th</sup> Chapter**.

When studying dead DS cells, the two most significant issues that had to be overcome were **1)** to find a simple and effective killing procedure for the algae, that inhibited potential dead cells aggregation and prevented both their shape and concentration from changing significantly, and **2)** to limit their related sedimentation, due to the fact that the cells are not neutrally-buoyant (*i.e.* they are denser than the medium [2]).

DS cells were killed thermally using the same oven used for the microfabrication (see **Figure 3.6 E** and **Section 5.3**).

The three parameters that affected the killing procedure were the final heating temperature, the residence time of the cells within the oven and the heated volume of algal suspension. I established that, if 1 ml of algal suspension was heated at 50°C for 8 minutes inside a 10-ml glass vial, all the living algae would die and their shapes would not change considerably, albeit the cells became slightly rounded, compared to the living ones (see **Figure 5.2**).

Once the heated vials had cooled down to room temperature, dead cells were ready for experimental investigations; nevertheless, the experimental setup had to be modified so as to inhibit sedimentation processes that would have occurred in the vials, syringes and in the microfluidic devices themselves and would have prevented dead cells from being visualised and tracked.

In particular, during the cooling process, dead cells tended to sediment within the vials, and therefore they had to be shaken gently, before drawing the cells for experiments, in order to ensure that uniform algal concentrations were investigated. The sedimentation phenomena within the syringes were reduced by setting the syringe pump vertically on a perforated table and exploiting the resulting gravitational effects (see **Figure 3.12**).

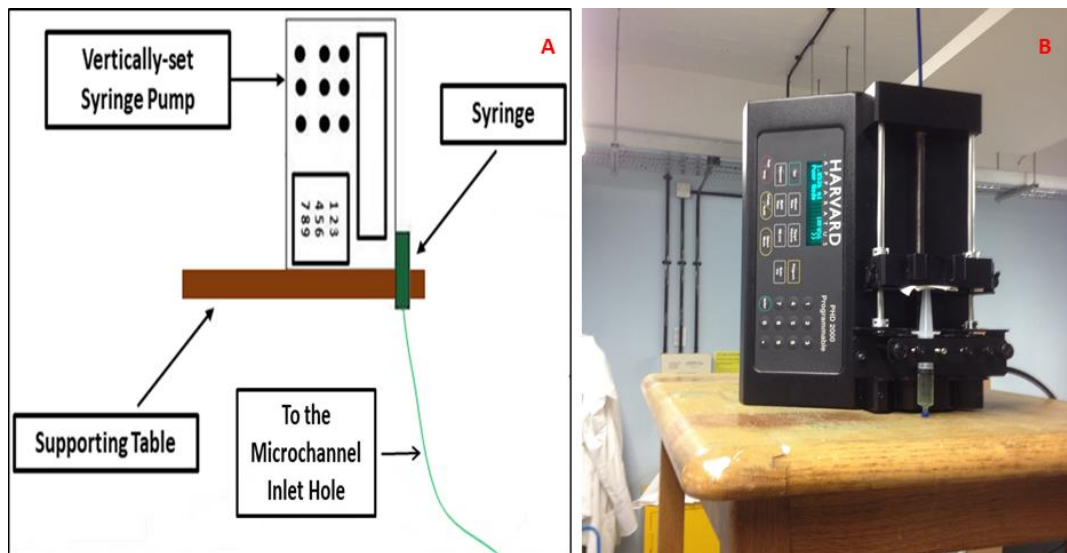


Figure 3.12 – (A) Schematic of the vertically-set syringe pump on the perforated table and the microbore tubing that connected the syringe to the microchannel inlet. (B) A frontal view of the syringe pump and the syringe containing the dead algal cells suspension. This experimental setup allowed to decrease the sedimentation issues.

As addressed in the 5<sup>th</sup> Chapter, apart from the vertically-set syringe pump, the experimental setup for the dead cells was very similar to the one used for the living ones. Although the cells were dead and therefore could not exhibit any phototactic behaviours, the red filter was retained, to ensure that the same illuminating light wavelength (*i.e.* the same depth of field) was employed during the experimental investigations of both live and dead cells.

### 3.6 The flow visualisation

This section provides additional technical detail about the devices used during the flow visualisation (*i.e.* the objectives and the monochrome camera) and the image capture conditions, focusing particular attention on the optimisation of the exposure time. The main experienced experimental issues are also mentioned.

After the experimental set up was arranged, the algal suspensions were pumped through the chosen microchannel long enough to ensure that it was entirely filled. At this point, the specimen was brought into focus, in order to observe the channel centreline to eliminate walls effects that could influence the algal behaviours. Next, suspension of cells was pumped through the channel at the desired rate and the experimental observations could be carried out.

The flow visualisation was performed using two different objectives, an Olympus 4X ( $NA = 0.1$ ) objective and an Olympus 10X ( $NA = 0.25$ ) objective. The 4X objective was used in order to cover relative long parts of the channels, while the 10 X objective allowed increased resolutions and therefore higher accuracy in the observed regions. Since the smallest resolvable feature size of the XM 10 camera was  $6.45 \mu\text{m}$  [212] and the imaging medium was air (*i.e.*  $ri$  is 1),  $DOF_{4X}$  was  $76.13 \mu\text{m}$  and a  $DOF_{10X}$  was  $12.18 \mu\text{m}$  (see *eq. 3.6*).

Once steady state within the channel had been reached, images and videos could be acquired through the CCD camera, which had a matrix of sensors that converts the received photons into pixel values, at the corresponding positions within the image. [213] The camera allowed different resolutions and binning modes, up to  $1376 \times 1032$  pixels. In the binning mode, the camera CCD's sensor combines neighbouring pixels into pixel blocks, which results in a higher sensitivity at lower resolution (see **Table 3.3**). [212]

**Table 3.3 – The table shows the camera binning modes and the corresponding resolution and frame rate values. Adapted from [212].**

Binning Mode		
Binning	Resolution	Frame Rate
Maximum Resolution	$1376 \times 1032$ pixels	15 images per second
Binning 2X	$688 \times 516$ pixels	25 images per second
Binning 4X	$344 \times 258$ pixels	50 images per second
Binning 8X	$172 \times 129$ pixels	80 images per second

The camera was also fully integrated with the digital imaging Olympus CellSens software, used to acquire images and videos, to analyse the results (*e.g.* allowing for distances in the experimental videos to be measured). The image capturing conditions (*e.g.* the resolution, the video duration, *etc.*) were monitored and adjusted, according to the fluid dynamic conditions being investigated (*e.g.* the flow rate, the used microgeometry, *etc.*). Each video was characterised by a certain number of frames, a total duration, an average number of tracked algae and a resolution. Higher resolutions would provide the clearest results but at the expense of longer processing times. Furthermore, a crucial feature that must always be optimised was the exposure time, as discussed in the next section.

### 3.6.1 The optimal exposure time

When performing experimental investigations and acquiring images and videos, the capturing conditions should always be optimised and then kept constant in order to avoid misinterpretation of data, giving particular attention to the exposure time (*i.e.* how long the camera is exposed to the light emitted from the observed samples); generally, the longer the exposure time, the more photons the detector will receive, leading to brighter images and videos. [214]

**Table 3.4 – Exposure time for the experiments using the 4X objective. The optimal exposure time values (or range) had to be assessed case by case since they depend on the experimental conditions, *e.g.* on the flow rate (*i.e.* increasing the flow rate, required the exposure time to be reduced accordingly).**

Experimental Flow Rates	Exposure Time
$Q < 3 \mu\text{l}\cdot\text{min}^{-1}$	4-5 ms
$3 \mu\text{l}\cdot\text{min}^{-1} < Q < 5 \mu\text{l}\cdot\text{min}^{-1}$	$\sim 1$ ms
$Q > 5 \mu\text{l}\cdot\text{min}^{-1}$	$< 1$ ms

If the exposure time is inappropriate, the cells will appear deformed or blurred, leading to incorrect results or may make the image analysis process impossible (see **Figure 3.13**).



**Figure 3.13 – The spatial positions of an algal cell in six different frames of an experimental video that had been acquired using an ECR 4-1 channel, a flow rate of  $5 \mu\text{l}\cdot\text{min}^{-1}$ , a resolution of  $688 \times 516$  pixels and an exposure time of 5 ms; the numbers above the cell indicate the various frames. At these experimental conditions, the cell had been dragged by the flow but, since the exposure time is too high, it could not be tracked and analysed properly (see the apparent elongation of cell in the 4<sup>th</sup> frame).**

The next section describes further problems that had also occurred, mainly due to the high salt concentrations of the algal cultures, unwanted air bubbles and the low statistical reliability of the acquired videos.

### 3.6.2 The most relevant experimental issues

There were no major hazards associated with the experiments, with the main concern represented by the fact that the algal cultures were salty and corrosive, resulting in potential damages to pieces of equipment, in particular the microscope. The culture medium could also generate problems in the microchannels. If the microchannels were not properly maintained, they became clogged by the salty solute, if the solvent evaporates. These “nutrients accumulations” may also have been able to affect the algal behaviours by chemotaxis, since during some experiments the DS cells were seen adhering to the channel boundaries and interacting extendedly with them (see **Section 4.7.1**). As a result, the microchannels had to be washed thoroughly after use and be refabricated, if irremediably compromised.

When working with microfluidics, another common problem that occurs is having air bubbles trapped within the channel, which disrupt the fluid flow and can skew the results, hence these needed to be eliminated, before starting the experiments. This was achieved by sending a flow rate of about  $15 \mu\text{l}\cdot\text{min}^{-1}$  through the channel and closing its outlet (*e.g.* through blocker tips), leading to an increasing of the internal pressure that caused the air to diffuse through the permeable PDMS boundaries and evacuate the channel.

Sometimes the acquired videos were not suitable for a proper statistical analysis, *e.g.* preferential swimming paths, too few algae could be tracked, *etc.* These issues could have been occurred due to different reasons (*e.g.* air bubbles still present in the syringe or in the channel, dead cells sedimentation problems, *etc.*) and they had to be investigated and solved case by case.

### 3.7 The image analysis process

This section is concerned with the image analysis process (IAP), which have been employed to assess and quantify the algal fluid dynamic behaviours from the captured experimental videos.

The IAP was performed through ImageJ, a freeware Java-based image processing software [215], which can be integrated with a vast selection of freely-available plugins and has been widely employed due to its versatility and ease to use. [216]

The IAP relies on the fact that a given image is comprised of individual pixels, which are represented by numerical values arranged as a matrix and indicating an intensity between black and white (*e.g.* 0 represents black and a value of 255 indicates the maximum allowable intensity of white). [52, 213]

Each pixel is converted into its corresponding grayness on a monitor screen, allowing the various images to be displayed; the width and the height of a given image are the pixel numbers in the x and y directions. [52, 213]

Image files have a specific bit-depth (*e.g.* 8-bit or 16-bit) that defines the number of gray levels for a given image; *i.e.* for 8-bit images and 16-bit images, the grayness between black and white is divided into 256 steps (from 0 to 255) and 65,536 steps (from 0 to 65,535) respectively. [213] A higher bit-depth results in a more detailed conversion of signal intensity to pixel values by the CCD camera (see **Section 3.6**). [213, 216]

The IAP permitted tracking of the observed cells, obtaining useful information (*e.g.* their spatial positions within the microfluidic devices, the algal shapes, *etc.*) and investigation of their motility at both single-cell and population levels by analysing the obtained data. [194]

Essentially, the IAP involved three phases: an initial video pre-processing, the filtering of the algal cells features and the tracking process (see **Figure 3.14**). [52]

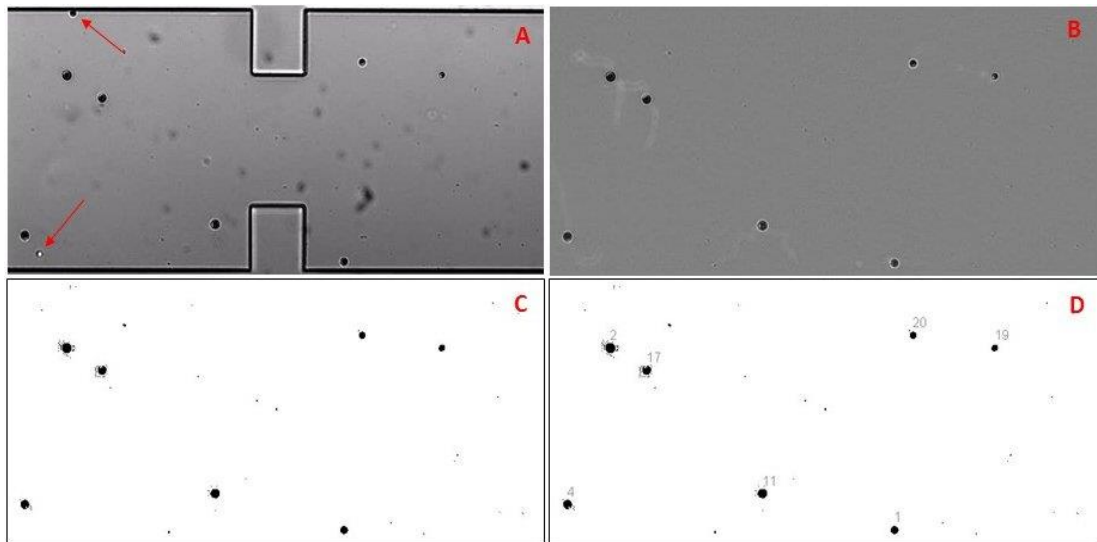


Figure 3.14 – (A) A given frame of an experimental video, regarding some live cells in an ECR 2-1 microchannel, as seen using the Olympus CellSens software. This is a typical image obtained through the brightfield observation technique, *i.e.* it contains dark particles on a brighter background and, generally the darker the sample, the more absorption of light has occurred. [203, 204] As can be seen, the image contains some unwanted information, like sedimented dead cells (see the red arrows) and therefore the video must be pre-processed. ImageJ can easily distinguish non-moving cells and particles as their positions do not change during the whole video. (B) The original image after being pre-processed, all the non-moving objects and speckles have been removed and its background has been evened out; the previously-mentioned dead cells have also been eliminated. (C) The image after being converted to binary format. (D) A frame of the labelled-algae video, resulting from the tracking process.

### 3.7.1 Pre-processing the experimental videos

As explained in the following sub-sections, in the initial part of the image analysis process, the experimental videos had to be pre-processed in order to remove unwanted non-moving objects (*e.g.* microchannel boundaries, speckles owing to the camera, sedimented dead cells, *etc.*), subtract their background, convert them into binary format and set the real scale, using the proper conversion factor between pixels and microns, so as to obtain the results in usable units (See **Figure 3.14 A, B, C**).

#### 3.7.1.1 Removing the fixed parts from experimental videos

The fixed parts of the experimental videos were removed employing the processing tools Z projection and Image Calculator (see **Figure 3.15 A and B**).

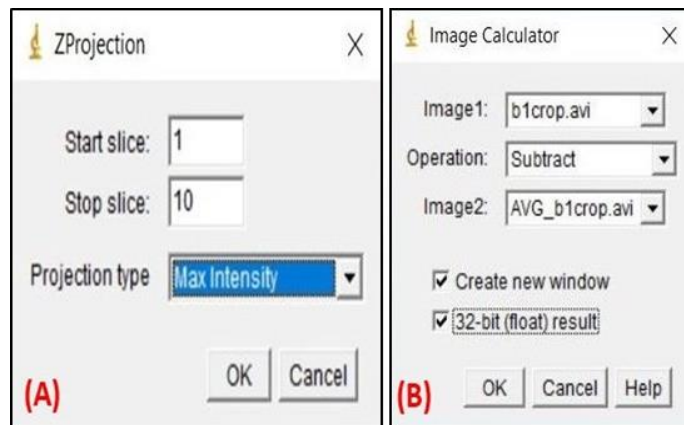


**Figure 3.15 – (A)** When the Z projection tool is opened, its dialog box will ask for a start and stop slices that will determine the range of the stack which will be included in the z projection. There are six different projection types which can be chosen, depending on the type of data being considered: average intensity, maximum intensity, slum slice, standard deviation and median. **(B)** The image calculator tool permits up to 12 arithmetic and logical operations to be performed between two images. More details about these processing tools can be found here: [213, 217, 218].

Generally, Z projection is used for treating Z-stacks; a stack combines a series of spatially-related or temporally-related images in a single file. All the images that make up a stack are called slices and they must have the same size and bit-depth. In a time stack, all slices have been acquired at different points of time (*e.g.* a time stack shows how the dimensions of a cell change with time) while, a spatial stack or Z-stack, contains images captured at different focus positions (Z-stacks are mainly used for experiments involving fluorescence microscopy). [219] ImageJ provides different tools for representing a 3-D stack as a 2-D image for publication purposes, amongst them there is Z projection. [213]

However, as suggested by Pedersen [220], applying the maximum intensity Z projection tool (see **Figure 3.15 A**) to a given experimental video, allows also to obtain an image containing all its non-moving elements. This image can then be subtracted from the original experimental video through the Image Calculator tool, obtaining a further video containing just the moving algal cells (see **Figure 3.14 B** and **Figure 3.14 B**). [213, 220]

### 3.7.1.2 Background subtraction

Although the moving cells are clearly visible to naked eyes, tracking software may have problems detecting them, since videos are often characterised by uneven backgrounds that must be adjusted through the ImageJ background subtraction function, which exploits the rolling ball radius method (RBRM) (see **Figure 3.16**). [213, 217, 220]

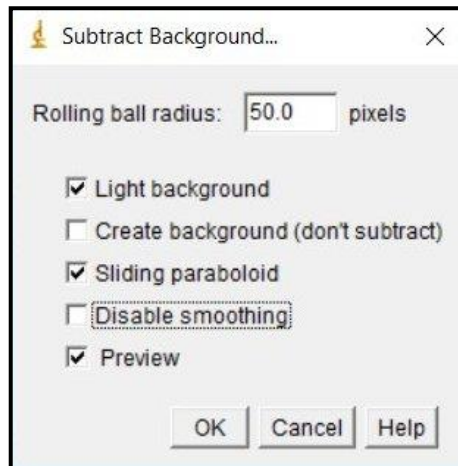


**Figure 3.16** – The dialog box of the ImageJ subtract background tool and the various options that can be exploited during the process. In particular, the light background option must be unchecked when processing fluorescence images and checked while dealing with brightfield images which comprise of dark objects over a brighter background (see Figure 3.15 B). More details about the background subtraction and its features can be found here: [213, 217, 218].

RBRM is based on the algorithm described by Sternberg (1983) [221] and implies the definition of a rolling ball radius which must be set to at least the size of the largest object on the foreground, since smaller radius sizes would lead to the subtraction of foreground signals. RBRM defines a local background intensity value for every pixel by averaging over a distance equivalent to the ball radius around the pixels, this averaged-intensity value will then be subtracted from the original image or video allowing to remove large spatial variations of the background intensities. [213, 217, 220]

### 3.7.1.3 Thresholding and binary conversion processes

Once the background has been adjusted, the videos must be converted into a black and white binary format, through the thresholding process, segmenting them into features of interest (*i.e.* the moving cells in the foreground) and background. [213, 217, 220]

The thresholding process allows a distinction to be made between foreground and background, employing two threshold values (a lower limit value  $T_1$  and an upper limit value  $T_2$  [see **Figure 3.17 A**]), *i.e.* all pixel values bigger than  $T_1$  and smaller than  $T_2$  are considered background and become white, otherwise they will belong to the foreground, becoming black (see **Figure 3.14 C**). [213, 216]

The ImageJ thresholding processing tool permits  $T_1$  and  $T_2$  to be set for a given image, either manually or automatically (see **Figure 3.17 A**). In particular, each image has a corresponding intensity histogram (*i.e.* a plot that shows the number of pixels at each different intensity value over a range of pixel values, typically the image bit depth [213]), which is useful for examining the signal and background pixel values, determining  $T_1$  and  $T_2$  and converting grayscale videos into binary videos. [213, 217, 218]

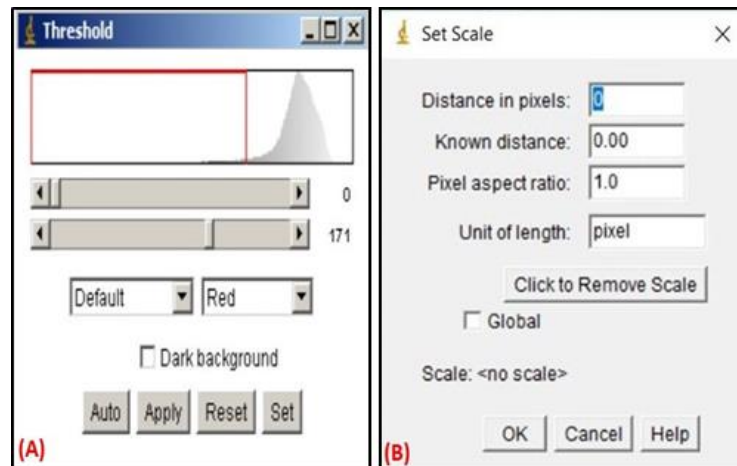


**Figure 3.17 – (A)** The dialog box of the thresholding processing tool. The upper and lower threshold values can be set manually, through the upper and lower sliders, or using various algorithms for their automatic determination (*e.g.* Otsu, Maximum Entropy, *etc.*); instead of trying one by one the different algorithms and assess which one suits better the required purposes, they can be tested simultaneously utilising the ImageJ auto threshold processing tool and then choose “Try all” in the dialog box. [217] In the image, the lower limit value  $T_1$  was set as 0 and the upper limit value  $T_2$  was set as 171; their range is highlighted by the red rectangular frame over the intensity histogram (the rectangular border colour depends on the selected display mode, *e.g.* if the black and white display mode is chosen, the rectangular border will be black). More details about the background subtraction and its features can be found here: [213, 217, 218] **(B)** The dialog box of the set scale tool; the real scale must be set before processing the videos. [220]

At the end of the thresholding process, the real scale must be set, employing the conversion factors between pixels and microns (see **Figure 3.17 B**). At this point, as better addressed in the next section, the characteristics of the algal cells in the binaried and rescaled videos had to be filtered so that only the desired features were considered.

### 3.7.2 Filtering the desired features of the algal cells

The next step was to filter the desired features of the algal cells by choosing some cutoff parameters, to ensure that only the wanted characteristics of the filtered cells were tracked and assessed properly (see **Section 3.7.3**).

The filtering process was carried out by using an ImageJ plugin called wrMTrck (see **Figure 3.18**), that had been developed by Pedersen [220]. The most important selectable parameters were the maximum and minimum acceptable cell areas which prevented potential noise from being mistaken for algal cells (*e.g.* pixelated background or small impurities); the maximum allowable algal velocity, *i.e.* the maximum velocity DS cells could travel between two frames, before being discarded (*e.g.* this ruled out lysed cells or salty impurities, which areas ranged between the maximum and minimum cell areas); the minimum number of frames that needed to be tracked, *i.e.* the minimum number of frames in length a particle track should be, before it will be disregarded (*e.g.* to take into account the DS cells that had swum in and out of the focal plane). [220]

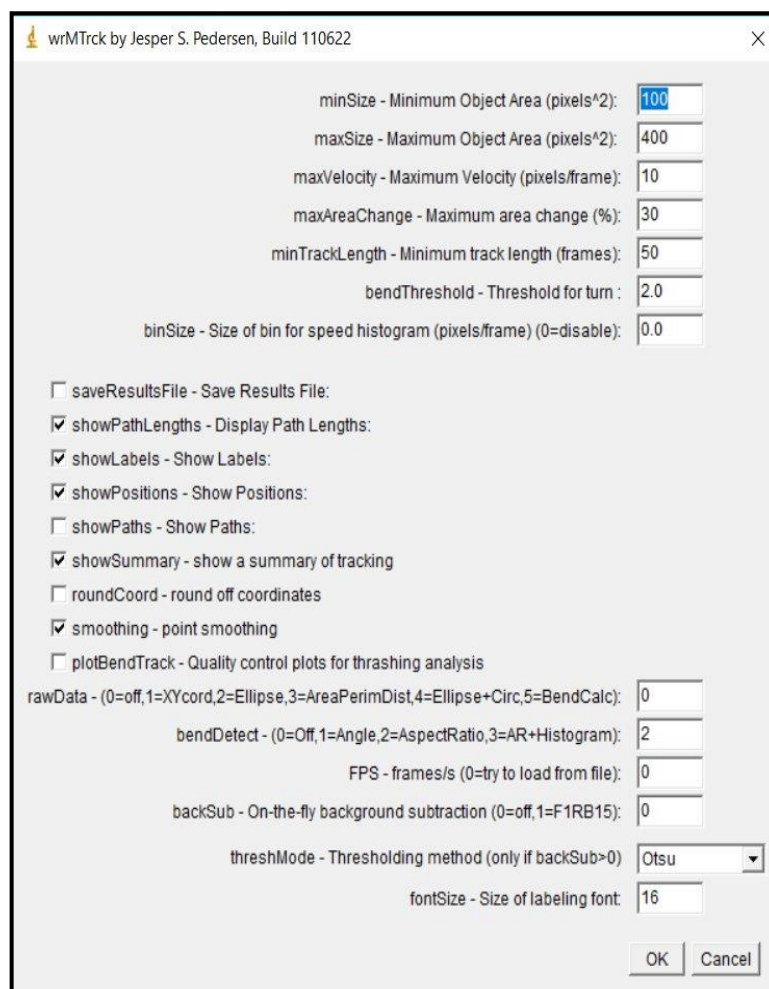


**Figure 3.18** – The dialog box of the plugin wrMTrck. Although in the image some of the cutoff parameters are expressed as pixels, they values must be coherent with the previously-set scale (see Section 3.7.1.3), *ergo* they must be set as microns. More details about the plugin wrMTrck can be found here: [220].

### 3.7.3 The tracking process and the analysis of the results

The wrMTrck plugin permitted choice of the outcomes of the tracking process (see **Figure 3.18**). [220] For example, when “showLabels” was chosen, the tracking process would provide a video where each DS cell was assigned an individual number and that could be compared with the original one (see **Figure 3.14 D**); in fact, despite the filtering parameters, unwanted objects may have been tracked anyway and they could be ruled out by comparing visually the two videos, to ensure no discrepancies in the results. As can be seen in the **Figure 3.18**, more outcomes could be chosen, *e.g.* a representation of the swimming trajectories (ShowPaths), the spatial positions of the cells within the microchannels, major and minor axes of an ellipse fitting a given DS cell, *etc.*

Once the algal cells had been filtered and the tracking process outcomes had been chosen, the plugin located and tracked the cells in each frame of a given video. Using the information recorded for each cell, the plugin established which cells in a given frame were likely to be the same cells that had been identified in previous neighbouring frames, according to the chosen filtering characteristics. [52]

The final outcomes of the tracking process were the labelled-algae video (see **Figure 3.14 D**) and an excel file containing the chosen raw data of each tracked cell, which depended on the previously-chosen outcomes.

As further explained in the next chapters, once the desired features of given cells had been identified, the data was processed through specifically-tailored Matlab codes, inferring information on their speed, the swimming trajectories, their eccentricities, *etc.* and the obtained results were finally represented and compared, exploiting software like Tecplot and Microsoft Excel.

### 3.7.4 Limits of the image analysis process

In this section, the main limitations of the image analysis are mentioned, in order to understand the results and some of their technical limits. The main advantages and drawbacks of my research work and the results obtained will be analysed and quantified in the next chapters, in particular in the 7<sup>th</sup> one, where some suggestions for potential further research work will also be provided.

Generally, during the tracking process of some algal cells at both the population and the single cell levels, there are some experimental and computational limiting factors that must be taken into account.

From an experimental point of view, the algal cells can be tracked provided the image-acquisition rate is high enough and the algal concentration is sufficiently low, in the order of  $10^6$  cells·ml<sup>-1</sup>, as higher concentrations could confuse the tracking and analysis processes, leading to wrong results. [52, 194] Another limitation is imposed by the finite depth of field (DOF) values of the microscope, which allow relatively short segments of the algal swimming trajectories to be observed. In fact, only the cells that lie within the DOF (*i.e.* the in-focus organisms) can properly be tracked while the out-of-focus ones cannot, due to their weak signals. [194]

Furthermore, for a generic experimental video, the processing time, required for carrying out the tracking part, depends on how powerful the used computer is (*i.e.* its RAM) and the video resolution; the higher the RAM is and the lower the video resolution is, the shorter the processing time will be.

### **3.8 Chapter summary**

In this chapter, the main experimental and image analysis procedures used and developed in this research work have been described, along with the algal cultivation, the experimental setups developed for both live and dead DS cells and the image analysis process.

The main issues which occurred during the experimental investigations using dead cells have also been discussed, focusing particular attention on the killing procedure and experimental setup, which will be further explored in the **5<sup>th</sup> Chapter**.

A comprehensive technical analysis of the two most important employed pieces of equipment, the inverted microscope and the microfluidic devices has been provided. As described in the future analysis, they represent a new inexpensive and effective approach for the development of PBRs, from the algal cells screening to the quality controls on the cultured organisms.

## – Chapter 4 –

# From microfluidic devices to photobioreactors: the study of living *Dunaliella Salina* cells

### 4.1 Chapter layout

This chapter describes the results concerning the live *Dunaliella* cells. In particular, main focus of this research work which was to develop a new approach which assumed the microfluidic devices as “simplified PBRs” and their microgeometries as static mixers, so as to achieve greater insight into the actual fluid dynamic experiences of the cells, to acquire helpful experimental data directly from the microalgae through the image analysis process and to exploit them for optimising the PBR design and utilisation processes.

Thus, to make the results easier to understand, in the first part of the chapter, the main stages needed for designing a closed PBR are described, with particular emphasis on the beneficial effects derived from the exploitation of static mixers in algal cultivations and analysing why microalgae characteristics should be taken into account while designing a PBR.

Next, the results concerning living *Dunaliella* cells at different fluid dynamic conditions are discussed (*e.g.* in stagnant flow conditions, while undergoing different flow rates within both the straight channel and contraction-expansion ones), focusing particular attention to the cell dispersion within the channels and their interaction with the walls, providing practical examples about how the results can be employed for enhancing the PBRs and justifying why both microfluidic devices and the image analysis technique should be considered as complementary tools for PBRs optimisation processes.

## 4.2 The current procedure for the design of PBRs

In order to understand the results and how to employ them in real applications, the main phases required for designing a PBR must be discussed. The technical solutions and configurations for PBRs are numerous [118] (see the 2<sup>nd</sup> Chapter), a technical analysis will be provided considering mainly microalgal suspensions cultivated outdoor in horizontal tubular PBRs.

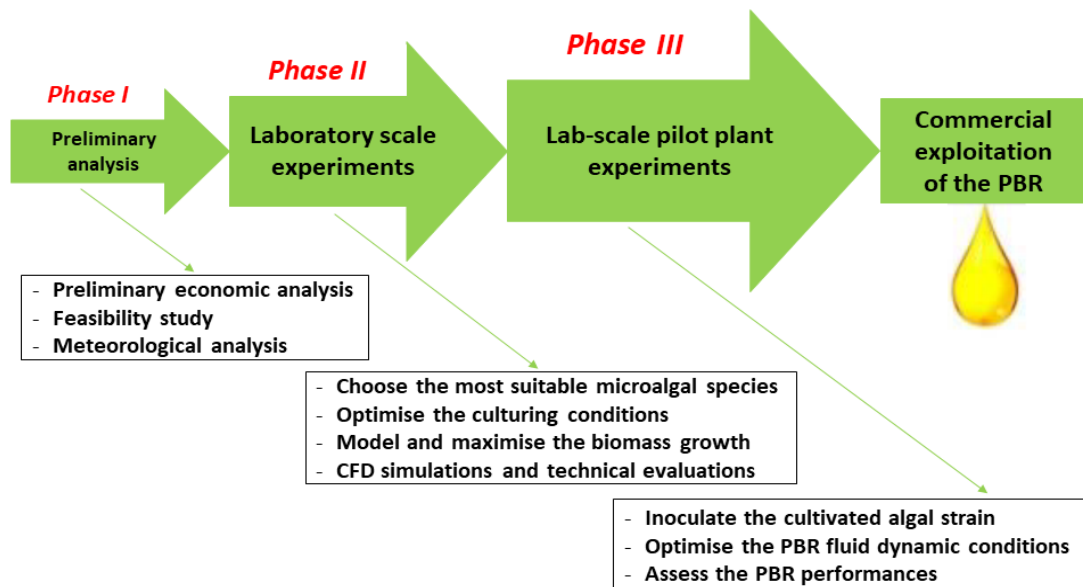


Figure 4.1 – The most important steps for designing a PBR and what must be accomplished during each phase. Once the culturing and fluid dynamic conditions in the lab-scale pilot plant have been optimised, it must be scaled up to the final commercial PBR. In principle, tubular PBRs can be scaled up by increasing either the length or the diameter of the tube but, in practise, they are both constrained mainly by the fragility of the cultured organisms, the accumulation of dissolved oxygen along the tube and the need of achieving optimal dark/light cycles frequencies (see Section 6.5). [139, 154] Adapted from [166].

As shown in the **Figure 4.1**, firstly a preliminary economic analysis must be conducted, which should include a market survey to decide the final attainable product(s), the potential legislative benefits/constraints, a business plan, *etc.* These aspects are then employed to perform a further feasibility study, aimed to assess the actual geographic position of the future plan, the availability of auxiliary fluids, carbon dioxide sources, *etc.* [118, 166] Next, a meteorological analysis of the chosen PBR location must be conducted, in order to verify its solar radiance, rainfall, annual temperature maps, *etc.*, since these factors will have both a technical influence (*e.g.* high solar irradiance values imply high temperature gradients within the reactor and a more complex cooling system) and a biological influence (*e.g.* affecting the algal growth, the obtained biomass, *etc.*). [118, 166]

At this point, some laboratory-scale experiments must be carried out so as to select, screen and identify the most appropriate microalgal strains, their toxicity, ease of culture, robustness, *etc.* [118, 166] Usually some algal pre-cultures are also cultivated under well-controlled conditions that must simulate the solar irradiance of the final PBR location, to avoid excessive environmental shock to the cells during their inoculation in the PBR. [222] Next, the pilot plant must be either designed and assembled or bought, some technical evaluations conducted and some computational fluid dynamic (CFD) simulations undertaken, in order to maximise its performance. [118, 222]

Once the cultures have pigmented enough, they will be inoculated in the pilot plant where some further experimental investigations must be carried out through daily microscopic observations to quantify fundamental features, such as the biomass growth, its quality, *etc.* [118, 166] The microalgal cultures must be continuously monitored (see **Figure 4.2**), focusing particular attention on the presence of potential contaminant organisms, the temperature profiles, the physiological state of the culture and the oxygen concentration, which is a reliable indicator that the culture is stressed and may quickly deteriorate. [139]

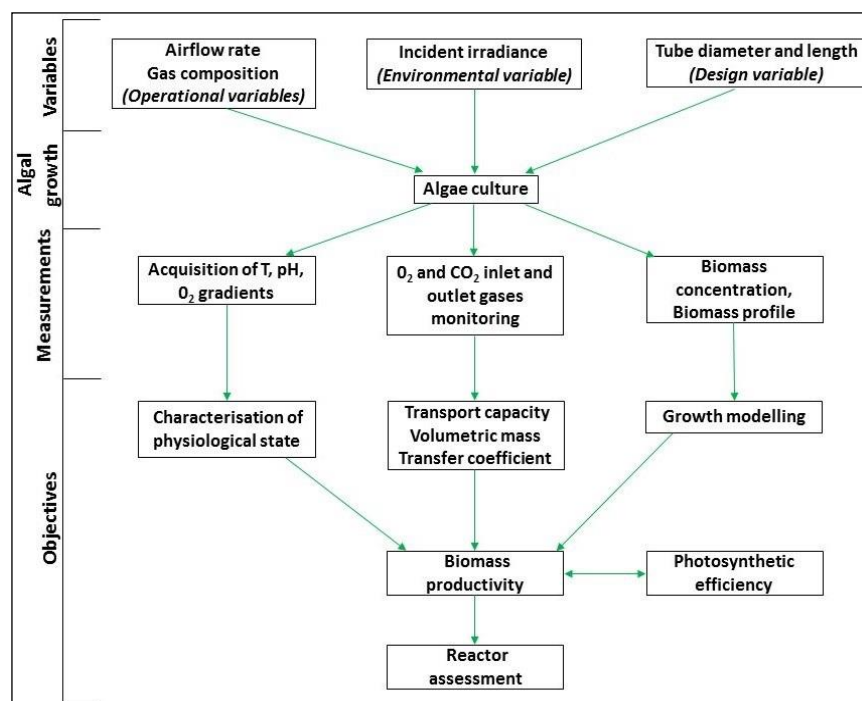


Figure 4.2 – The lab-scale pilot plant permits investigation of the effects of operational, environmental and design variables on the microalgal cells, allowing also to assess different PBRs configurations. [118, 166]

Adapted from [223].

Eventually, once the optimisation processes have been carried out, the pilot plant can be scaled up to the final PBR that, along with its related downstream processes, will permit commercial exploitation. [118, 166]

The main biological and engineering challenges regarding PBRs have been summarised in the **Figure 4.3** (see also the **2<sup>nd</sup> Chapter**).

The biomass production process requires also daily quality controls on both the culture (e.g. the algal concentration, the potential presence of contaminants, etc.) and the biomass (i.e. its quality and quantity) (see **Figure 4.3**). [166]

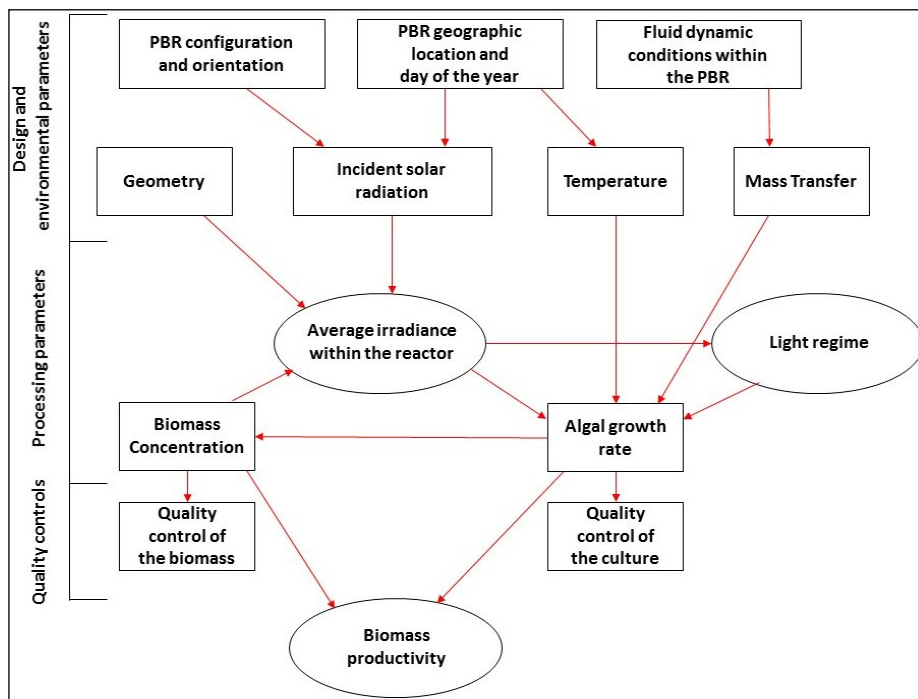


**Figure 4.3** – The design and processing parameters that affect PBR performance and the final biomass productivity. The production process also involves periodical quality controls of both the biomass and the culture. Adapted from [223].

Nonetheless, as previously discussed in the **2<sup>nd</sup> Chapter**, current approaches for the design of tubular PBRs and the various production processes employ some energetically-costly solutions (see **Section 2.9**). As a result, each of the previously discussed design phases has been intensively researched and multiple technical and biological solutions have been proposed in order to enhance the viability of algal biomass production (see **Section 2.6**).

As discussed in the next section, one of the most promising solutions consists of employing static mixers, also known as motionless mixers, which are installed within PBRs to enhance their performance. [224, 225]

### 4.3 The exploitation of static mixers in photobioreactors

Industrially, static mixers (SMs) are employed in numerous applications (*e.g.* fermentation bioreactors, food production, *etc.*) since they represent an attractive alternative to conventional agitators or they have an important impact on mass and heat transfer characteristics, can be arranged in various geometries (*e.g.* blades, helices, corrugated plates, *etc.*), can be made of different materials (*i.e.* steel, ceramic or plastic) and are characterised by lower energy consumptions, as they do not have moving parts. [226, 227] Using the flow energy of the fluid, SMs enhance the mixing levels by twisting, distorting and expanding the fluid streamlines in specially-designed arrangements. [226, 227]

SMs have also been investigated in different PBRs with encouraging results; different algal strains were assessed in various PBRs configurations, with processing parameters (*e.g.* different irradiance conditions, flow and aeration rates, *etc.*) and different SM geometries. For example, Ugwu and co-workers used an inclined tubular PBR for the outdoor cultivation of *Chlorella sorokiniana* cells, quantifying experimentally the effects of different SM geometries and materials. [228] Moreover, Huang *et al.* investigated numerically a flat plate PBR (see **Section 2.6.2.1**) equipped with special baffles, aimed to improve the light path and growth rates of some *Chlorella pyrenoidosa* cultures. [224]

Generally, these studies compared the performances of the lab-scale PBRs with and without SMs, emphasising that SMs had contributed to increase the algal volumetric biomass productivity (see **Table 4.1**). Nonetheless, as we will see in the **6<sup>th</sup> Chapter**, these research works also demonstrated that the geometrical arrangements of SMs must be optimised as they can affect the mixing time within PBRs (*i.e.* the time required to achieve a definite degree of homogeneity, after the injection of a tracer solution). They also increase the local turbulence by forming energy-dissipating microeddies and leading to shear-induced damage to the algal cells, which could hamper their viability and the biomass production. [139, 229]

**Table 4.1 – The most important improvements achieved by investigating different PBRs equipped with motionless mixers.**

Observed benefits due to SMs	Achieved by	References
Increase of the light utilisation efficiency through the exploitation of the flashing light effect.	Optimising dark/light cycle frequencies, providing more regular mixing patterns, reducing the photoinhibition and the dark zones within PBRs (see <b>Section 2.7.3</b> ).	[222, 224-226, 228, 230, 231]
Increase the mixing levels within the PBR.	Increasing mass and gases transfer rates (see <b>Section 2.9</b> ).	[224, 225, 228, 230, 231]
Reduction of the detrimental effects on the algal cells due to excess photosynthetically-generated oxygen.	Inhibiting oxygen accumulations within PBRs and decreasing bubble size (see <b>Section 2.8</b> ).	[224, 225, 228, 230]
Reduction of the algal stagnation, accumulation and biofouling phenomena.	Increasing local shear rates within PBRs.	[224, 225, 227, 228, 231]
Reduction of the overall costs.	Reducing the energy requirement.	[224-228, 230]
Increase the algal volumetric biomass productivity.	Optimising the overall fluid dynamic conditions of PBRs.	[222, 224, 225, 228, 230, 231]

However, a trend observed in all these studies is that all the results have been inferred by considering only one algal species, *ergo* they are not generalised or, in other words, the suggested SMs geometries may not be beneficial if the same PBR configurations would be used for culturing other algal strains. What is more, the results have usually been analysed by considering specific criteria like the potential fluid dynamic, engineering and economic benefits for PBRs, but without taking into account the specific algal characteristics and assuming that the cells will adapt to any of those “optimal” solutions, as if they were passive particles (see **Section 2.10**). [147, 148, 222, 230]

Nevertheless, as described in the next section, successful design of PBRs must rely on attaining a proper balance between engineering and algal biological factors that are dependent on the cultured species. [142]

#### **4.4 Intrinsic features of different microalgal strains and their effects on photobioreactors**

As previously discussed (see **Section 4.2**), during the second phase of the PBR design procedure, the most suitable microalgal strains must be identified and evaluated, based on their ability to deliver the final desired product(s) and the ultimate location of the PBR.

The different algal species should carefully be screened taking into account fundamental culture-specific features, such as their tendency for clumping, settling, their specific growth rates, their shear and temperature sensitivities, *etc.* [142] In fact, as shown in the **Table 4.2**, algal intrinsic characteristics should play a vital role in the design, processing, maintenance of PBRs and their related quality controls and downstream processes.

**Table 4.2 – The most important features of different algal strains and their main effects on the design process (DP), cultivation process (CP) and the quality control (QC) of the culture.**

Some of these contributions have been modelled elsewhere: [229, 232, 233].

Algal feature	Main effects	What phases are affected	References
Photosynthetic characteristics	Affect the limits between dark and photic zones, the photoinhibition and dark/light cycle frequencies.	DP, CP	[139, 142, 176, 223, 233]
Fluid dynamic behaviours	Different taxis effects, biofouling, tendency to form preferential swimming paths.	DP, CP	[10, 139, 142, 176, 223, 233]
Growth rate under the considered climatic conditions	The algal concentrations within the reactor, the carbon dioxide consumption rate, the biomass production.	DP, CP	[139, 154, 233]
Morphology and size	Different nutrient uptake rates and cellular metabolisms.	DP, CP	[234]
Physiology	Different growth mediums and stressing procedures required.	DP, CP	[181, 183]
Algal fragility	The more fragile the cells, the easier they will be shear-stressed or damaged.	DP, CP, QC	[198, 229, 235, 236]
Algal adaptability	The intrinsic tolerance to both chemical and biological contaminants.	DP, CP, QC	[129, 140]
Temperature resistance	The cooling system of the PBR must carefully be designed.	DP, CP	[129, 158]
Oxygen inhibitory levels	Influence the maximum allowable oxygen concentration within the PBR and its scale up process (see <b>Section 6.5</b> ).	DP, CP	[139, 142, 232]
Different algal pigments	Different absorbed wavelengths, different extinction coefficients, affect light paths within PBR.	DP, CP	[118, 223]

Hence, microalgal characteristics cannot be overlooked but, on the contrary, must be considered during both process design and operation. Consequently, it is necessary to devise a new inexpensive, reliable and versatile methodology to acquire experimental data directly from the microalgae, to take into account their intrinsic properties and use them for optimising all the phases of the PBR design and operation.

Therefore, as explained in the next sections, this research has investigated the possibility of exploiting microfluidic devices and the image analysis technique as complementary tools for PBRs optimisation processes, since they have allowed quantification of algal cells behaviour under different fluid dynamic conditions.

## **4.5 Why should microfluidic devices and the image analysis be employed for optimising PBRs?**

The objective of this research work was to investigate microfluidic devices as hypothetical horizontal PBRs and their microgeometries as static mixers (SMs) in order to achieve more insight into the actual experience of the cells within both lab-scale and process-scale PBRs. As reported in the results and discussion sections, amongst other advantages, the experiments show that this approach would permit:

- investigation of the interactions of DS cells with channel walls,
- characterisation of the algal responses at both single cell and population levels,
- quantification of the algal cells motility, size and shape,
- preliminary experimental assessments and comparisons of SMs and PBR performances, even during the laboratory scale phase, which currently is just exploited for pre-cultivation or CFD simulations purposes,
- studying crucial parts of the microchannels (*i.e.* the centreline or the contraction) through targeted image analysis processes and tailored Matlab codes, *etc.*

Moreover, although all the results of this PhD were attained studying “biologically-normal” DS cells (meaning that they had not previously been either stressed or genetically modified), the procedure which has been developed is also very flexible since results can also be obtained for different algal strains, simplifying the screening and comparison processes between them. Most importantly, the final objective is to pave the way towards a new mentality whereby PBRs, their configurations and processing conditions will be set and adapted starting from specific algal characteristics.

However, my hypothesis presented various biological and engineering limits that will be introduced and analysed in detail in the **7<sup>th</sup> Chapter**, where further suggestions for potential future research work will also be provided.

## 4.6 Experimental results regarding living *Dunaliella* cells

The results relating to living *Dunaliella* cells were obtained by analysing at least three experimental videos.

During the experiments, the following aspects have been neglected: **1)** the algal death and birth processes, because their time-scales are much longer than the average residence times spent by the algal cells in the channels during the experiments [55]; **2)** cell-cell interactions, since dilute suspensions were considered.

In experimental investigations where the live cells were subject to different flow rates, their terminal sinking velocity was much smaller than their swimming velocities (*i.e.* the gravitational sedimentation processes were not taken into account). However, under particular fluid dynamic conditions, the two velocities were comparable (*e.g.* while the algae had been interacting with the channel boundaries) and the sedimentation velocity played also a vital role in the experiments involving dead cells (see the **5<sup>th</sup> Chapter**), therefore it is quantified in the next section.

### 4.6.1 Terminal sinking velocity of a *Dunaliella* cell

The motion of a solid spherical particle settling under the gravitational force in a fluid at rest can be analysed by considering the forces acting on it (see **Figure 4.4**).

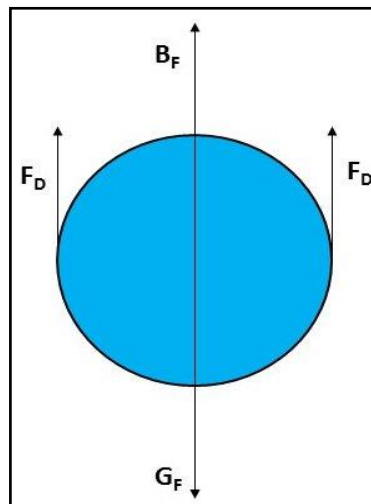


**Figure 4.4** – The physical setup used for studying the terminal velocity of a particle settling through a stagnant fluid. The gravitational force is counteracted by the buoyancy force and the drag force. Adapted from [237].

Precisely, a force balance on the settling sphere will give:

$$m_p \cdot \frac{d\mathbf{u}_p}{dt} = \sum (\mathbf{Forces}) \quad (\text{eq. 4.1})$$

where  $m_p$  and  $\mathbf{u}_p$  are the mass and the velocity of the particle.

The forces exerted on the sphere are the gravitational force  $\mathbf{G}_F$ , the buoyant force  $\mathbf{B}_F$  (also known as Archimedes' force) and the drag force  $\mathbf{F}_d$ , defined as:

$$G_F = \rho_p V_p g \quad (\text{eq. 4.2})$$

$$B_F = \rho_f V_p g \quad (\text{eq. 4.3})$$

$$F_d = 6\pi\mu u_p R \quad (\text{eq. 4.4})$$

$R$ ,  $V_p$ ,  $\rho_p$  are the radius, volume, density of the particle,  $g$  the gravitational acceleration, while  $\rho_f$  and  $\mu$  are the density and dynamic viscosity of the surrounding fluid. [72]

Eq. 4.4 expresses the drag force exerted by the flow on a single spherical isolated particle located far away from boundaries. [72]

Assuming the downwards direction as positive:

$$m_p \cdot \frac{d\mathbf{u}_p}{dt} = \mathbf{G}_F - \mathbf{B}_F - \mathbf{F}_d = \rho_p V_p g - \rho_f V_p g - 6\pi\mu u_p R \quad (\text{eq. 4.5})$$

When  $\frac{d\mathbf{u}_p}{dt} = 0$  the particle will be settling at a steady velocity, called the Stokes settling velocity  $\mathbf{V}_T$ , therefore eq. 4.5 becomes:

$$\frac{4}{3}\pi R^3 g(\rho_p - \rho_f) = 6\pi\mu V_T R \quad (\text{eq. 4.6})$$

leading to:

$$V_T = \frac{2}{9} \frac{g}{\nu} \frac{\rho_p - \rho_f}{\rho_p} R^2 \quad (\text{eq. 4.7})$$

$\nu$  is the kinematic viscosity of the fluid. [72]

Therefore, the terminal velocity of a spherical living *Dunaliella* cell (LDC) will be given by:

$$V_{T,LDC} = \frac{2}{9} \frac{g}{\nu_m} \frac{\rho_{LDC} - \rho_m}{\rho_m} a^2 \quad (\text{eq. 4.8})$$

$\nu_m$  and  $\rho_m$  are the kinematic viscosity and the density of the culture medium,  $\rho_{LDC}$  is the density of the living algal cell and  $a$  is its radius.

Interestingly, eq. 4.8 shows that the sinking terminal velocity for a spherical algal cell is proportional to  $a^2$ ; nevertheless, settling velocities of various species of algae were found to depend on  $a^{1.18}$  (*i.e.* they tend to sediment slower than what theory predicts), but no valid explanation has been provided for this. [238]

Since  $\rho_m$  is  $1043.1 \text{ kg}\cdot\text{m}^{-3}$ ,  $\nu_m$  is  $1.12 \times 10^{-6} \text{ m}^2\cdot\text{s}^{-1}$ ,  $\rho_{LDC}$  is  $1092.1 \text{ kg}\cdot\text{m}^{-3}$ , (see **Appendix 3.1** and **3.2**) and the average diameter of the employed living DS cells was found to be  $15 \text{ }\mu\text{m}$  (see **Section 6.4.3**),  $V_{T,LDC}$  is  $5.14 \text{ }\mu\text{m}\cdot\text{s}^{-1}$ .

As explained in the **Section 1.11**, the sedimentation velocity  $V_T$  can usually be neglected for swimming organisms since its magnitude is smaller than that of typical swimming velocities [2]; nevertheless, at stagnant flow conditions, due to cells-boundary interactions, the swimming and sinking velocities may have the same order of magnitude and consequently the latter cannot be ignored, this is addressed in the next section.

## 4.7 Dunaliella cells at stagnant flow conditions

The experimental investigations started by studying algal behaviour under stagnant conditions, *i.e.* no fluid flow was applied through the syringe pump thereby allowing the DS cells to swim freely. In particular, after arranging the experimental setup for the live algae (see **Section 3.5**) and injecting the algal cells in the channel under investigation, the pump was switched off and the fluid left to settle, imposing a zero net flow.

Under these conditions and in the absence of external taxis factors that may cause a bias to any particular direction, the cells motility can be considered as a measure of their viability [235] and its quantification allows us to attain some useful information directly from the algae, such as their swimming velocity vectors spatial distributions and swimming velocity histograms (See **Figure 4.5**).

The cells motility was determined by processing some experimental videos, establishing the algal  $X$  and  $Y$  positions by image analysis and calculating the swimming velocity magnitude as  $V_{SW} = \sqrt{V_x^2 + V_y^2}$ , where  $V_x$  and  $V_y$  are the algal velocities between two consecutive frames in the  $x$  and  $y$  directions; *i.e.* if  $\mathbf{p}_i(X_i, Y_i)$  and  $\mathbf{p}_{i+1}(X_{i+1}, Y_{i+1})$  are the position vectors of an algal cell between the two neighbouring  $i$ -th and  $i+1$ -th frames and  $tbf$  is the time interval value between the two frames,  $V_x$  and  $V_y$  are given by  $V_x = \frac{X_{i+1} - X_i}{tbf}$  and  $V_y = \frac{Y_{i+1} - Y_i}{tbf}$ .

As we shall see in the next section, at stagnant conditions, DS cells were seen to swim randomly throughout the channel, albeit their behaviours had been affected by the microfluidic geometries that stimulated the algal tendency to swim and interact with the walls, without orientating them towards any preferential swimming paths.

While swimming, the cells tended to shift in and out of focus within the depth of field (DOF) (see **Section 3.4.4**), affecting the tracking of their positions and making it difficult to obtain statistically significant data about their shapes; however, as discussed in the **Section 6.4.3**, the living algal cells used in this PhD were ellipsoidal in shape, with an average major axis of 15  $\mu\text{m}$  and a mean eccentricity of 0.4.

#### **4.7.1 Effects of microfluidic geometries on algal behaviours at stagnant conditions**

At zero net flow conditions, regardless the microfluidic geometry employed, the cells swam randomly and no theoretical predictions about their trajectories could be made, providing that potential external taxis factors had been eliminated. Nonetheless, the experiments reveal that the algal tendency to swim depended on the microfluidic geometry selected.

Within the straight channel, despite the relatively large available volume (*i.e.* for a channel with a width of 400  $\mu\text{m}$ , a depth of 100  $\mu\text{m}$  and a length of  $\sim 56$  mm, measured between its inlet and outlet holes, the volume was  $\sim 2.24$  mm<sup>3</sup> [ $2.24 \times 10^9$   $\mu\text{m}^3$ ]), the cells swam relatively slowly, rotating around their axes and interacting with the walls by swimming in their proximity, adhering to them and wobbling. In the experiments involving an expansion/contraction ratio (ECR) 2-1 channel, the algae tended to swim faster, moving back and forth along the contraction and interacting with its boundaries, the channel walls and the corners between them.

These different behaviours could be explained considering that, for the algal cells, the straight geometry represented a uniform and stationary environment, hence the cells were not prompted to explore the surroundings, but rather were inclined to reduce their velocities and hover along relative limited parts of the channel. This was further confirmed by the fact that, in the experimental videos of the straight geometry, lower average numbers of cells were observed, demonstrating their “sedentary” behaviours.

On the other hand, in experimental observations involving the ECR 2-1 geometry, the cells were seen to be more active and more stimulated to explore the surrounding environment, resulting in the spatial distribution of swimming velocity vectors being different from the one of the straight channel (see **Figure 4.5 A** and **B**) and the average swimming velocities were higher (see **Figure 4.5 C** and **D**).

This increased dynamism may be explained considering the intrinsic attraction of microalgal cells to solid boundaries [30, 76] which offer anchoring points for the formation of biofilms [10] and facilitate the accumulations of nutrients [30, 239], this latter effect that could have occurred while waiting for the flow to settle, may have been increased by the contraction corners and might have induced potential chemotactic-biased behaviours to the DS cells.

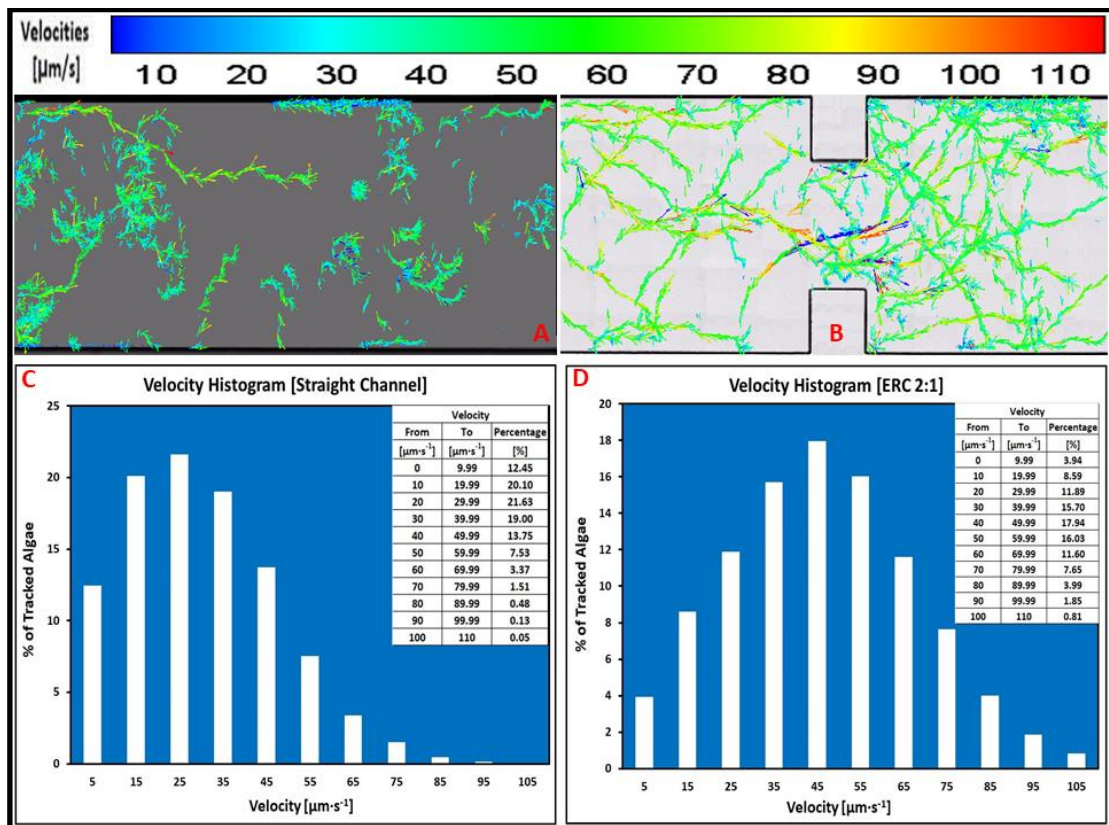
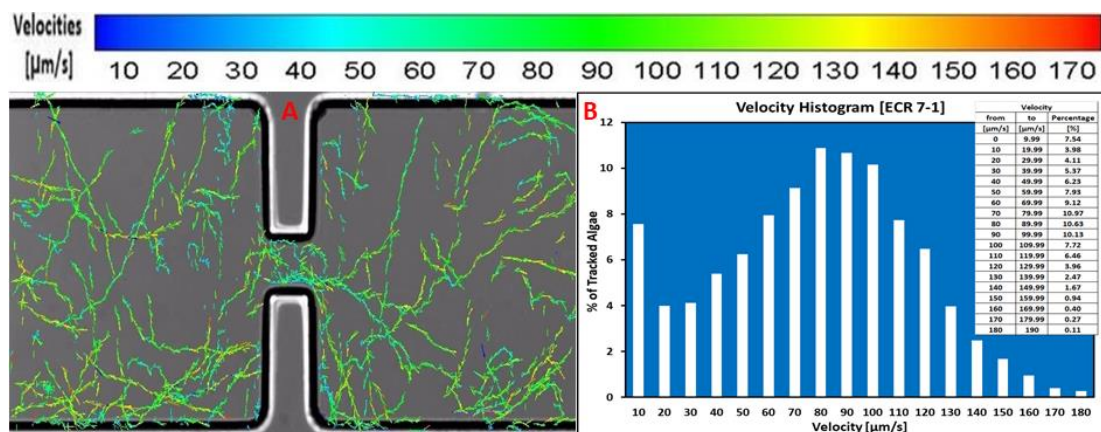


Figure 4.5 – The swimming velocity vectors spatial distributions of some DS cells in the straight channel (A), in the ERC 2-1 channel (B) and their corresponding swimming velocity histograms (C and D); the velocities were measured across the whole channels, both in the contraction regions and outside them. The average number of observed cells was 15 in the straight geometry and 35 in the ERC 2-1 geometry; however, owing to the cells swimming continuously in and out of focus, the numbers of tracked algae in these experiments were always higher than the ones of the cells that could actually be visualised (see Section 3.7.4). The experiments were carried out using the 10X objective and an exposure time ranging from 4 ms to 5 ms.

Moreover, the two swimming velocity histograms show also that the cells swam at average swimming velocities lower than the values expected from the literature (*i.e.* 60-100  $\mu\text{m}\cdot\text{s}^{-1}$  [39, 43]); this could be due to the fact that those swimming values are usually estimated considering unbounded environments [39, 43] while, within the channels, the cells were in geometrically-confined environments (the average depth was  $\sim 100 \mu\text{m}$ ) and this may have contributed to the decrease of the average swimming speeds, since the presence of boundaries leads to an increase of the required metabolic working rate that the microswimmers have to provide to maintain the same flagellar waveform (see Section 1.10.4). The available swimming space was further reduced by the fact that usually the flagella prevent the algal body from touching solid surfaces, when the cells are hovering in their proximity. [76]

Similar behaviours were also found when considering the narrower contractions (*i.e.* at higher ECRs). In the experimental investigations of ECR 4-1, the ECR 7-1 and the elongated geometries, some oscillatory flows had developed within the contractions, which stopped the stagnant conditions from being achieved and, even after waiting more than three hours for the flow to settle, both the swimming velocities and trajectories of the cells were still affected. In particular, if a given cell swam downstream in the oscillatory flow, it would have been accelerated, whereas when swimming upstream, the cells were either slowed down or diverted away from the contractions, leading to both swimming velocity vectors spatial distributions and velocity histograms which are different from the expected ones (*i.e.* the one concerning the ECR 2-1 geometry, where the oscillatory effects were not observed, see **Figure 4.5** and **4.6**).



**Figure 4.6** – The swimming velocity vectors spatial distribution (A) and the velocity histogram (B) of some DS cells in the ECR 7-1 channel. The algal cells were still stimulated by the microgeometry, despite their swimming behaviours being affected by the oscillatory flow that accelerated the downstream-swimming cells and either decelerated or re-orientated the upstream-swimming ones. The experiments were carried out using the 10X objective, an exposure time ranging from 4 ms to 5 ms and the average number of observed cells was 40.

As analysed in the next section, the quantification of cells viability and their interactions with the walls can be beneficial for PBRs, therefore the study of freely swimming microalgae within microfluidic devices must be carried out in the absence of oscillatory flows that can lead to deceiving results.

## 4.7.2 The study of freely swimming microalgae: potential benefits for photobioreactors

As better explained in the 6<sup>th</sup> Chapter, one of the major advantages of studying the algal behaviours using microfluidic devices is the possibility of quantifying the actual fluid dynamic experiences of the cells in some specific regions of the microchannels by targeting the image analysis process and employing tailored Matlab codes. This procedure was used to obtain the velocity histograms of the algae that swam in the red 20-micron-width regions and for quantifying the algal interactions with the walls (see **Figure 4.7 C and D**).

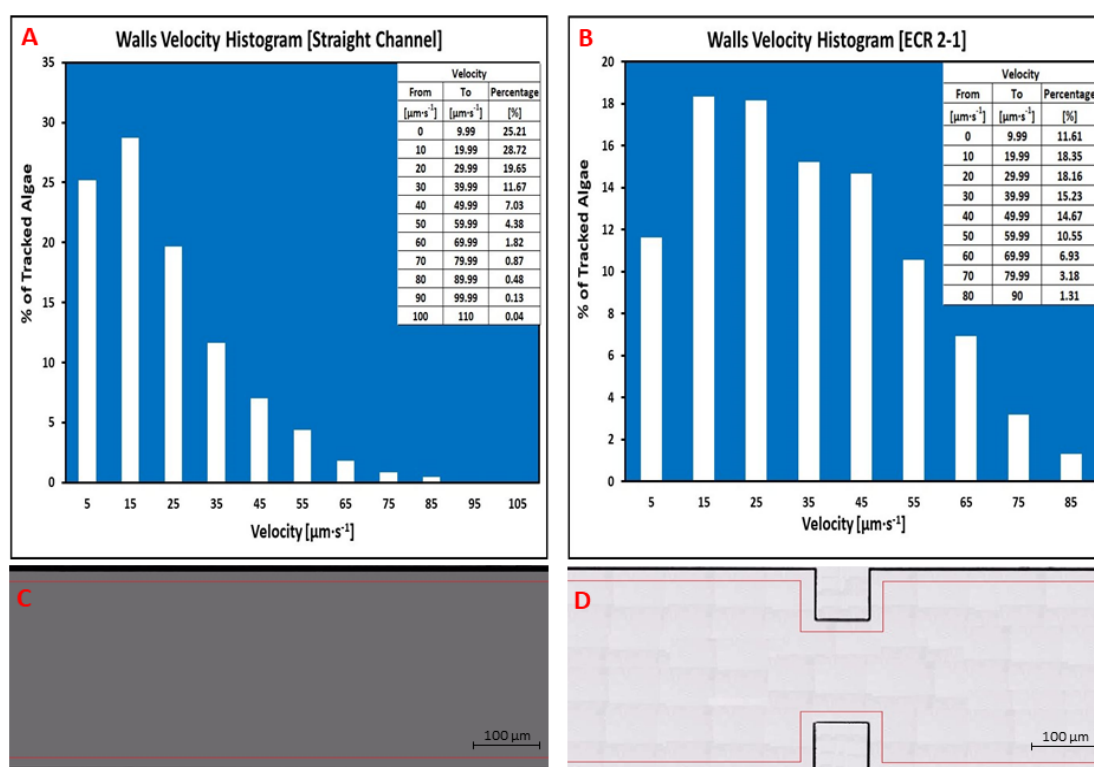


**Figure 4.7** – The swimming velocity histograms of the DS cells that swam in the 20-micron-width red regions of the straight channel (C) and the ECR 2-1 channel (D). They were obtained by analysing the same experimental videos that gave the results shown in Figure 4.6 but, through a specifically-designed Matlab code, only the algae that had been interacting with the walls were considered, providing useful data about their tendency for biofouling. However, although the adhering and wobbling cells could clearly be visualised in the experimental videos, during the image analysis process, they were assumed as non-moving objects by ImageJ and removed along with the other fixed parts in the videos (see Section 3.7.1), therefore their contribution has not been taken into account in the velocity histograms of Figure 4.5, 4.6 and 4.7. The average number of observed cells was 10 in the straight geometry and 25 in the ECR 2-1 geometry.

During experimental investigations involving both the straight and ECR 2-1 geometries, the cells interacted with the channel boundaries by either hovering in their proximity for a certain amount of time before swimming away or adhering to them and wobbling slowly.

As explained in the **Section 1.10.4**, when a microswimmer swims close to a solid surface, there will be an increase of the work rate required to maintain the same flagellar beat frequency, or in other words, there will be an increase of the propulsion costs that may result in a decrease of the swimming velocity, if the organism swims with constant power [30]. This implies a higher residence time for the cells close to the walls (*i.e.* an increase of shading effects). In fact, the higher the percentages of cells that swim at low velocities, the higher the average time spent by the cells close to a given boundary and the higher their tendency for biofouling will be. Potentially, these effects may also be emphasised by the fact that, if the swimming velocities become very low, the algal terminal velocity  $V_T$  may not be neglectable anymore ( $V_T$  for a living DS cell has been estimated to be  $5.14 \mu\text{m}\cdot\text{s}^{-1}$ , see **Section 4.6.1**), causing a further increase of the metabolic energy required for swimming.

However, the “microgeometry effects” described in the **Section 4.7.1** were also found to affect the cell-boundary interactions, resulting in an increased swimming propensity of the cells and slightly higher swimming velocities. Specifically, as can be seen in the **Figure 4.7 A and B**, the percentages of the algae that swam at swimming velocities  $V_s < 20 \mu\text{m}\cdot\text{s}^{-1}$  were about 54% within the straight geometry and 30% in the ECR 2-1 geometry, hence the microgeometry led also to a reduction of the algal average residence times nearby the walls and the resulting shading effects.

Theoretically, all the experimental observations described under stagnant conditions can be employed for PBRs optimisation processes; for example, the motility quantification of freely-swimming algal cells and their interactions with the walls can be exploited during **1)** the algal screening (*e.g.* for obtaining realistic data regarding the fluid dynamic properties of the strains evaluated, their tendency for biofouling, *etc.*); **2)** the cultivation and quality control processes (*i.e.* evaluating the cells viability before being inoculated in the PBR and while being circulated within it).

In fact, the extent of damage to the cultivated algal cells are often assessed employing subjective visual techniques (*e.g.* by observing the induced deformation of the cells or their reduced motility [235, 240]) which may lead to deceptive results. These aspects will be further analysed in the **6<sup>th</sup> Chapter** and in the **Section 7.3.1**.

In the majority of industrial applications, the algal cells are subject to different flow rates that can strongly influence their behaviours, hence after studying the algal cells under stagnant conditions, the experimental approach was used to explore algal behaviours at different flow rates within the straight channel, which was considered to be representative of a horizontal PBR.

## **4.8 Effect of fluid flow on algal cell behaviours: straight geometry**

In this section, the effects of various fluid flows on algal behaviours within a straight channel are explored; firstly the governing equations are mentioned; the continuity equation, the Navier-Stokes equation, the conservation of cells equation and the advection-diffusion equation. Together these equations can be used to describe the phenomena involved in algal movement.

Subsequently, the cell behaviours are analysed and quantified, focusing particular attention to their dispersion within the channel and their interactions with the walls.

### **4.8.1 The governing equations**

The governing equations are the continuity equation, the Navier-Stokes equation, which are useful for obtaining the theoretical velocity profile within a straight channel, the conservation of cells equation and the advection-diffusion equation that addresses the transport of dissolved components to cells.

### 4.8.1.1 Fully-developed laminar flow within a rectangular channel

Poiseuille flows in an arbitrarily-shaped cross-section channel can be described using the conservation of mass and momentum equations (see **Section 1.8.2**), which for an isothermal Newtonian incompressible fluid reduce to: [20, 241]

$$\nabla \mathbf{U} = 0 \quad (\text{eq. 4.9})$$

$$\rho_f \left( \frac{\partial \mathbf{U}}{\partial t} + \mathbf{U} \cdot \nabla \mathbf{U} \right) = -\nabla p + \mu \nabla^2 \mathbf{U} + \mathbf{f} \quad (\text{eq. 4.10})$$

However, the straight geometry used in this research constituted of a constant rectangular cross-section horizontal microchannel (see **Section 3.3**), thus the only external force acting on the fluid in experiments was the gravitational one that could be neglected.

Moreover all the experimental videos recorded in the straight geometry experiments were acquired under fully-developed flow conditions (*i.e.* far away from both the inlet and outlet of the microchannel); meaning that the all the velocity derivatives vanish in the x direction, the pressure varies linearly along the channel and the shear stress has a linear distribution along the cross-section. [61, 241]

As a result, the steady-state Navier-Stokes equation becomes:

$$\mu \cdot \left[ \frac{\partial^2 \mathbf{U}(y, z)}{\partial y^2} + \frac{\partial^2 \mathbf{U}(y, z)}{\partial z^2} \right] = \frac{\partial p(x)}{\partial x} \quad (\text{eq. 4.11})$$

Considering a constant pressure gradient along the channel and the no-slip boundary conditions (see **Figure 4.8**), it is possible to obtain:

$$\left[ \frac{\partial^2 \mathbf{U}(y, z)}{\partial y^2} + \frac{\partial^2 \mathbf{U}(y, z)}{\partial z^2} \right] = \frac{\Delta P}{\mu L_C} \quad \text{for} \quad -\frac{1}{2} W_C < y < \frac{1}{2} W_C, \quad 0 < z < H_C$$

$$\mathbf{U}(y, z) = 0 \quad \text{for} \quad y = \pm \frac{1}{2} W_C, \quad z = 0, \quad z = H_C$$

Where  $L_C$  is the length of the microchannel and  $\frac{\Delta P}{L_C}$  is the pressure gradient. [241]

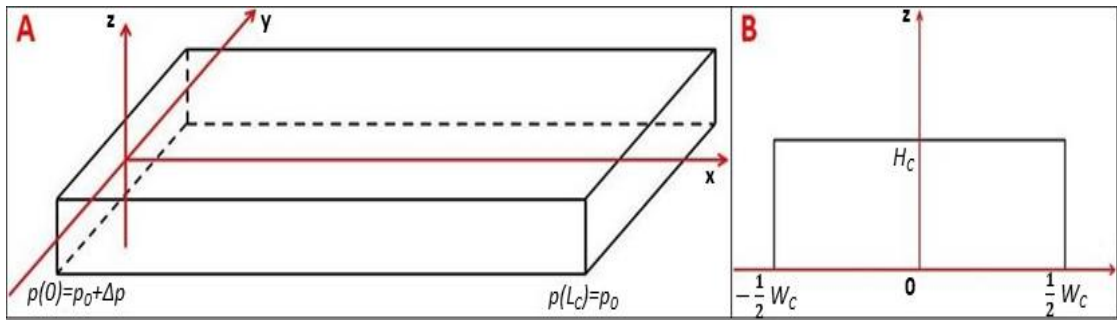


Figure 4.8 – (A) A schematic representation of a straight microchannel and (B) the definition of its rectangular cross-section of height  $H_c$  and width  $W_c$ . During the experiments, the flows were driven by pressure gradients externally imposed through the syringe pump, hence the pressure at the channel inlet was higher than the one at its outlet. Adapted from [241].

As demonstrated by Bruus [241], the above equations can be used to obtain the theoretical fully-developed velocity profile for a Newtonian fluid in a rectangular channel:

$$U(y, z) = \frac{48Q}{\pi^3 H_c W_c} \frac{\sum_{n, \text{odd}} \frac{1}{n^3} \cdot \left[ 1 - \frac{\cosh\left(n\pi \frac{y}{H_c}\right)}{\cosh\left(n\pi \frac{W_c}{2H_c}\right)} \right] \cdot \sin\left(n\pi \frac{z}{H_c}\right)}{\left[ 1 - \sum_{n, \text{odd}} \frac{192H_c}{n^5 \pi^5 W_c} \cdot \tanh\left(n\pi \frac{W_c}{2H_c}\right) \right]} \quad (\text{eq. 4.12})$$

In particular, the theoretical velocity profiles depicted in the **Figure 4.11** (p.150) have been computed employing the above equation.

### 4.8.1.2 The continuum model for dilute algal suspensions and the advection-diffusion equation

The advection-diffusion equation can be employed for modelling the main mechanisms that regulate the transport of dissolved components at the microscopic scale (*e.g.* nutrients, waste products, *etc.*) and for describing some biological phenomena (*e.g.* nutrients uptake by an osmotroph). [80]

A dilute incompressible suspension of gyrotactic microalgae within a flow field can be approximated as a continuum employing the conservation of mass, the conservation of momentum and the conservation of cells equations. The continuum model has been exploited for modelling algal bioconvection [2] and obtaining analytical predictions of transport properties of algal suspensions in channel and pipe flows at both laminar and turbulent conditions. [56, 167]

## 4.8.2 Algal behaviours in the straight channel

The experimental observations involving the straight channel were run under the hypothesis that the fluid dynamic experience of the cells could be compared to the ones that actually occur in real horizontal PBRs. Various “processing conditions” were simulated by pumping cell suspensions at different flow rates within the channel, in order to achieve more insight about the effect on the cells, particular attention was paid to their dispersion within the channel and their interactions with the walls. As shown in the **Table 4.3**, the algae exhibited five different behaviours, depending on the applied flow rate.

**Table 4.3 – The observed fluid dynamic behaviours of the algal cells in a straight channel, which was assumed to represent a horizontal PBR. The experimental conditions were calculated using the formulas described in the Section 3.3 (see also Figure 4.9).**

Experimental Conditions	Observed behaviour
$Q \leq 0.1 \mu\text{l}\cdot\text{min}^{-1}$ ; $\bar{U} \leq 4.06 \times 10^{-5} \text{ m}\cdot\text{s}^{-1}$ ; $Re \leq 5.91 \times 10^{-3}$ ; $\dot{\gamma}_W \leq 2.391 \text{ s}^{-1}$ .	The cells swam randomly within the channel (see <b>Section 4.6</b> ).
$0.1 \mu\text{l}\cdot\text{min}^{-1} < Q \leq 0.4 \mu\text{l}\cdot\text{min}^{-1}$ ; $4.06 \times 10^{-5} \text{ m}\cdot\text{s}^{-1} < \bar{U} \leq 1.63 \times 10^{-4} \text{ m}\cdot\text{s}^{-1}$ ; $5.91 \times 10^{-3} < Re \leq 2.36 \times 10^{-2}$ ; $2.391 \text{ s}^{-1} < \dot{\gamma}_W \leq 9.564 \text{ s}^{-1}$ .	The algae were able to swim upstream and interact consistently with the walls.
$0.4 \mu\text{l}\cdot\text{min}^{-1} < Q \leq 3.5 \mu\text{l}\cdot\text{min}^{-1}$ ; $1.63 \times 10^{-4} \text{ m}\cdot\text{s}^{-1} < \bar{U} \leq 1.42 \times 10^{-3} \text{ m}\cdot\text{s}^{-1}$ ; $2.36 \times 10^{-2} < Re \leq 2.07 \times 10^{-1}$ ; $9.564 \text{ s}^{-1} < \dot{\gamma}_W \leq 83.684 \text{ s}^{-1}$ .	The lower the experimental flow rate, the more the algae could overcome the fluid streamlines, disperse throughout the channel and the more they managed to interact with the walls, even adhering to them.
$3.5 \mu\text{l}\cdot\text{min}^{-1} < Q \leq 4 \mu\text{l}\cdot\text{min}^{-1}$ $1.42 \times 10^{-3} \text{ m}\cdot\text{s}^{-1} < \bar{U} \leq 1.63 \times 10^{-3} \text{ m}\cdot\text{s}^{-1}$ ; $2.07 \times 10^{-1} < Re \leq 2.36 \times 10^{-1}$ ; $83.684 \text{ s}^{-1} < \dot{\gamma}_W \leq 95.639 \text{ s}^{-1}$ .	The cells were not able to overcome the fluid streamlines anymore, however some instantaneous interactions with the channel walls were still observed.
$Q > 4 \mu\text{l}\cdot\text{min}^{-1}$ ; $\bar{U} > 1.63 \times 10^{-3} \text{ m}\cdot\text{s}^{-1}$ ; $Re > 2.36 \times 10^{-1}$ ; $\dot{\gamma}_W > 95.639 \text{ s}^{-1}$ ;	The algae were passively advected by the flow, hence they tended to follow the streamlines and could not interact with the channel walls.

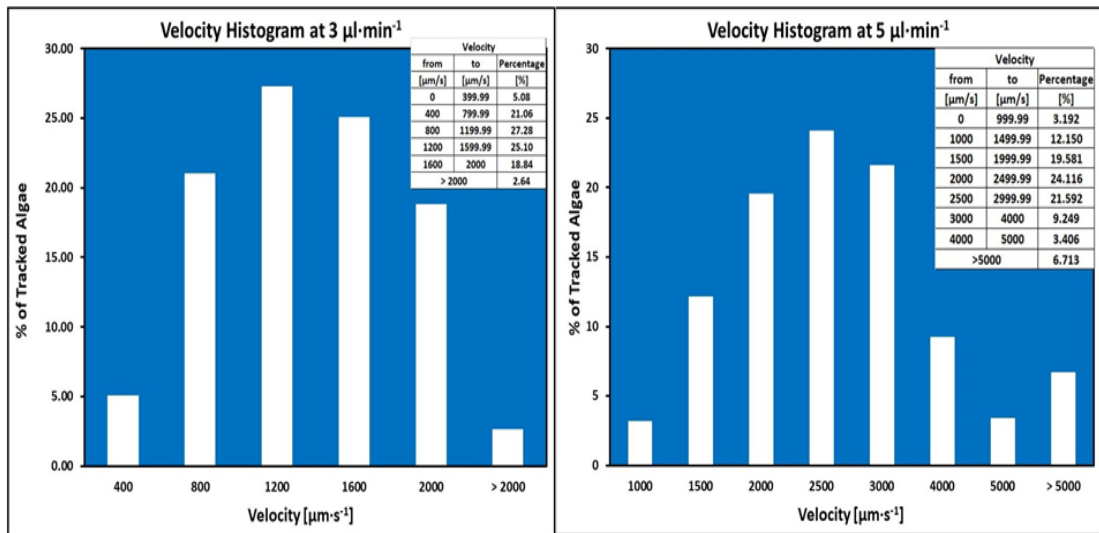


Figure 4.9 – The swimming velocity histograms of DS cells in the straight channel at 3  $\mu\text{l}\cdot\text{min}^{-1}$  and 5  $\mu\text{l}\cdot\text{min}^{-1}$ . These two flow rates have been analysed in detail since, from a practical point of view, they had proven to be the most interesting ones (see Section 4.8.2).

As explained in the 2<sup>nd</sup> Chapter, ideally a PBR should be run so as to inhibit the algal interactions with the walls to minimise biofouling, to achieve more homogeneous light paths, a reduction of the dark zones and more uniform algal concentrations. Nevertheless, the experiments involving the straight channel demonstrated that cell-wall interactions could only be impeded by increasing the flow rates and having the cells passively advected by the flow (see Table 4.3). This is similar to what happens in tubular PBRs, where the cultures are pumped turbulently (see Section 2.10).

Further experimental investigations were carried out employing some of the microfluidic geometries, which had been chosen as static mixers, in order to quantify their effects on the cells, to achieve more insight into their actual fluid dynamic experience, and to assess whether the PBR geometrical configuration can be exploited for reducing the overall energy requirements.

### 4.8.2.1 The most significant algal responses and the microgrid employed for the straight channel

The effects of the microfluidic geometries on DS cells were investigated at two flow rates (*i.e.*  $3 \mu\text{l}\cdot\text{min}^{-1}$  and  $5 \mu\text{l}\cdot\text{min}^{-1}$ ) (see **Figure 4.10**). At  $3 \mu\text{l}\cdot\text{min}^{-1}$  the algae showed a certain “degree of freedom” and they could still control their swimming trajectories since, despite swimming downstream, they were able to overcome the fluid streamlines, to interact with the walls and to swim in their proximity, but without adhering to them (these “partially-free” swimming conditions are usually avoided in tubular PBRs [10]).

Whereas, at  $5 \mu\text{l}\cdot\text{min}^{-1}$  the cells were passively advected by the flow throughout the whole geometry of the channel and therefore, although the walls interactions were negligible, even so using high flow rates was not able to prevent cells from being dragged close to the walls (see **Figure 4.10 B**) and this might imply potential shading effects. Moreover, as we shall see in the next chapter, algal suspensions always contain a certain percentage of dead cells which tend either to sediment or to be dragged by the flow, moving slower than the living algae, further contributing to affect the light distribution within PBRs.

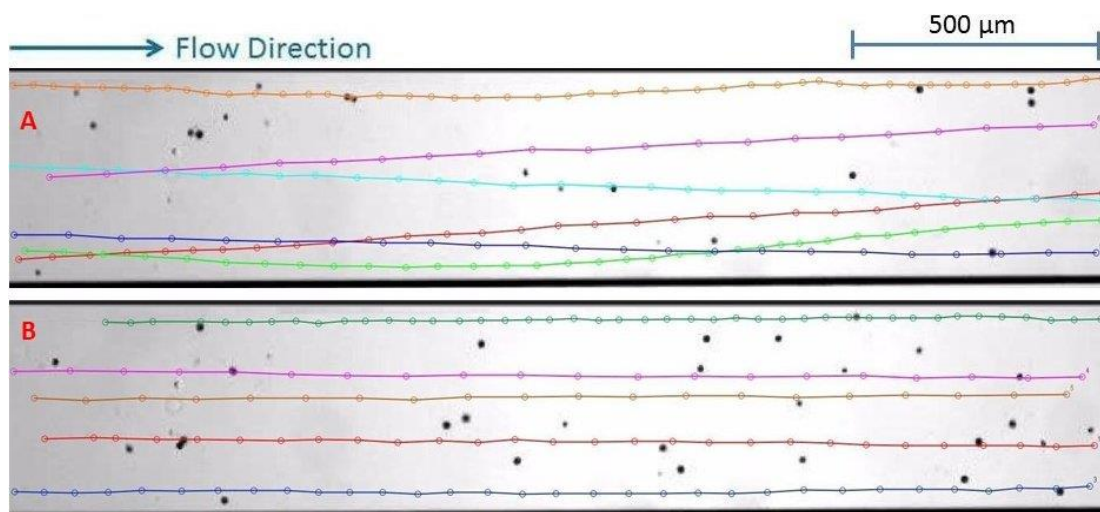


**Figure 4.10** – Manually-tracked swimming trajectories of some DS cells at  $3 \mu\text{l}\cdot\text{min}^{-1}$  (A) and  $5 \mu\text{l}\cdot\text{min}^{-1}$  (B). Particularly, at  $3 \mu\text{l}\cdot\text{min}^{-1}$ , the algae swam nearby the walls, dispersing along the channel and overcoming the fluid streamlines, while at  $5 \mu\text{l}\cdot\text{min}^{-1}$ , although the algal dispersion had been hampered, the cells were still advected in proximity of the channel walls, affecting the light path within the PBR (see the green and blue tracking lines in (B)). The swimming trajectories were obtained through an ImageJ plugin called MTrackJ.

These two flow rates were explored because, from a practical point of view, they had proven to be the most interesting ones. At flow rates lower than  $3 \mu\text{L}\cdot\text{min}^{-1}$ , the cells would interact consistently with the walls or even adhere to them; leading to conditions that are not practicable in tubular PBRs. At  $3 \mu\text{L}\cdot\text{min}^{-1}$ , an optimal compromise was achieved between the algal cell wall interaction and their capacity to controlling their swimming trajectories (*i.e.* the algae were not advected and showed negligible wall interactions); therefore the experimental observations at this flow rate were meant to provide a comprehensive analysis regarding the possibility of exploiting the combined effects of the microfluidic geometries and the “partially-free” swimming properties of the cells in practical applications. In fact, as addressed in the results sections, this may result in an enhancement of the processing conditions of PBRs, leading to a reduction of the biofouling and the overall energy required. On the other hand, the experiments at  $5 \mu\text{L}\cdot\text{min}^{-1}$  were meant to investigate in details the real processing conditions employed in PBRs, *i.e.* the passive advection of the cells.

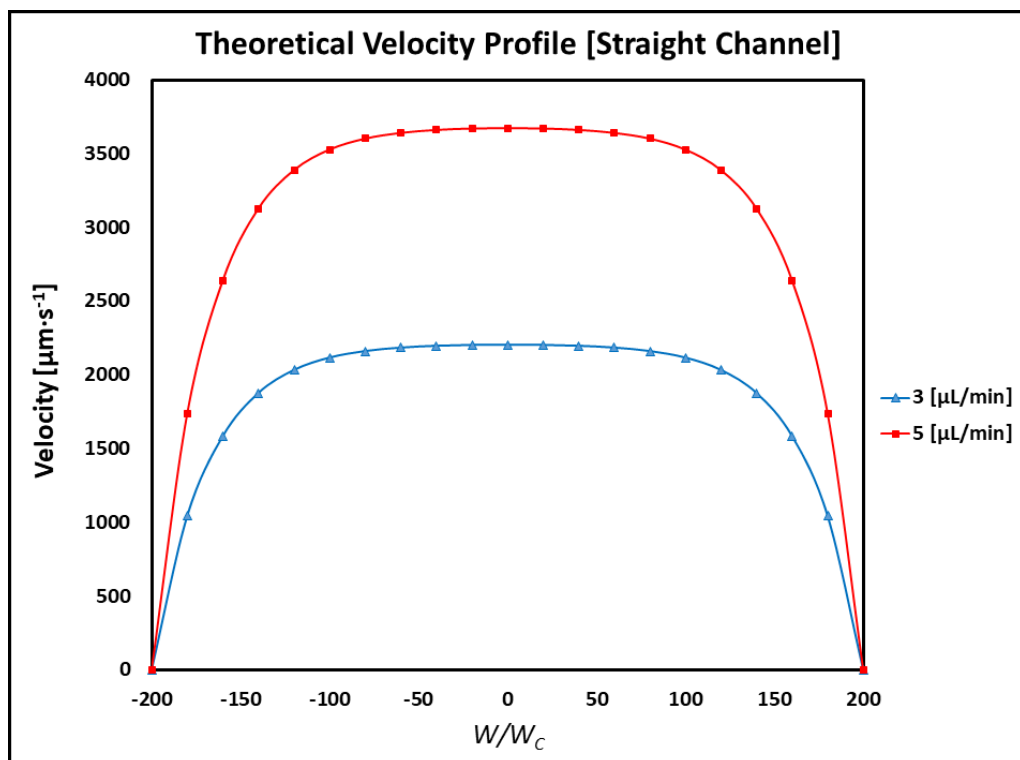


Figure 4.11 – The theoretical velocity profiles of the fully-developed laminar flows at  $3 \mu\text{L}\cdot\text{min}^{-1}$  and  $5 \mu\text{L}\cdot\text{min}^{-1}$ , computed at the centreline of the straight channel through eq. 4.12 (see Section 4.8.1.1).

The algal behaviours described above and the effects of the microfluidic geometries on them were quantified by acquiring some experimental videos at the desired fluid dynamic conditions, attaining from them the algal cells positions through ImageJ (see **Section 3.7**) and processing the data using various specifically-designed Matlab codes, which allowed useful information to be obtained directly from the microalgae, such as the cell swimming trajectories, the algal distribution percentages in various parts of the channels, the actual microalgal swimming velocities vectors spatial distributions, *etc.*

Precisely, knowing the algal positions, their swimming trajectories and swimming velocities were obtained by computing respectively the magnitudes of the position and the velocity vectors of all the cells that had been tracked during the image analyses process. In particular, the cells swimming trajectories, which represented the various parts of the channels where the algae were able to swim, were symbolised using green vectors, whereas the microalgal swimming velocity vectors spatial distributions represented their actual relative swimming velocities at the different conditions. Both the position and velocity vectors were depicted through Tecplot, utilising the various microgeometries images as backgrounds.

Moreover, the knowledge of the cell spatial positions allowed to be determined the algal cell distribution percentages (ACDPs) in the different zones of the channels, exploiting some “microgrids”, which had been obtained by dividing the channels into horizontal and vertical zones. In the case of the straight geometry, as shown in the **Figure 4.12**, the channel had been split into four horizontal zones (*i.e.* z1, z2, z3 and z4) and three vertical ones (*i.e.* A, B, C); the zones z2, z3 and z4 had a width of 120  $\mu\text{m}$  each, while the zone z1, which took into account the algae that had swum close to the walls, had been separated into two further 40- $\mu\text{m}$ -width parts (*i.e.* z1a and z1b), so that more algae could have been considered in the statistical analysis. The vertical zones were obtained dividing by three the total displayable length of the straight channel.

z1a			
z2			
z3	A [743 $\mu\text{m}$ ]	B [743 $\mu\text{m}$ ]	C [743 $\mu\text{m}$ ]
z4			
z1b			

Figure 4.12 – The microgrid that was used to quantify the algal behaviours within the straight geometry. Particular emphasis was given to the z1a and z1b zones, which were utilised to quantify cell-wall interactions and zone z3, where the centreline lies.

In particular, ACDPs were calculated employing a tailored Matlab code which, starting from the algal positions, analysed independently each of the defined vertical zones of the microgrid, pinpointing all the DS cells that had swum through them and calculating their distribution percentages along their corresponding horizontal zones; thus, for a given zone of the channel, the higher the number of cells that swam along it was, the higher its corresponding distribution percentage would be.

As we shall see in the last part of this chapter and in the next ones, the analysis of the results provided crucial information regarding the algal fluid dynamic behaviours under the experimental conditions investigated. In particular, the algal swimming trajectories and their dispersion percentages were exploited for quantifying the cellular dispersion within the channels and their interactions with the walls. Different microfluidic geometries were compared and potential benefits for the PBRs processing conditions were inferred, while the velocity vector spatial distributions permitted the investigation of the microgeometry-induced inertial effects on the cells.

### 4.8.3 Quantification of dispersion and walls interactions of *Dunaliella* cells within a straight channel

In this section, the algal cells dispersion within the straight channel and their interactions with the walls are quantified employing their swimming trajectories, the dispersion percentages and the velocity vector spatial distributions of the DS cells. As previously discussed, at the two flow rates investigated, the experiments involving the straight microchannel indicated that the algal cells were able to occupy the whole geometry of the channel, despite showing two different fluid dynamic behaviours (see **Figure 4.10**).

In fact, at  $3 \mu\text{l}\cdot\text{min}^{-1}$ , the algae were able to overcome the fluid streamlines, disperse along the channel and swim close to the boundaries. This explained the relatively high dispersion percentages close to the walls (*i.e.* in the zones z1a and z1b) and the swimming trajectories that covered the whole channel geometry (see **Figure 4.13**).

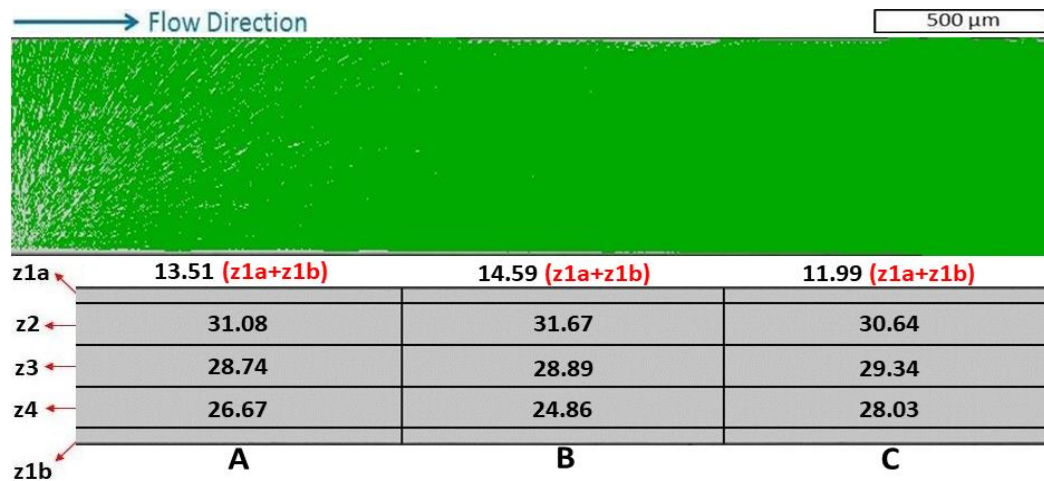


**Figure 4.13** – The swimming trajectories and the dispersion percentages of DS cells in a straight channel at  $3 \mu\text{l}\cdot\text{min}^{-1}$ . At these conditions  $\bar{U}$  was  $1.22 \times 10^{-3} \text{ m}\cdot\text{s}^{-1}$ ,  $Re$   $1.77 \times 10^{-1}$  and  $\dot{\gamma}_W$   $71.729 \text{ s}^{-1}$ , these values have been calculated based on the geometrical characteristics and the formulas described in the Section 3.3. The experimental videos were captured using a resolution of  $688 \times 516$  pixels, the 4X objective and an exposure time of  $\sim 1 \text{ ms}$  (see Section 3.6.1).

At a flow rate of  $5 \mu\text{l}\cdot\text{min}^{-1}$ , the algae were advected by the flow along the whole geometry of the channel, even close its boundaries, meaning that operating with higher flow rates does not prevent the cells from being dragged close to the walls (see **Figure 4.10 B**). Although two different observed algal responses were observed, similar swimming trajectories were obtained in both cases (see **Figure 4.13** and **4.14**).

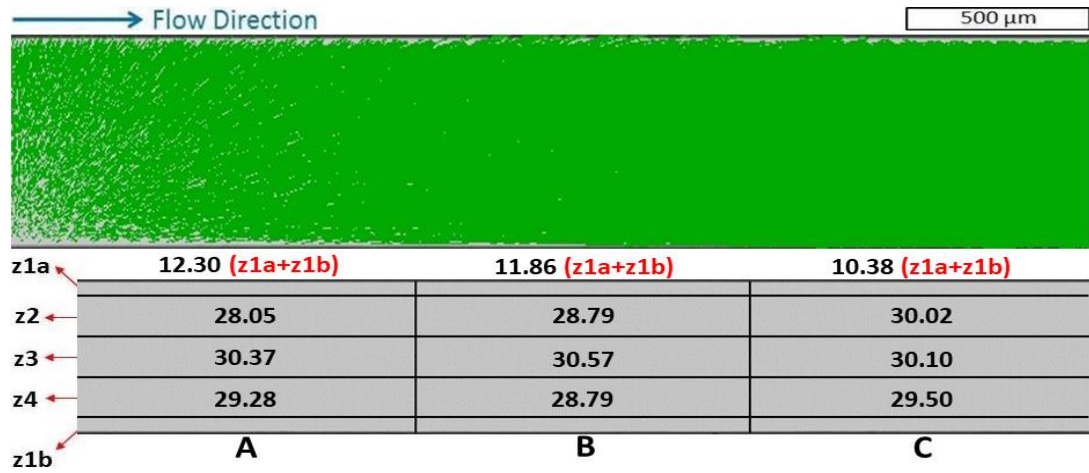


Figure 4.14 – The swimming trajectories and the dispersion percentages of the DS cells in the straight channel at  $5 \mu\text{l}\cdot\text{min}^{-1}$ . At these conditions  $\bar{U}$  was  $2.03 \times 10^{-3} \text{ m}\cdot\text{s}^{-1}$ ,  $Re$   $2.95 \times 10^{-1}$  and  $\dot{\gamma}_W$   $119.548 \text{ s}^{-1}$ , these values have been calculated using the geometrical characteristics and the formulas described in the Section 3.3. The experimental videos were captured using a resolution of  $688 \times 516$  pixels, the 4X objective and an exposure time of  $\sim 1 \text{ ms}$  (see Section 3.6.1).

More information can be inferred by considering the arithmetic mean values of the algal cells dispersion percentages ( $\overline{ACDPs}$ ) calculated for the various horizontal zones. For a given horizontal zone  $z_i$ , the relative  $\overline{ACDPs}$  was obtained as:

$$\left(\overline{ACDP}\right)_{z_i} = \frac{1}{3} \cdot (ACDP_A + ACDP_B + ACDP_C)_{z_i} \quad (\text{eq. 4.13})$$

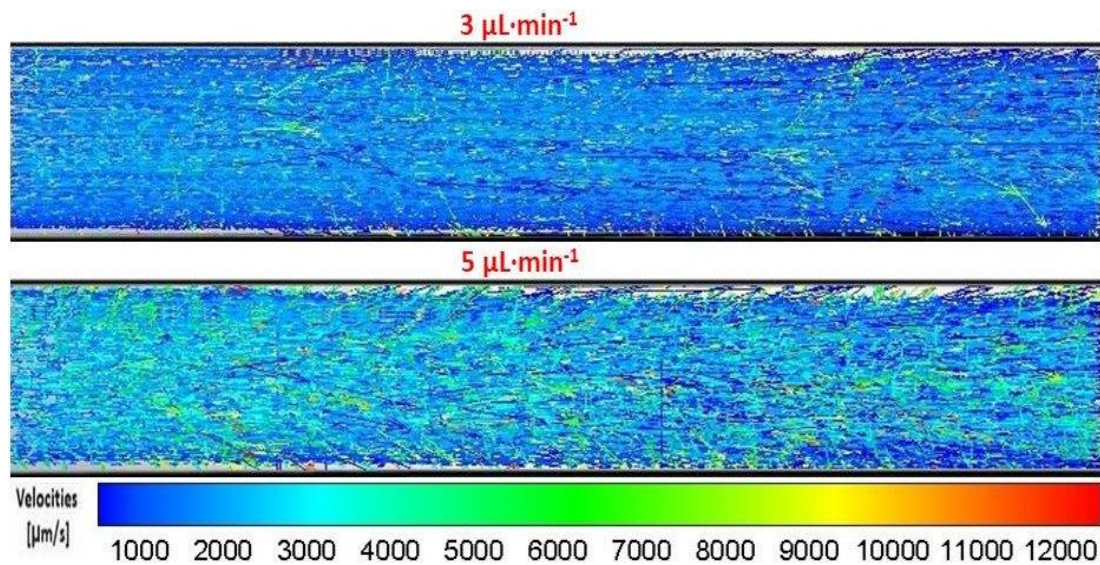
where the subscripts A, B and C are referred to the vertical zones (see Figure 4.12).

Table 4.4 –  $\overline{ACDPs}$  and their related error bars (See eq. 6.9) for the various horizontal zones.

Horizontal Zones	The algal cells drifted along the fluid streamlines $[3 \mu\text{l}\cdot\text{min}^{-1}]$	Passive advection $[5 \mu\text{l}\cdot\text{min}^{-1}]$
z1a+z1b	$13.36 \pm 0.75$	$11.51 \pm 0.58$
z2	$31.13 \pm 0.30$	$28.95 \pm 0.57$
z3	$28.99 \pm 0.18$	$30.35 \pm 0.14$
z4	$26.52 \pm 0.92$	$29.19 \pm 0.21$

The fact that at  $3 \mu\text{l}\cdot\text{min}^{-1}$  the algae were able to partially control their swimming trajectories and overcome the fluid streamlines resulted in asymmetric average dispersion percentages, compared to the ones of the passively-dragged cells at  $5 \mu\text{l}\cdot\text{min}^{-1}$  (see the  $\overline{ACDPs}$  in the z2 and z4 zones for the two flow rates, in the Table 4.4).

The dispersion percentages at the boundaries were comparable, meaning that, in the two cases investigated, the numbers of algal cells that swam in the proximity of the channel walls were alike, albeit at  $5 \mu\text{L}\cdot\text{min}^{-1}$ , the cells were faster and consequently their interaction with the walls were characterised by shorter average residence time values (see **Figure 4.15**).



**Figure 4.15** – The swimming velocity vectors spatial distribution in the straight channel at  $3 \mu\text{L}\cdot\text{min}^{-1}$  and  $5 \mu\text{L}\cdot\text{min}^{-1}$ . In the latter case, which was assumed to represent the processing conditions employed in real PBRs, the cells were faster and passively advected, hence their interaction with the walls were negligible.

Hypothetically, if a real photobioreactor was to be run using processing conditions that lead to the algal behaviour observed at  $3 \mu\text{L}\cdot\text{min}^{-1}$ , although the cells may not adhere to the boundaries, their wall interactions could compromise the light path and therefore these cultivation conditions are not utilised in practical applications. In fact, in real cultivation facilities, biofouling phenomena are prevented at the expense of passively advecting the microalgae (as observed at  $5 \mu\text{L}\cdot\text{min}^{-1}$ ), stressing or damaging them and utilising energetically-costly solutions (see **Sections 2.9** and **2.10**). As our experiments involving the straight geometry have demonstrated, employing high flow rates can hamper the cell-boundary interactions and their accumulations nearby to solid surfaces, but is not able to prevent the cells from being dragged close to the walls (see **Figure 4.10 B**); leading to potential shading effects, particularly when the concentration of the cultured organisms increases within the cultivation device.

Consequently, further experimental investigations were carried out employing the ECR 4-1, ECR 7-1 and elongated geometries, which had been assumed to function as static mixers, in order to quantify their effects on the cell dispersion and their interactions with the walls, to compare them to those measured in the straight geometries and assess whether better processing conditions could be achieved by modifying the PBR geometrical configuration, ideally taking into account and exploiting the swimming properties of the cells.

## **4.9 *Dunaliella* cells and static mixers**

To provide a context for the study of microgeometries, the first part of this section discusses the effects of abrupt contraction and expansion geometries on different fluids. This provides also an analysis of the fluid dynamic behaviour of a fluid moving through a channel with an abrupt contraction. In the second part of the section, the results of the experimental investigations concerning the contraction-expansion channels and living algal cells are presented and discussed.

### **4.9.1 General effects of contraction and expansion geometries on flows of different fluids**

The flow of Newtonian and non-Newtonian fluids in channels with variable cross-sections, including contractions and expansions, represents a benchmark fluid mechanics problem that has been investigated in a number of experimental and numerical studies, due to its importance in practical applications, *e.g.* in the polymer processing industry, inkjet printing, fertilizer spraying, *etc.* [207, 242]

For example, Sousa *et al.* investigated numerically and experimentally laminar flows of three fluids through a square cross-section channel, employing a wide range of flow rates ( $Re < 20$ ), studying various abrupt expansion geometries with different expansion ratios (ER) (*i.e.* ER = 2.4, 4, 8 and 12) and focusing on the resulting flow patterns. They considered a Newtonian fluid, and two non-Newtonian fluids, *i.e.* a Boger fluid (for which the viscosity is nearly independent of the shear rate) and a shear-thinning viscoelastic fluid.

In particular, regardless of the ER used, a corner vortex was observed downstream of the expansion; in the case of a Newtonian fluid, the vortex size increased monotonically when the flow inertia rose, whereas for the non-Newtonian fluids, the vortex decreased in size and strength when the elasticity of the flow was increased. [243] There are also several research works that report the development of asymmetric flows in planar expansions for Newtonian and non-Newtonian fluids; a detailed review of them can be found in Sousa's and co-workers' paper: [243].

Fluid flows through sudden contractions have received broader attention than flows through abrupt expansions, possibly due to the interesting nature of the flow patterns occurring, in particular with viscoelastic fluids (*i.e.* vortex enhancement, divergent and unsteady flows). [243] For instance, Sousa *et al.* explored numerically and experimentally the laminar flows of both a Newtonian fluid and a shear-thinning viscoelastic fluid through square cross-section channels with different contraction ratios (CR) (*i.e.* CR = 2.4, 4, 8 and 12), assessing the influence of the CRs upon the flow patterns and the velocity fields at various flow rates ( $Re < 20$ ). The Newtonian fluid was seen to behave similarly under all the experimental conditions, exhibiting a concave-shaped corner vortex, located upstream of the contraction and the size of which decreased when the flow inertia increased. Regarding the viscoelastic fluid, at low flow rates (*i.e.* when both inertial and elastic effects could be neglected), a Newtonian behaviour was seen whereas, increasing the elasticity or the flow rate, three different flow regimes were observed, the vortex growth regime (the vortex became bigger when the elasticity increased), the onset of diverging streamlines upstream of the contraction plane, mainly observed at the lower contraction ratios, and an elasticity instability where the size of the recirculations had been varying in time in a complex way. [244]

In the next section, the fluid dynamic behaviour of developing flows within a sudden contraction is analysed further, introducing some key concepts such as the vena contracta and the entrance length. The flow patterns induced by the chosen microgeometries at the chosen experimental conditions will also be shown.

## 4.9.2 Fluid dynamic effects induced by an abrupt contraction on a laminar flow

The development of the velocity profiles of Newtonian and non-Newtonian fluids, while entering a pipe or flowing through a channel with an abrupt contraction, and the effects of the re-entrant corners on their flow patterns is one of the most widely-studied hydrodynamic problem, since such flows are encountered in almost every industrial processes (*e.g.* a fluid flowing from a reservoir into a pipe). [245, 246]

In the specific case of microfluidic devices, fluid flows are prevalently laminar and, commonly the lower the  $Re$  number, the shorter the entrance length will be (*i.e.* the distance required by a given flow to develop hydrodynamically) [246]; nevertheless, in some of their applications, microchannels may be characterised by short lengths, which could not be sufficient to give rise to fully-developed flows. [247] Hence, understanding the physical behaviour of a given fluid while it is flowing in laminar regime within the entrance region of a channel is vitally important and will be addressed in this section, which describes a fluid dynamical similar case concerning a fluid moving laminarily in a channel equipped with a sudden contraction.

Mathematically, isothermal and laminar Newtonian fluids flowing through channels with sudden cross-sectional reductions are modelled employing the conservation of mass and the Navier-Stokes equations, along with the no-slip boundary conditions, and are nonlinear problems since the advection term  $\mathbf{U} \cdot \nabla \mathbf{U}$  cannot usually be neglected, making it difficult to obtain exact solutions. [61]

Physically, when a given Newtonian fluid is flowing laminarily within a channel and encounters an abrupt contraction, regardless of its cross sectional geometry, it will require a certain distance to adjust from the upstream conditions to the fully-developed pattern, *i.e.* the hydrodynamic entrance length  $L_{EN}$  that is defined as the length of the channel between the contraction inlet and the axial position at which the centreline flow velocity reaches the 99% of its fully-developed value. [245]

In particular, as shown in **Figure 4.16**, on approaching the entrance region of the contraction the flow tends to accelerate, and the inlet corners cause a disturbance on the flow field, forcing the streamlines to contract, affecting the flow pattern and producing a vena contracta (VC) that leads to flow separation effects; VC represents the point where the effective flow cross sectional area reaches a minimum and the fluid velocity reaches its maximum. [246] The VC size depends on the flow *Re* number, the higher the *Re* number, the more extended the VC will be. This may have a big impact on flows within channels characterised by high aspect ratios, due to the proximity of the channel walls to each other. [246]

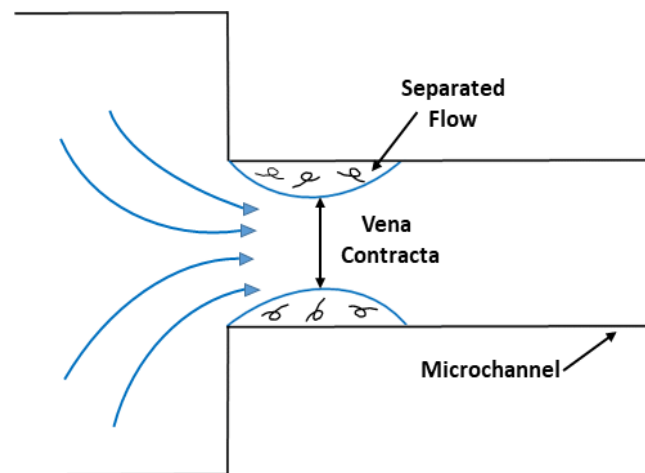


**Figure 4.16** – A schematic of the theoretical flow pattern that is found in the entrance region of a contraction due to its corners, showing both the vena contracta and the flow separation regions; vena contracta formations can also occur in fluids flowing from a tank into a pipe or in case of a stream issuing out of a nozzle (orifice). [246] Adapted from [246].

After flowing through the vena contracta region, the flow will diverge reoccupying the whole cross sectional area of the now constricted channel. Due to the no slip conditions, the velocity of the fluid particles in contact with the channel walls is immediately reduced to zero, decelerating the motion of adjacent fluid layers and creating a boundary layer that propagates from the walls towards the centre of the channel (see **Figure 4.17**). [246, 248]

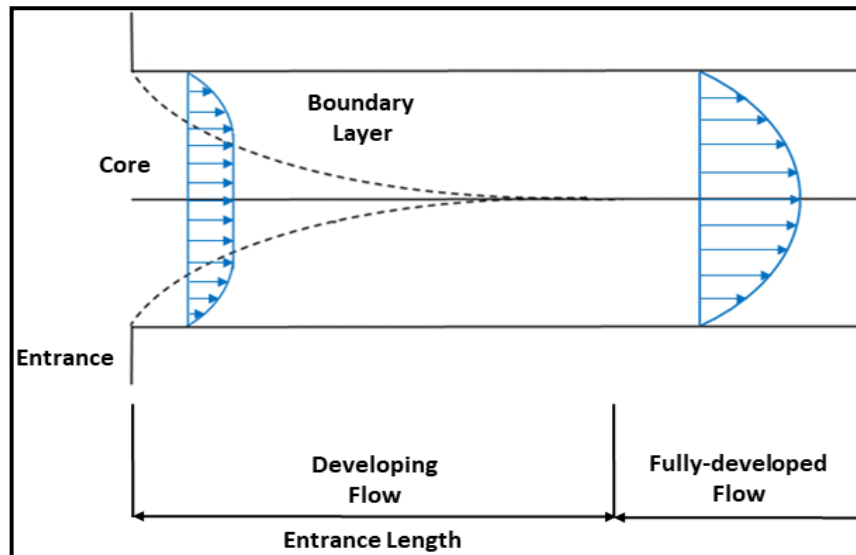


Figure 4.17 – The wall shear stress is higher at the contraction inlet, where the boundary layer thickness is the smallest and decreases along the flow direction. [207, 242] Various empirical equations for estimating the laminar hydrodynamic development length in microchannels with various cross-sectional geometries have been proposed, which are valid for certain ranges of channel aspect ratios, hydraulic diameters and  $Re$  numbers. [246, 247] Adapted from [61].

In particular, as the fluid moves along the axial position, its velocity decreases within the boundary layer and increases in the core so as to satisfy continuity; in fact, the derivative  $\frac{\partial u}{\partial x} \neq 0$  and therefore the continuity equation  $\frac{\partial u}{\partial x} + \frac{\partial v}{\partial y} = 0$  requires that  $v \neq 0$ , ergo the flow is not parallel to the walls, within the entrance zone. [61, 246] This process will continue until the entire flow field adjusts to the no-slip boundary conditions at the channel walls, becoming fully developed. [246] In the same way, after leaving the contraction, the fluid velocity profile also undergoes rearrangements becoming fully-developed again after an exit length  $L_{EX}$ ; for common pipes, at low  $Re$ ,  $L_{EX}$  is about one pipe radius while, at  $Re > 100$ ,  $L_{EX}$  is essentially zero. [248]

However, despite the effects described above and in the **Section 4.9.1**, the flow rates employed during our experimental investigations were relatively low, therefore no vortices were observed either upstream or downstream the microgeometries, which mainly distorted the streamlines, leading to an increase of both inertial effects and shear stress values (see **Figure 4.18**). [207, 242] Nonetheless, as we shall see in the **6<sup>th</sup> Chapter**, local shear increases may be dangerous for the cultured organisms and must be taken into account when designing and operating static mixers.

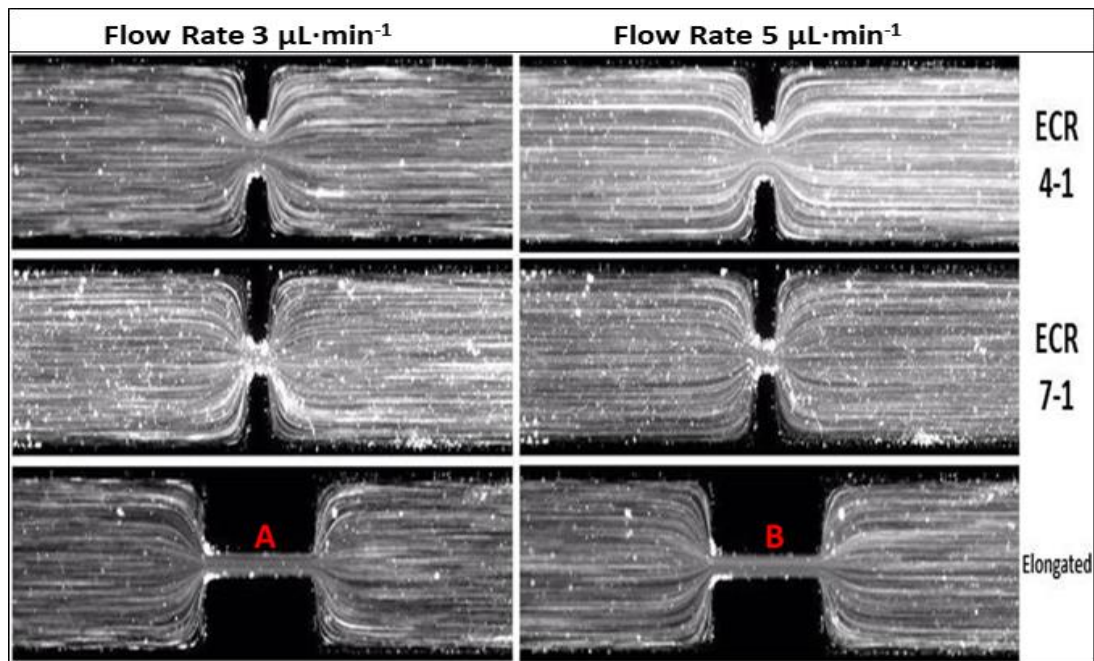


Figure 4.18 – The flow patterns induced at a flow rate of  $3 \mu\text{L}\cdot\text{min}^{-1}$  (A) and  $5 \mu\text{L}\cdot\text{min}^{-1}$  (B) by the microgeometries utilised for the experimental investigations. The flow streamlines were visualised by adding some Fluospheres® tracer particles [nile red, (Ex 535 nm/ Em 575 nm), nominal bead diameter  $1.0 \mu\text{m}$ ] to the culture medium. The images were acquired using fluorescence in the inverted microscope, the 4X objective and a dichroic filter (U-MWIGA3 Olympus) with excitation and emission bands of 530 – 550 and 575 – 625 nm, respectively. The metal halide lamp (Lumen 200, PRIOR) was used to excite the particles; the exposure time ranged between 20 to 40 ms, depending on the considered geometry and flow rate.

### 4.9.3 Qualitative effects of the contraction-expansion geometries on the algal behaviours

In the final part of this chapter, the results obtained during the experiments involving the living algae and the contraction-expansion geometries (CEGs) are discussed. The main objective of the experimental observations was to achieve more insight about how the algal behaviours were affected by the microgeometries, assumed to simulate inline static mixers. For comparison purposes, the same flow rates used previously were investigated to assess whether better processing conditions can be achieved by optimising the PBRs geometrical configuration and, ideally, exploiting the algal swimming characteristics. The results discussed in this section were obtained studying the cells at the population level and disregarding their fluid dynamic experiences within the microgeometries or, in other words, the results depict the entrance and exit effects of the CEGs, without considering what actual happened to the cells within the different contractions.

However, more details about the algal cells behaviours in crucial parts of the microchannels (*i.e.* the centreline and the contraction geometries) will be provided in the **6<sup>th</sup> Chapter**.

The effects of the CEGs on the algal cells were observed to be qualitatively similar for all the microgeometries investigated. Away from the CEGs, the flow was fully-developed therefore, the algal behaviours resembled the ones described in the straight channel (see **Section 4.8.2** and **Figure 4.10**).

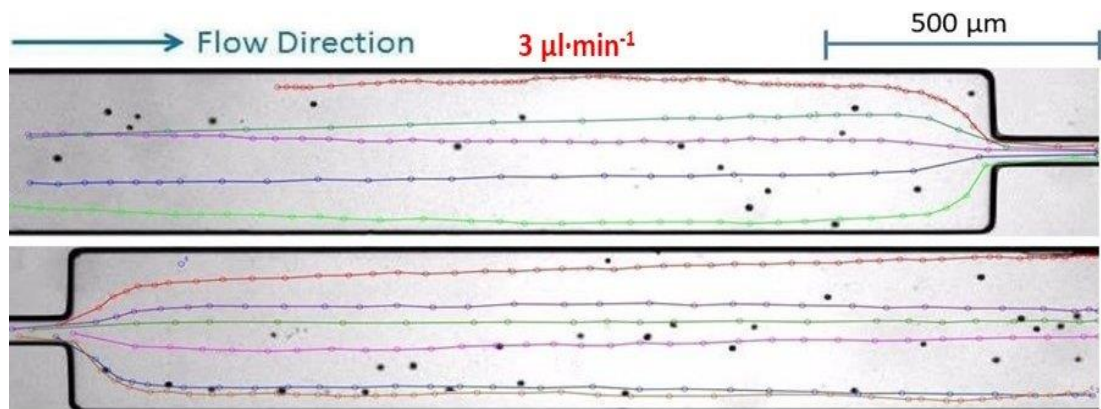


Figure 4.19 – Qualitative effects of the elongated geometry on algal cells at  $3 \mu\text{l}\cdot\text{min}^{-1}$ . Far away from the contraction, the cells were still able to interact with the walls and drift across the fluid streamlines while both the entrance and exit effects of the microgeometries led to algal patterns and plumes which may be beneficial for PBRs. This figure was obtained by employing an ImageJ plugin called MTrackJ.

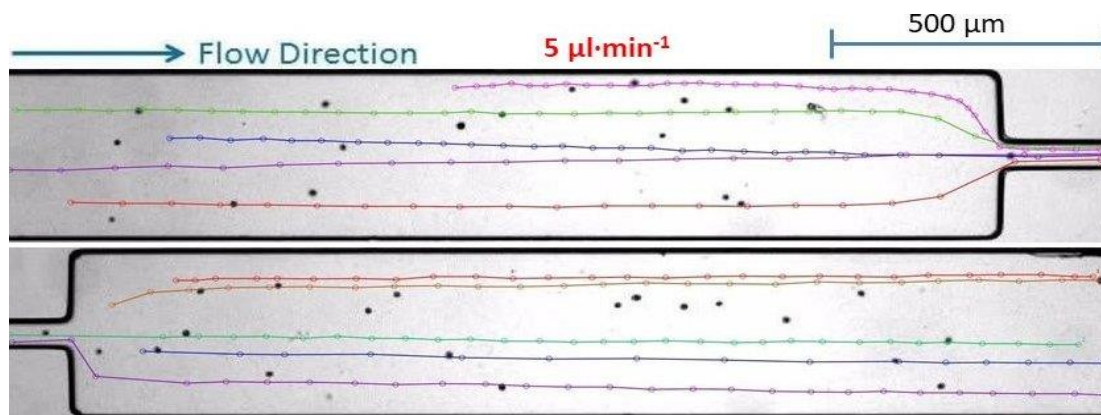
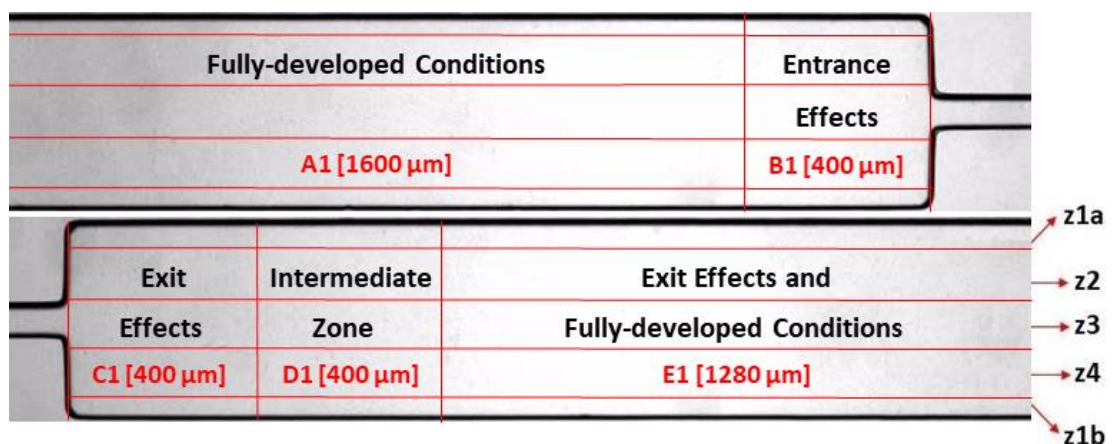


Figure 4.20 – Qualitative effects of the elongated geometry on algal cells at  $5 \mu\text{l}\cdot\text{min}^{-1}$ . Far away from the contraction, the cells were passively advected by the flow throughout the whole geometry of the channel, leading to high algal dispersion values; nevertheless, the entrance and exit effects of the CEG and the resulting algal plume helped to reduce the algal biofouling and to prevent the cells from being dragged close to the walls. This figure was obtained by employing an ImageJ plugin called MTrackJ.

The closer the algae approached the contraction entrance (*i.e.* the more the fluid streamlines were distorted and both the inertial effects and the shear stress increased), the more the CEG tended to draw the cells over, reducing their wall interactions and inhibiting their dispersion along the channel; however, these “algal entrance effects” were only significant in the proximity of the contraction (*i.e.* in a limited portion of the channel) (see **Figure 4.19** and **4.20**).

At the exit of the microgeometry, an algal plume was developed which compacted the flow of the cells along the channel and reduced their wall interactions; these effects were quantified through the swimming trajectories and the algal dispersion percentages, calculated employing a microgrid similar to the one utilised for the straight channel.

The results discussed in this section and in the **5<sup>th</sup> Chapter** demonstrate that the exploitation of static mixers in PBRs would also allow the incident solar light to penetrate deeper into the reactor, leading to more homogeneous light intensity distributions and improving the cultivation conditions (see **Section 5.7**). [118]



**Figure 4.21** – The microgrid that was used for studying how the geometrical configurations of the channels could influence the cell dispersion and their interactions with the walls and how they could lead to the potential benefits for the PBRs. The different vertical zones A1, B1, C1, D1 and E1 permitted to analyse different crucial parts of the channel and compare the employed microgeometries.

The microgrid employed for studying the contraction-expansion channels was formed by the same horizontal zones previously-described for the straight geometry (*i.e.* z1, z2, z3 and z4) (see **Section 4.8.2**) and by five vertical zones (*i.e.* A1, B1, C1, D1 and E1) (see **Figure 4.21**). Zone A1 was selected to analyse the effects of the fully-developed flow conditions, zones B1 and C1 took into account respectively the entrance and exit effects owing to the contractions, zone D1 can be thought as an intermediate zone between the end of the contraction and the fully-developed flow and zone E1 served to analyse the combined effects of the algal plumes and the fully-developed flow conditions.

In the next section, the microgrid was used for exploring the algal fluid dynamic experiences in crucial parts of the channels, attain experimental data directly from the cells and assessing potential benefits for PBRs.

#### 4.9.4 Quantification of the effects due to microgeometries on living algal cells

The experiments involving microgeometries were carried out using the procedures and conditions previously described (see **Sections 3.5, 3.6 and tables 4.5 and 4.6**), the experimental videos were analysed using the image analysis process and tailored Matlab codes (see **Section 3.7**).

The main experimental conditions are summarised in the **Tables 4.5 and 4.6**.

**Table 4.5 – The main experimental conditions for the experiments at 3  $\mu\text{l}\cdot\text{min}^{-1}$ .**

Geometry	Flow rate	Straight Region		Contraction Geometry		Red Filter	Lights
		Mean Fluid Velocity	<i>Re</i>	Mean Fluid Velocity	<i>Re</i>		
	[ $\mu\text{l}\cdot\text{min}^{-1}$ ]	[ $\text{m}\cdot\text{s}^{-1}$ ]		[ $\text{m}\cdot\text{s}^{-1}$ ]			
ECR 4-1	3.00	$1.22 \times 10^{-3}$	$1.78 \times 10^{-1}$	$4.38 \times 10^{-3}$	$4.17 \times 10^{-1}$	On	Off
ECR 7-1	3.00	$1.23 \times 10^{-3}$	$1.78 \times 10^{-1}$	$8.62 \times 10^{-3}$	$5.63 \times 10^{-1}$	On	Off
Elongated	3.00	$1.23 \times 10^{-3}$	$1.78 \times 10^{-1}$	$8.64 \times 10^{-3}$	$5.63 \times 10^{-1}$	On	Off

**Table 4.6 – The main experimental conditions for the experiments at 5  $\mu\text{l}\cdot\text{min}^{-1}$ .**

Geometry	Flow Rate	Straight Region		Contraction Geometry		Red Filter	Lights
		Mean Fluid Velocity	<i>Re</i>	Mean Fluid Velocity	<i>Re</i>		
	[ $\mu\text{l}\cdot\text{min}^{-1}$ ]	[ $\text{m}\cdot\text{s}^{-1}$ ]		[ $\text{m}\cdot\text{s}^{-1}$ ]			
ECR 4-1	5.00	$2.04 \times 10^{-3}$	$2.96 \times 10^{-1}$	$7.29 \times 10^{-3}$	$6.95 \times 10^{-1}$	On	Off
ECR 7-1	5.00	$2.04 \times 10^{-3}$	$2.96 \times 10^{-1}$	$1.44 \times 10^{-2}$	$9.38 \times 10^{-1}$	On	Off
Elongated	5.00	$2.05 \times 10^{-3}$	$2.97 \times 10^{-1}$	$1.44 \times 10^{-2}$	$9.39 \times 10^{-1}$	On	Off

Using the approach used for the straight geometry (see **Section 4.8.3**), the main effects of three contraction-expansion geometries (CEGs) on the microalgae were explored giving particular emphasis to cells dispersion along the channel, their interactions with the walls, which were quantified employing the algal swimming trajectories and the dispersion percentages of the cells, obtained through the microgrid (see **Section 4.9.3**).

**ECR 4-1 – LIVE Cells –  $3 \mu\text{l}\cdot\text{min}^{-1}$**

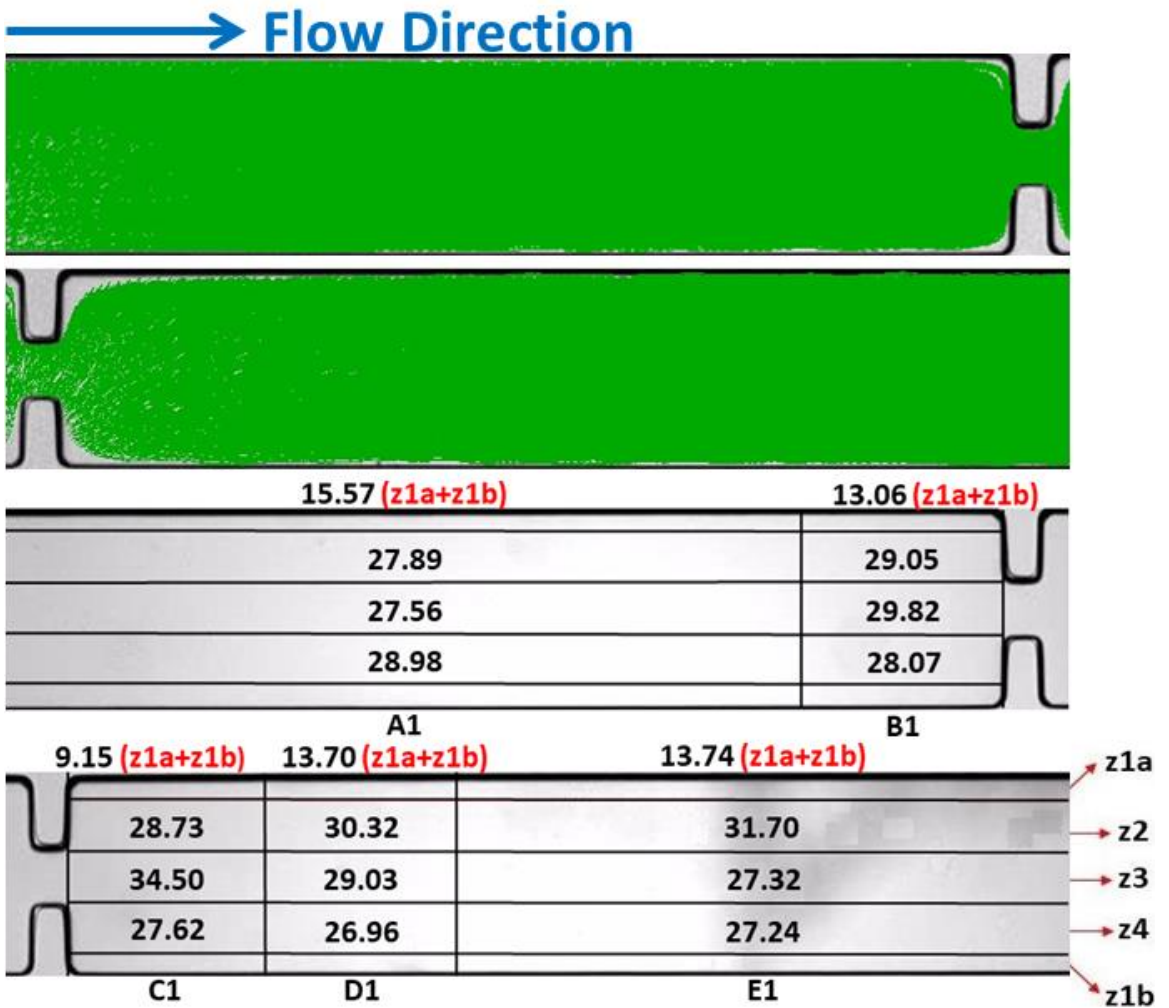


Figure 4.22 – Algal swimming trajectories and dispersion percentages in the ECR 4-1 geometry at  $3 \mu\text{l}\cdot\text{min}^{-1}$ . The experimental videos were captured using a resolution of  $688 \times 516$  pixels, the 4X objective and an exposure time of  $\sim 1$  ms (see Section 3.6.1). For statistical reasons, all the results were obtained by analysing at least three experimental videos.

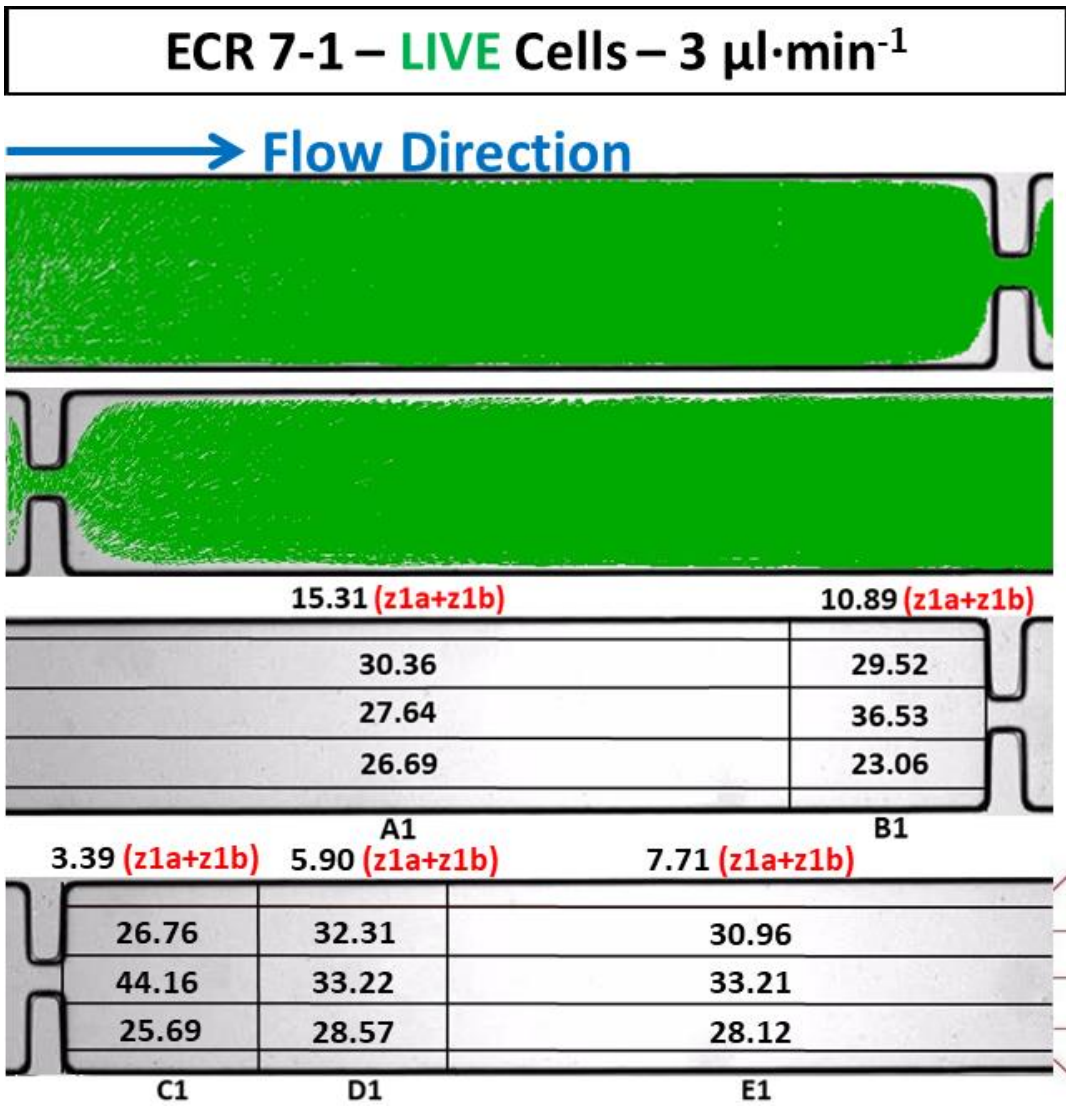


Figure 4.23 – Algal swimming trajectories and dispersion percentages in the ECR 7-1 geometry at  $3 \mu\text{l}\cdot\text{min}^{-1}$ . The experimental videos were captured using a resolution of  $688 \times 516$  pixels, the 4X objective and an exposure time of  $< 1$  ms (see Section 3.6.1). For statistical reasons, all the results were obtained by analysing at least three experimental videos.

**Elongated – LIVE Cells –  $3 \mu\text{l}\cdot\text{min}^{-1}$**

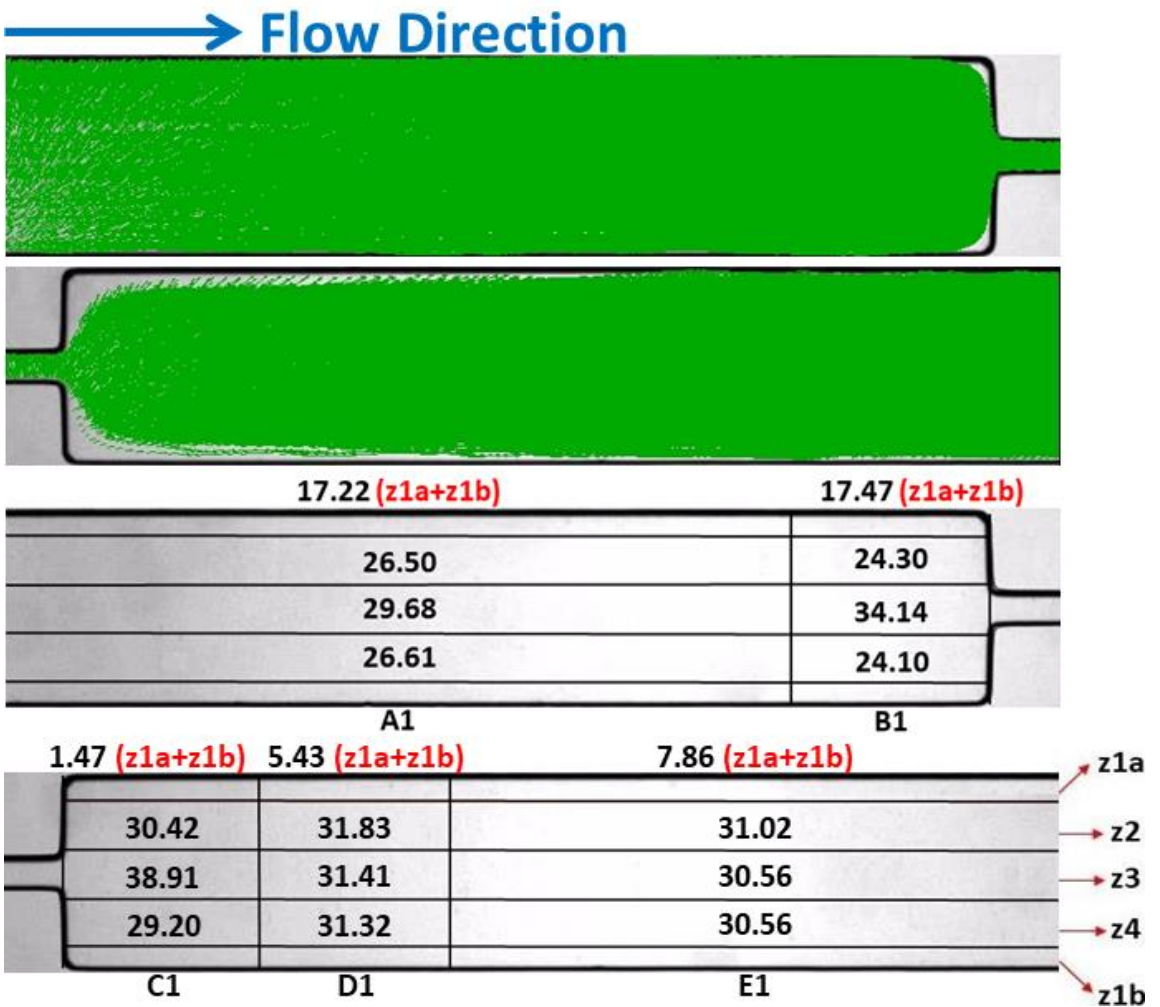


Figure 4.24 – Algal swimming trajectories and dispersion percentages in the elongated geometry at  $3 \mu\text{l}\cdot\text{min}^{-1}$ . The experimental videos were captured using a resolution of  $688 \times 516$  pixels, the 4X objective and an exposure time of  $< 1$  ms (see Section 3.6.1). For statistical reasons, all the results were obtained by analysing at least three experimental videos.

**ECR 4-1 – LIVE Cells –  $5 \mu\text{l}\cdot\text{min}^{-1}$**

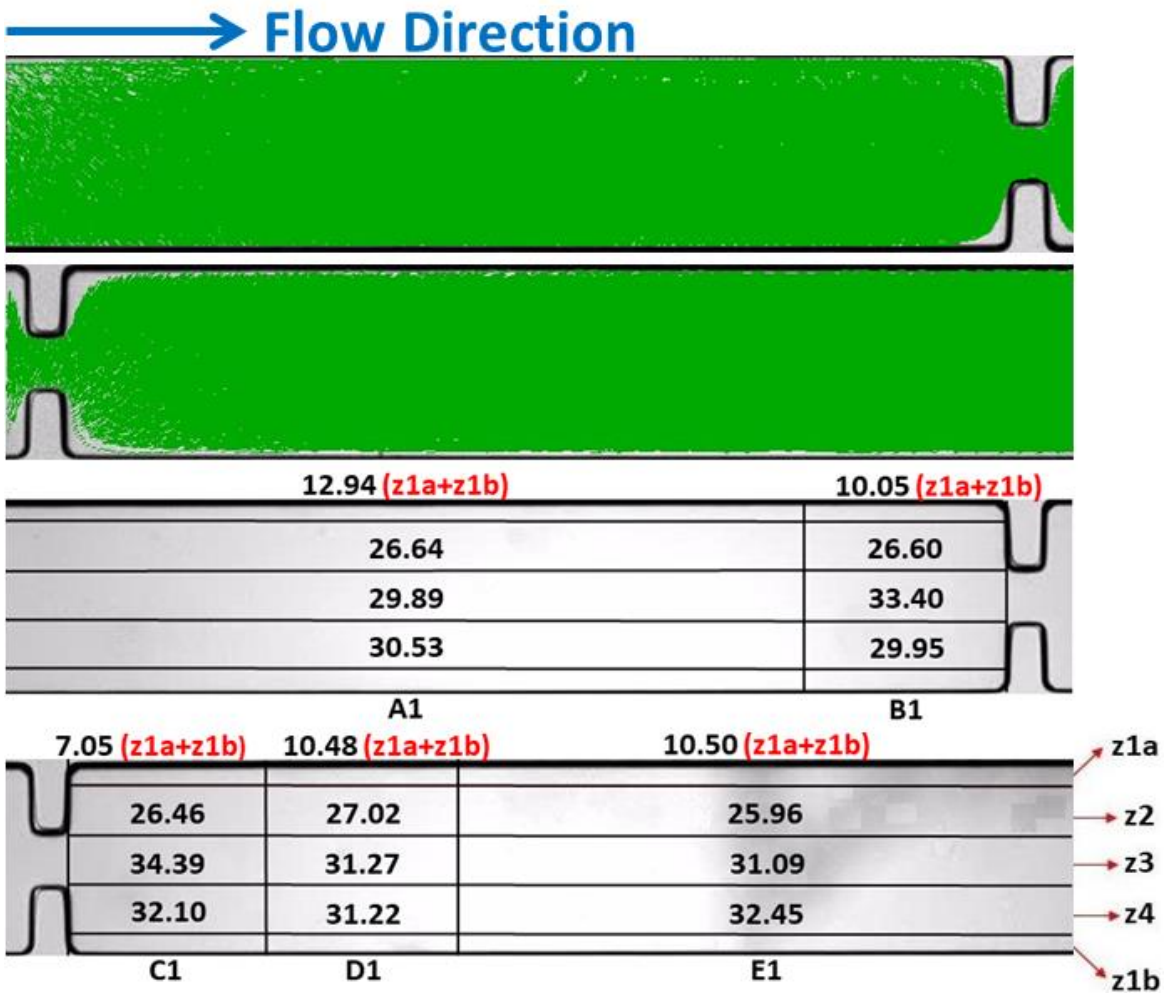


Figure 4.25 – Algal swimming trajectories and dispersion percentages in the ECR 4-1 geometry at  $5 \mu\text{l}\cdot\text{min}^{-1}$ . The experimental videos were captured using a resolution of  $688 \times 516$  pixels, the 4X objective and an exposure time of  $\sim 1$  ms (see Section 3.6.1). For statistical reasons, all the results were obtained by analysing at least three experimental videos.

**ECR 7-1 – LIVE Cells –  $5 \mu\text{l}\cdot\text{min}^{-1}$**

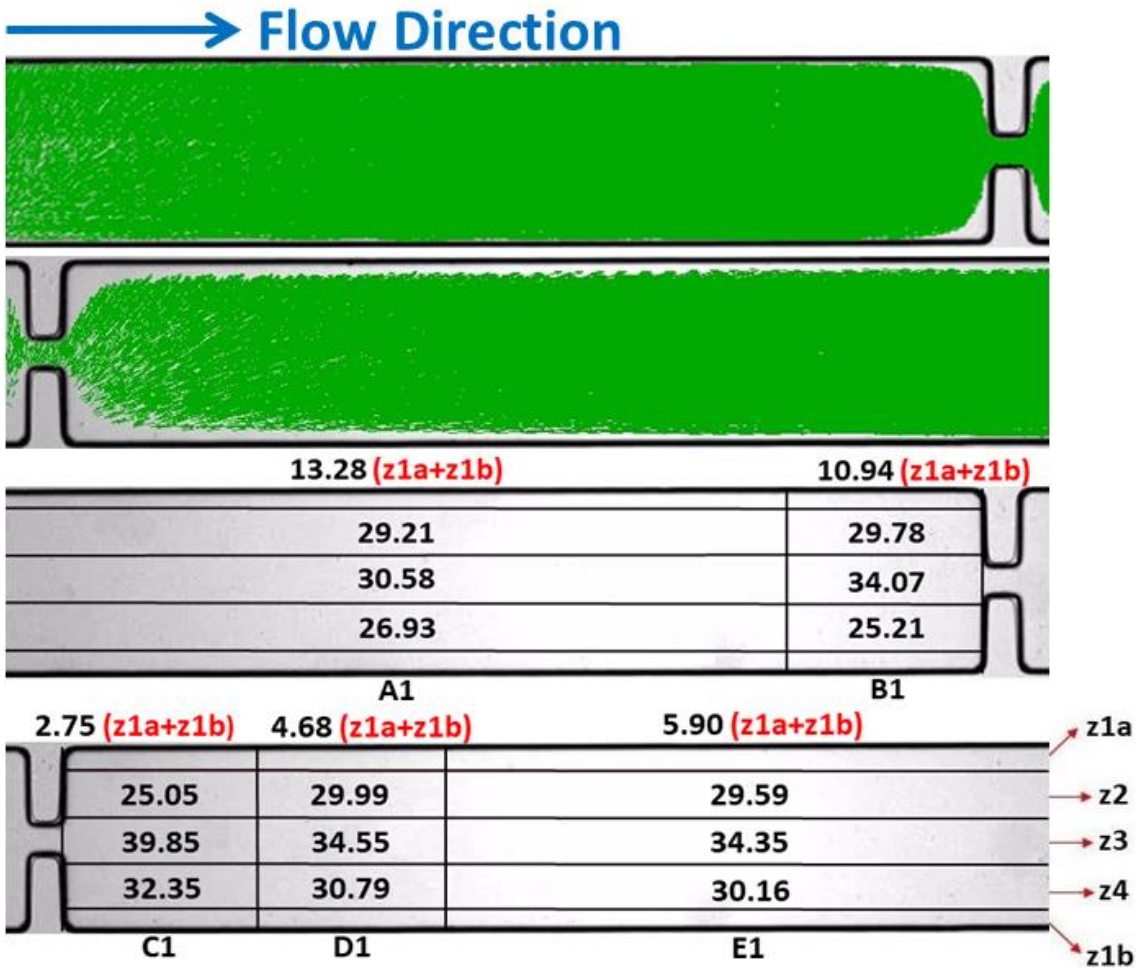


Figure 4.26 – Algal swimming trajectories and dispersion percentages in the ECR 7-1 geometry at  $5 \mu\text{l}\cdot\text{min}^{-1}$ . The experimental videos were captured using a resolution of  $688 \times 516$  pixels, the 4X objective and an exposure time of  $< 1$  ms (see Section 3.6.1). For statistical reasons, all the results were obtained by analysing at least three experimental videos.

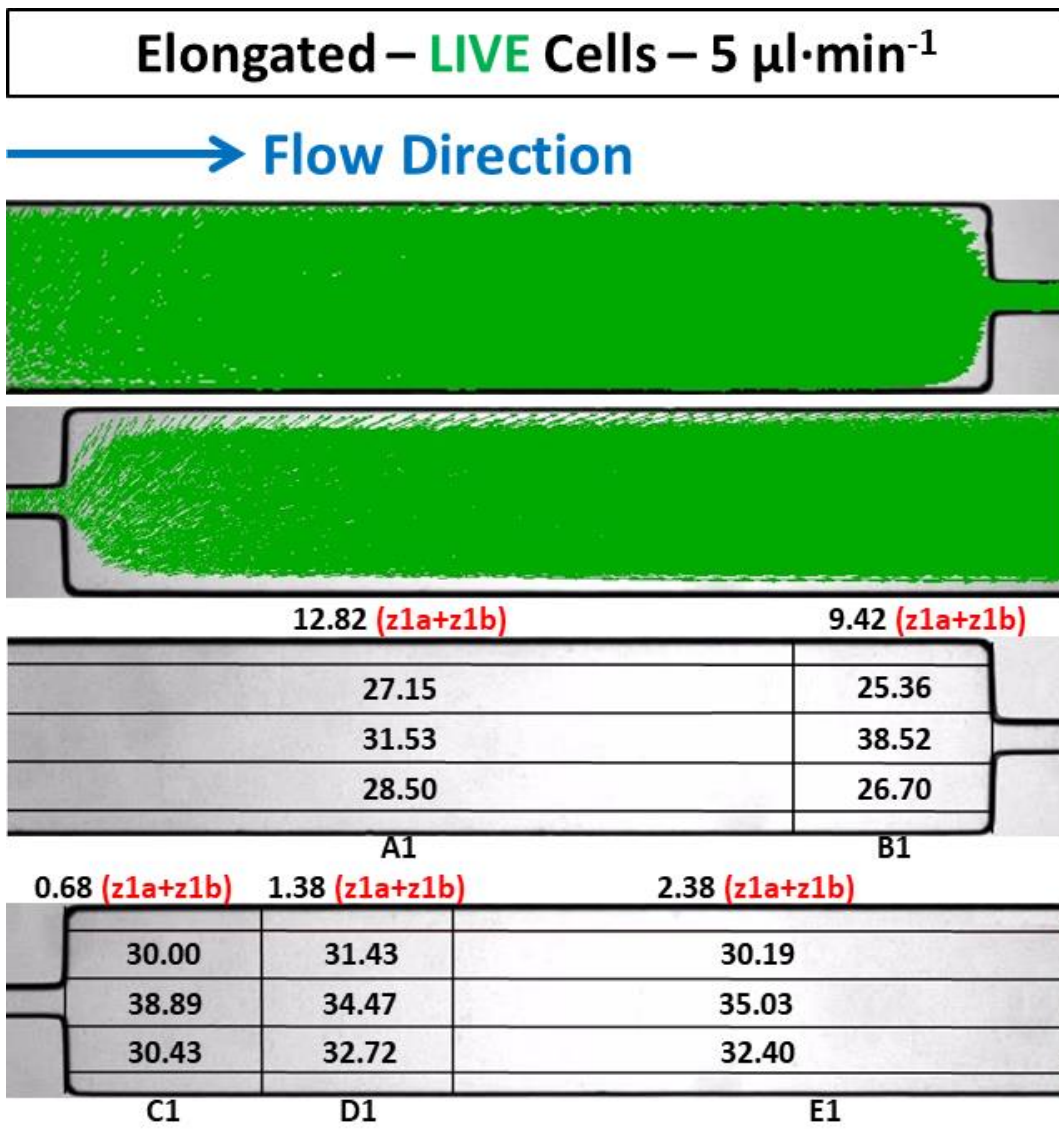


Figure 4.27 – Algal swimming trajectories and dispersion percentages in the elongated geometry at  $3 \mu\text{l}\cdot\text{min}^{-1}$ . The experimental videos were captured using a resolution of  $688 \times 516$  pixels, the 4X objective and an exposure time of  $< 1$  ms (see Section 3.6.1). For statistical reasons, all the results were obtained by analysing at least three experimental videos.

For both the studied flow rates, far away from the contraction (*i.e.* in the A1 zone, at fully-developed flow conditions), the algal behaviours were similar to the ones observed in the straight channel, at  $3 \mu\text{l}\cdot\text{min}^{-1}$  the cells could still drift along the streamlines while, at  $5 \mu\text{l}\cdot\text{min}^{-1}$  they were passively advected by the flow (see **Section 4.8.2** and **Figure 4.10**); in both cases the cells were able to swim throughout the whole geometry of the channel.

#### **Zone B1: the entrance effects**

At both the flow rates, while approaching the microgeometries (*i.e.* in the B1 zone), the cells were drawn out by the contraction owing to the entrance effects. In particular, at  $3 \mu\text{l}\cdot\text{min}^{-1}$  the algae could not overcome the streamlines anymore but, owing to the increase of the inertial effects, they were advected by the flow and followed the distorted streamlines, similarly to the cells at  $5 \mu\text{l}\cdot\text{min}^{-1}$ .

Potentially, the entrance effects could also have been able to influence the algal swimming trajectories even in the last part of the A1 zone (*i.e.* the one close to the B1 zone) and this would explain both the asymmetric algal cells distribution percentages (ACDPs) values found in the A1 zones (*e.g.* see the algal distribution percentages for the A1 zones of the ECR 7-1 geometries at  $3 \mu\text{l}\cdot\text{min}^{-1}$  and the ones for the ECR 4-1 and ECR 7-1 geometries at  $5 \mu\text{l}\cdot\text{min}^{-1}$ , **Figures 4.23, 4.25, and 4.26**) and also why the ACDPs values did not change significantly between the two vertical zones. Furthermore, a general trend observed in the B1 zones was an increase of the ACDPs values in the centreline (*i.e.* the z3 zones) and a slight reduction of the walls ACDPs values, induced by the drawing effects of the contractions.

#### **Zone C1, D1 and E1: the exit effects and the algal plumes**

The cells behaviours were mostly affected by the inertial effects induced by the microgeometries, which resulted in the development of algal plumes that reduced the walls interactions and compacted the cells, preventing them from swimming throughout the whole geometry; however, for increasing distances from the microgeometries, these “plume effects” were seen to fade with different velocities that depended on both the employed microgeometry and flow rate (see **Figures 4.28 and 4.29**).

As seen in the **Figures 4.22** and **4.25**, within the ECR 4-1 geometry for both the flow rates, the ACDPs values after passing the microgeometries were observed to become similar to the ones before the contraction in a relative short portion of the channel length (*i.e.* within the C1 zone that corresponded to about a channel width, see the **Figure 4.22**). For both the flow rates, the most significant effects on the algal behaviours were induced by the ECR 7-1 and elongated geometries, since their resulting plumes caused a significant reduction of the shading phenomena and their effects were still consistent along the complete displayable length of the channel (*i.e.* even when the flow had reached the fully-developed conditions again). In particular, for both geometries, at  $5 \mu\text{l}\cdot\text{min}^{-1}$  the walls ACDPs values were lower and the plume effects tended to last longer than those at  $3 \mu\text{l}\cdot\text{min}^{-1}$  (see **Figure 4.28** and **4.29**).

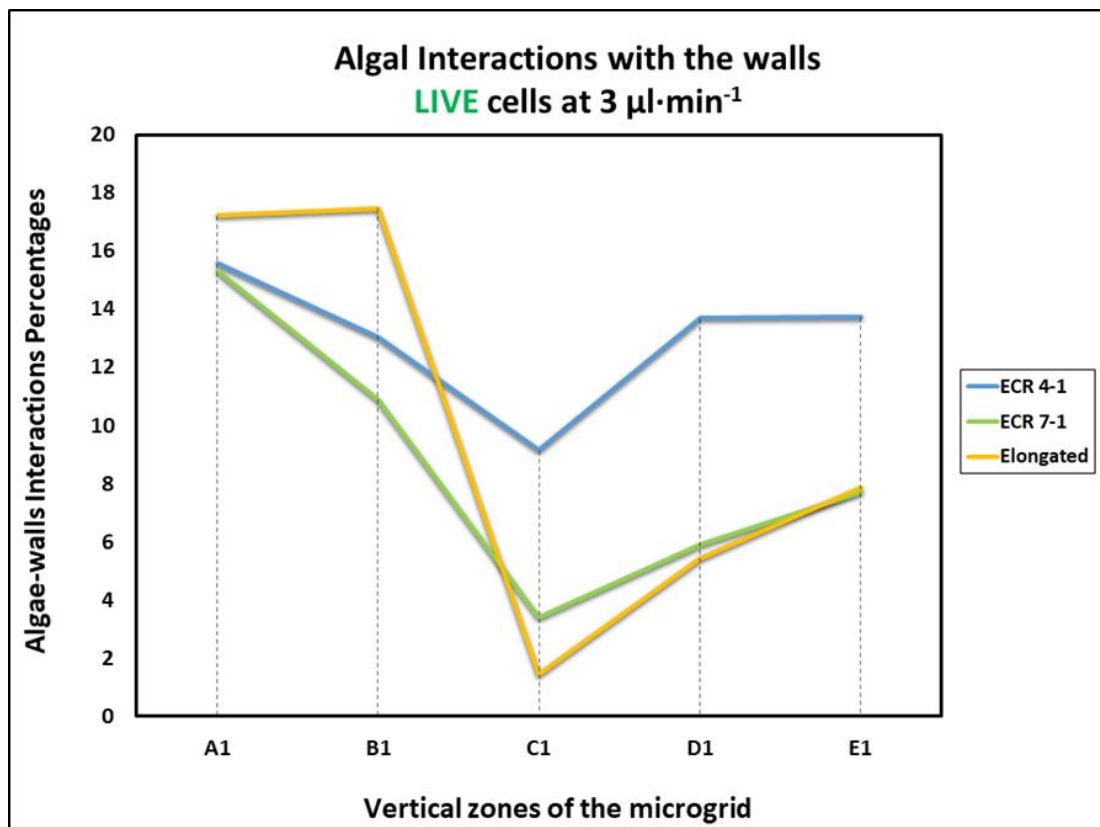


**Figure 4.28** – Live algal cells dispersion percentages close to the walls induced by the 3 different microgeometries at  $3 \mu\text{l}\cdot\text{min}^{-1}$ . As can be seen in the B1 zone, the entrance effects implied a general reduction of the algal cell wall interactions, albeit the biofouling phenomena were significantly inhibited by the inertial effects (zone C1); the plume effects can be observed decreasing along the zones C1, D1 and E1. The ECR 4-1 geometry proved to be the least effective contraction based on the experimental investigations involving the live cells (see **Figure 4.29**).

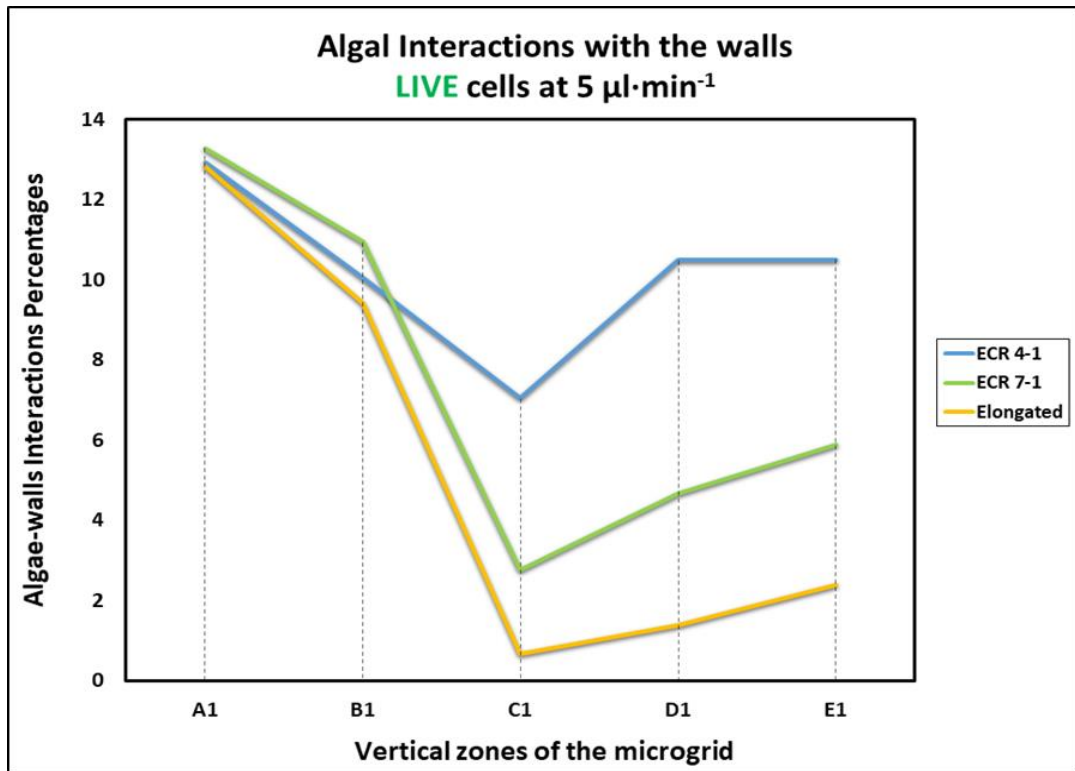


Figure 4.29 – Live algal cells dispersion percentages close to the walls induced by the various microgeometries investigated at  $5 \mu\text{l}\cdot\text{min}^{-1}$ . The increase of the flow rate led to lower ACDPs values (*i.e.* a reduction of the cells that swam close to the walls) and longer “plume effects”. However, as discussed in the next Chapter, this is not true for the dead algal cells for which an increase of the inertial effects led to detrimental consequences (see Section 5.6).

These obtained results can be understood by considering the inertial effects induced by the microgeometries on the cells (see **Figures 4.30** and **4.31**). In particular, the overall trend for both the flow rates was similar; in the vicinity of the contractions, the algal cells were seen to accelerate due to entrance effects and, within the contractions, their velocity rose consistently, reaching its maximum value just before the expansion plane. When the cells entered the expansion regions, their spatial distributions were influenced by the algal plumes that led to the formation of algal cell free regions and inhibited the walls interactions; nevertheless, while flowing downwards the channel, the cells velocity tended to decrease, causing the plume effects to fade. Generally, the higher the inertial effects acting on the living cells, the longer and more consistent the algal plume effects were.

However, as we shall see in the next chapter, the same conclusions cannot be drawn for the dead *Dunaliella* cells that showed opposite behaviours in comparison with the living ones, since growing inertial effects caused their biofouling tendency to increase, demonstrating once more that living cells cannot be treated as passive particles.

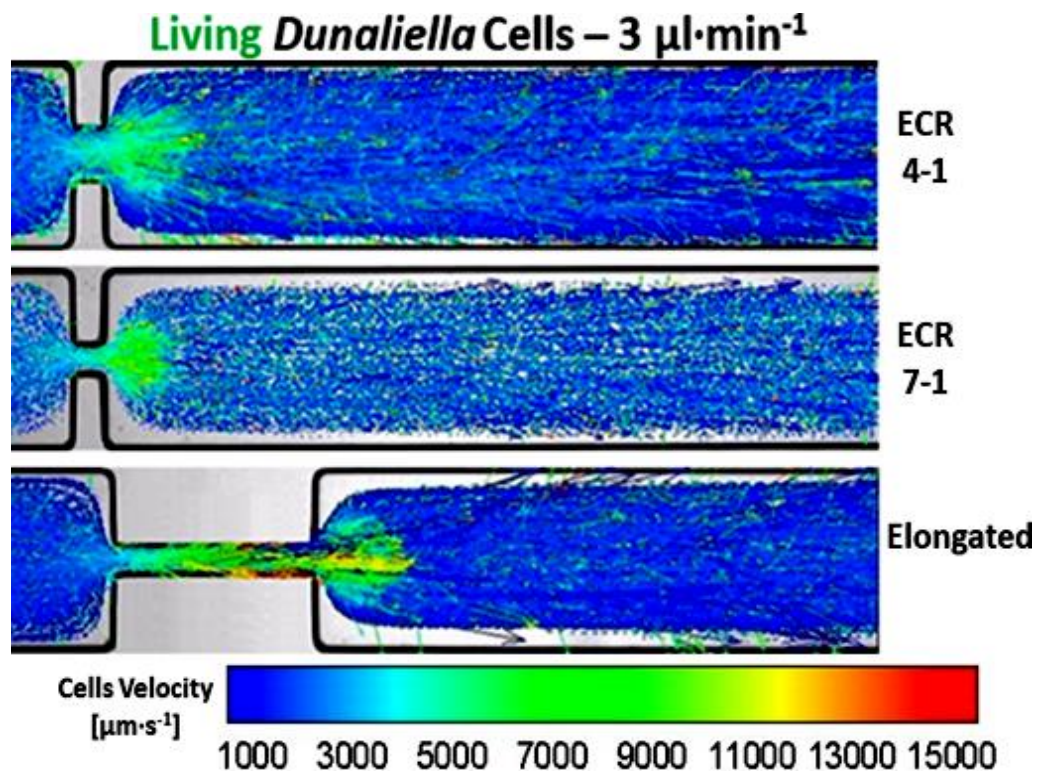


Figure 4.30 – The velocity vectors spatial distributions of the living *Dunaliella* cells at 3  $\mu\text{l}\cdot\text{min}^{-1}$ . The susceptibility to hydrodynamic and mechanical shear forces must carefully be assessed and taken into account while screening the most appropriate microalgal strains to culture, since the increase of the shear rate and the cells velocity may damage and lead to demise of cultured fragile cells. [198]

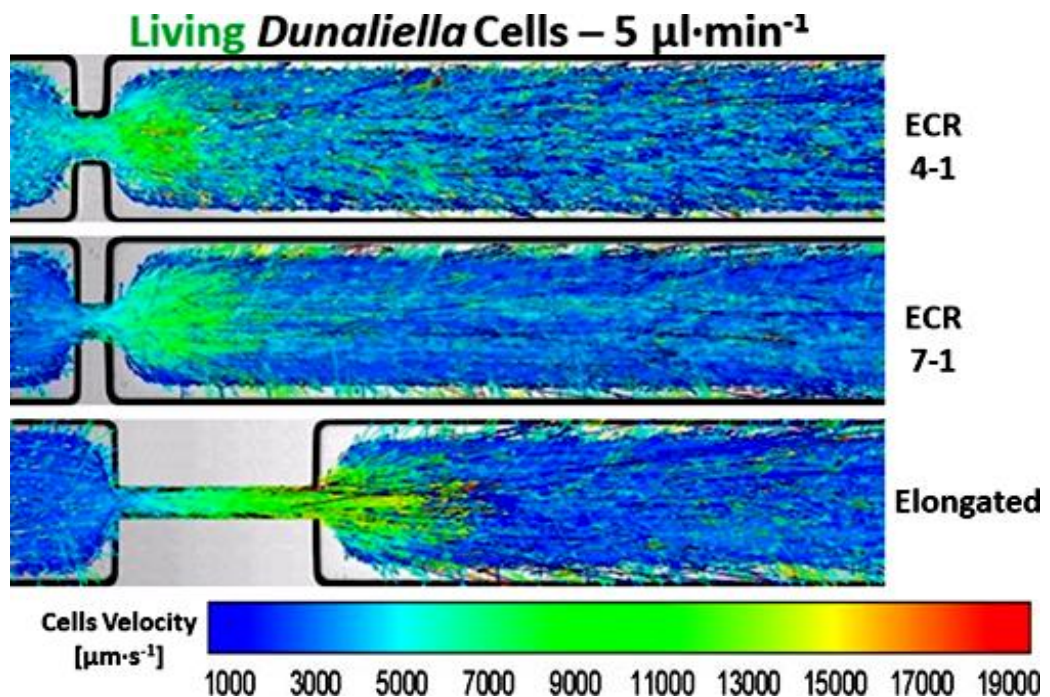


Figure 4.31 – The velocity vectors spatial distributions of the living *Dunaliella* cells at 5  $\mu\text{l}\cdot\text{min}^{-1}$ . The inertial effects due to the elongated geometry were found to be the most effective ones and the only ones that induced similar behaviours to both living and dead cells (see Section 5.6).

### **The most relevant implications for PBRs**

The experimental investigations were carried out assuming that the fluid dynamic experiences of the cells could be compared to those which occur in horizontal PBRs. The reported results demonstrate that optimising the geometrical configuration of culturing devices would also lead to an enhancement of the light distribution (*i.e.* the light can diffuse deeper within the reactor, even in parts that in the straight channel were occupied by the algae, see **Section 4.8.3**) and a reduction of the dark zones, resulting in an increase of the biomass productivity [118]. These aspects will be discussed in details in the **Section 5.7**.

These promising results were attained considering the same flow rates used for analysing the straight geometry or, in other words, employing the same amount of energy, further demonstrating that the exploitation of static mixers within PBRs can considerably improve the processing conditions, without increasing the operational costs.

Improvements induced by the microgeometries at  $5 \mu\text{l}\cdot\text{min}^{-1}$  were found to be slightly better than those obtained at  $3 \mu\text{l}\cdot\text{min}^{-1}$  (*i.e.* generally, at  $5 \mu\text{l}\cdot\text{min}^{-1}$  the walls interactions were lower than those observed at  $3 \mu\text{l}\cdot\text{min}^{-1}$  and the plume effects faded slower), the results also demonstrate that another cost-reducing aspect that must be taken into account are undoubtedly the algal cells themselves. In fact, the main difference between the two flow rates evaluated were the algal responses: since at  $3 \mu\text{l}\cdot\text{min}^{-1}$  the algae could drift along the fluid streamlines, it would be possible to exploit the combined effects of the microfluidic geometries and the “partially-free” swimming properties of the cells, which at the moment are overlooked and thrown out as insignificant complications. [10] For example, in the parts of the channel where the plume effects tend to fade (*i.e.* the algae are not advected anymore), the cells would be swimming spontaneously between the photic and dark zones of the reactor, potentially exploiting the flash light effect that is usually achieved by turbulently pumping the algal suspensions (see **Section 2.7.3**). Moreover, employing these combined effects would also imply using lower flow rates (*i.e.* less energy-consuming process conditions), as the passive advection of the cells would not be necessary anymore.

Such a this solution would require optimisation of the PBR geometrical configuration, where currently straight parts should be interchanged with static mixers or, an optimal spacing distance between two mixers should be designed so as to exploit their benefits and also hamper the wall interactions, when they will become consistent again. The optimisation process must also take into account other aspects, such as the behaviours of dead algal cells within the reactor, the relative velocities induced by motionless mixers on the cells, *etc.* which will be explored in details in the 5<sup>th</sup> and 6<sup>th</sup> Chapters.

## 4.10 Chapter Summary

This chapter presented and discussed the results of the experimental investigations involving the living *Dunaliella* cells, carried out in stagnant flow conditions and while the algae had been undergoing different flow rates within the straight, ECR 4-1, ECR 7-1 and elongated geometries. The described results were obtained assuming the microchannels as simplified horizontal PRBs and their microgeometries as static mixers, in order to achieve more insight into the actual fluid dynamic experiences of the cells within both lab-scale and real PBRs, focusing particular attention to the cells dispersion within the channels and their interaction with the walls.

The experimental observations of freely swimming microalgae permitted cell motility to be quantified (showing that the microfluidic geometries had stimulated their tendency to swim and explore the surrounding environments) and for their interactions with the channel boundaries to be quantified. The cells motility can be considered as a measure of their viability [235], therefore its quantification can be exploited during the algal screening process and for quality control of the algal cultures (see **Section 4.2** and **4.7**).

The cells fluid dynamic behaviours were also investigated at various flow rates within the straight geometry, which were supposed to simulate the algal experiences at different processing conditions in horizontal PBRs (see **Section 4.8.2**). Two flow rates were analysed in detail because, from a practical point of view, they had proven to be the most interesting ones: 3  $\mu\text{l}\cdot\text{min}^{-1}$  (the cells were able to overcome the fluid streamlines and interact with the walls, without adhering to them) and 5  $\mu\text{l}\cdot\text{min}^{-1}$  (the cells were advected by the flow and the walls interactions were negligible).

The results demonstrate that, at both flow rates, the cells were still able to occupy the whole geometry of the channel (leading to potential shading effects) and the algal walls interactions could only be hampered by increasing the flow rates used.

Further experimental investigations were carried out employing the contraction-expansion geometries and the previously-considered flow rates used to quantify their effects on the cells and assess whether improved processing conditions could be achieved by optimising the PBRs geometrical configuration. Our results suggest that the inertial effects induced by the microgeometries, which resulted in the development of algal plumes, compacted the algal flow along the channel and reduced the wall interactions (in particular for the ECR 7-1 and elongated geometries). These processing conditions would also lead to an enhancement of the light distribution and a significant reduction of the shading phenomena within the cultivation devices (see **Section 5.7**).

However, in the next chapter, the fact that algal suspensions always include a certain percentage of dead cells for which fluid dynamic behaviours must be taken into account during the design and optimisation of static mixers, along with other aspects such as potential shear-induced damages on the algal cells (see **Section 6.3.4**).

## – Chapter 5 –

# Dead *Dunaliella Salina* cells: implications for photobioreactors and static mixers

## 5.1 Chapter layout

This chapter discusses the results concerning the dead *Dunaliella* cells; initially, the main causes of algal cells demise in PBRs will be analysed, focusing particular attention on predatory organisms and impacts due to the variations of light intensity distributions and temperatures. To provide a context for these experimental investigations, the main detrimental effects of dead cells accumulations within algal culture devices will also be considered. Furthermore, the different “experimental issues” that had been experienced and solved during the experimental observations will be described, to understand how they had eventually led to the optimised thermal killing procedure and the experimental setup.

Since the dead cells were assumed to be passive particles, in the second part of the chapter, the most significant behaviours of suspended spherical and non-spherical particles, while flowing within macro and microchannels, will be addressed. Next, the obtained results will be presented, analysing the qualitative fluid dynamic behaviours of the dead cells within the microchannels and providing a comparison between the results concerning living and dead microalgae. The results will also demonstrate that the exploitation of static mixers can lead to more homogeneous irradiance profiles within the algal cultures and an increase of the biomass productivity.

## 5.2 From optimal culturing conditions to algal demise

In this section the main causes of algal cell death within cultivation devices are discussed, focusing particular attention on the algal demise caused by predatory organisms, temperature effects and variations of light intensity distributions within PBRs.

Large-scale cultivation of microalgal cultures requires optimisation of several operational and environmental variables, in order to fulfil the growth requirements of the selected strain, avoiding algal accumulations and eliminating gradients of light, nutrients, gases and temperature within the reactor. In fact, if the PBR processing conditions are not constantly monitored and adjusted, negative effects on the algal cultures may occur (*e.g.* inhibition of the photosynthesis, reduction of the biomass production, *etc.*), which may cause high stress to the cells and ultimately their demise. [118]

In general, culture devices should recreate the algae’s natural environments, albeit many “differences” are often deliberately imposed through the stressing procedures (*i.e.* high salinity, high light intensities, oligotrophic environments [138, 249]), enhancing the production and accumulation of biomass but forcing the cells to adapt and survive under stress conditions, exploiting different species-specific biological mechanisms (*e.g.* under high light intensities, DS cells can produce and accumulate carotenoids to prevent chlorophyll photo-damages (see **Section 2.3.2**)) [250]. Extreme stressing conditions may cause the algal cells to die. [154, 161] Further examples of processing conditions that might result in the death of the cells and the related approaches available for mitigating the damaging effects have been summarised in the **Table 5.1**.

**Table 5.1 – The main causes of algal cells demise in outdoor cultures.**

<b>Conditions which may cause the death of algal cells</b>	<b>Main potential precautions</b>	<b>References</b>
Photoinhibition (see <b>Section 5.2.2</b> )	Reduce the intensity of the incident solar light by optimising the PBR geometric arrangement and increase its surface-to-volume ratio to spread the sunlight over a larger reactor surface area. Optimise dark/light cycles within the PBR.	[118, 154, 161]
Biological death of the cells	Optimise the permanence time of the algae within the PBR carrying out periodical quality controls of the culture so that the cells can be harvested when the desired algal substrate has reached its maximum concentration.	[166, 175]
Temperatures higher than 40°C	The PBR must be equipped with temperature control and cooling systems (see <b>Section 5.2.3</b> ).	[139, 251, 252]
Shear-induced death ( <i>e.g.</i> during the recirculation or the harvesting processes)	Assess the shear field related to the employed processing conditions and the circulation device (see <b>Section 6.3.4</b> ).	[139, 198]
Cells being predated or infected and killed by pathogenic organisms	The culture must routinely be monitored, the most likely predator-prey scenarios must be assessed and proper crop protection strategies should be planned accordingly, taking also into account their effects on the final product(s).	[253-255]

Some of these causes of algal death will be analysed in detail in this chapter; the following section considers how non-homogeneous light intensity distributions in PBRs affect the biomass production and may result in algal cells demise.

### 5.2.1 Light effects on the algal cells

In PBRs, after the fulfilment of nutritional growth needs, optimal temperature gradients and fluid dynamic conditions, light availability becomes the only limiting factor that determines the productivity of the system (see **Section 2.7**); therefore, it is crucial to obtain the maximum biomass yield at the expenses of the actual available light [223].

The light intensity within PBRs is related to the incident solar light, which can be divided into direct light and disperse light. The fraction of direct solar light impinging on the surface of a certain PBR depends on its geometrical configuration, its location and the position of the sun at a given moment, while the disperse radiation is the sum of the diffuse radiation and the radiation reflected off by the PBR surfaces, hence it has no specific direction. [256]

On reaching the PBR surface, the solar light travels within the culture while being attenuated by the algal cells through shading and scattering phenomena that reduce its intensity; these effects are usually inhibited by increasing the mixing levels (*e.g.* turbulently pumping the algal suspensions, see **Section 2.9**) in order to prevent potential microalgal accumulations. The light intensity is further reduced by the cells which absorb the photosynthetic active radiation (PAR) fraction of the light and transform it into biomass through the photosynthetic process (see **Section 2.7**). [118, 256]

Therefore, variations in the incident solar light during the day and attenuations phenomena due to the biomass give rise to non-homogeneous irradiance profiles inside the culture, creating zones of different illuminations (see **Figure 5.1 B**) [154]; the effects of incident light intensities on the algal cells growth rate are usually represented through culture-specific kinetic curves (see **Figure 5.1 A**). [223]

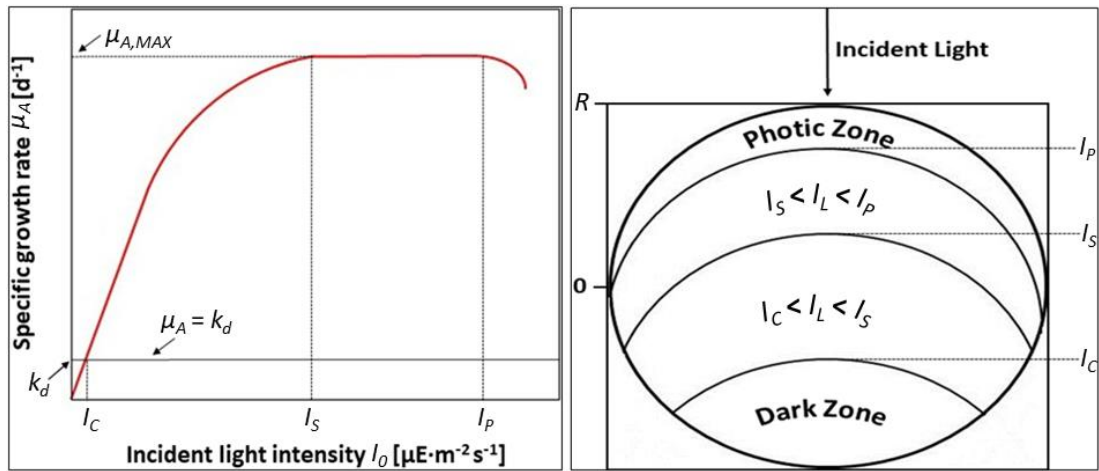


Figure 5.1 – (A) A typical kinetic curve that describes how the algal growth rate is related to the light intensity impinging on the PBR surface. The direct light increases from dawn to noon, declining again when the evening sets, implying that the algal cells may be photoinhibited at noon and light limited in the evening. (B) An example of the irradiance profiles inside the PBR tube, where photolimited and photoinhibited cells may coexist. Adapted from [118, 154, 223].

For each algal strain, some typical light intensity values can be defined, specifically **1)** the compensation intensity  $I_C$ , *i.e.* the minimum light intensity required for the photosynthetic process; **2)** the saturation intensity  $I_S$ , *i.e.* the light intensity that allows cells to achieve the highest growth rate and **3)** the photoinhibition intensity  $I_P$ , beyond which occurs light-induced reductions of the algal photosynthetic capacity. [118, 154, 223]

Defining  $I_L$  as the punctual light intensity within the PBR, as shown in **Figure 5.1 A**, when  $I_L < I_C$  (*i.e.* in the dark zones of the reactor), there is no net photosynthesis, the biomass is consumed through dark respiration, the cells are photolimited and therefore their decay prevails over their growth (*i.e.*  $\mu_A < k_d$ , being  $k_d$  the algal decay coefficient); at  $I_L = I_C$  cells growth balances their decay ( $\mu_A = k_d$ ) and the net growth rate is zero. In the part of the PBR where the light intensity goes from  $I_C$  to  $I_S$ , there is an increase of the growth rate with increasing light intensity, represented by the slope of the kinetic curve. At the saturation intensity  $I_S$ , the growth rate will reach its maximum efficiency ( $\mu_A = \mu_{A,MAX}$ ); hence, for a given algal strain, the higher  $I_S$ , the better the cells can adapt to high light intensities and the less their biomass production will be hampered by photoinhibition. The growth rate will still be the highest one even when the light intensity is between  $I_S$  and  $I_P$ ; within this interval the cells can collect and store some light which will be used in the dark zones, exploiting the flashing light effect (see **Section 2.7.3**). [118, 223]

In the photic zones of the PBR (*i.e.* when  $I_L > I_p$ ), the cells tend to absorb higher amounts of energy than they can process and, since the cellular photosynthetic apparatus can only handle limited amounts of energy, this results in photoinhibition leading to a decrease in the biomass production rate. This may also cause cellular damage and premature population demise; the light that the cells are not able to process is wasted as fluorescence and eventually heat. [160, 161] In order to prevent these detrimental effects, the cells must periodically be recirculated between the bright region close to the PBR surface and its dark regions in order to ensure suitable dark/light cycles (see **Section 2.7.3**). [161]

The two next sections discuss how algal cells can also die due to high temperature gradients [257] and the presence of predatory/pathogenic organisms, which can also lead to algal lysis (*i.e.* the breaking down of the cellular membrane and the consequent release of intercellular fluids). [253, 254] Moreover, as we shall see in the **Section 6.2**, the algal cell demise can also be shear-induced. [139, 198]

## 5.2.2 Temperature effects on algal cultures

Temperatures of outdoor algal cultures are governed by the sunlight regimen and tend to vary with the day-night cycles, with amplitude and duration affected by the seasons. For example, at midday in hot climates, exposure to natural solar light can cause the absorption of large amounts of heat and a substantial increase of the culture temperature which can reach 45°C, while at night time it can decrease below 0°C. [157]

Studies in both open ponds and closed PBRs have demonstrated that culture temperature can strongly affect the biomass productivity and, in some cases, even its biochemical composition [251, 258]; what is more, the biomass lost through dark respiration at night time may be affected by the daytime temperature history. [259] Thus, it is paramount to cultivate the cells at their most suitable growth temperatures. For many industrially-cultivated algal species, the preferred range is between 24 – 40°C. [252]

Generally low temperatures do not lead to algal demise but they can affect the biomass growth rate, depressing the cell yield; on the other hand, temperatures around 40°C may promote carotenoid induction [249] but, at the same time, they trigger the respiration process, inhibiting the photosynthesis. [251] Higher temperatures can cause the algal cells to lyse and die. [257]

Temperature effects are more significant in open ponds than closed PBRs, since they may also result in high evaporative water loss and excessive rise in salinity. [251] Closed PBRs can also overheat and therefore require some temperature control systems, usually provided by either a heat exchanger or evaporative cooling of water sprayed to the surface of the reactor. [139, 251]

### 5.2.3 Effects of parasitic organisms on algal cultures

Ideally, cultures should contain only one species (*i.e.* they must be axenic), nevertheless they may be subject to biological contamination caused by other fast-growing opportunistic organisms that may compete for light and nutrients against the cultivated cells and even predate them [138]; for example, some species of fungi belonging to the class of *Chytrids* can attack some microalgal species, such as *Chlorella* and *Haematococcus*. [139] Cultures may also be compromised by pathogenic organisms (*e.g.* the bacterium *Vampirovibrio chlorellavorus* and bacteria from the group *Cytophagia* [253]), which are able to infect the cells and cause leakages of lysed intercellular fluids that may be exploited as organic carbon sources by parasitic organisms. [253, 254]

These unwanted organisms may also have devastating effects for the biological and processing conditions of culture devices, *e.g.* they may accumulate on PBR walls, preventing the light penetration, providing a shelter from many other contaminants and even leading to the algal extinction. [138, 255]

However, the presence of other organisms in algal cultures is not necessarily a drawback; recent studies have shown promising positive effects of algae-bacteria mutual interactions, *e.g.* algae and bacteria were observed altering their metabolisms to meet one another's needs and exchanging nutrients between them [260], enhancing both the algal growth and the biomass production. [254]

Once some of the main causes of algal cells death have been described, in the next section, the main effects of dead cells accumulations within PBRs are analysed, in order to better understand why the fluid dynamic behaviours of dead cells should be studied.

## 5.2.4 Effects of dead cells accumulations on algal cultures

When microalgae are killed or die biologically, their concentration within the PBR tends to increase, leading to different effects for the culture. Firstly, since the dead cells are not neutrally-buoyant, they tend to sediment, deposit and accumulate in critical PBRs parts (*e.g.* bends, gas transfer devices, paddlewheels of open ponds, *etc.*), causing biofilm formations and potentially requiring the shutdown of the PBR for cleaning and sterilisation. If the dead algae do not sediment, they are recirculated passively around the reactor, without producing any net biomass. They represent a potential contaminant for the final product(s) and may even promote the proliferation of opportunistic organisms. [166, 253]

If the dead microalgal concentration increases substantially, the number of biomass-producing cells will decline accordingly, resulting in their potential washout, meaning that the number of cells harvested from the reactor is bigger than the number of the cells growing in it, therefore the culture will not be able to sustain itself and the algal concentration will decrease drastically [251]. Hence, algal cells demise must be avoided by taking suitable precautions that depend on the different potential causes of death (see **Table 5.1**).

For these reasons, the fluid dynamic behaviour of dead cells must be explored in order to understand their effects on algal cultures and determine whether the PRB processing conditions can be optimised to minimise the negative effects described above. It is useful to note that the final cellular shapes may indicate which causes of death applied.

In general, except when being predated by other organisms that cause the cell rupture and destruction, algal death is always preceded by stressing conditions and adaptation processes, where the cells try to resist and survive exploiting some species-specific biological mechanisms (*e.g.* accumulation of carotenoids, glycerol, *etc.* [250]), which may lead to the deformation of the cells. Thus, final shapes of dead cells may deviate from their original morphology and must be assessed case by case. [235, 250]

In the specific case of *Dunaliella* cells, being fragile and lacking of a rigid cell wall (see **Section 2.3.2**), final shapes and fluid dynamic behaviours of the dead cells are consistently influenced by the cause of their death, as described in the next section.

## 5.3 Dead *Dunaliella* cells: the killing procedure and experimental setup

This section describes the different “issues” that had been experienced and solved during the experimental investigations of the dead *Dunaliella* cells (DDCs) and how they eventually led to the final killing procedure and the associated experimental setup (see **Section 3.5**). The two most significant “issues” that had to be overcome were **1)** finding an effective killing procedure for living cells, which prevented their shapes from changing significantly and **2)** limiting the DDCs sedimentation due to the fact that the cells are denser than the medium.

### 5.3.1 The development of the killing procedure

In order to study the dead *Dunaliella* cells (DDCs), a procedure had to be developed that allowed living cells to be killed rapidly, efficiently (*i.e.* ensuring 100% of mortality), without affecting their shape and concentration is reliable and reproducible (*i.e.* achieving similar final algal shapes). Since DS cells lack a rigid cell wall, cellular shape preservation was the most difficult objective to achieve (see **Figure 5.2**). All the “killing attempts” were carried on two-week old cultures (*i.e.* they were pigmented enough, see **Section 3.2.3**), each approach involved inducing a given stressing condition to the cells and checking periodically the effects on them.

The first attempt consisted of keeping some flasks containing 50 ml of culture each in the dark; initially the microalgae managed to survive because they still had nutrients available, albeit were not able to carry out the photosynthesis and therefore their biomass was consumed through dark respiration. [261] Nonetheless, after about three weeks, the cells ran out of food, died biologically and lysed, giving rise to very irregular shapes due to the collapsed membrane structure (see **Figure 5.2 A**); hence, this procedure was not employed because led to a change of the original cellular shape and was very time-consuming.

During the second attempt, the cells were frozen at  $\sim -20^{\circ}\text{C}$  in some 10-ml glass vials containing 1 ml of algal suspension each. Within the first 24 hours most of the cells had survived, even if their vitality was reduced significantly (*i.e.* they were seen to swim more slowly).

After one day the majority of the cells died assuming rounded shapes (see **Figure 5.2 B**) but some of them were still alive and some started to lyse; at longer times the percentage of lysed cells increased greatly, resulting in unpredictable morphological changes. This methodology was not used because was difficult to reproduce and did not guarantee the total demise of the cells.

Next, the cells were killed thermally by heating some 10-ml glass vials containing 1 ml of algal suspension each, employing the same oven used for the microfabrication (see **Figure 3.6 E**); specifically, if the heated volume of living cells was kept constant, this procedure was mostly affected by the final heating temperature and the residence time of the cells within the oven.

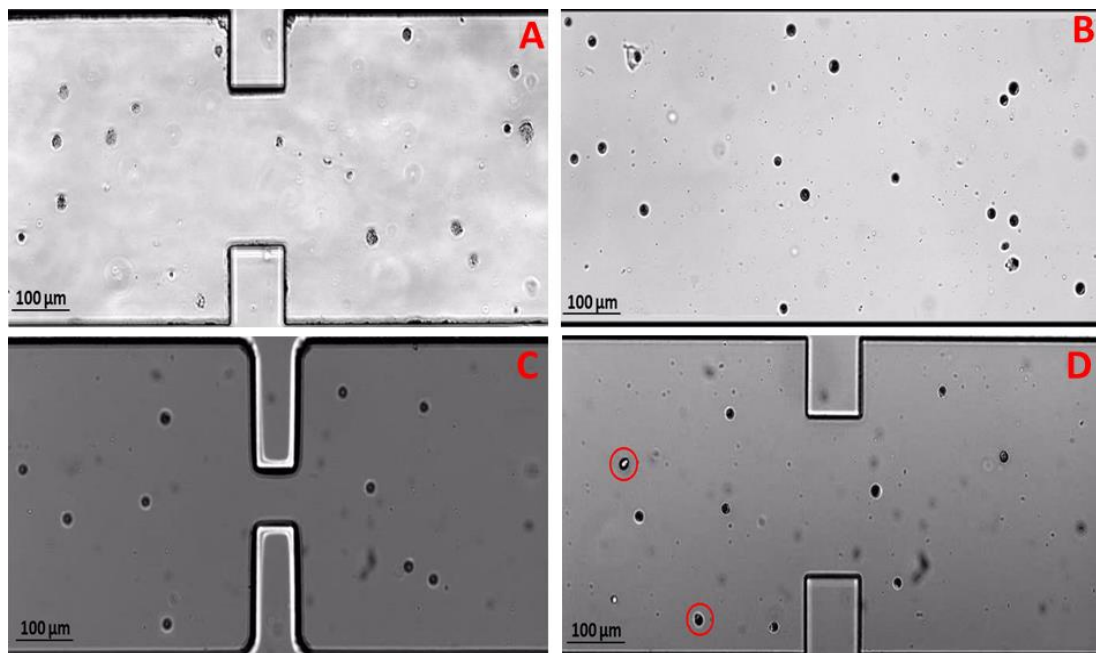


**Figure 5.2** – (A) Naturally-died algal cells: due to the lysed cellular material and its release in the surrounding fluid, the cells can be seen having very irregular shapes and absorbing less incident light from the microscope (*i.e.* they are “less black” than the other cells in the rest of the image), making them more difficult to track. (B) Algal cells after being frozen at  $-20^{\circ}\text{C}$  for 24 hr. At these conditions the cells exhibited rounded shapes but some of them were still alive; generally, the longer they were kept frozen, the more tended to lyse. (C) Algal cells killed thermally: those were the dead cells used for the experimental investigations. (D) Living *Dunaliella* cells: compared with the DDCs, they are slightly elliptical, see the cells in the red circles to appreciate this.

As shown in the **Table 5.2**, at 40°C and residence times up to 20 minutes, the cells survived while, when heated at 50°C for 8 minutes, all the living cells died and their shapes did not change significantly, albeit they became slight rounded compared with their original morphology (see **Figure 5.2 C and D**); specifically, DDCs had an average diameter of 17.5 µm and a mean eccentricity of 0.35 (see **Section 6.4.3**). The rounded shape can be explained considering that DS cells lack of a cell wall, often becoming spherical under unfavourable conditions. [249] Since this thermal killing procedure was easily reproducible and extremely efficient, it was the one employed for obtaining DDCs.

**Table 5.2 – The different attempts tried to kill the algal cells thermally.**

Attempt	Temperature [°C]	Time [min]	Killed	Shape Changed?
1	40°C	5	No	No
2	40°C	10	No	No
3	40°C	15	No	No
4	40°C	20	No	No
5	50°C	5	No	No
<b>6</b>	<b>50°C</b>	<b>8</b>	<b>Yes</b>	<b>Rounded</b>
7	50°C	10	Yes	Rounded/Swollen
8	50°C	12	Yes	Rounded/Swollen
9	50°C	15	Yes	Swollen/Lysed
10	50°C	20	Yes	Swollen/Lysed

The **Table 5.2** shows also an example of how crucial algal residence time in the oven was, in fact at 50°C, within 5 minutes (*i.e.* from 5 min to 10 min, see attempts 5, 6 and 7), the cells ranged from being alive, to become rounded and eventually to swell, before lysing (see **Figure 5.3**).

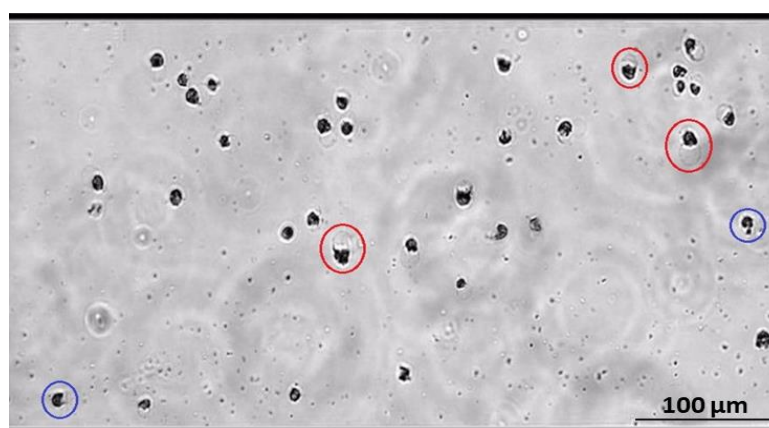


**Figure 5.3 – At 50°C and residence times higher than 10 minutes, DS cells tended to inflate (see the cells within the red circles), before starting to release their intercellular fluids and organelles into the growth medium (see the cells in the blue circles).**

As we shall see better in the next sections, the experimental setup and procedure had also to be optimised in order to overcome the sedimentation problems related to the dead algae, owing to the fact that the cells were not neutrally-buoyant (see **Appendix 5.1**).

### 5.3.2 The development of the experimental setup

This section describes the main experimental issues that were experienced while studying the dead *Dunaliella* cells (DDCs) and led to the final experimental setup employed for the experimental investigations of DDCs (see **Section 3.5**).

In particular, DDCs were not neutrally-buoyant, their density was almost unchanged from the living *Dunaliella* cells (LDCs) (see **Appendix 5.1**) (*i.e.* the thermal killing procedure did not affect the algal density), therefore the dead cells tended to sediment with a terminal velocity  $V_{T,DDC}$  of  $7.00 \mu\text{m}\cdot\text{s}^{-1}$  (see **Section 4.6.1**); the buoyancy effects can be quantified through the dimensionless buoyancy number  $B_N$  defined as: [262]

$$B_N = \frac{V_{T,DDC}}{\bar{U}} = \frac{1}{\bar{U}} \cdot \frac{2}{9} \frac{g}{\nu_m} \frac{\rho_{DDC} - \rho_m}{\rho_m} a^2 \quad (\text{eq. 5.1})$$

where  $\bar{U}$  is the average flow velocity,  $a$  the radius of a dead algal cell,  $\nu_m$  and  $\rho_m$  are the kinematic viscosity and the density of the culture medium. [72] Generally, the bigger  $B_N$ , the more the sedimentation effects play a part; *eq. 5.1* shows that increasing the average flow velocity (*i.e.* *Re* numbers),  $B_N$  decreases accordingly (see **Section 5.6**). [262]

The sedimentation phenomena also caused aggregation to occur in the vials, the syringes and the microfluidic devices themselves; for example, after being thermally killed, during the cooling process, the cells sedimented and clumped within the vials which had to be shaken gently, before drawing DDCs samples for experiments, in order to consider uniform algal concentrations and get rid of potential algal aggregations that could have skewed the results (see **Figure 5.4**).

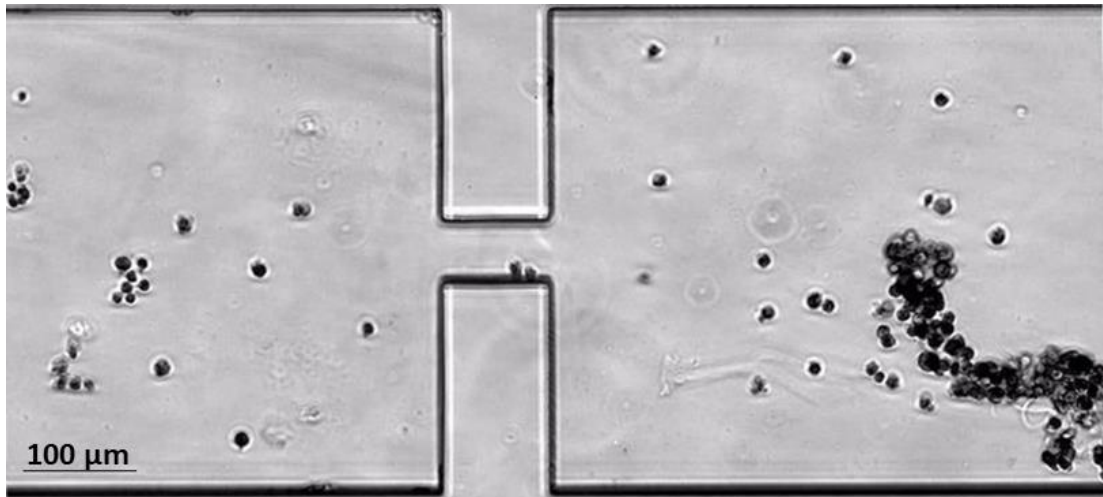


Figure 5.4 – Some examples of small and consistent DDC aggregations. When DS cells were killed thermally, by starvation or were frozen, aggregations and clumping were observed. They had to be avoided since the experimental investigations involving DDCs were aimed to compare their fluid dynamic behaviours with those of the living cells, where cell-cell interactions had been neglected. Potentially, the tendency of DDCs to clump may be due to the external amorphous mucilaginous coating (*i.e.* the glycocalyx) that surrounds the cellular membrane and also takes part in adhesion processes. [107]

As a result, due to the above-mentioned aspects, the experimental setup and procedure for DDCs had to be modified and adapted.

Specifically, the experiments involving DDCs started by employing the same experimental setup used for the living DS cells (see **Section 3.5**) but the algal sedimentation processes either prevented DDCs from being visualised and tracked or led to random preferential paths within the channels. In order to prevent this, attempts were made moving and shaking the syringe gently, its piston and the entering microbore tubing. These solutions did not inhibit the algal deposits and caused irregular flow fluctuations in the channels.

However, the experiments were mainly compromised by the sedimentation processes occurring within the syringes and therefore the “inclination” of the syringe pump was changed (see **Figure 5.5 A**) to exploit the gravitational effects but this led to small improvements. Eventually, the syringe pump was set on a perforated table, causing DDCs to settle in the proximity of the syringe outlet, due to gravity (see **Figure 5.5 B**). Nevertheless, since the suspensions were dilute and DDCs were continuously being sent in the channels, this solution did not result in algal accumulations, aggregations and clumping (similarly to what had happened within the vials) and reduced consistently the sedimentation effects, allowing DDCs to be experimentally investigated.

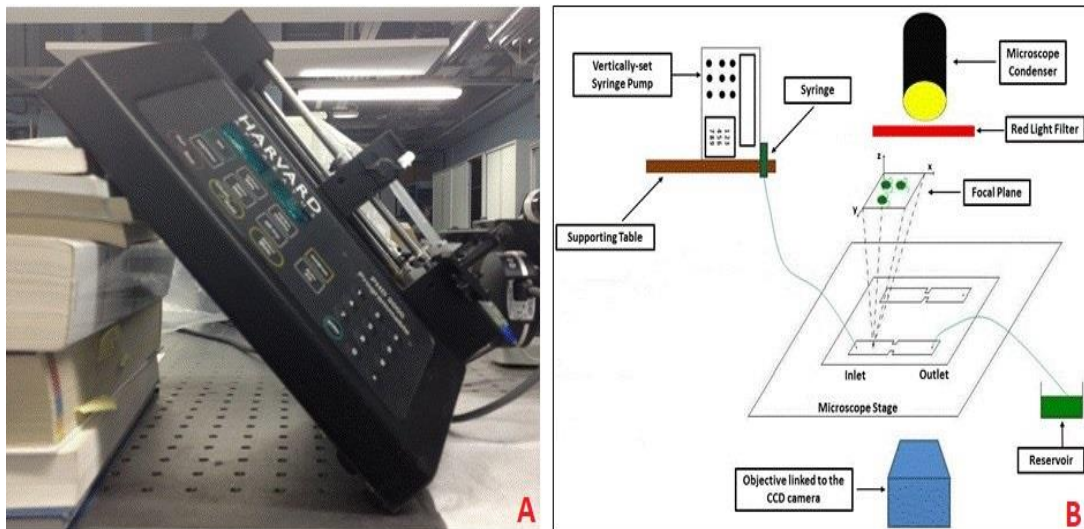


Figure 5.5 – (A) Algal sedimentation processes within the syringe were slightly inhibited by increasing the syringe pump inclination and exploiting the gravitational effects. (B) Schematic of the setup for the experiments involving DDCs. The DDC experimental setup was very similar to the living ones, with the main difference represented by the vertically-set syringe pump (see Section 3.5).

However, before describing the main objectives, the hypothesis and the results of the experiments, the next section will address some fundamental behaviours of suspended passive particles in bounded flows.

## 5.4 Fluid dynamic behaviours of passive particles in flow

During the experimental investigations, the dead algal cells were assumed to behave as passive particles (see Section 5.5) and therefore this section addresses qualitatively the most significant behaviours of suspended spherical and non-spherical particles, while flowing within macro and microchannels.

The section introduces a fundamental dimensionless number that can be used to describe the behaviour of particles in bounded flows: the particle Reynold number. The mechanisms and underlying physics of inertial lateral migration of particles will be explored, (*i.e.* a phenomenon where randomly-dispersed particles migrate across the fluid streamlines and converge to predictable equilibrium positions that depend on the geometrical cross-sectional configuration of the channel), considering also the main lift forces exerted on particles in wall-bounded fully-developed Poiseuille flows.

Although these phenomena are unlikely to occur in classical microfluidic devices [263], the inertial equilibrium positions may be seen as preferential paths for the microalgal cells and all the passive particles flowing within a given horizontal tubular PBR, depending on its processing conditions and geometrical configurations.

### 5.4.1 Particle Reynolds number

In recent decades, a large body of work has addressed the study of suspended particles in flows because transport and deposition of dispersed particles are encountered in many industrial applications (*e.g.* concrete mixing, papermaking, processes involving combustions, *etc.*) or environmental and biological phenomena (*e.g.* sediment transport in rivers, smoggy city skies, transport of particles in the respiratory system, *etc.*). [264, 265]

In conventional microfluidic devices, fluid inertia is negligible (*i.e.*  $Re \ll 1$ ), flows remain in Stokes regime and therefore, within a given channel, suspended neutrally-buoyant particles tend to follow the flow pattern with the same distribution as seen earlier in the channel inlet. [263] Inertial microfluidics work at higher  $Re$  numbers ( $\sim 1 < Re < \sim 100$ ), where flow inertia gives rise to several intriguing effects including lateral migration: a phenomenon where randomly-dispersed particles migrate across the fluid streamlines and converge to predictable equilibrium positions. [263, 266]

Fluid dynamic behaviours of suspended particles within bounded flows can be described through the dimensionless particle Reynolds number  $Re_p$ , defined as:

$$Re_p = \frac{U_M \cdot d_p^2}{\nu \cdot D_H} = Re_c \cdot \frac{d_p^2}{D_H^2} \quad (\text{eq. 5.2})$$

where  $U_M$  is the maximum flow velocity,  $D_H$  is the channel hydraulic diameter (see **Section 3.3**),  $d_p$  is the mean diameter of the particles and  $\nu$  the kinematic viscosity of the surrounding fluid.  $Re_p$  takes into account the inertial and viscous forces occurring by interactions of the cells and the fluid, while  $Re_c$  is the dimensionless channel Reynolds number that describes the unperturbed channel flow [263, 266, 267]; the definition of  $Re$  number based on the mean channel velocity can be related to  $Re_c$  as  $Re = \frac{2}{3} Re_c$ . [263]

When  $Re_p \ll 1$ , particles are subject to viscous drag and follow fluid patterns without migrating across the streamlines, whereas with increasing  $Re_p$  numbers, inertial effects prevail, the linearity of Stokes equation breaks and inertial lift forces become dominant, resulting in lateral migrations of particles. [263, 266]

## 5.4.2 The tubular pinch effect for spherical and non-spherical particles

These puzzling phenomena were firstly observed by Segrè and Silberberg in 1962 [268] who investigated the behaviours of rigid, spherical neutrally-buoyant, polymethylmethacrylate particles, undergoing fully-developed Poiseuille flows ( $Re < 30$ ) through a vertical tube. The particles were found to stay randomly distributed if the flow velocities were low or the distances from the tube mouth were small; however, for higher velocities and sufficiently long channels, the particles converged towards an equilibrium position over the cross-section, located at 0.6 radii from the axis of the tube. [268]

This radial migration was termed the tubular pinch effect to indicate that the randomly-dispersed particles converged (or they were pinched) into a narrow annular region (see **Figure 5.6 A**), which tends to be closer to the walls for increasing inertial effects. [262, 268]. Later, Matas *et al.* confirmed these results considering polystyrene spherical particles flowing in a vertical tube at  $Re$  numbers up to 2400. [262]

Nevertheless, the equilibrium positions of the particles depend also on the geometrical configuration of the channel, *e.g.* in a square cross-section channel, particles focus to four wall-centred equilibrium positions, exhibiting the so-called four-fold symmetry (see **Figure 5.6 B**). [263, 266] Moreover, in rectangular cross-section channels, uniformly-dispersed particles will initially show the four-fold symmetry but, as flowing downwards, they will converge to two equilibrium positions (see **Figure 5.6 C**), which final location depends on the channel aspect ratio ( $AR$ ) ( $AR = H/W$ , being  $H$  and  $W$  the height and the width of the channel); *e.g.* in a rectangular channel with  $AR$  of 0.5, particles were found to focus at about  $0.2 D_H$  from the centre of the long walls. [263, 266, 269]

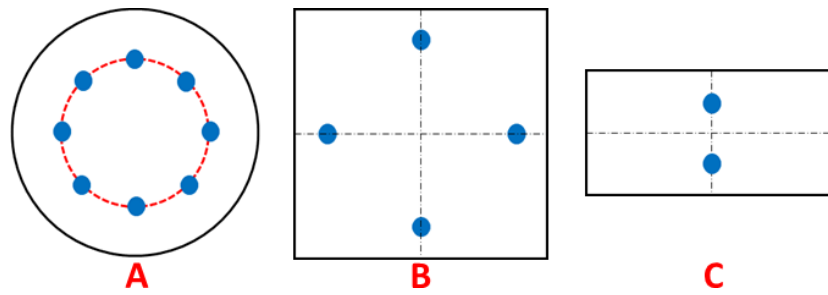


**Figure 5.6 – Final equilibrium positions of flowing particles in a straight channel with different geometrical cross-sectional configurations: circular (A), square (B) and rectangular (C). An explanation about the final two equilibrium positions shown by particles within rectangular cross-section channels was provided by Zhou and Papautsky through a two-stage migration model. [269] They assumed that initially the particles tend to exhibit four-fold symmetry but, due to their proximity to the channel corners, they are then affected by dominant wall effects acting from two directions which manage to repel the particles away towards the two final equilibrium positions. [263, 269] Adapted from [266].**

Although solid spherical particles can be employed as a simple model to study hydrodynamic behaviours of flowing particles within macro and microchannels, the majority of industrial and natural particles are non-spherical and therefore shape effects must be taken into account when studying their behaviours. [264, 265]

A complete description of their motion requires the coupled translational and rotational equations to be considered simultaneously, in order to obtain orientations and positions of the particles. [264] Therefore, although some analytical solutions have been inferred to describe the motion of non-spherical particles with simple shapes [58, 270, 271], this fluid dynamical problem is commonly solved numerically, treating the particles as points whose centre of mass are advected with the flow as a passive tracer and whose rotation can be calculated using Jeffery equations [270] or similar ones that depend on the considered fluid dynamic conditions (*e.g.* Zastawny *et al.* [272] have developed some correlations for assessing hydrodynamic forces and torques beyond the creeping flow region). [264, 265]

However, both numerical and experimental investigations concerning elliptical particles, disks and rods have shown that these rigid non-spherical particles had converged to predictable inertial equilibrium positions, when flowing laminarily through straight circular pipes. [273, 274]

### 5.4.3 The governing lift forces

Starting from these counter-intuitive results, a series of experiments were carried out to explore the underlying physical mechanisms of these phenomena, finding that when rigid particles undergo wall-bounded Poiseuille flows, apart from the viscous drag acting on them, there are four further lateral forces that must be taken into account: the Magnus force, the Saffman force, the wall lift force and the shear gradient force (see **Figure 5.7**). These forces were found to govern the inertial lateral migrations and therefore they will be discussed in this section, considering the specific case of a rigid spherical particle while undergoing a fully-developed Poiseuille flow through a pipe and demonstrating that the migrating phenomenon can be explained taking into account both the inertial effects and those induced by the presence of the tube walls. [262, 266]

Firstly, the solid boundaries create a fluid velocity gradient (shear rate) which leads to a shear-induced rotational motion of the particle and a consequent asymmetry of the streamlines, causing the fluid velocity at the bottom of the sphere to be lower than the one at its upper part. Consequently, due to the Bernoulli principle, a transverse pressure difference occurs on the surface of the particle, giving rise to a particular lift force, called Magnus force, which moves the sphere in the direction of the lower-pressure side [262, 275]. If the particle is simultaneously rotating and translating, the direction of the Magnus force is perpendicular to the plane defined by the vector of the relative spherical velocity and the axis of rotation (see **Figure 5.7 A**). [266]

Moreover, solid walls generate an extra drag [72] that makes the particle lag behind the fluid, resulting in a Stokeslet velocity field which interacts with the velocity gradient of the bulk flow, leading to a lateral lift force called Saffman force [276]. If the considered particle is neutrally-buoyant, no Saffman force will act on it since its Stokeslet field is balanced by an opposite Stokeslet due to the fluid velocity profile. Nevertheless, in the case of non-neutrally buoyant particles, Saffman force will be directed to the centreline when the particles lag behind the flow and toward the walls when the particles lead the flow (see **Figure 5.7 B**). [262, 266, 277]

The presence of wall also modifies the flow field around the particle and therefore the inertial effects will differ from those of a particle in an unbounded flow. Considering a single wall on one side of the immersed particle (*i.e.* when the characteristic dimension of the particle is much smaller than the dimension of the channel), the main effects of the boundary will be to decelerate the motion of the sphere (or analogously, walls increase the drag coefficient) and to repel the particle away through a transverse lift force, causing its migration towards the pipe centre. These effects are observed whether the particle is moving either in perpendicular or parallel directions to the wall; in the latter case, an additional wall lift force occurs, directed perpendicularly to the main flow direction (see **Figure 5.7 C**). [262, 266, 278] Finally, the presence of solid boundaries generates a parabolic fluid velocity profile which causes a dissymmetry of the relative velocity (*i.e.* its magnitude is much higher on the left side of the particle than that on the right side), resulting in a lower pressure on the left side of the particle and a consequent shear gradient lift effect that forces particles to migrate towards the walls (see **Figure 5.7 D**). [262, 263, 266]

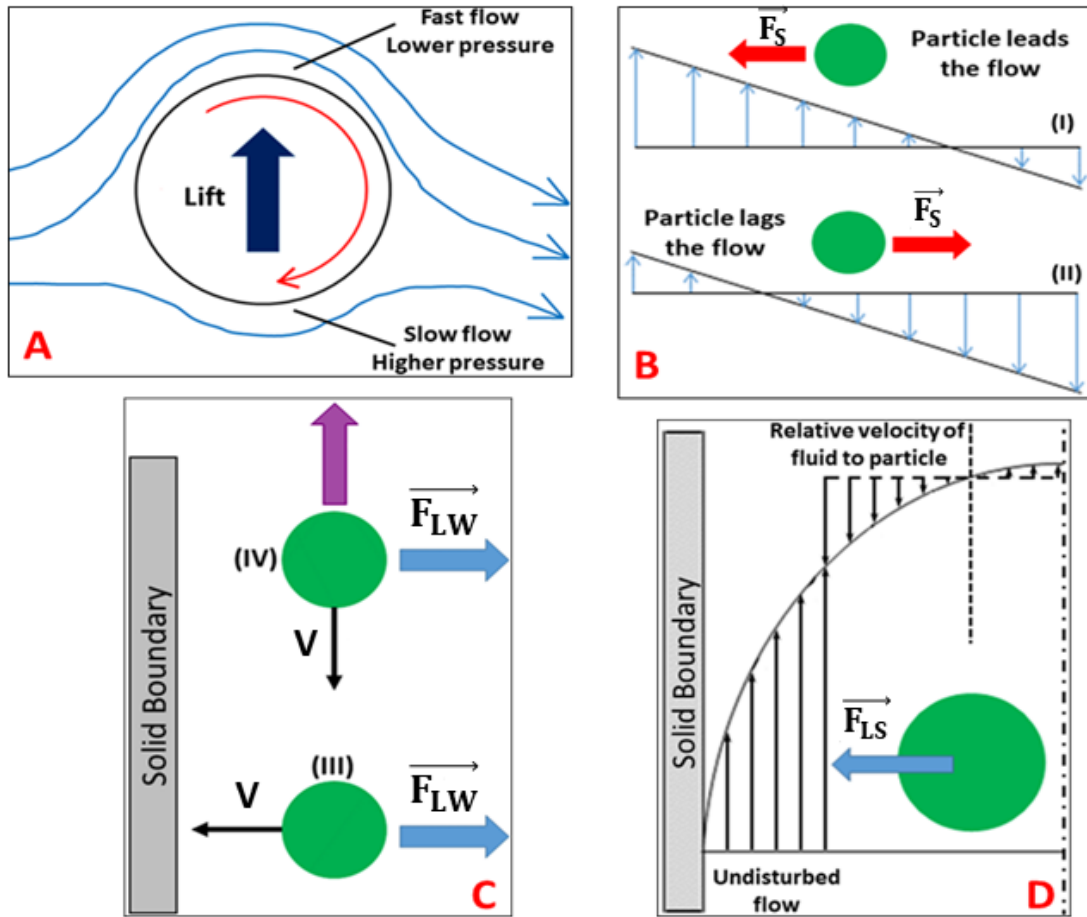
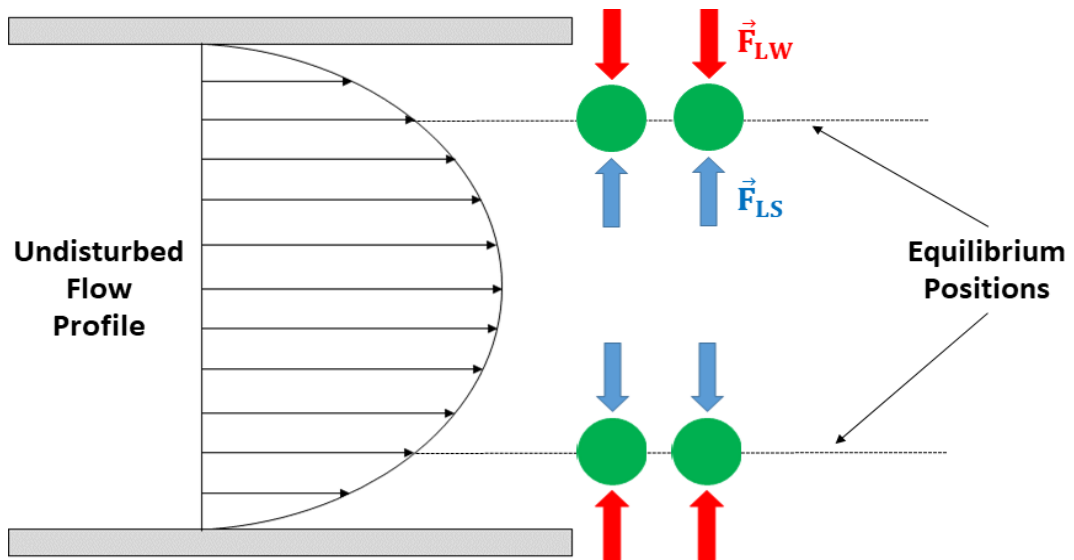


Figure 5.7 – The lateral lift forces acting on a spherical rigid particle when undergoing wall-bounded fully-developed Poiseuille flows. (A) The Magnus force: assuming no slip velocity at the surface of the particle, the shear-induced rotational motion causes the pressure at the bottom of the sphere to be higher than the one at its upper part, giving rise to the Magnus effect. The Magnus effect is important in the study of the physics of many ball sports since, owing to this phenomenon, a spinning sphere curves away from the arc it would follow if it was not spinning. [266, 279] (B) The Saffman force  $\vec{F}_S$  is independent of the shear-induced rotation of the particle and is always directed towards the side where the magnitude of the relative velocity is maximum. [266] For non-neutrally buoyant spherical particles in a vertical flow, this force was found to be directed towards the walls for particles leading the flow (I) and towards the axis for particles lagging the flow (II). [262, 266] (C) When a solid spherical particle moves with a relative velocity  $V$  in the proximity of a given solid boundary, its motion will be decelerated and the sphere will be repelled away through a wall-induced lift force  $\vec{F}_{LW}$ . These effects are observed whether the particle is moving either in perpendicular (III) or parallel (IV) directions to the wall; in the latter case, an additional wall lift force occurs, directed perpendicularly to the main flow direction (see the purple arrow). [262, 266, 278] (D) Due to the parabolic velocity profile induced by the presence of boundaries, the relative velocity of fluid to particle is higher on the wall side and therefore the resulting shear gradient lift force  $\vec{F}_{LS}$  will direct toward the near-by wall. [266] Adapted from [266, 280]

Theoretically, all the forces described above and shown in **Figure 5.7** contribute to the particles lateral migration phenomenon; however, the Saffman and Magnus forces are often negligible, therefore the wall lift force and the shear gradient lift force are the dominant effects and the balance between them can explain the equilibrium particle positions (see **Figure 5.8**) [263, 266]



**Figure 5.8** – Inertial lift forces exerted on rigid spheres in a fully-developed Poiseuille flow. The balance between the shear gradient lift force  $\vec{F}_{LS}$  (blue arrows) and the wall-induced lift force  $\vec{F}_{LW}$  (red arrows) results in the inertial equilibrium positions. [266, 267] Adapted from [266].

Lateral migration phenomena are exploited in inertial microfluidics systems that have been attracting attention owing to their ability to focus, concentrate and separate particles of different characteristics and sizes, making them ideal for applications ranging from flow cytometry to blood cells separation. [266, 267, 281] Inertial microfluidics have also been employed successfully for selective shape-based separations of microalgal cells, *e.g.* the strain *Euglena gracilis*. [282, 283]

#### 5.4.4 Potential implications for photobioreactors

These lateral migration phenomena and the resulting equilibrium positions may also be seen as preferential paths for microalgal cells and all passive particles flowing within a given horizontal tubular PBR. Depending on its processing conditions and geometrical configuration; lateral migrations may affect the advected dead algal cells or the plastic beads, usually employed in PBRs for enhancing the mixing levels and cleaning purposes (see **Section 2.6.2.3**).

Therefore, these potentially detrimental phenomena must be taken into account because, as explained in the **2<sup>nd</sup> Chapter** and in the **Section 5.2.1**, accumulative behaviours or preferential trajectories may cause solar light attenuation, a decrease of the overall mixing levels, *etc.* In addition, when inertial effects increase (*i.e.* for higher *Re* numbers), the equilibrium positions will be closer to PBRs walls. [262, 268]

It must also be stressed that inertial migrations in PBRs would occur under “laminar processing conditions” (*i.e.*  $Re < 2400$  [262]) while, when microalgae are turbulently-pumped other damaging phenomena may arise, *e.g.* some energy-dissipating microeddies may be generated that could lead to shear-induced negative effects on the cells, depending on their relative dimensions to the length scale of the microeddies, this is addressed in the **6<sup>th</sup> Chapter**. [139, 198]

After giving context for the study of passive particles in flows, the next section discusses the results obtained through the experimental investigations of the dead algal cells. Firstly, the main objectives and assumptions concerning the experiments will be described, then the qualitative fluid dynamic behaviours of the DDCs within the microchannels will be analysed and a comparison between the results of living and dead *Dunaliella* cells is made.

## **5.5 Exploring dead cell behaviour: objectives and procedures**

In this section the hypothesis and procedures of the experiments concerning the dead *Dunaliella* cells (DDCs) are described. The main consequences that may occur if dead microalgal concentrations increase consistently within PBRs are that DDCs tend to either sediment or be passively advected by the flow around the reactor (see **Section 5.2.4**). Therefore, the experiments were aimed to study the behaviours of the cells dragged by the flow, exploring and quantifying how they were affected by the microgeometries. Assuming that their fluid dynamic experiences in the channels resembled the ones that actually occur in real PBRs equipped with static mixers, it is possible to assess whether the PBR geometrical arrangement can be exploited to prevent the negative effects of dead cells on cultures.

DDCs were considered as passive particles in order to investigate the role of motility in algal behaviours. Comparing the differences between dead and living algal cells' responses to the same experimental conditions, demonstrated that living microalgae cannot be considered as passive particles (see **Section 2.10**).

Similarly to what had been done for the living cells, dilute algal suspensions were studied at the population level, without considering their actual fluid dynamic experiences within the different contraction/expansion geometries.

In particular, after the algal cells had been killed and the vials had cooled down to room temperature, DDCs were ready for experimental investigations and therefore, after arranging the experimental setup, the dead cells could be drawn into the syringe and propelled in the channels at the desired flow rate. For comparison purposes, the same flow rates used previously were investigated (*i.e.*  $3 \mu\text{l}\cdot\text{min}^{-1}$  and  $5 \mu\text{l}\cdot\text{min}^{-1}$ , see **Section 4.8.2**) and, although the cells were dead (*i.e.* they could not be affected by phototaxis), the red filter was used to employ the same incident wavelength (*i.e.* the same depth of field) for both living and dead cells.

Once steady state was reached, some experimental videos were acquired and analysed through ImageJ (see **Section 3.7**), attaining the algal cells positions and processing the data using specifically-tailored Matlab codes, which allowed the algal trajectories, the microalgal swimming velocity vectors spatial distributions and the algal cell distribution percentages in the different zones of the channels to be assessed through the same microgrid used previously (see **Section 4.9.3**). This allowed to explore DDCs fluid dynamic behaviours to be examined under comparable experimental conditions.

## **5.6 Quantification of the microgeometries effects on dead *Dunaliella* cells**

The experimental parameters are summed up in the **Table 5.3**, where the dead *Dunaliella* cells (DDCs) buoyancy effects have been estimated through the dimensionless buoyancy number  $B_N$  (see **Section 5.3.2**) and the DDCs behaviours within the microchannels have been assessed through the particle Reynolds number  $Re_p$  (see **Section 5.4.1**).

**Table 5.3 – The main experimental parameters of the experiments at flow rates of 3  $\mu\text{l}\cdot\text{min}^{-1}$  and 5  $\mu\text{l}\cdot\text{min}^{-1}$ , assessed for both the straight region (SR) and the contraction-expansion geometries (CEG) of the microchannels. The data has been obtained based on an average diameter of 17.5  $\mu\text{m}$  for the DDCs (see Section 6.4.3).**

	Flow Rate 3 $\mu\text{l}\cdot\text{min}^{-1}$						
	ECR 4-1		ECR 7-1		Elongated		
	SR	CEG	SR	CEG	SR	CEG	
$\bar{U}$ [ $\text{m}\cdot\text{s}^{-1}$ ]	$1.22 \times 10^{-3}$	$4.38 \times 10^{-3}$	$1.23 \times 10^{-3}$	$8.62 \times 10^{-3}$	$1.23 \times 10^{-3}$	$8.62 \times 10^{-3}$	
$Re$	$1.78 \times 10^{-1}$	$4.17 \times 10^{-1}$	$1.78 \times 10^{-1}$	$5.63 \times 10^{-1}$	$1.78 \times 10^{-1}$	$5.63 \times 10^{-1}$	
$B_N$	$5.73 \times 10^{-3}$	$1.60 \times 10^{-3}$	$5.71 \times 10^{-3}$	$8.12 \times 10^{-4}$	$5.69 \times 10^{-3}$	$8.10 \times 10^{-4}$	
$Re_p$	$3.08 \times 10^{-3}$	$1.68 \times 10^{-2}$	$3.10 \times 10^{-3}$	$4.84 \times 10^{-2}$	$3.12 \times 10^{-3}$	$4.85 \times 10^{-2}$	
	Flow Rate 5 $\mu\text{l}\cdot\text{min}^{-1}$						
	$\bar{U}$ [ $\text{m}\cdot\text{s}^{-1}$ ]	$2.04 \times 10^{-3}$	$7.29 \times 10^{-3}$	$2.04 \times 10^{-3}$	$1.44 \times 10^{-2}$	$2.05 \times 10^{-3}$	$1.44 \times 10^{-2}$
	$Re$	$2.96 \times 10^{-1}$	$6.95 \times 10^{-1}$	$2.96 \times 10^{-1}$	$9.38 \times 10^{-1}$	$2.97 \times 10^{-1}$	$9.38 \times 10^{-1}$
	$B_N$	$3.44 \times 10^{-3}$	$9.60 \times 10^{-4}$	$3.43 \times 10^{-3}$	$4.87 \times 10^{-4}$	$3.41 \times 10^{-3}$	$4.86 \times 10^{-4}$
	$Re_p$	$5.14 \times 10^{-3}$	$2.80 \times 10^{-2}$	$5.16 \times 10^{-3}$	$8.07 \times 10^{-2}$	$5.20 \times 10^{-3}$	$8.09 \times 10^{-2}$

As expected, under the chosen experimental conditions, DDCs were characterised by low  $Re_p$  values ( $Re_p \ll 1$ ), meaning that the cells were dragged passively by the flow, following the streamlines without exhibiting any lateral migration (see Section 5.4.1). Moreover, the relatively low  $B_N$  values indicated that the sedimentation phenomena, which affected the experimental investigations (see Section 5.3.2), mainly occurred in the “static parts” of the experimental setup (*i.e.* the vials and the syringes), while they were neglectable within the microchannels. As a consequence, if a tubular PBR were run at processing conditions similar to our experimental conditions, the percentages of passively-advected DDCs would be much higher than those of the sedimenting ones.

In order to understand the results for DDCs, the main outcomes obtained for the living cells are summarised in the Table 5.4, emphasising their fluid dynamic behaviours and algal cell distribution percentages (ACDPs) at the walls (see Section 4.9.4).

**Table 5.4 – The main experimental results for living *Dunaliella* cells flowing through the different microchannels at both 3  $\mu\text{l}\cdot\text{min}^{-1}$  and 5  $\mu\text{l}\cdot\text{min}^{-1}$ .**

<b>Fluid dynamic conditions</b>	<b>At 3 <math>\mu\text{l}\cdot\text{min}^{-1}</math></b>	<b>At 5 <math>\mu\text{l}\cdot\text{min}^{-1}</math></b>
<b>Fully-developed flow [A1 Zone]</b>	The cells could overcome the fluid streamlines and partially interact with the walls.	The cells were advected by the flow and showed lower walls interaction percentages than those at 3 $\mu\text{l}\cdot\text{min}^{-1}$ .
<b>Approaching the microgeometry entrance [B1 zone]</b>	Due to the entrance effects, the cells were advected by the flow. The ACDPs at the walls were lower than those of the A1 zone.	Due to the entrance effects, the cells were advected by the flow. The ACDPs at the walls were slightly lower than those of the A1 zone and those observed at 3 $\mu\text{l}\cdot\text{min}^{-1}$ .
<b>Algal Plume [C1, D1, E1 zones]</b>	The algal plume reduced the walls interactions and compacted the cells; at increasing distances from the microgeometries, these effects were seen to decrease with different fading velocities that depended on the geometry and flow rate.	The algal plume reduced the walls interactions and compacted the cells; at increasing distances from the microgeometries, these effects were seen to reduce with different fading velocities that depended on the used geometry and flow rate. For all the employed geometries, the walls interactions were slightly lower than those observed at 3 $\mu\text{l}\cdot\text{min}^{-1}$ and the plume effects faded slower.
<b>Algal Plume [ECR 4-1]</b>	The geometry-induced effects were observed to fade in a relatively short portion of the channel.	The geometry-induced effects were observed to fade in a relatively short portion of the channel.
<b>Algal Plume [ECR 7-1]</b>	The walls interactions were significantly reduced and the plume effects were still consistent along the complete displayable length of the channel.	The walls interactions were significantly reduced and the plume effects were still consistent along the complete displayable length of the channel.
<b>Algal Plume [Elongated]</b>	The walls interactions were lower and the plume effects lasted longer, compared to the ones observed for the ECR 7-1.	The walls interactions were lower and the plume effects lasted longer, compared to the ones observed for the ECR 7-1.

The results for DDCs are discussed considering their fluid dynamic behaviours observed within the microchannels and a comparison is made between the results of living and dead *Dunaliella* cells, focusing particular attention on their interactions with the walls due to the inertial effects induced by the microgeometries.

# ECR 4-1 – DEAD Cells – $3 \mu\text{l}\cdot\text{min}^{-1}$

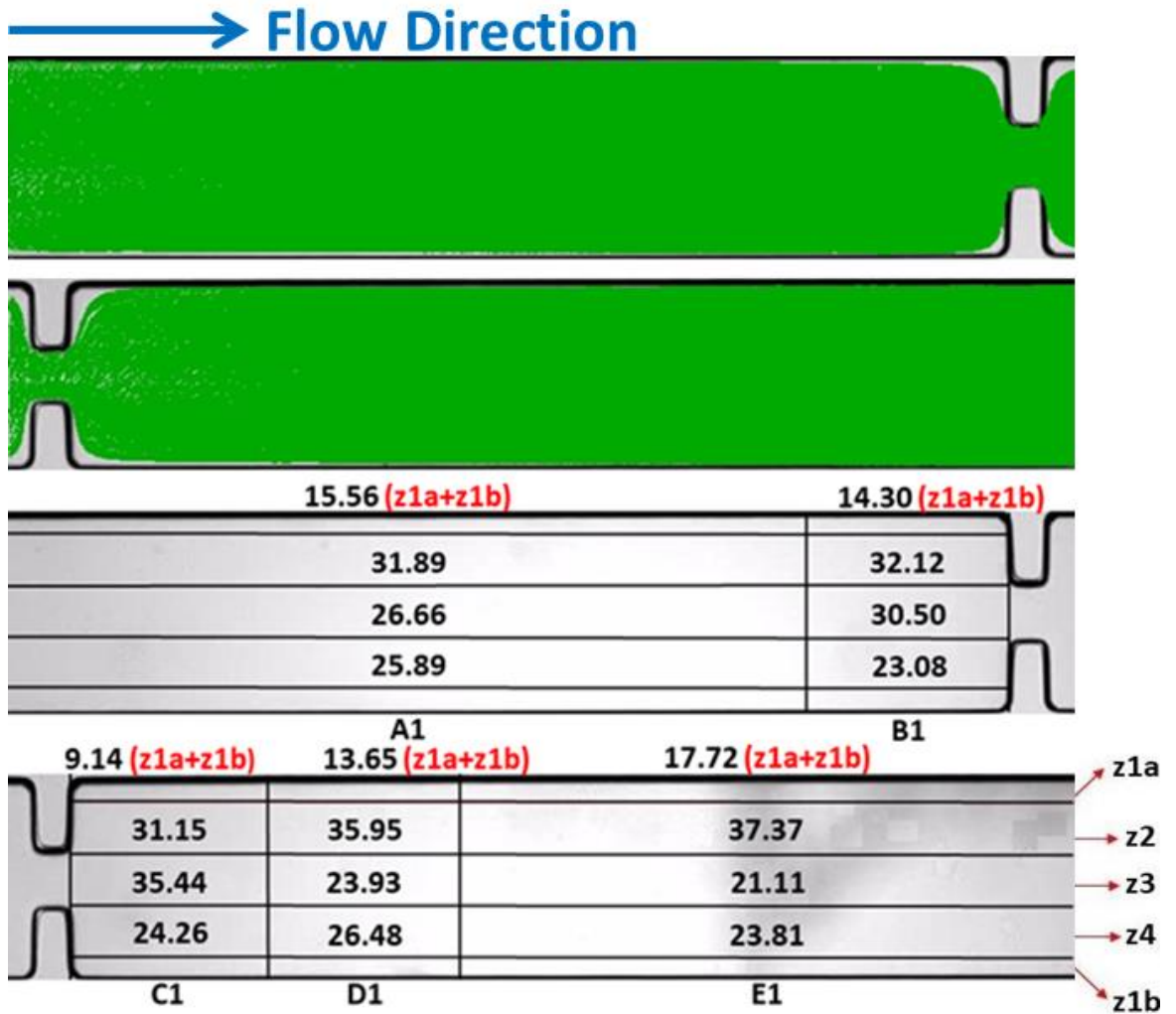


Figure 5.9 – Algal swimming trajectories and dispersion percentages in the ECR 4-1 geometry at  $3 \mu\text{l}\cdot\text{min}^{-1}$ . The experimental videos were captured using a resolution of  $688 \times 516$  pixels, the 4X objective and an exposure time of  $\sim 1$  ms (see Section 3.6.1). For statistical reasons, all the results were obtained by analysing at least three experimental videos.

# ECR 7-1 – DEAD Cells – $3 \mu\text{l}\cdot\text{min}^{-1}$

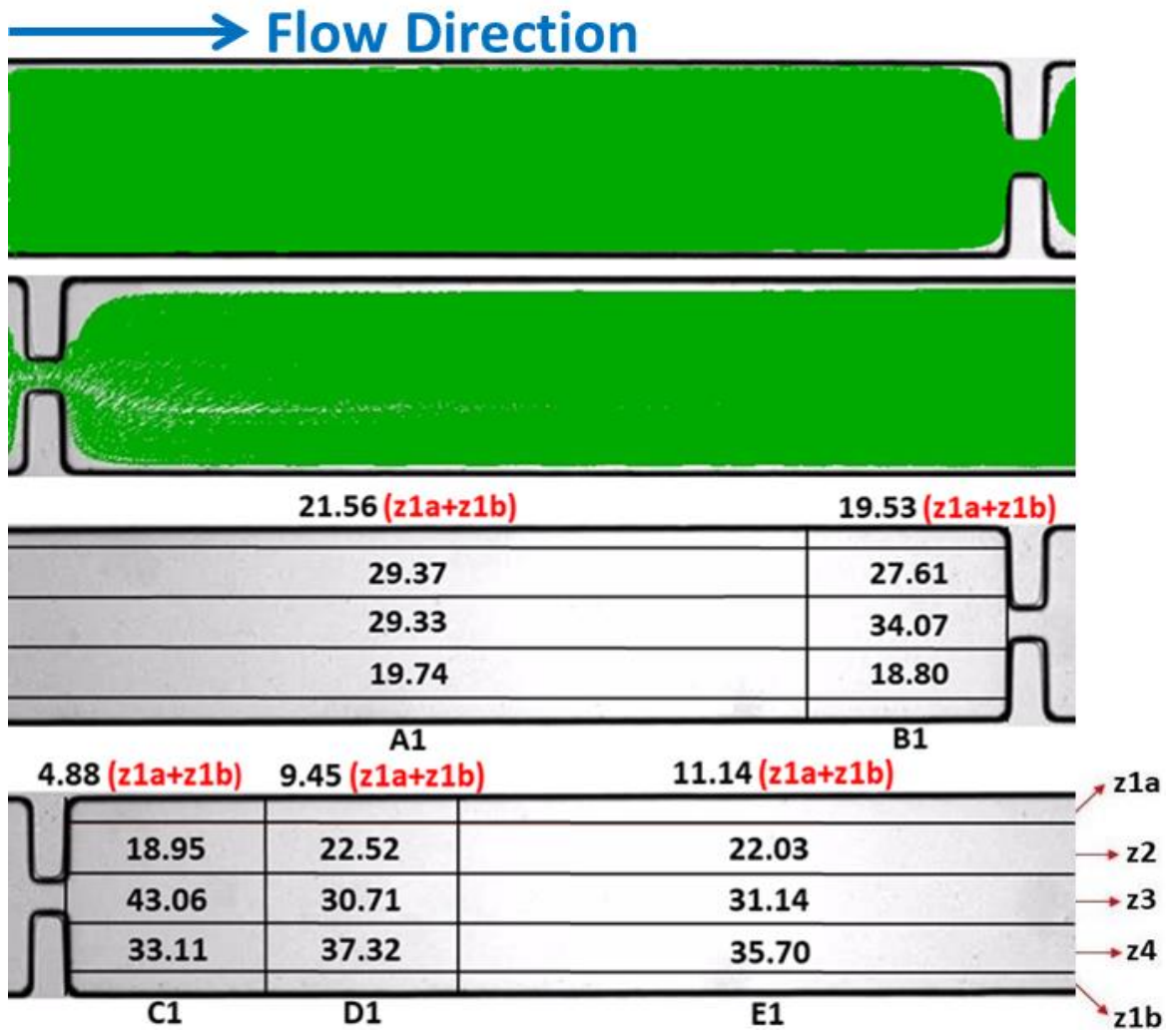


Figure 5.10 – Algal swimming trajectories and dispersion percentages in the ECR 7-1 geometry at  $3 \mu\text{l}\cdot\text{min}^{-1}$ . The experimental videos were captured using a resolution of  $688 \times 516$  pixels, the 4X objective and an exposure time of  $< 1$  ms (see Section 3.6.1). For statistical reasons, all the results were obtained by analysing at least three experimental videos.

## Elongated – DEAD Cells – $3 \mu\text{l}\cdot\text{min}^{-1}$

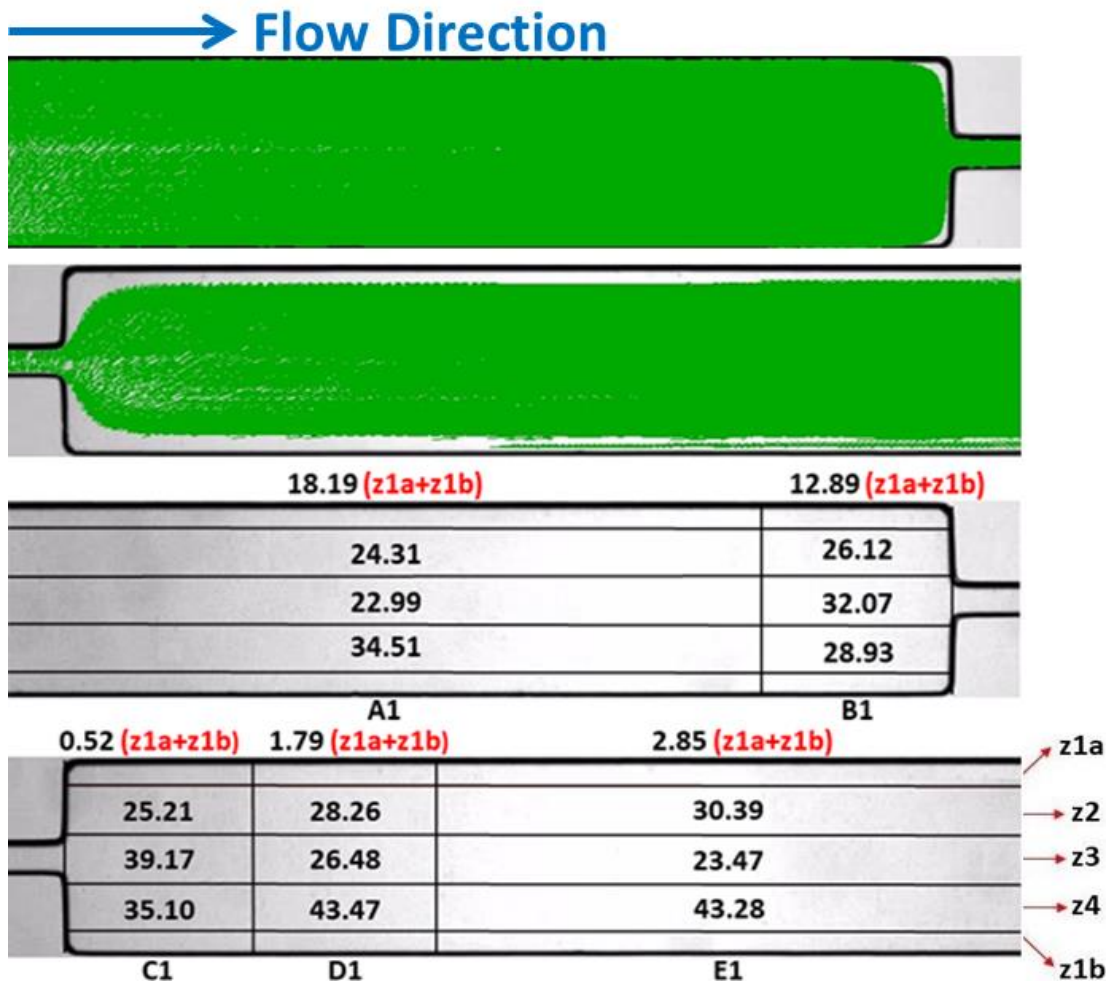


Figure 5.11 – Algal swimming trajectories and dispersion percentages in the elongated geometry at  $3 \mu\text{l}\cdot\text{min}^{-1}$ . The experimental videos were captured using a resolution of  $688 \times 516$  pixels, the 4X objective and an exposure time of  $< 1$  ms (see Section 3.6.1). For statistical reasons, all the results were obtained by analysing at least three experimental videos.

# ECR 4-1 – DEAD Cells – $5 \mu\text{l}\cdot\text{min}^{-1}$

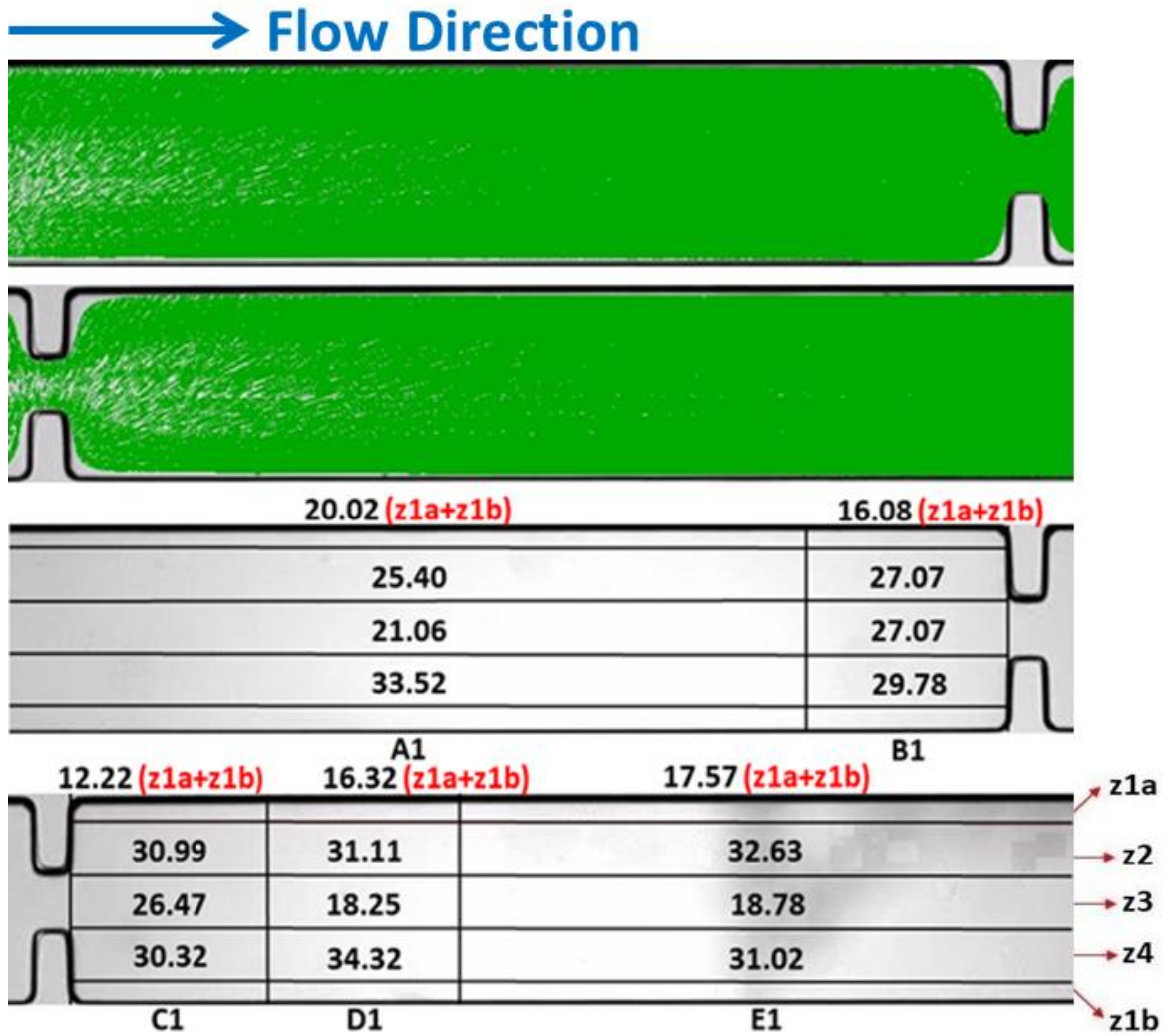


Figure 5.12 – Algal swimming trajectories and dispersion percentages in the ECR 4-1 geometry at  $5 \mu\text{l}\cdot\text{min}^{-1}$ . The experimental videos were captured using a resolution of  $688 \times 516$  pixels, the 4X objective and an exposure time of  $\sim 1$  ms (see Section 3.6.1). For statistical reasons, all the results were obtained by analysing at least three experimental videos.

**ECR 7-1 – DEAD Cells –  $5 \mu\text{l}\cdot\text{min}^{-1}$**

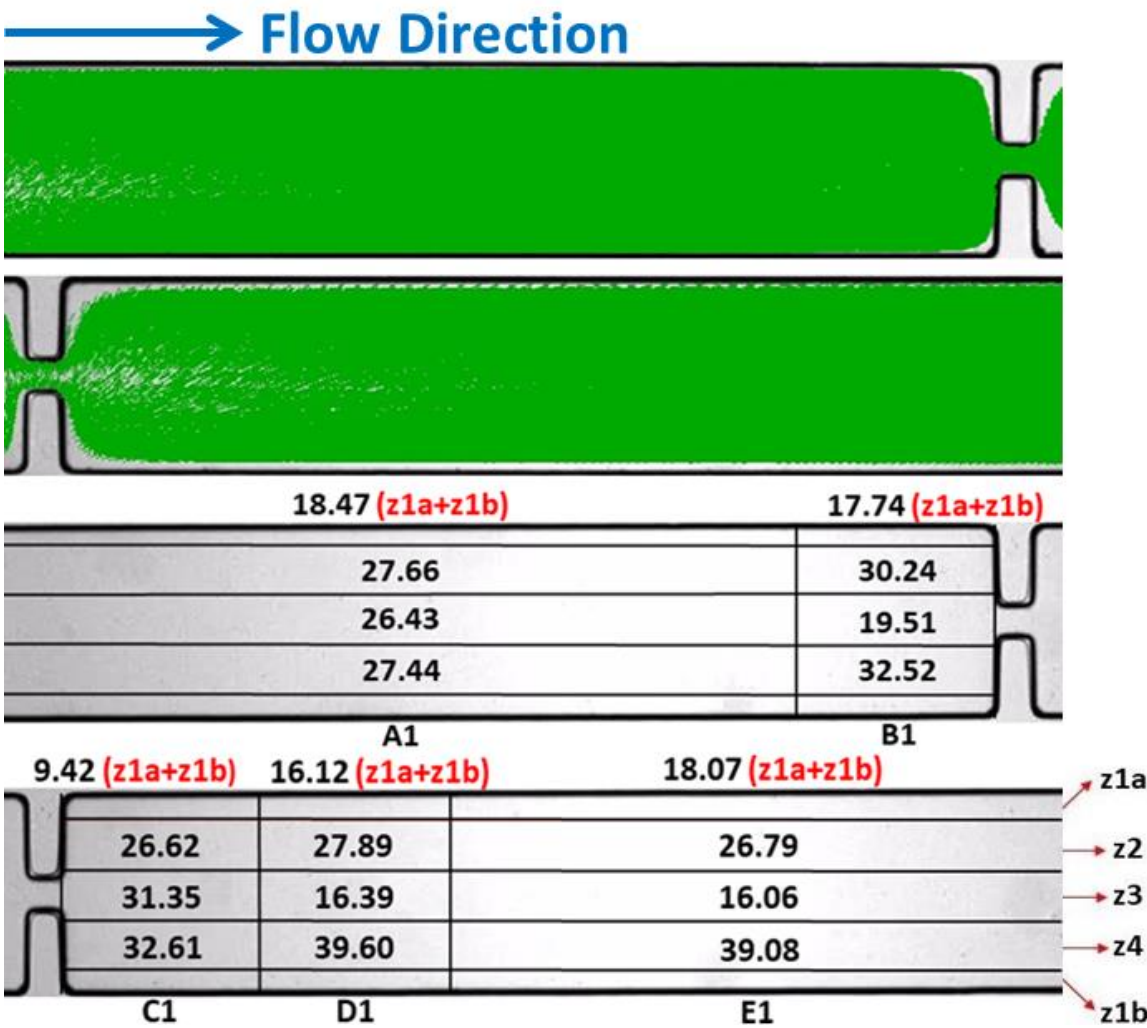


Figure 5.13 – Algal swimming trajectories and dispersion percentages in the ECR 7-1 geometry at  $5 \mu\text{l}\cdot\text{min}^{-1}$ . The experimental videos were captured using a resolution of 688 x 516 pixels, the 4X objective and an exposure time of  $< 1 \text{ ms}$  (see Section 3.6.1). For statistical reasons, all the results were obtained by analysing at least three experimental videos.

## Elongated – DEAD Cells – $5 \mu\text{l}\cdot\text{min}^{-1}$

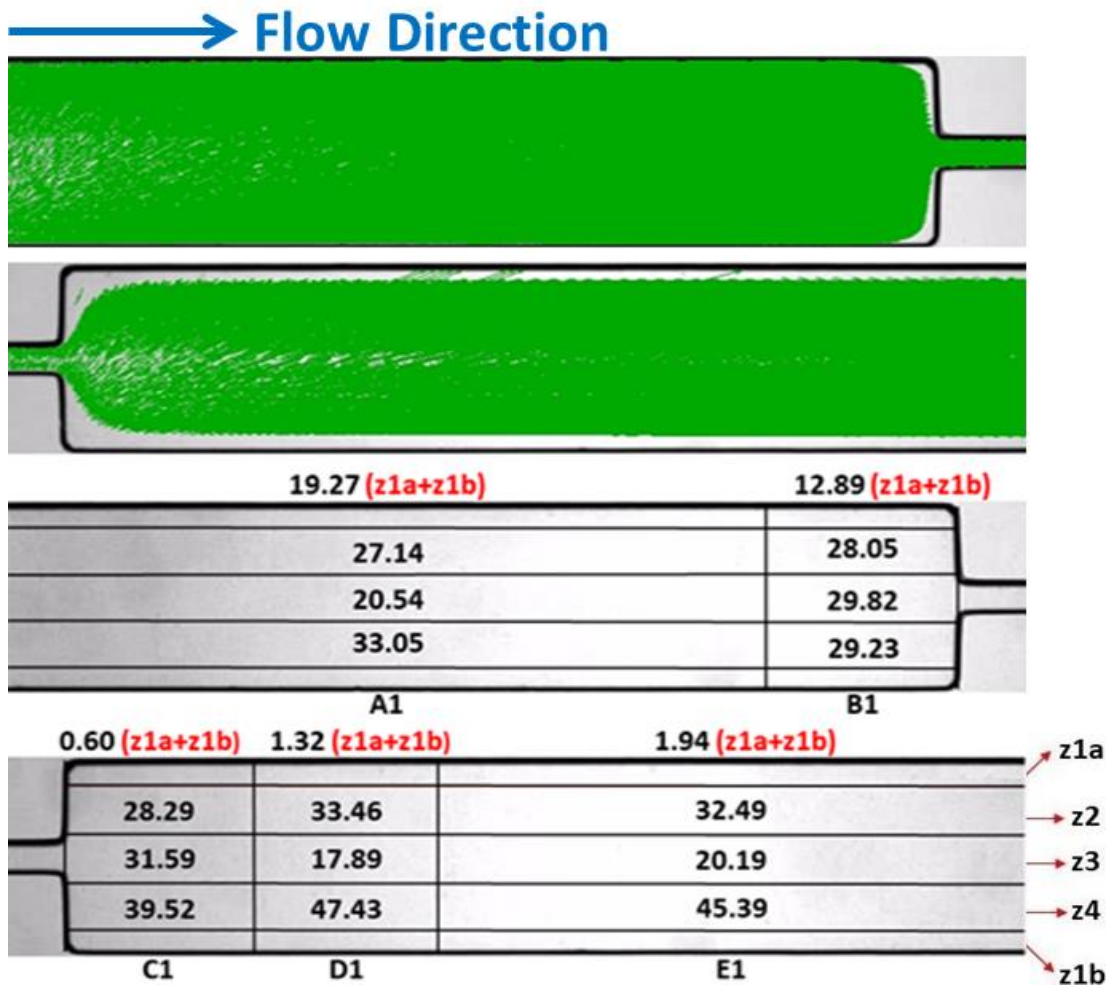


Figure 5.14 – Algal swimming trajectories and dispersion percentages in the elongated geometry at  $5 \mu\text{l}\cdot\text{min}^{-1}$ . The experimental videos were captured using a resolution of  $688 \times 516$  pixels, the 4X objective and an exposure time of  $< 1$  ms (see Section 3.6.1). For statistical reasons, all the results were obtained by analysing at least three experimental videos.

### Qualitative fluid dynamic behaviours of the dead cells

At both flow rates, under fully-developed flow conditions (*i.e.* in the A1 zones), DDCs were passively advected by the flow throughout the whole geometry of the channel and, while approaching the contraction-expansion geometries (CEGs) (*i.e.* the B1 zones), DDCs were drawn over by them, due to the increasing inertial effects. A general trend observed in the B1 zone was an increase of the ACDPs values in the centreline (*i.e.* the z3 zones). As shown in the **Figures 5.15** and **5.16**, at both flow rates, the drawing effects of the ECGs caused slight reductions of the DDCs walls interactions.

Similarly to what happened for the living cells, at the exit of the CEGs, an algal plume was developed which mostly compacted the DDCs along the channel and reduced their wall interactions (see the decreases of the walls ACDPS between the zone B1 and C1 in the **Figures 5.15** and **5.16**); however, these effects were characterised by different fading velocities that depended on the geometry and flow rate.

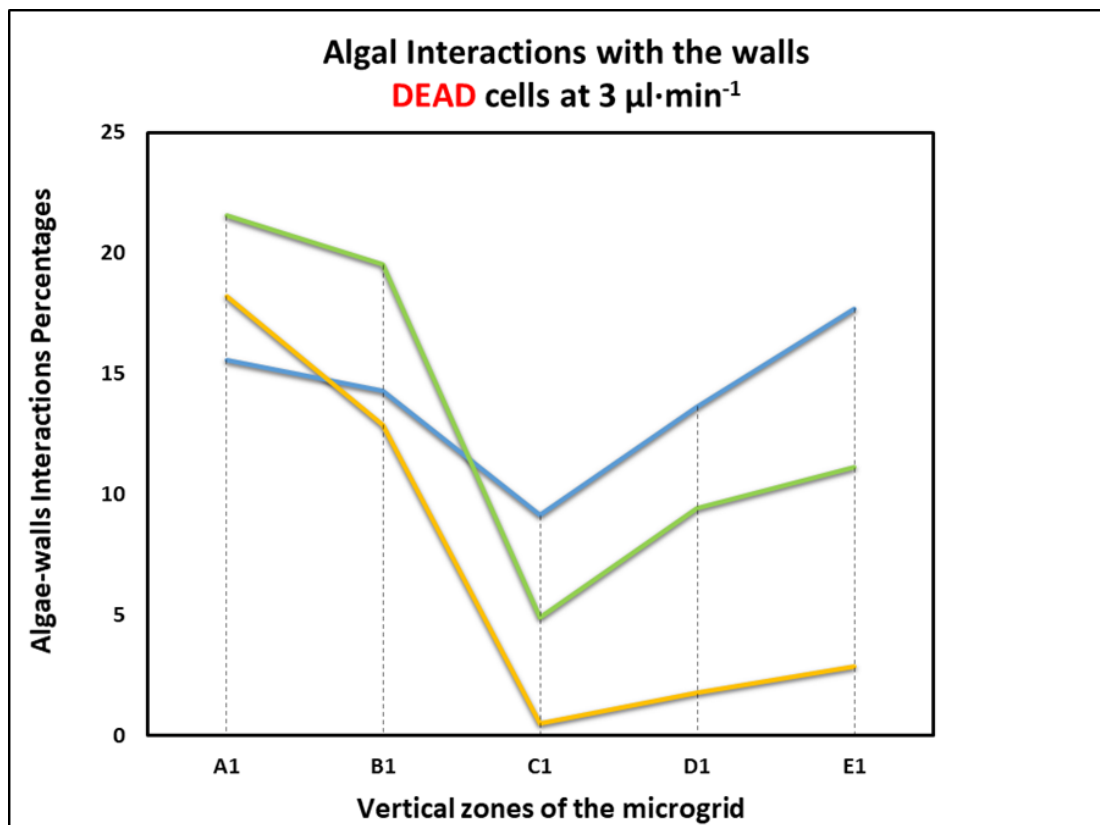


Figure 5.15 – The dead algal cells dispersion percentages close to the walls induced by the various microgeometries at  $3 \mu\text{l}\cdot\text{min}^{-1}$ . Both the entrance effects (*i.e.* those in the B1 zone) and the inertial effects induced by the ECR 4-1 geometry were not significant, since the algal walls interactions remained consistent within this channel.

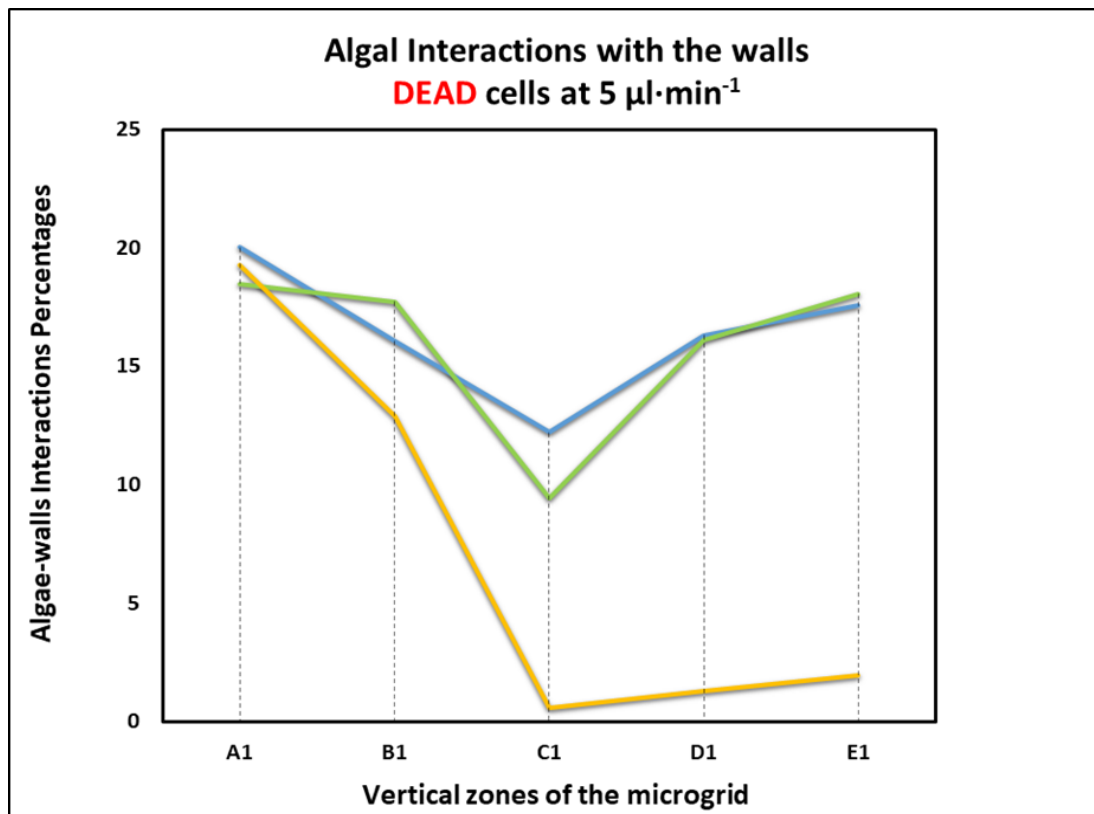


Figure 5.16 – The dead algal cells dispersion percentages close to the walls induced by the various microgeometries at 5  $\mu\text{l}\cdot\text{min}^{-1}$ . Although in PBRs, the concentration of sedimenting and passively-advected dead cells must be kept as low as possible by routinely checking the cultures and taking precautions to limit the potential causes of algal cells demise (see Table 5.1), the optimisation of the PBR geometrical configuration must take into account DDCs fluid dynamic behaviours, since they may cause shading phenomena or show preferential paths (e.g. the tubular pinch effect, see Section 5.4.2), depending on the processing conditions.

#### Specific effects of the microgeometries on the dead cells

At both flow rates, within the ECR 4-1 geometry, DDCs behaviours were comparable to the ones of the living cells (see **Figure 4.28** and **4.29**) as the geometry exit effects involved only a short portion of the channel, *i.e.* the walls ACDPs values were found to become similar to the ones before the contraction in a relative short distance.

The cells exhibited opposite behaviours within the ECR 7-1 geometry at the two flow rates; at 3  $\mu\text{l}\cdot\text{min}^{-1}$  the walls interactions were significantly reduced and the plume effects were still consistent along the complete displayable length of the channel, while at 5  $\mu\text{l}\cdot\text{min}^{-1}$ , the geometry-induced effects were observed to fade rapidly. The elongated geometry proved to be the only one for which the walls ACDPs values and fading velocity of the plume effects were comparable to the ones of the living cells for both flow rates.

### **Comparison between the living and the dead cells behaviours**

These results have clearly demonstrated that living and dead cells exhibit different fluid dynamic behaviours for increasing inertial effects. Specifically, as described in the **Section 4.9.4**, for both flow rates, the algal plumes compacted the living cells, preventing them from swimming throughout the whole geometry; a general trend observed for the living swimming cells was that the higher the flow inertia, the longer and more consistent the algal plume effects were.

When the flow rate was increased, especially within the “shorter geometries” channels (*i.e.* the ECR 4-1 and ECR 7-1 geometries), the DDCs walls interactions were always seen to rise accordingly, or in other words, the walls ACDPs values at  $5 \mu\text{l}\cdot\text{min}^{-1}$  were slightly higher than those at  $3 \mu\text{l}\cdot\text{min}^{-1}$ , meaning that for growing inertial effects, the tendency for biofouling of the dead cells becomes higher.

For both flow rates, the walls ACDPs values of the dead cells were seen to be always higher than those observed for the living ones (see the **Figures 4.28, 4.29, 5.15 and 5.16**), suggesting that the number of dead cells that flowed close to the channel boundaries was higher.

As can be seen considering the velocity vectors spatial distributions of the dead algal cells (see **Figure 5.17 and 5.18**); for both flow rates and along the whole channel, the dead cells were found to flow slower than the living ones (see **Figures 4.30 and 4.31**), *i.e.* they were characterised by longer average residence time values in the proximity of the walls, meaning that their shading phenomena were greater than those showed by the living cells at the same conditions.

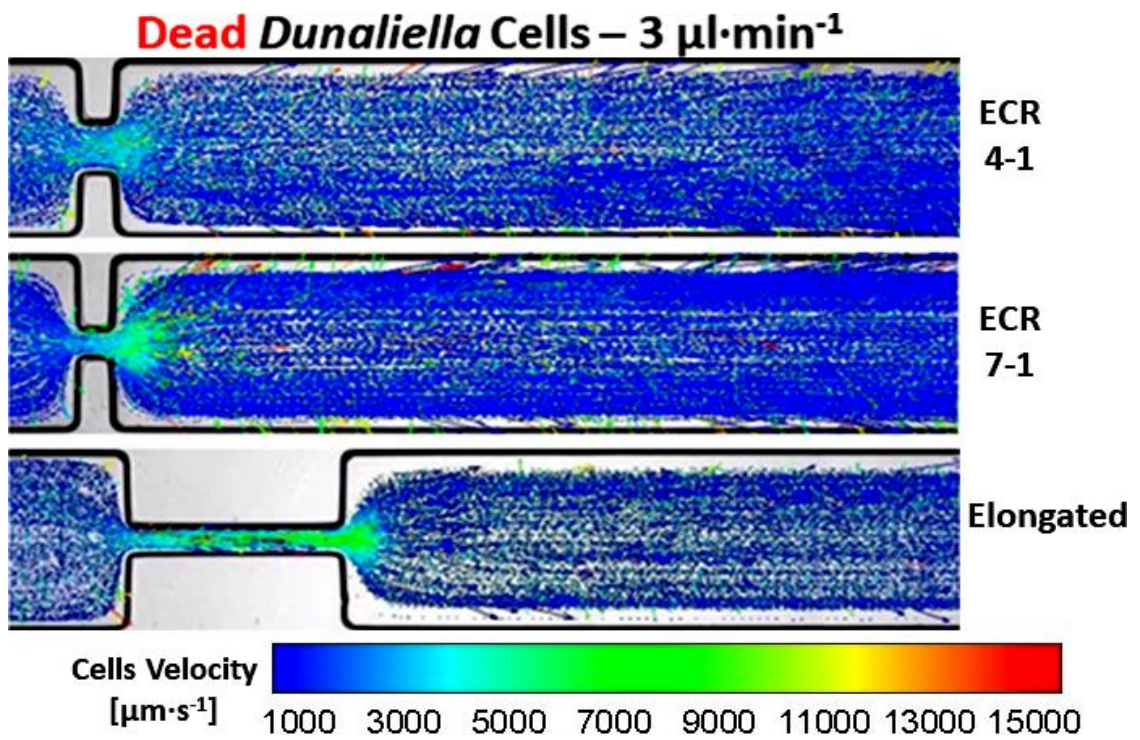


Figure 5.17 – The velocity vectors spatial distributions of dead *Dunaliella* cells at 3  $\mu\text{l}\cdot\text{min}^{-1}$ . Similarly to what happened for the living cells, when DDCs entered the expansion regions, the algal plumes affected their spatial distributions, leading to the formation of cell depleted regions.

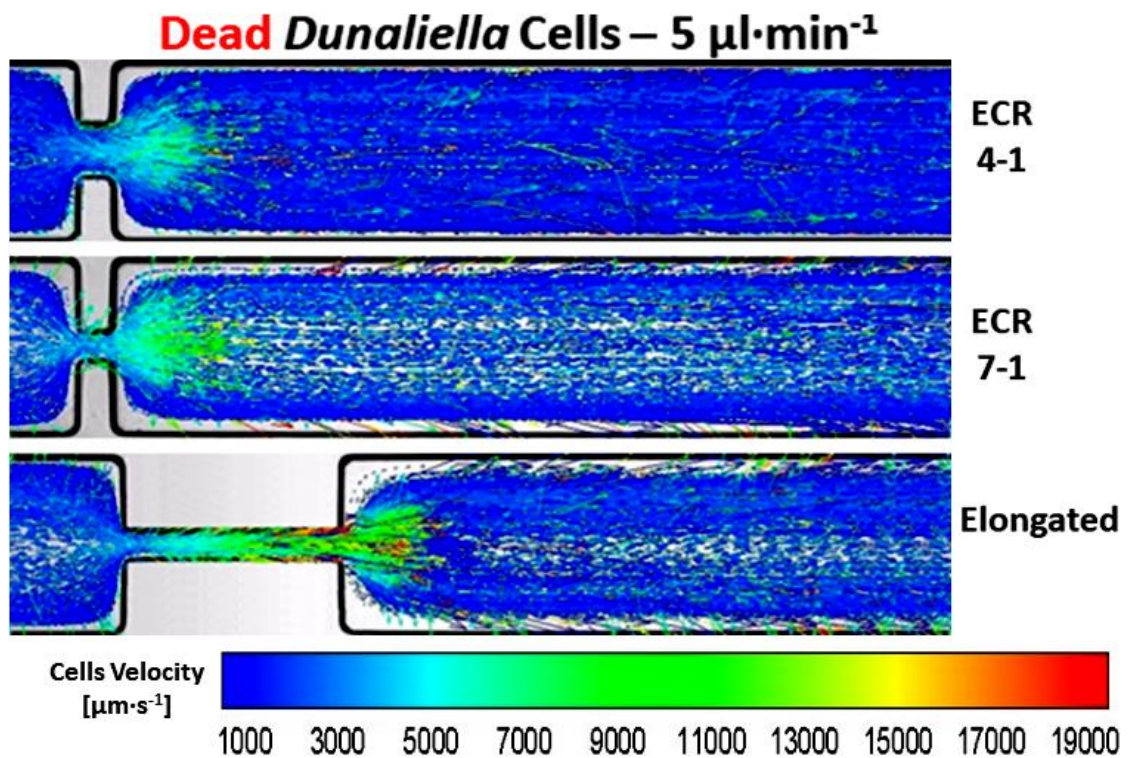


Figure 5.18 – The velocity vectors spatial distributions of dead *Dunaliella* cells at 5  $\mu\text{l}\cdot\text{min}^{-1}$ . The higher inertial effects induced by the elongated geometry caused the living and dead cells to behave similarly, despite this they showed two different spatial distributions along the channels.

These opposite fluid dynamic behaviours of living and dead cells can be explained considering the different spatial distributions induced by the inertial effects. These can be better appreciated by converting the images of the algal plumes into a black and white binary shown in **Figures 5.19** and **5.20**.

In fact, depending on the experimental conditions, some “low algal concentration (LAC) regions” were observed downstream the expansion planes (*i.e.* the white regions in the plumes, shown in the **Figures 5.19** and **5.20**). These can be considered as a measure of the inertial-induced compactness of the algal cells. In particular, the more extended a given LAC zone was, the less uniformly distributed the cells were, the more the cells that had flowed close to the walls (*i.e.* the more the cells that had concentrated in the proximity of the plume borders), the higher their tendency for biofouling was.

As can be seen in the **Figures 5.19** and **5.20**, the living cells showed less consistent LAC regions, meaning that the algal plumes managed to compact the cells, preventing them from swimming throughout the whole geometry. The LAC regions were found to be broader for the dead cells and to decrease along the channel (*i.e.* while the plume effects had been fading away). These different cells distributions explain why, at the same flow rate, the wall interactions of the dead cells were always higher than those of the living algae.

Under the selected experimental conditions, DDCs were characterised by  $Re_p \ll 1$  (see **Table 5.3**), *i.e.* dead cells did not exhibit any lateral migrations and did not converge towards any equilibrium position, as observed elsewhere [284]. Instead, within the ECR 4-1 and ECR 7-1 channels, DDCs followed the streamlines and were dragged passively by the flow that caused them to accumulate close to the channel boundaries, resulting in non-uniform spatial distributions. The experimental observations involving DDCs within the short microgeometries demonstrated that the stronger the inertial effects (*i.e.* the higher the employed flow rate), the more extended the resulting LAC regions and the higher the biofouling tendency of DDCs will be, provided that  $Re_p \ll 1$ .

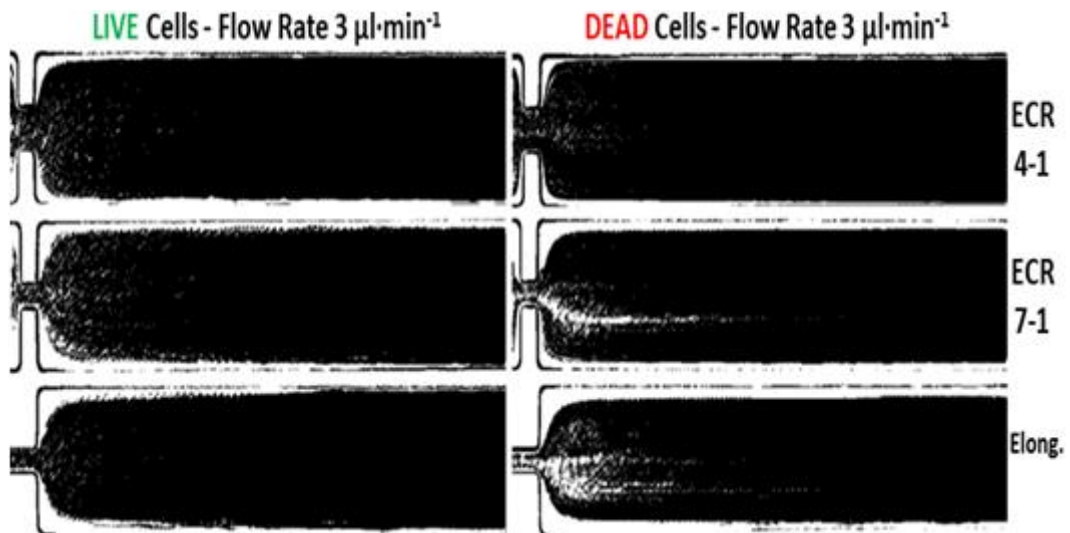


Figure 5.19 – The thresholded images of the algal plumes obtained from the experiments involving living and dead cells at  $3 \mu\text{l}\cdot\text{min}^{-1}$ . The binary images and the inertial-induced low algal concentration regions allow improved visualisation of the different spatial distribution of the cells.

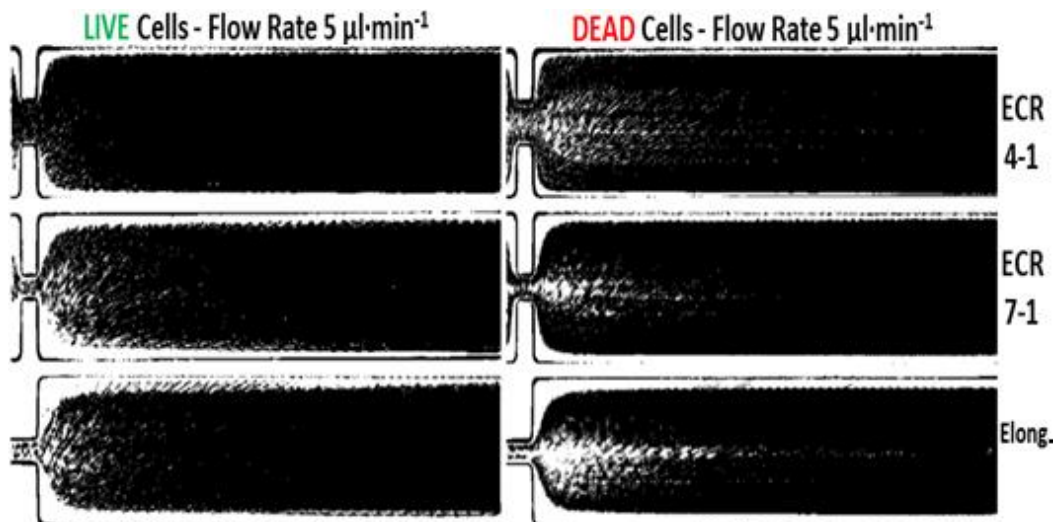


Figure 5.20 – The thresholded images of the algal plumes obtained from the experiments involving living and dead cells at  $5 \mu\text{l}\cdot\text{min}^{-1}$ . As better addressed in the Section 5.7, since the low algal concentrations regions were characterised by negligible algal-induced mitigation phenomena, they were found to increase the path length travelled by the incident solar light within the PBR.

Interestingly, within the microchannel equipped with the elongated microgeometry, at both the flow rates, the wall interactions and the fading velocities of the plume effects for both living and dead cells were found to be comparable, even though the cells showed two different spatial distributions. As shown in the **Figures 5.19** and **5.20**, the living cells were more uniformly distributed (*i.e.* the LAC regions were relatively small or negligible), while the dead cells were seen to concentrate in the proximity of the plume borders.

This could probably be due to the higher inertial effects induced by the elongated geometry (see **Figures 5.17** and **5.18**) that caused the resulting algal plumes to be more compact than those observed within the “shorter” geometries, preventing both living and dead cells from being passively-advected in the proximity of the channel walls.

The results have also confirmed that the swimming algal cells cannot be considered as passive particles because their distributions in flows are different from those of lifeless cells, since they could drift faster across the streamlines and disperse less. Different fluid dynamic behaviours of living cells and passive particle have also been observed in flows through vertical pipes, as discussed in the **Sections 1.11** and **2.10**.

These results are discussed further in the next section from a “photobioreactors” point of view, demonstrating that the exploitation of static mixers within cultivation devices can lead to more homogeneous irradiance profiles within algal cultures. In particular the areas of the inertial-induced cells depleted regions will be assessed because these zones are characterised by very low algal concentrations (*i.e.* negligible algal-induced light attenuation phenomena) and therefore they can be considered as a measure of the increase of the path length travelled by the incident solar light within the PBR.

## **5.7 Effects of the geometrical configuration on the photobioreactor productivity**

Thus far the results have been discussed from a “microalgal” point of view since, in the **Sections 4.9.4** and **5.6**, the microgeometry-induced inertial effects on both living and dead cells have been explored, describing how the resulting algal plumes affected the algal biofouling tendency, compacted the cells along the channels and led to the formation of cells free zones near the walls.

The experimental investigations were also designed to assess whether better processing conditions can be achieved by optimising the PBRs geometrical configuration and were carried out assuming that the microchannels represent hypothetical horizontal PBRs, the microgeometries represent inline static mixers and that the fluid dynamic experiences of the cells could be compared to the ones that actually occur in real PBRs.

Therefore, this section addresses the results considered from a “photobioreactors” point of view, analysing the technical advantages derived from the modification of the PBR geometrical arrangement and focusing particular attention on the resulting enhancement of the light intensity distribution and the beneficial effects on the PBR performance.

As explained in the **Sections 2.7** and **5.2.1**, the light intensity distribution within a given PBR depends on the incident solar light impinging on its surface and on attenuation phenomena owing to the cultured algal cells that can scatter, shade or absorb the light and transform it into biomass, by photosynthesis. [118, 256] However, the variation of the solar light during the day (*e.g.* depending on the position of the sun at a given moment, the local weather of the actual PBR location, *etc.*) and the algal mitigation phenomena give rise to non-homogeneous irradiance profiles inside the culture, creating zones of different illumination, *i.e.* the photic zones close to the walls and the dark zones in the depth of the culture. [118, 256] Nevertheless, ensuring homogeneous light intensity distributions (HLIDs) within the cultivation devices is important because the light availability may become the only limiting factor which determines the productivity of the system and can limit the concentrations of both photoinhibited cells (*i.e.* those located in the dark zones, where the light intensity is below that required for the photosynthetic process) and photolimited cells (*i.e.* those located in the photic zones, where light-induced reductions of the algal photosynthetic capacity may occur) (see **Figure 5.1**). [118, 139, 161]

Currently, HLIDs in closed PBRs are achieved by optimising the solar light harvesting through high surface-to-volume ratios and increasing the mixing levels (*e.g.* turbulently pumping the algal suspensions, see **Section 2.9**) in order to prevent potential microalgal accumulations and ensure optimal dark/light cycles. [139, 161]

The results discussed in the next sections will show that more HLIDs can also be obtained by employing PBRs equipped with static mixers, *i.e.* by modifying the geometrical configuration of a given PBR. This will be demonstrated by quantifying through ImageJ the areas of cell depleted regions induced by the various algal plumes which, not being occupied by the organisms anymore, are characterised by lower algal-induced mitigation phenomena and therefore better local distributions of the incident solar light within the cultivation device.

### 5.7.1 Area of the cell free region: a potential indicator for the improvement of light distribution within PBRs

In this section, the inertial-induced cell free regions areas (CFRAs) will be assessed through ImageJ; specifically, for a certain channel CFRA is obtained as the difference between the total area of the channel and the net channel area occupied by an algal plume. Since the cell depleted zones are characterised by low algal concentrations, the higher their areas, the lower the algal-induced attenuation phenomena, the further the solar light will diffuse, allowing more uniform irradiance levels to be obtained inside the culture.

For a given channel, its “total” area (TA) represents the total space occupied by the cells if the channel was equipped with microgeometry modifying elements (as the results of the experiments involving the straight channel have demonstrated, see **Section 4.8.3**) or similarly, if a horizontal PBR was to be run without a static mixer.

The net algal plumes area (NAPA) indicates the actual portion of the channel occupied by the algal cells due to the algal plumes (see **Figure 5.21**).

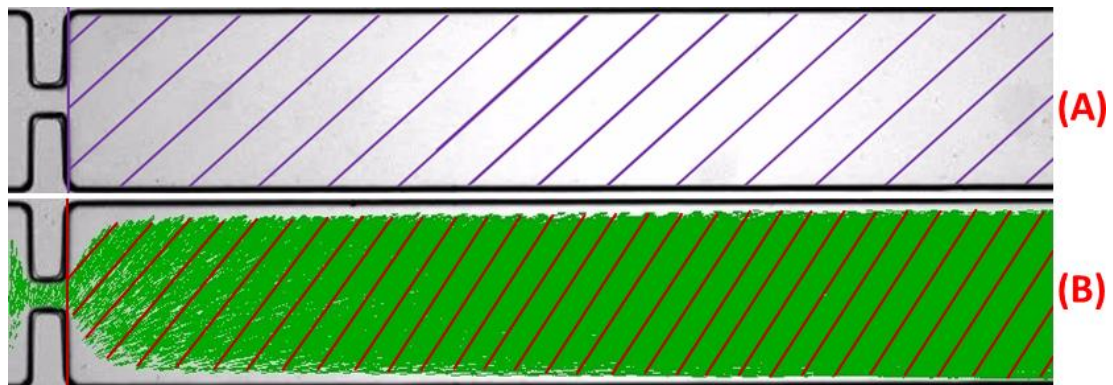
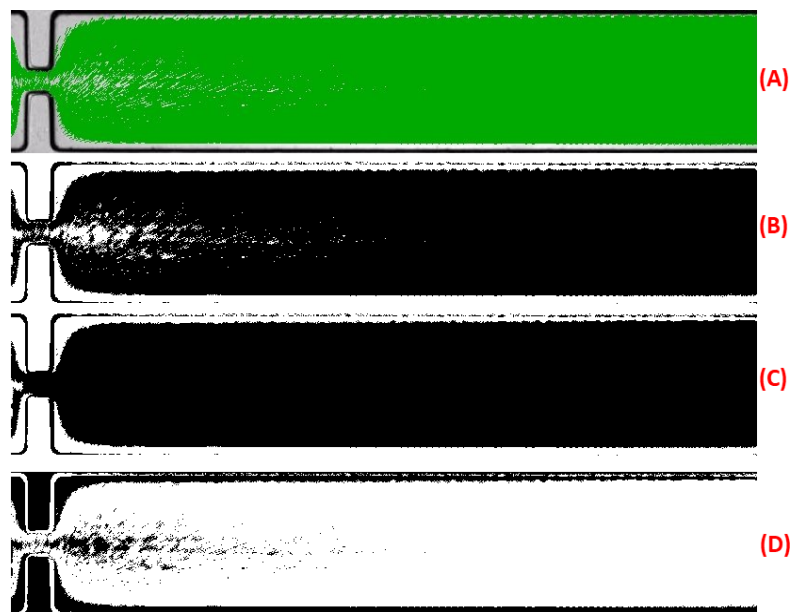


Figure 5.21 – (A) Total channel area, (B) Net algal plumes area; the plume shown was obtained during the experimental investigation involving the living cells at  $5 \mu\text{l}\cdot\text{min}^{-1}$  within the ERC 7-1 channel, just considering the areas of the cell free regions owing to the exit effects since they have proven to be the most effective ones in influencing the algal behaviours.

Since the various CFRAs were assessed considering the microgeometry-induced inertial effects on living and dead cells downstream of the contraction regions (*i.e.* CFRAs were calculated considering the algal plumes shown in **Figures 4.22 – 4.27** and **5.9 – 5.14** (see **Sections 4.9.4** and **5.6**)), the TA of a channel was encompassed between its boundaries, the expansion plane and the displayable length (see **Figure 5.21 A**) and was assessed through ImageJ by enclosing the region of interest with the rectangular selection tool and measuring it, after setting the proper pixel/micron conversion factor.

ImageJ was also employed to determine NAPAs; firstly the quality of the images was enhanced by adjusting their Brightness/Contrast and subtracting their background, then the images were grayscaled and eventually converted to binary format by adjusting their threshold levels through the automatic algorithm Max Entropy [217] and, when required, refining the levels manually so that the plume outlines and the channel borders were clearly distinguishable (see **Figure 5.22 B**). More technical details about the different steps of the image analysis procedure can be found in the **Section 3.7**.



**Figure 5.22 – (A)** Algal plume obtained during the investigations involving dead cells at  $5 \mu\text{l}\cdot\text{min}^{-1}$  within the ECR 7-1 channel. **(B)** The corresponding thresholded image showing the low algal concentration region. **(C)** Full algal plume area, obtained by applying the “fill the holes tool” on the thresholded image. **(D)** Empty-plume region area, obtained by selecting the dark background option during the image thresholding process (see **Section 3.7.1.3**).

Nevertheless, the various low algal concentration (LAC) regions (see **Section 5.6**) have also been considered as cell free zones and therefore were taken into account while assessing the total CFRA. Hence, each NAPA was obtained as the difference between two areas, the “full algal plume area”, *i.e.* the area of the plume as if it was fully-compacted (see **Figure 5.22 C**) and the LAC region area (see **Figure 5.22 D**). The various areas were measured automatically utilising the Analyze Particles function in ImageJ, after setting the proper pixel/micron conversion factors.

Once the channel TAs and the NAPAs were assessed, CFRA were obtained as:

$$CFRA = TA - NAPA \quad (eq. 5.3)$$

For a better comparison between the different channels and processing conditions, the areas of the cell depleted regions were expressed in terms of percentage of the channel area as:

$$\%_{CFRA} = \frac{TA - NAPA}{TA} \cdot 100 \quad (eq. 5.4)$$

These percentages can be thought as a measure of the fraction of the channel surface that would not be occupied by cells, implying a reduction of the mitigation phenomena and an improvement of the light distribution in the PBR.

The channels total areas (TAs), the net algal plume areas (APAs), the cell free regions areas (CFRAs) and the CFRA percentages (*i.e.*  $\%_{CFRA}$ ) have been summarised in the **Table 5.5**; the percentages value have also been depicted in the **Figure 5.23**.

**Table 5.5 – The channel total areas (TAs), the compacted algal plume areas (APAs), the low algal concentration (LAC) APAs areas, the net APAS, the cell free region areas (CFRAs) and the CFRAs expressed as percentages of the channel empty area at the considered fluid dynamic conditions.**

<b>Flow rate 3 <math>\mu\text{l}\cdot\text{min}^{-1}</math> [LIVE Cells]</b>						
<b>Geometry</b>	<b>Channel TA</b>	<b>Compacted APA</b>	<b>LAC region Area</b>	<b>Net APA</b>	<b>CFRA</b>	<b>%<sub>CFRA</sub></b>
	[mm <sup>2</sup> ]	[mm <sup>2</sup> ]	[mm <sup>2</sup> ]	[mm <sup>2</sup> ]	[mm <sup>2</sup> ]	
ECR 4-1	$8.30 \times 10^{-1}$	$7.63 \times 10^{-1}$	$4.22 \times 10^{-3}$	$7.59 \times 10^{-1}$	$7.07 \times 10^{-2}$	<b>8.53</b>
ECR 7-1	$8.44 \times 10^{-1}$	$7.35 \times 10^{-1}$	$9.65 \times 10^{-3}$	$7.25 \times 10^{-1}$	$1.19 \times 10^{-1}$	<b>14.13</b>
Elongated	$8.37 \times 10^{-1}$	$7.31 \times 10^{-1}$	$2.45 \times 10^{-3}$	$7.28 \times 10^{-1}$	$1.09 \times 10^{-1}$	<b>12.98</b>
<b>Flow rate 5 <math>\mu\text{l}\cdot\text{min}^{-1}</math> [LIVE Cells]</b>						
ECR 4-1	$8.20 \times 10^{-1}$	$7.31 \times 10^{-1}$	$3.89 \times 10^{-3}$	$7.27 \times 10^{-1}$	$9.27 \times 10^{-2}$	<b>11.32</b>
ECR 7-1	$8.44 \times 10^{-1}$	$6.95 \times 10^{-1}$	$1.32 \times 10^{-2}$	$6.82 \times 10^{-1}$	$1.63 \times 10^{-1}$	<b>19.26</b>
Elongated	$8.27 \times 10^{-1}$	$6.66 \times 10^{-1}$	$1.37 \times 10^{-2}$	$6.52 \times 10^{-1}$	$1.75 \times 10^{-1}$	<b>21.13</b>
<b>Flow rate 3 <math>\mu\text{l}\cdot\text{min}^{-1}</math> [DEAD Cells]</b>						
ECR 4-1	$8.23 \times 10^{-1}$	$7.62 \times 10^{-1}$	$5.45 \times 10^{-3}$	$7.57 \times 10^{-1}$	$6.59 \times 10^{-2}$	<b>8.01</b>
ECR 7-1	$8.47 \times 10^{-1}$	$7.28 \times 10^{-1}$	$5.20 \times 10^{-3}$	$7.23 \times 10^{-1}$	$1.24 \times 10^{-1}$	<b>14.65</b>
Elongated	$8.27 \times 10^{-1}$	$6.70 \times 10^{-1}$	$1.04 \times 10^{-2}$	$6.59 \times 10^{-1}$	$1.67 \times 10^{-1}$	<b>20.25</b>
<b>Flow rate 5 <math>\mu\text{l}\cdot\text{min}^{-1}</math> [DEAD Cells]</b>						
ECR 4-1	$8.23 \times 10^{-1}$	$7.57 \times 10^{-1}$	$1.57 \times 10^{-2}$	$7.41 \times 10^{-1}$	$8.15 \times 10^{-2}$	<b>9.90</b>
ECR 7-1	$8.44 \times 10^{-1}$	$7.33 \times 10^{-1}$	$1.72 \times 10^{-2}$	$7.15 \times 10^{-1}$	$1.29 \times 10^{-1}$	<b>15.29</b>
Elongated	$8.28 \times 10^{-1}$	$6.66 \times 10^{-1}$	$3.17 \times 10^{-2}$	$6.34 \times 10^{-1}$	$1.93 \times 10^{-1}$	<b>23.36</b>

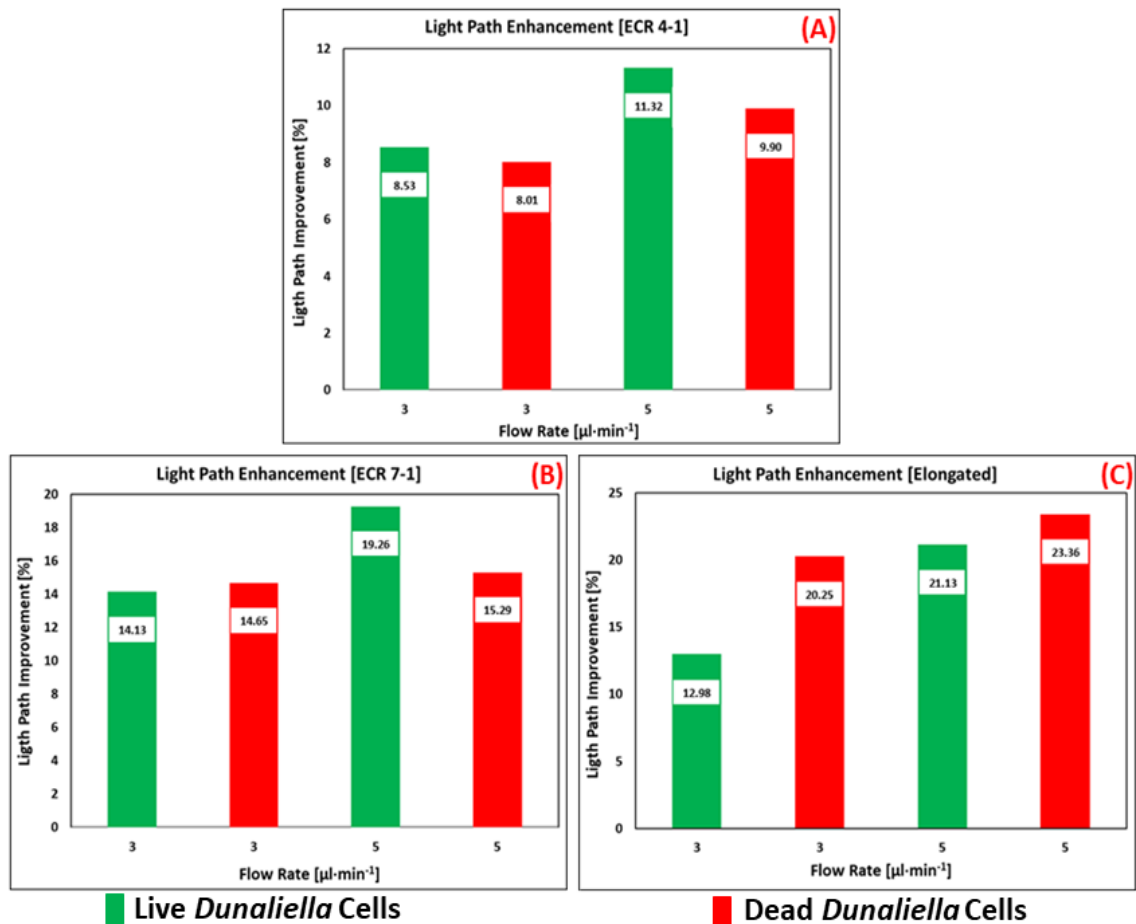


Figure 5.23 – The cell depleted regions areas expressed as percentages of the channel surface area for the living and dead cells within the ECR 4-1 channel (A), the ECR 7-1 channel (B) and the elongated channel (C). For both living and dead cells, an increase of the flow rate resulted in higher CFRAs values within all the microchannels. In particular, for the living cells, this tendency has confirmed the results discussed in the Section 4.9.4, *i.e.* for increasing inertial effects, the algal plumes were found to compact more the living cells and reduce their interactions with the walls, leading to higher cell depleted regions area and therefore more uniform irradiance levels inside the cultures. Concerning the dead cells, despite the growing inertial effects resulting in an increase of the shading effects, their spatial distributions resulted in the formation of more extended low algal concentration zones (see Section 5.6), which contributed to increase the CFRAs values.

Since the experiments were carried out assuming the microgeometries as static mixers, the CFRAs percentages permit quantification of how the microgeometry-induced inertial effects can increase the path lengths travelled by the incident light within the reactor (*i.e.* the light will be able to diffuse in regions that in the straight geometry were occupied by the algae, see Section 4.8.3), leading to more uniform irradiance levels and better performance of the cultivation devices.

This approach and the resulting CFRA percentages can also be used to compare the enhancements of light intensity distributions in PBRs with different geometrical configurations run at the same processing conditions (*i.e.* the same algal concentration and flow rate) or the same PBR run at different processing conditions.

The results have also shown that the exploitation of static mixers can significantly enhance the light distribution within PBRs, without the need for turbulent pumping of the cultured microalgae and treating them as passive particles. In fact, these promising results were attained considering the same flow rates used for analysing the straight geometry or, in other words, employing the same amount of energy, further demonstrating that modifying the PBR geometrical configuration can considerably improve the processing conditions, without increasing the operational costs.

These results will be discussed further in the next section by introducing a model developed by Sevilla *et al.* [256] for estimating the average irradiance inside the reactor. This allows improved understanding of how the improvement of the light distribution can lead to an increase of both algal growth rate and biomass productivity.

## 5.7.2 Effects of homogeneous irradiance levels on biomass productivity

As discussed in the **Section 5.1.2**, the light intensity distribution within a given PBR depends on the incident solar light hitting on its surface (which intensity tends to vary during the day) and on light intensity mitigation phenomena due to the biomass, resulting in non-homogeneous irradiance profiles inside the cultures [154]; these effects have been modelled by Sevilla and co-workers by exploiting the Lambert-Beer's law, allowing estimation of the average irradiance  $I_{AV}$  inside the reactor, which is given by: [256]

$$I_{AV}(\lambda) = I_0(\lambda) \cdot \exp(-K_a(\lambda) \cdot p_L \cdot C_b) \quad (\text{eq. 5.5})$$

where  $I_0$  is the incident radiation,  $p_L$  is the path length travelled by the light within the PBR,  $K_a(\lambda)$  is the characteristic extinction coefficient for each wavelength, which depends on the algal pigments (*i.e.* it is an intrinsic feature of the cultivated strain) and  $C_b$  is the concentration of the biomass in the PBR.

The model operates on the assumption that the direction of the incident radiation was constant, the radiation is monochromatic and it neglects the scattering effects, therefore it is only valid for well-mixed dilute cultures and would overestimate the real local intensities in concentrated algal cultures. For this reason, several other models have been proposed which consider scattering and absorption phenomena [285] or variable extinction coefficients as a function of the biomass concentration. [286]

$I_{AV}$  can be used to estimate the decrease of  $I_0$  in the PBR and therefore to calculate the punctual light intensity  $I_L$  as:

$$I_L = I_0 - I_{AV} \quad (\text{eq. 5.6})$$

Eq. 5.5 shows that if  $p_L$  is increased,  $I_{AV}$  will decrease and it will be possible to ensure more uniform irradiance levels within the culture (*i.e.* higher punctual light intensities, see eq. 5.6).

Molina *et al.* [154] developed a model for estimating the algal growth rate  $\mu_A$  for outdoor microalgal cultures:

$$\mu_A = \frac{\mu_{A,MAX} \cdot I_L^{n_A}}{I_k^{n_A} + I_L^{n_A}} \quad (\text{eq. 5.7})$$

where  $I_k$  is a constant dependent on the algal species and culture conditions and  $n_A$  is an empirically-established exponent. [154, 223]

Once the specific algal growth rate is known, the biomass productivity  $p_{Biomass}$  can be calculated as: [154]

$$p_{Biomass} = \mu_A \cdot C_b \quad (\text{eq. 5.8})$$

Eq. 5.7 and 5.8 demonstrate that an improvement of the irradiance distribution within the reactor will result in an increase of both the algal growth rate and the biomass productivity.

Within PBRs, the incident light transmission can be enhanced by maximising the solar light harvesting through high surface-to-volume ratios and minimising the algal-induced mitigation phenomena [118] and, as discussed in the **Section 5.7.1**, the latter can be inhibited by employing PBRs equipped with static mixers that should be designed and adapted taking into account the intrinsic features of the cultured algal strains.

All the results described in this chapter and in the 4<sup>th</sup> one have demonstrated that microfluidic devices and the image analysis technique developed in this research should be exploited as complementary tools for PBRs optimisation processes, as they allow quantification of algal cell behaviours under different fluid dynamic conditions, acquiring experimental data directly from the microalgae.

For a given algal strain, these results have shown the value of this approach to investigate cell dispersion, motility and interactions with the channel walls, to characterise the algal responses at both the single cell and the population levels and to carry out some preliminary experimental assessments and comparison about the static mixers and PBRs performances (*e.g.* the quantification of the percentages of the cell free regions areas under different conditions).

Further examples of the benefits of the suggested methodology will be provided in the next chapter, where DS cell behaviours will be studied in crucial parts of the microchannels (*i.e.* the centreline and the contraction regions) and both sizes and shapes of the studied algal cells will also be quantified.

The hypothesis of assuming that the microfluidic devices behave as horizontal PBRs and their microgeometries as static mixers present various biological and engineering limits that will be introduced and analysed in detail in the **7<sup>th</sup> Chapter**, where further suggestions for potential future research work will also be provided.

## **5.8 Chapter Summary**

This chapter was concerned with the results of the experimental investigations involving the dead *Dunaliella* cells (DDCs) flowing within the microchannels equipped with the ECR 4-1, ECR 7-1 and elongated geometries, at the same flow rates previously considered for the living cells (*i.e.* 3  $\mu\text{l}\cdot\text{min}^{-1}$  and 5  $\mu\text{l}\cdot\text{min}^{-1}$ ). The main objective of the experiments was to explore how the DDCs behaviours were affected by the microgeometries, assuming that their fluid dynamic experiences in the channels resembled the ones that actually occur in real PBRs.

Similarly to what had happened for the living cells, the inertial effects induced by the microgeometries led to the development of algal plumes, albeit living and dead cells were found to exhibit different fluid dynamic behaviours for increasing inertial effects, especially in the channels equipped with “shorter geometries” (*i.e.* the ECR 4-1 and ECR 7-1 geometries). In fact, within these microchannels, the algal plumes compacted the living cells and inhibited their interactions with the walls, whereas they caused the DDCs tendency for biofouling to become higher.

However, within the channel with the elongated geometry, the wall interactions and fading velocity of the plume effects for both living and dead cells were comparable. Moreover, at the same flow rate, the dead cells were observed to flow slower than the living ones and their wall interactions were always higher. These different behaviours can be explained considering the different spatial distributions of living and dead cells induced by the inertial effects.

The results have also proved that the exploitation of static mixers can lead to more homogeneous irradiance profiles within the algal cultures leading to beneficial effects on the PBR performance; this was demonstrated by quantifying the areas of the cell depleted zones induced by the various algal plumes and expressing them as percentages of the total channel surface, allowing easier comparisons between different PBRs and processing conditions.

All the results described in this chapter and in the 4<sup>th</sup> one show that the effects induced by the microgeometries caused an increase of the shear rate and the algal velocities. However, as examined in **Chapter 6**, the susceptibility to hydrodynamic and mechanical shear forces of the algal cells must be taken into account while designing a static mixer and setting the processing conditions for a PBR, in order to avoid shear-induced damages or demise of the cultured microalgae. [198]

## – Chapter 6 –

# Effects of cell fragility on algal cultures: exploiting microfluidic devices for quality controls purposes

## 6.1 Chapter layout

In the 4<sup>th</sup> and 5<sup>th</sup> Chapters, the results from experiments involving both living and dead *Dunaliella* cells gathered at different flow rates within the ECR 4-1, ECR 7-1 and elongated geometries were presented, demonstrating that the optimisation of PBR geometrical configurations can reduce cell-wall interactions and lead to more homogeneous irradiance profiles within the culture. Therefore, these results gave particular emphasis to the exploitation of microfluidic devices for design purposes. This chapter is concerned with the utilisation of microchannels for carrying out quality controls on the cultured organisms.

Initially, the chapter analyses the effects due to shear-induced damages on algal cultures while being recirculated along tubular horizontal PBRs equipped with static mixers and emphasises the importance of monitoring the fragility of the cells during the whole biomass production process, considering also that, while cultured and stressed, the cells tend to change their sizes, shapes, compositions and therefore their sensitivity to shear. [139, 198] The results demonstrate that microfluidic devices can be employed to investigate these effects, since they allow to study the fluid dynamic experiences of the cells in crucial regions of the channels through targeted image analysis processes and to assess how their shape and size distributions vary over time, as long as they are used in parallel with the currently-employed PBRs optimisation procedures.

The experimental procedures employed for assessing size and shape distributions of both living and dead *Dunaliella* cells used in this PhD are presented. The chapter ends with a general overview of the main constraints concerning the scale up process of tubular PBRs, in order to understand the results presented in this thesis and introduce their main limitations.

## 6.2 Effects of shear-induced damage on cultured cells

In culturing devices, high mixing rates have been shown to result in beneficial effects on the cultured cells [139, 229]. However, when turbulence is too intense, the resulting hydrodynamic forces may hamper the viability of the organisms and even lead to their demise. The magnitude of these fluid dynamic forces is often expressed in terms of shear rate or shear stress which are consequently employed for assessing potential damage to the cells and must be kept below a culture-specific threshold value. [229, 235]

In this section a technical analysis is conducted on the susceptibility to shear of a given cultured organism, in order to understand the effects of shear-induced damage on the cells, how the critical threshold value can be measured and how it must be considered when designing and operating a culturing device, focusing particular attention on *Dunaliella* cells while flowing in tubular PBRs equipped with static mixers.

### 6.2.1 Sensitivity of cultured cells to shear

In **Section 2.9**, the optimal fluid dynamic conditions were described must be ensured within PBRs in order to guarantee proper mixing levels, to prevent algal aggregates, to obtain the most favourable dark/light cycles and to avoid gas gradients. Effective mixing rates can be accomplished through a variety of ways depending on the employed cultivation device, *e.g.* in bubble columns, the carbon dioxide required for the photosynthesis is usually bubbled through perforated tubes (*i.e.* mixing is enhanced through gas sparging); when the reactor configuration corresponds to only one vessel, cultures can be agitated through a stirrer (*i.e.* mixing is improved through mechanical agitation); in tubular PBRs, high mixing levels are obtained by turbulently pumping the algal suspensions, using either airlift circulators or various types of pumps. [118, 227] An improvement of the mixing conditions can also be achieved through baffles and static mixers which do not employ moving parts as they can increase the culture velocity using the flow energy of the fluid (see **Section 4.3**). [227]

Until certain levels, an increase of mixing conditions was found to improve the growth of several microalgal strains (*e.g.* growing aeration rates or agitation speeds enhanced the biomass productivity of *Dunaliella* and *Phaeodactylum tricornutum* cultures [229]) albeit, when turbulence is too intense, the resulting hydrodynamic forces could be too severe for sensitive cells, hampering their viability and even causing their death. [229, 235]

The magnitude of fluid mechanical forces is often expressed as shear stress  $\tau$  or shear rate  $\gamma$  which may be employed to assess the potential for cell damage in moving fluids. [198] Therefore, shear stress levels must be kept below a culture-specific threshold value, the accurate determination of which is becoming increasingly important [235], since it should be taken into account when assessing mechanical and shear effects that are admissible during routine operation of biotechnological processes (see **Section 6.2.3**). [118, 139]

In particular, intense shear fields can disintegrate even the most robust species and, even when they are not sufficiently powerful to damage the cultured cells, they may still impact upon their growth rate, viability, tendency to lyse, biochemical composition, morphology and even attachments and detachments from surfaces. [198] For example, high superficial gas velocities in bubble columns were found to rise death rates of *Dunaliella* and *Protoceratium reticulatum* cells, likewise within tubular PBRs, turbulently pumping led to loss of motility for *Tertselmis suecica*, chain breaking for *Skeletomena costatum* and damaging to *Haslea ostrearia* cells. [235]

The susceptibility to shear of a given cultured organism depends on its biological features (e.g. type, size and morphology of the cell, characteristics of its cell wall, etc.) and culturing conditions (temperature, stressing procedure, etc.) [198]. For example, when *Chlamydomonas* cells are cultivated in sulphur-deficient conditions, their ability to tolerate shear-induced damage reduces [139] or when microalgal cells are grown at high specific rates, they often produce weaker cells. [198]

Generally, amongst the main industrially-cultured microorganisms, yeasts, bacteria and mycelial microfungi are not easily damaged under typical process conditions, whereas, animal cells, plant cells and cyanobacteria cells are more susceptible to shear damage. Shear sensitivity varies greatly amongst microalgal species, e.g. *Dunaliella Salina* is extremely fragile since its cell is enclosed by a thin elastic membrane and lacks of a cell wall, whereas many other species are able to tolerate high levels of turbulence. [198]

Thus, for a given cultured species, the specific shear threshold should be assessed carefully because, when it is exceeded, cells may be irretrievably damaged. For this reason it plays a part in the design and process of PBRs (see **Section 6.2.3**); therefore, the next section describes how shear limit values can be obtained, considering in particular the case of DS cells.

## 6.2.2 The critical shear threshold value for *Dunaliella* cells

Kokkinos and co-workers investigated experimentally the effects of increasing shear stress levels on *Dunaliella Salina* cells through a narrow-gap rheometer with parallel plate geometry, in order to determine the critical shear stress value that leads to cell deformation and rupture. [235] In particular, 200- $\mu$ l algal samples were sheared laminarly at constant maximum shear stress between 0 and 90 Pa for 1000 s within a gap of 30  $\mu$ m at ambient temperature. The distribution of shear stresses between the two plates varies linearly with the radial position  $r_{pl}$  on the plate:

$$\tau(r_{pl}) = \frac{r_{pl}}{R_{pl}} \cdot \tau_{max} \quad (\text{eq. 6.1})$$

being  $R_{pl}$  the radius of the upper plate and  $\tau_{max}$  the maximum shear stress at the edge of the plate. Eq. 6.1 implies that the cells at the boundary of the upper plate experienced the maximum shear stress. [235]

After each experiment, the sheared microalgae were analysed through a microscope to assess their motility and deformation, which can be considered indicators of cell damages; as a consequence, the cells were distinguished between being intact (*i.e.* the cells preserved their original shape) or deformed, calculating also the percentages of intact cells with respect to the total number of cells. [235]

When the shear stress was less than 15 Pa, more than 90% of cells remained undamaged and motile, albeit for increasing shear stresses, the percentages of intact cells decreased accordingly; *e.g.* when the shear stress reached 60 Pa, more than 80% of the cells were deformed (and killed), presenting also visible damages on their membranes (*i.e.* potential leakages of intercellular material). The critical shear stress value was assumed as the one that caused the deformation of at least the 20% of the cells and was found to be 18 Pa, which corresponded to a critical shear rate of  $1.6 \times 10^4 \text{ s}^{-1}$ . [235]

These experiments showed that most of the cells were deformed within the shearing duration time (*i.e.* 1000 s); similar results were obtained by Michels *et al.* who explored the effects of growing shear stresses on the viability of the microalga *Chaetoceros muelleri* under laminar flow conditions, employing four Couette shearing devices characterised by different geometrical dimensions. They found that, beyond a critical threshold value of 1.3 Pa, higher shear stresses required only a few minutes to harm the considered cells (*e.g.* at 5.89 Pa, the cells viability reduced to 82% after 1 minute and continued decreasing at a reduced rate for longer shearing times). [235, 287] Thus, shear-induced damage was found to be almost time independent, compared to the usual microalgal cultivation times, which may last several days [288]; in other words, a damaging shear level in a PBR would immediately impact negatively on the culture, further increasing the importance on designing culture devices that work below critical shear thresholds. [235, 287]

Nonetheless, shear threshold values for different microorganisms should be compared taking carefully into account the different experimental conditions employed for measuring and assessing them (*e.g.* the shearing devices, flow conditions, whether thickening agents were used, *etc.*), in order not to draw misleading conclusions. [235, 287]

The next section analyses how the critical shear threshold value of a given microorganism can be used to set the culturing conditions in order to prevent the cells from being damaged and killed, focusing particular attention on tubular PBRs.

### **6.2.3 Preventing cells from being damaged: the case of photobioreactors equipped with static mixers**

As discussed in the **Section 6.2.1**, potential damage to cells cultured in a moving fluid can be assessed considering either the shear stress or shear rate magnitudes, albeit these quantities are difficult to measure in most turbulent environments of cell culture devices. [198, 235] However, regardless of the photobioreactor configuration, damage to the cultured cells occurs when the need to achieve high mixing rates leads to turbulence fields where the length scale of the resulting energy-dissipating microeddies approaches the cellular dimensions. For this reason, the expected microeddy length can be employed to assess the potential damage derived from cell-eddy interactions. [139, 198]

When a microorganism is much smaller than the average microeddy size, the cell is simply carried around by the fluid and does not experience any disruptive forces. Whereas, if the particle dimension is comparable to the microeddy length, it will experience a pressure differential on its surface and could be stressed or broken by the resulting forces. [265]

Kolmogoroff microeddy length scale  $l$  is defined as:

$$l = \left( \frac{\mu}{\rho_f} \right)^{0.75} \cdot E^{-0.25} \quad (\text{eq. 6.2})$$

where  $\rho_f$  and  $\mu$  are density and viscosity of the surrounding fluid and  $E$  is the rate of energy dissipation of the turbulence field per unit mass of fluid. In most cases, all the energy is dispersed as fluid eddies and therefore  $E$  is usually assumed as the rate of energy input. [139, 198, 235]

Being related to shear levels and microeddy size,  $E$  can be considered as a measure of the turbulence intensity and can be used to compare different biotechnological processes. For a given organism, a critical value  $E_{crit}$  can be defined considering its shear rate threshold  $\gamma_{crit}$  as: [235]

$$E_{crit} = \mu \cdot (\gamma_{crit})^2 \quad (\text{eq. 6.3})$$

when  $E_{crit}$  is exceeded, the microeddies will damage the cultured cells. [235]

In the particular case of tubular PBRs,  $E$  is related with the pressure drop  $\Delta P$  as:

$$E = \frac{\bar{U} \cdot \Delta P}{\rho_f \cdot L_t} \quad (\text{eq. 6.4})$$

where  $L_t$  is the length of the PBR tube and  $\bar{U}$  the mean flow velocity.

For a homogeneous, isothermal, incompressible Newtonian fluid that is flowing turbulently in a tubular PBR of diameter  $d_t$ ,  $\Delta P$  is given by:

$$\Delta P = 2C_f \frac{L_t}{d_t} \rho_f \bar{U}^2 \quad (\text{eq. 6.5})$$

where  $C_f$  is the Fanning friction factor which is related with the  $Re$  number through the Blasius equation:

$$C_f = 0.0792 \cdot \left( \frac{\rho_f \cdot \bar{U} \cdot d_t}{\mu} \right)^{-0.25} \quad (\text{eq. 6.6})$$

Thus, eq. 6.2 and 6.4 – 6.6 can be employed to calculate a maximum allowable culture velocity that prevents shear-induced damage to the cells; *e.g.* if a PBR with a length of 5 m and a diameter of 0.06 m is employed to grow 45- $\mu\text{m}$  *Phaeodactylum tricornutum* cells, the culture velocity would have to exceed 1.14  $\text{m}\cdot\text{s}^{-1}$  to cause damages to the cultured microalgae. [198, 229] Under typical processing conditions, the maximum culture velocities are in the order of 0.5  $\text{m}\cdot\text{s}^{-1}$  due to the limited mechanical strength of the plastic tubes and therefore cell damage in tubular horizontal PBRs is usually negligible. [154, 229]

This may not be true when PBRs are equipped with static mixers because they tend to cause local increases of the culture velocity that may result in distress for the organisms. In fact, when a given culture flows through a static mixer the cells can either remain intact, can temporarily be damaged (*e.g.* loss of motility, reduction of viability, inhibition of the growth rate, *etc.* [198]) or can irremediably be compromised (*e.g.* the organisms are deformed, killed and may also sustain damages to their membranes that could cause lysis [235]).

However, this procedure to quantify shear-induced damage on the culture (*i.e.* assessing whether the length scale of the microeddies approaches the cellular size) can just be used to determine whether the proposed processing conditions will cause “irreversible” damage, but it does not consider the “reversible” damage. Therefore, when designing and operating a motionless mixer in a PBR, all the potential inertial-induced damaging effects must be carefully assessed, ensuring that they can be tolerated and considering that they can immediately impact negatively on the organisms. [235, 287]

Moreover, a culture is a dynamic system containing cells with different dimensions, morphologies and susceptibilities to shear (*e.g.* organisms at different stages of growth, different biomass concentrations, *etc.*, see **Section 6.4**) [198]; thus; the assumption that the organisms have the same size, shape and fragility during the whole cultivation and stressing processes could lead to incorrect conclusions and therefore their variations should be taken into account in order to adapt the PBR operational conditions accordingly.

Hence, it is necessary to devise a new approach that considers the actual fluid dynamic experience of the cultured cells flowing through a given static mixer, to quantify the inertial-induced effects on their swimming velocities and to assess correctly how shape and size distributions of the cells vary over time, in order to optimise the flow rate and the geometric configuration of the static mixers to avoid any damage to the cells. As the results described in the next sections will show, the exploitation of microfluidic devices and the image analysis technique represent a very powerful instrument to investigate these effects.

### **6.3 Exploitation of targeted image analysis for quality controls purposes: a practical example**

This section provides an example showing how the targeted image analysis technique can be employed to study the fluid dynamic experience of cells in crucial regions of the channels. The first part describes the experimental procedure employed to investigate the behaviours of both living and dead *Dunaliella* cells while flowing at four different flow rates in a 40-micron-width interval that included the centreline and the contraction region of the 7-1 expansion-contraction ratio (ECR) channel. The results obtained by processing the experimental videos through ImageJ and Matlab allowed quantification of the inertial-induced effects influencing the cells in the whole microgeometry imaged region.

The second part of the section emphasises the importance of correctly assessing the susceptibility of cells to shear during the whole cultivation process by carrying out a technical analysis of the role of shear in the optimisation of the PBR processing conditions and also demonstrating that cell fragility influences the maximum allowable flow rate and the choice of the recirculating device.

#### **6.3.1 Experimental study of the 7-1 ECR channel centreline**

The utilisation of microfluidic devices and the image analysis technique to study algal cell behaviour is very versatile and can be tailored either during the acquisition of the experimental videos (*e.g.* using different capturing conditions, observing different portions of the channel, *etc.*) or when the videos are processed through specific codes.

One of the major advantages of this approach is the possibility of exploring in detail crucial parts of the microchannel (*e.g.* the centreline, the channel boundaries, *etc.*) through targeted image analysis using tailored codes; *e.g.* this procedure was exploited in the **Section 4.7.2** to study the interactions of the living microalgae with the channel boundary, considering only the algae that swam at stagnant conditions within a 20-micron-width region located in the proximity of the walls.

A further example of the approach was to investigate the behaviours of both living and dead DS cells within a 40-micron-width horizontal interval which included the centreline of the 7-1 ECR channel (see **Figure 6.1**), in order to achieve more insight into the actual fluid dynamic experience of the microalgae in the region of the channel where the microgeometry-induced inertial effects are the highest.

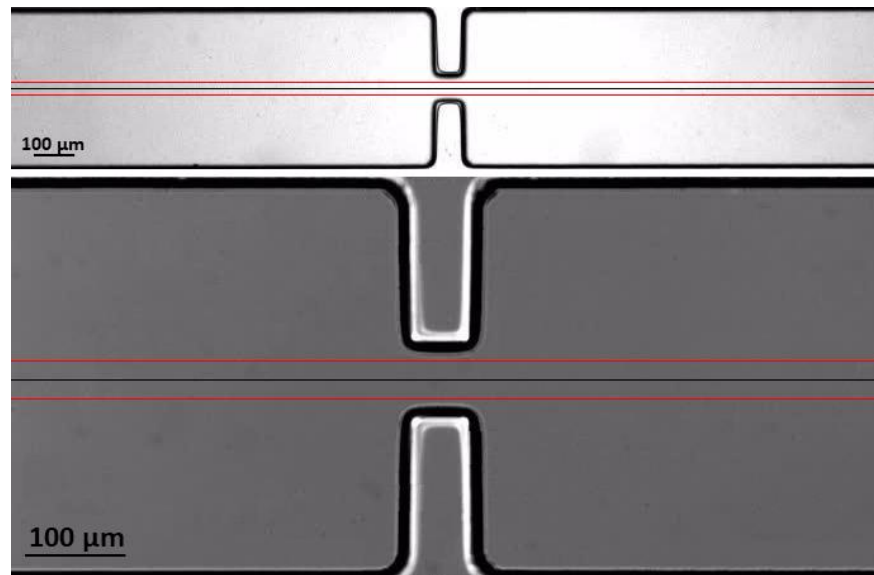


**Figure 6.1** – The 40-micron-width horizontal interval employed to investigate the fluid dynamic behaviours of both living and dead cells at four different flow rates to attain crucial information directly from the motion of the microalgae, *e.g.* their instantaneous and average velocities.

The algal cells were studied at the population level employing dilute algal suspensions as described in the **Section 5.5**, the dead *Dunaliella* cells (DDCs) were assumed to behave as passive particles.

The microgeometry was assumed to represent an inline static mixer and four flow rates were considered ( $1 \mu\text{l}\cdot\text{min}^{-1}$ ,  $2 \mu\text{l}\cdot\text{min}^{-1}$ ,  $5 \mu\text{l}\cdot\text{min}^{-1}$  and  $10 \mu\text{l}\cdot\text{min}^{-1}$ ), to simulate and compare different processing conditions and investigate their effects on the cells.

The experiments involving the  $1 \mu\text{l}\cdot\text{min}^{-1}$ ,  $2 \mu\text{l}\cdot\text{min}^{-1}$  and  $5 \mu\text{l}\cdot\text{min}^{-1}$  flow rates were carried out employing the 10X objective in order to achieve detailed inferences, while those at  $10 \mu\text{l}\cdot\text{min}^{-1}$  were performed using the 4X objective as, with the cells moving rapidly, the 10X objective would not have permitted sufficient data to be obtained, whereas, the 4X object allowed longer portions of the channel to be observed, making the cells easier to track.

The experiments were run utilising the same experimental setup and procedures described previously (see Sections 3.5, 5.3.1 and 5.3.2) and, although dead cells could not be affected by phototaxis, the red filter was used anyway to employ the same incident wavelength (*i.e.* the same depth of field) for both living and dead cells.

The main experimental conditions are summarised in the **Table 6.1**, where the buoyancy effects of the dead cells have been estimated through the dimensionless buoyancy number  $B_N$  (see **Section 5.3.2**) and the DDCs behaviours within the microchannels have been assessed using the particle Reynolds number  $Re_p$  (see **Section 5.4.1**).

**Table 6.1 – The main experimental parameters of the observations involving the 7-1 ECR microchannel at  $1 \mu\text{l}\cdot\text{min}^{-1}$ ,  $2 \mu\text{l}\cdot\text{min}^{-1}$ ,  $5 \mu\text{l}\cdot\text{min}^{-1}$  and  $10 \mu\text{l}\cdot\text{min}^{-1}$ . The data has been obtained presuming an average diameter of  $17.5 \mu\text{m}$  for the DDCs (see Section 6.4.3).**

Flow rate	Straight Region				Contraction Geometry			
	Mean Fluid Velocity	$Re$	$B_N$	$Re_p$	Mean Fluid Velocity	$Re$	$B_N$	$Re_p$
$[\mu\text{l}\cdot\text{min}^{-1}]$	$[\text{m}\cdot\text{s}^{-1}]$				$[\text{m}\cdot\text{s}^{-1}]$			
1	$4.09 \times 10^{-4}$	$5.92 \times 10^{-2}$	$1.71 \times 10^{-2}$	$1.03 \times 10^{-3}$	$2.87 \times 10^{-3}$	$1.88 \times 10^{-1}$	$2.44 \times 10^{-3}$	$1.61 \times 10^{-2}$
2	$8.17 \times 10^{-4}$	$1.18 \times 10^{-1}$	$8.57 \times 10^{-3}$	$2.07 \times 10^{-3}$	$5.75 \times 10^{-3}$	$3.75 \times 10^{-1}$	$1.22 \times 10^{-3}$	$3.23 \times 10^{-2}$
5	$2.04 \times 10^{-3}$	$2.92 \times 10^{-1}$	$3.43 \times 10^{-3}$	$5.24 \times 10^{-3}$	$1.44 \times 10^{-2}$	$9.38 \times 10^{-1}$	$4.87 \times 10^{-4}$	$8.07 \times 10^{-2}$
10	$4.09 \times 10^{-3}$	$5.24 \times 10^{-1}$	$1.71 \times 10^{-3}$	$1.03 \times 10^{-2}$	$2.87 \times 10^{-2}$	1.88	$2.44 \times 10^{-4}$	$1.61 \times 10^{-1}$

In particular, the low  $Rep$  values ( $Rep \ll 1$ ) indicate that DDCs had been dragged passively by the flow and followed the fluid streamlines while the low  $B_N$  values demonstrate that sedimentation phenomena were negligible within the microchannel, under the experimental conditions.

Concerning the living cells, as previously discussed in the **Sections 4.8.2** and **4.9.4**, the experimental observations showed that, far away from the contraction, at  $1 \mu\text{l}\cdot\text{min}^{-1}$  and  $2 \mu\text{l}\cdot\text{min}^{-1}$ , the microalgae were able to overcome the fluid streamlines, disperse throughout the channel and interact with the walls, while at  $5 \mu\text{l}\cdot\text{min}^{-1}$  and  $10 \mu\text{l}\cdot\text{min}^{-1}$ , the cells were passively advected by the flow. Nevertheless, for all the flow rates used, in the proximity of the microgeometries, the cells were drawn out by the contraction and followed the distorted streamlines, showing similar behaviour to the DDCs.

Once the experimental videos had been acquired, they were analysed using ImageJ attaining the algal spatial positions (see **Section 3.7**); as described in the next section, the data were then processed using various specifically-designed Matlab codes in order to obtain the instantaneous and average velocities of the cells and the swimming velocities vectors spatial distributions.

### 6.3.2 Instantaneous and average velocities of the cells

This section addresses how the spatial positions determined by targeted image analysis were processed through Matlab, allowing the velocity vector distributions to be obtained by computing the swimming velocity magnitudes of both living and dead algae that swam throughout the whole channel (see **Section 4.7**) and the instantaneous velocities by considering only the cells that had swum within the selected horizontal interval.

In addition, the average velocities of the algae that were passively advected within the horizontal interval were also assessed using a further tailored code which divided the displayable length of the channel in 16 subintervals, computing the instantaneous velocities of all the cells that swam in each of them and calculating their corresponding average values.

If a set of  $N$  algal instantaneous velocity values  $V_{ins}$  were obtained for the  $j$ -th subinterval, the corresponding average velocity  $\bar{V}_j$  was computed as:

$$\bar{V}_j = \frac{1}{N} \sum_{k=1}^N V_{ins,k} \quad (\text{eq. 6.7})$$

The code also calculated the standard deviation  $SD_j$  and standard error  $SE_j$  values as:

$$SD_j = \sqrt{\frac{1}{N-1} \sum_{k=1}^N (V_{ins,k} - \bar{V}_j)^2} \quad (\text{eq. 6.8})$$

$$SE_j = \frac{SD_j}{\sqrt{N}} \quad (\text{eq. 6.9})$$

the subscript  $j$  refers to the  $j$ -th subinterval.

The next sections will show that the results obtained allowed quantification of how the inertial-induced effects influenced the algal swimming velocities under the experimental conditions. This suggests that microfluidic devices represent a useful tool for PBR design and for routine cell screenings, provided they are used along with the currently PBRs optimisation and quality controls procedures.

### 6.3.3 Quantification of the inertial-induced effects on the algal behaviours

As described in the previous section, targeted image analysis allowed velocity vector spatial distributions to be obtained. This provided further insight into how the inertial effects had influenced the cells in the whole microgeometry region. The algal instantaneous and average velocities allowed comparison of the responses of living and dead algae under the same experimental conditions delivering further insight into their fluid dynamic experiences while flowing in the region of the channel where the culture velocities were the highest.

As can be seen in **Figures 6.2, 6.3, 6.4, 6.5** and **6.6**, the results showed that at  $1 \mu\text{l}\cdot\text{min}^{-1}$ ,  $2 \mu\text{l}\cdot\text{min}^{-1}$  and  $5 \mu\text{l}\cdot\text{min}^{-1}$ , the living organisms always flowed faster than the dead *Dunaliella* cells, while at  $10 \mu\text{l}\cdot\text{min}^{-1}$ , the cells were passively dragged at very similar velocities probably because relatively high flow rates prevented the living cells from swimming, rendering them as passive particles. Clearly, dead cells cannot experience the previously-defined “reversible” effects (e.g. inhibition of the viability, biomass production, etc., see **Section 6.2.1**), therefore a potential damaging shear field can only break and disintegrate them, resulting in leakage of lysed intercellular fluids that may be exploited as nutrient sources by parasitic organisms. [253, 254]

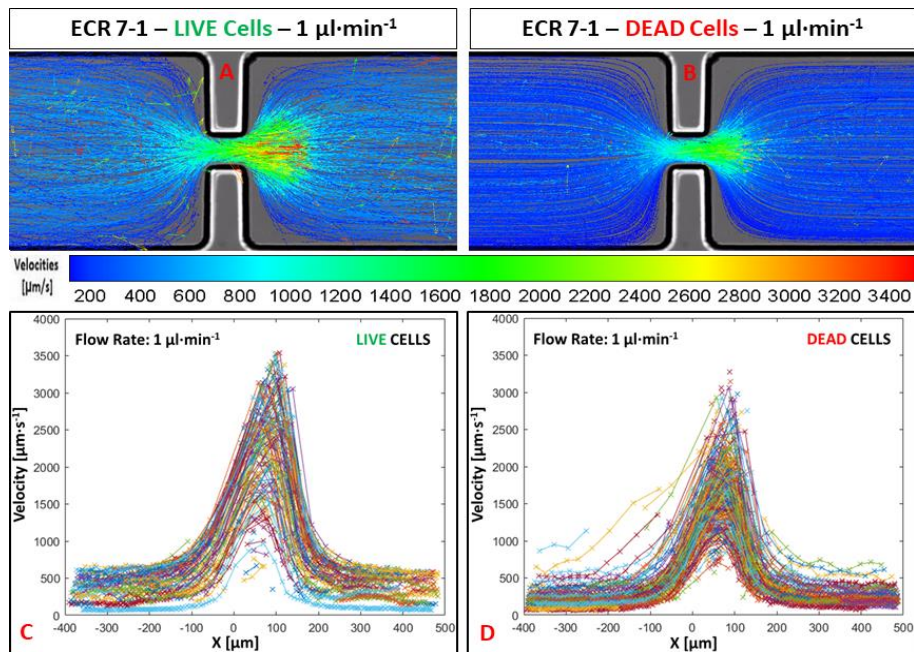


Figure 6.2 – Velocity vector spatial distributions of both living (A) and dead (B) *Dunaliella* cells tracked while flowing at  $1 \mu\text{l}\cdot\text{min}^{-1}$ . The algal instantaneous velocities of both living (C) and dead (D) *Dunaliella* cells while being transported through within the 40-micron-width horizontal interval (see Figure 6.1). The experimental videos were captured using a resolution of 688 x 516 pixels and an exposure time ranging from 3 to 4 ms.

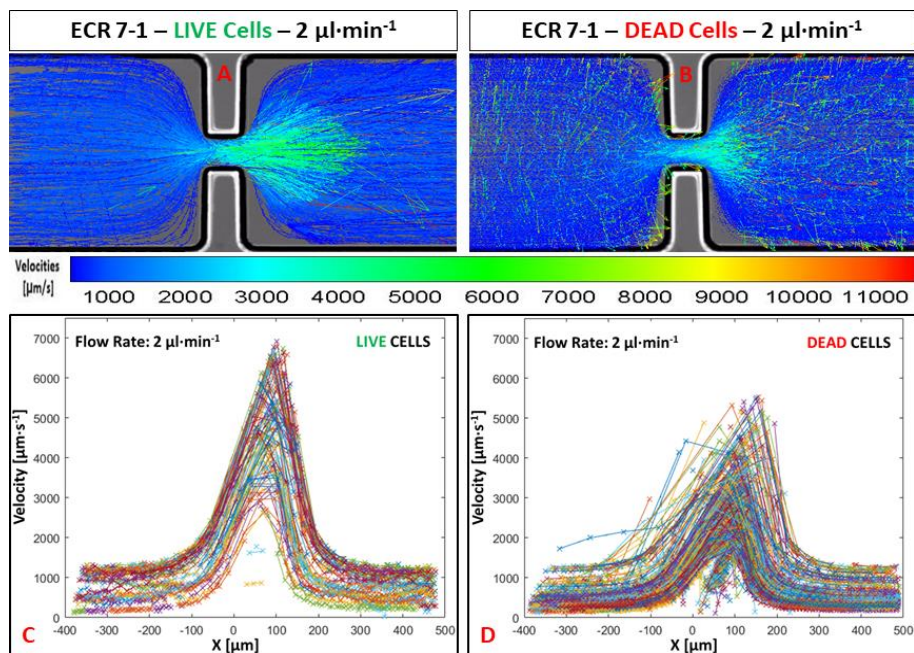


Figure 6.3 – Velocity vector spatial distributions of both living (A) and dead (B) *Dunaliella* cells tracked while flowing at  $2 \mu\text{l}\cdot\text{min}^{-1}$ . The algal instantaneous velocities of both living (C) and dead (D) *Dunaliella* cells while being transported through within the 40-micron-width horizontal interval (see Figure 6.1). The experimental videos were acquired using a resolution of 688 x 516 pixels and an exposure time ranging from 2 to 3 ms.

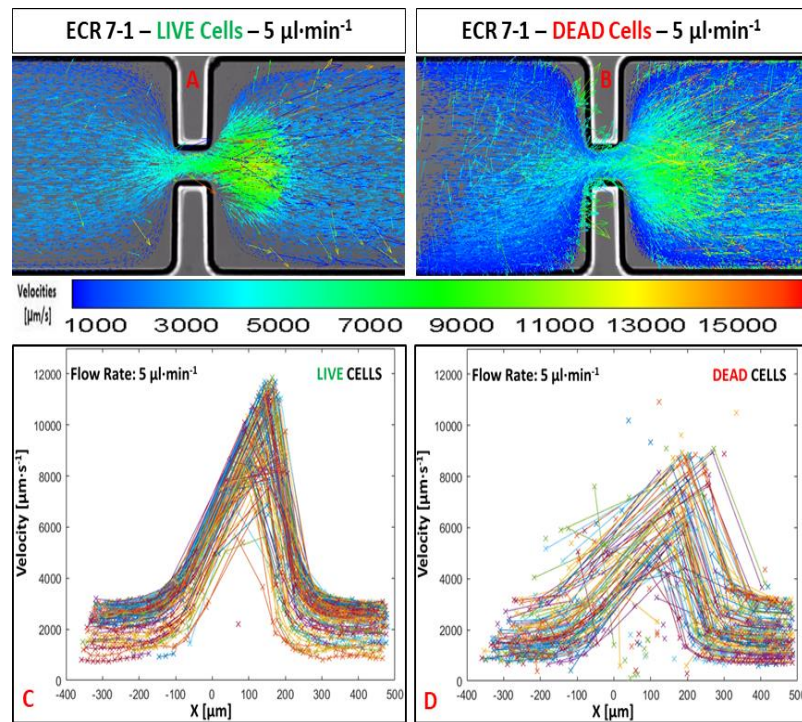


Figure 6.4 – Velocity vector spatial distributions of both living (A) and dead (B) *Dunaliella* cells tracked while flowing at  $5 \mu\text{l}\cdot\text{min}^{-1}$ . The algal instantaneous velocities of both living (C) and dead (D) *Dunaliella* cells while being transported through within the 40-micron-width horizontal interval (see Figure 6.1). The experimental videos were captured using a resolution of  $688 \times 516$  pixels and an exposure time  $< 1$  ms.

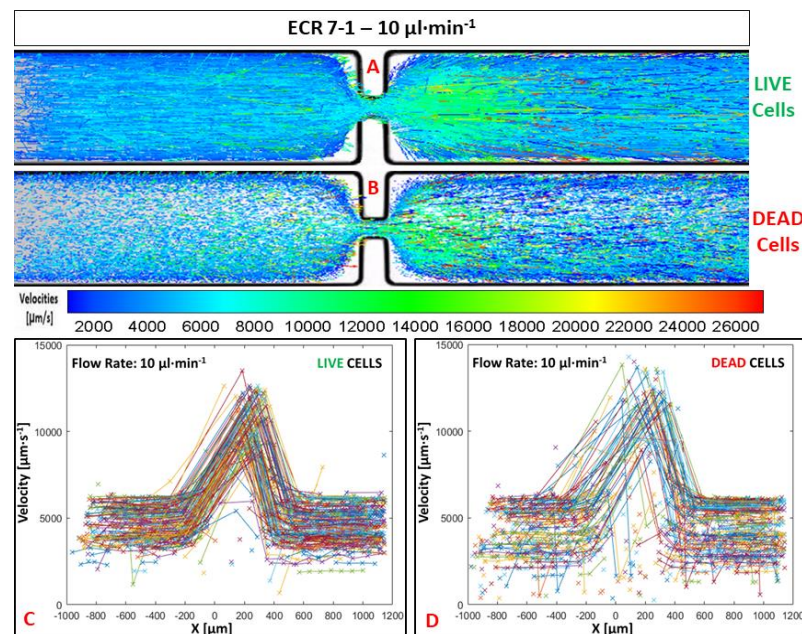


Figure 6.5 – Velocity vector spatial distributions of both living (A) and dead (B) *Dunaliella* cells tracked while flowing at  $10 \mu\text{l}\cdot\text{min}^{-1}$ . The algal instantaneous velocities of both living (C) and dead (D) *Dunaliella* cells while being passively dragged within the 40-micron-width horizontal interval (see Figure 6.1). The experimental videos were acquired using a resolution of  $688 \times 516$  pixels and an exposure time  $< 1$  ms.

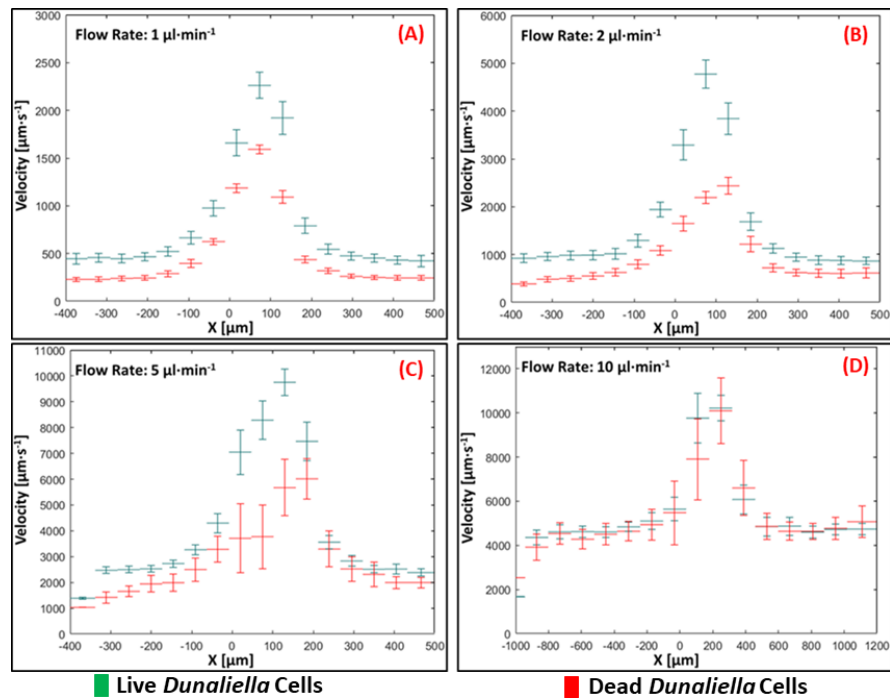


Figure 6.6 – The algal average velocities of both living and dead *Dunaliella* cells while flowing within the 40-micron-width horizontal interval at  $1 \mu\text{l}\cdot\text{min}^{-1}$  (A),  $2 \mu\text{l}\cdot\text{min}^{-1}$  (B),  $5 \mu\text{l}\cdot\text{min}^{-1}$  (C) and  $10 \mu\text{l}\cdot\text{min}^{-1}$  (D). For the experiments involving the 10X objective (*i.e.* those at  $1 \mu\text{l}\cdot\text{min}^{-1}$ ,  $2 \mu\text{l}\cdot\text{min}^{-1}$  and  $5 \mu\text{l}\cdot\text{min}^{-1}$ ), the displayable length of the channel was about  $900 \mu\text{m}$  (*i.e.* each sub-interval was  $\sim 56 \mu\text{m}$  long); while at  $10 \mu\text{l}\cdot\text{min}^{-1}$ , the observable portion of the channel was about  $2200 \mu\text{m}$  (*i.e.* each sub-interval was  $\sim 138 \mu\text{m}$  long).

The results discussed in this section and those described subsequently are intended to demonstrate that microchannels can be employed for periodic monitoring of a given culture to quantify both how the inertial-induced effects can influence the fluid dynamic behaviours of the organisms and the variations of the algal size and shape distributions (see Section 6.4), during the whole cultivation and stressing processes.

When operating PBRs equipped with static mixers, local increases of the culture velocity occur and consequently all the potential inertial-induced detrimental effects exerted on the cultivated organisms must be assessed carefully in order to ensure that they can be tolerated by the cells during the whole cultivation process. Even if operation conditions are assessed to be safe for the culture (*i.e.* the expected microeddy length scale is bigger than the average cell size) and therefore the resulting shear fields are not sufficiently powerful to deform and kill the organisms, they may still cause distress to them. [235, 287]

Throughout the time the cells are being cultivated and stressed, the organisms must continuously be recirculated through the PBR and its static mixers and, during these repeated passages, their sizes, shapes and biological compositions develop, *ergo* their sensitivity to shear tends to change over time. Thus, a given culture is a dynamic system containing organisms at various stages of growth, along with lysed and dead cells. [21, 240]

This means that cells with distinct characteristics are influenced in different ways by the operational conditions, particularly the geometrical configuration of the static mixers and the flow rate. These will govern their interactions with the surrounding fluid. Generally, the more the cultured organisms are accelerated by the inertial effects, the more likely they will be affected by the increasing shear.

Therefore, it is fundamental to verify that the utilised growing conditions are not harmful to the algae. Potentially, this can be achieved by screening and monitoring the culture routinely through the microfluidic devices described in this thesis in order to quantify how inertia can influence the fluid dynamic behaviours of the organisms, identify the critical phase(s) of the cultivation process (*i.e.* the one(s) where the inertial effects on the cells are the highest and therefore the most damaging), detect possible early shear-induced damage to the cells and adapt the processing conditions accordingly. Furthermore, microfluidic devices could also permit investigation of crucial parts of the channel through the targeted image analysis process, further demonstrating that this represents a valuable approach for routine cell screening, to supplement the currently used quality control methodologies (see the examples in the **Section 7.3.1**).

These concepts are discussed further in the **Section 6.4** that analyses the potential utilisation of microchannels to investigate morphological and dimensional variations of the cells and the resulting effects on their fragility, a fundamental feature that must always be monitored carefully at any stage of the cultivation process, as addressed in the next section.

### 6.3.4 Sensitivity to shear: implications for photobioreactors

The sensitivity of cultured cells to shear represents one of the biggest constraints for the optimisation of the operational conditions in photobioreactors; in particular, for tubular PBRs equipped with static mixers, the requirement of preventing the microeddies size from approaching the cells dimensions poses an upper limit on the maximum allowable flow rate and therefore on the local increases of the culture circulation velocity. The higher the flow rate, the higher the rate of energy dissipation  $E$  of the turbulence field, the smaller the resulting microeddies (see eq. 6.2), the more likely the cells will be stressed or damaged). [139, 198]

A further constrain on the processing conditions (*i.e.* the geometrical configuration of the static mixers and the flow rate) which must be considered is the mechanical resistance of the plastic tubes; *i.e.* if the induced mechanical stresses are too intense, the PBR must be manufactured employing more resistant and more expensive materials. It must also be taken into account that plastic tubes of outdoor PBRs tend to deteriorate under the sunlight or they may be compromised by inclement weather, therefore their mechanical resistance decreases over time. [139, 142]

Although optimal culture conditions may be achieved within the solar collector, the cultured organisms must also be recirculated along the PBR through a suitable pumping system (*e.g.* centrifugal pump, airlift, *etc.*) which should be chosen taking into account the fragility of the cells, in order to avoid damaging shear levels encountered during the repeated passage through the recirculation device. [240] Pumping-induced damage had been investigated extensively, demonstrating that cultures recirculated with different devices exhibited different specific growth rates and the detrimental effects depend on the type of pump. For example, Gudin *et al.* showed that, depending on the cultured cells, it is possible to double the productivity of a PBR by using screw pumps instead of centrifugal pumps. [236] In its simplest form, a screw pump consists of a screw that rotates inside a hollow pipe, moving fluids and suspensions along the screw's spindle. [289]

However, regardless of the type of pump, other important features that must be taken into account include intrinsic characteristics (*e.g.* capacity, internal volume, *etc.*) and operational conditions (*e.g.* rotation speed, number of cycles, *etc.*). [236, 240, 290] Generally, fragile cells should be circulated through airlift devices since they do not employ moving parts and so limit the damage associated with the mechanical pumping. In addition, both the aeration and degassing of the suspensions are achieved using the airlift pump. [152, 154]

Cells fragility also influences the downstream operations, *i.e.* the harvesting and concentration processes that are employed to physically remove the cells from the cultivation site, separate them from the growth medium, concentrate them and extract the substrate (see **Section 2.4.2**).

Algal cells can be harvested and concentrated through various techniques (*e.g.* filtration, centrifugation, *etc.*) that depend on the algal species and the desired final product(s). [112] For example, when fragile organisms are enriched with glycerol or other water soluble compounds and they are harvested using centrifuges or filtration, the cells may be damaged and broken, causing the biomass to leak in the surrounding water, making it costly to recover. In such cases, different harvesting techniques should be considered (*e.g.* low shear microfiltration). [240, 291]

Susceptibility to shear is a critical parameter and consequently it must be assessed carefully, taking into account that it also depends on the dimension and morphology distributions of the cells being cultured [139, 198]. Therefore, it is paramount to correctly determine the shape and size distributions of the cells and how these aspects tend to change over time during the cultivation process.

## **6.4 Size and shape distribution of used *Dunaliella* cells**

This section presents the procedure employed to assess the dimensions and morphology distributions of both the living and dead *Dunaliella* cells. The experimental videos were processed through ImageJ and Matlab, the major axes, minor axes and eccentricities of the cells were obtained and used to find the average size and shape of the cells used in this PhD.

It is clear that a culture cannot be modelled assuming that cells maintain the same size and shape during the whole cultivation process, the next section provides a few examples to demonstrate how misleading that hypothesis could be.

### 6.4.1 The role of size and shape in the cultivation process

An algal culture is a dynamic system that includes cells at various stages of growth and stressing levels (*i.e.* different substrate concentrations), meaning that sizes and shapes of the cultured organisms are non-uniform and change over time, influencing their biological behaviours and interactions with the surrounding fluid, *i.e.* their metabolism, shear-induced rotations and susceptibility to shear, *etc.* [21, 22]

For instance, smaller cells achieve higher rates of photosynthesis, have higher specific growth rates and higher metabolism rates (*i.e.* smaller cells have higher surface-to-volume ratios and therefore they can better uptake dissolved nutrients, see **Section 1.12**) [21, 23], implying that smaller organisms are better competitors for food than larger ones at specific stressing conditions (*e.g.* when the concentration of some key nutrients are deliberately kept low to trigger the accumulation of particular substrates). [10, 292]

Moreover, shear-induced rotation and orientation of elongated cells within a flow field could influence the propagation of the incident solar light in cultivation devices, due to scattering and attenuation phenomena. [19, 20]

Cellular features can also depend on the culturing conditions, *e.g.* the microalgal *Haematococcus pluvialis* cells are normally green, have two anterior flagella and can swim at  $20 \mu\text{m}\cdot\text{s}^{-1}$  in a water-like medium, whereas when being stressed, the cells tend to lose the flagella, to accumulate carotenoids and to turn into spherical red cysts. Biologically, a cyst is a dormant or resting stage that helps microorganisms to survive under unfavourable environmental conditions, since cells slow down their metabolic processes and cease all activities (*e.g.* feeding, locomotion, *etc.*). [236, 293]

As a result, the assumption that organisms of a given culture have the same dimension and shape during the whole cultivation period and during the various stages of growth could lead to deceptive conclusions and cells having different sizes will be described erroneously. The variation of the cellular size and shape distributions over time should be considered, in order to take into account the phenomena described above and optimise the PBR operational conditions accordingly. [229, 294]

Determining the actual size distribution of the cultured organisms can also be beneficial for the downstream processes, *e.g.* when the cells are harvested through microfiltration, it would be possible to optimise the dimension of the filter pores and prevent them from being clogged rapidly or from not filtering the cells efficiently. [175]

As the next sections will address, microfluidic devices and the image analysis technique can be exploited for monitoring periodically a given culture and assess how morphologies and dimensions of the organisms vary over time; therefore, this approach was also employed for determining the size and shape distributions of both living and dead *Dunaliella* cells.

## **6.4.2 Experimental procedure for assessing size and shape distributions**

This section describes how microfluidic devices and the image analysis technique were employed to quantify size and shape distributions of both living and dead *Dunaliella* cells that were studied in this PhD. This illustrates how these techniques represent a useful tool to quantify the dimension and morphology of a cultured species during its various stages of growth and stressing.

Sizes and shapes of DS cells were assessed experimentally by evaluating the microalgae while at  $1 \mu\text{l}\cdot\text{min}^{-1}$  within the 7-1 ECR and the elongated geometries, observing them through the 10X objective. The algal cells were studied at the population level, employing dilute suspensions (*i.e.* neglecting cell-cell interactions) and assuming that the dead cells behave as passive particles.

The  $1 \mu\text{l}\cdot\text{min}^{-1}$  flow rate proved to be the optimal one for tracking the sizes and shapes of the cells through ImageJ. The closer the algae approached the contraction entrance, the more they were accelerated by the increasing inertial effects, the more the cells were drawn out by the microgeometry, reducing significantly their walls interactions and dispersion along the channel, stopping them from swimming in and out of focus and therefore making it possible to visualise them well. At lower flow rates, the cells had the best changes to overcome the fluid streamlines, swimming in and out of focus, interacting with the walls and making it difficult to assess their dimensions and morphologies correctly. Higher flow rates would have dragged the cells too rapidly, preventing them from being visualised properly.

The experiments were carried out utilising the experimental setup and procedures previously described (see Sections 3.5, 5.3.1 and 5.3.2).

The main experimental conditions have been summarised in the **Table 6.2**.

**Table 6.2 – The main parameters of the experiments involving the 7-1 ECR and elongated microchannels at  $1 \mu\text{l}\cdot\text{min}^{-1}$ . The data has been calculated presuming an average diameter of  $17.5 \mu\text{m}$  for the DDCs.**

	Straight Region				Contraction Geometry			
Flow rate	Mean Fluid Velocity	$Re$	$B_N$	$Re_p$	Mean Fluid Velocity	$Re$	$B_N$	$Re_p$
$[\mu\text{l}\cdot\text{min}^{-1}]$	$[\text{m}\cdot\text{s}^{-1}]$				$[\text{m}\cdot\text{s}^{-1}]$			
<b>7-1 ECR Channel</b>								
1	$4.09 \times 10^{-4}$	$5.92 \times 10^{-2}$	$1.71 \times 10^{-2}$	$1.03 \times 10^{-3}$	$2.87 \times 10^{-3}$	$1.88 \times 10^{-1}$	$2.44 \times 10^{-3}$	$1.61 \times 10^{-2}$
<b>Elongated Channel</b>								
1	$4.10 \times 10^{-4}$	$5.93 \times 10^{-2}$	$1.71 \times 10^{-2}$	$1.04 \times 10^{-3}$	$2.88 \times 10^{-3}$	$1.88 \times 10^{-1}$	$2.43 \times 10^{-3}$	$1.62 \times 10^{-2}$

During the video acquisition, the image capturing conditions had to be optimised and kept constant, particular attention was paid to the exposure time, in order to avoid the cells appearing deformed, blurred or elongated and therefore skewing the results.

The experimental videos were processed through ImageJ following the procedure described in the **Section 3.7**; *i.e.* removing unwanted non-moving objects (*e.g.* microchannel boundaries, speckles owing to the camera, *etc.*), subtracting the background, converting them into binary format and setting the real scale, using the conversion factors between pixels and microns, so as to obtain the results in more useful units. The next step was to filter the desired features of the algal cells by choosing some cutoff parameters (*e.g.* the maximum and minimum acceptable cell areas, the maximum allowable algal velocity, *etc.*) to ensure that only the wanted characteristics of the filtered cells were tracked and assessed properly.

The wrMTrck plugin. [220], used to locate and track the filtered cells, employed an algorithm that fitted each alga in each frame with a corresponding ellipse that had the same area, orientation and centroid as the original selection, providing also the major and minor axes of the best fitting ellipse [217], which were then used to quantify the size distributions and the eccentricities of the cells (*i.e.* their shapes) through a specifically-tailored Matlab code.

### **6.4.3 Assessing size and shape distributions: data analysis and results discussion**

This section outlines how the major and minor axes of the fitting ellipses were processed through Matlab, in order to obtain the size distributions of the cells and how the code computed the cells eccentricities, allowing their shape distributions to be inferred. The results were then used to find the average size and eccentricity of both living and dead cells and to compare how the different residence times of the organisms within PBRs and microfluidic devices can influence their morphological and dimensional changes.

The eccentricity  $e_e$  of a generic ellipse with a major axis  $a_e$  and minor axis  $b_e$  can be thought as a measure of how much it deviates from being circular and is defined as:

$$e_e = \frac{c_e}{a_e} \quad (\text{eq. 6.10})$$

Where  $c_e$  is the distance of a focal point  $F_e$  from the centre (see **Figure 6.7**), given by:

$$c_e = \sqrt{a_e^2 - b_e^2} \quad (\text{eq. 6.11})$$

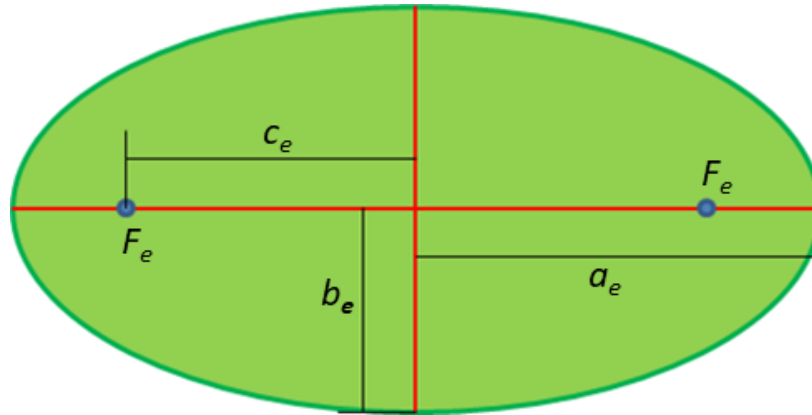


**Figure 6.7** – Geometrically, an ellipse is a curve in a plane surrounding two focal points such that the sum of the distances to the two focal points is constant for every point on the curve. A circle is a special type of ellipse having both focal points at the same location. Adapted from [295].

The eccentricity of an ellipse is encompassed from 0 to arbitrarily close to but less than 1 ( $0 \leq e_e < 1$ ); in particular, when  $e_e = 0$ , the ellipse coincides to a circle, while the more  $e_e$  tends towards 1, the more the ellipse becomes elongated (see **Figure 6.8**). [295]

The eccentricity is also related to the axes ratio  $r$  that can be defined as:

$$r = \frac{a_e}{b_e} \quad (\text{eq. 6.12})$$

Combining *eq. 6.10* and *eq. 6.11* gives:

$$e_e \cdot a_e = \sqrt{a_e^2 - b_e^2} \quad (\text{eq. 6.13})$$

Which leads to:

$$b_e = a_e \cdot \sqrt{1 - e_e^2} \quad (\text{eq. 6.14})$$

Substituting *eq. 6.14* into *eq. 6.12* allows to obtain:

$$r = \frac{a_e}{b_e} = \frac{1}{\sqrt{1 - e_e^2}} = \frac{\sqrt{1 - e_e^2}}{1 - e_e^2} \quad (\text{eq. 6.15})$$

Eq. 6.15 expresses how the ratio between the major axis and minor axis of a given ellipse vary with its eccentricity (see **Figure 6.8**). [295]

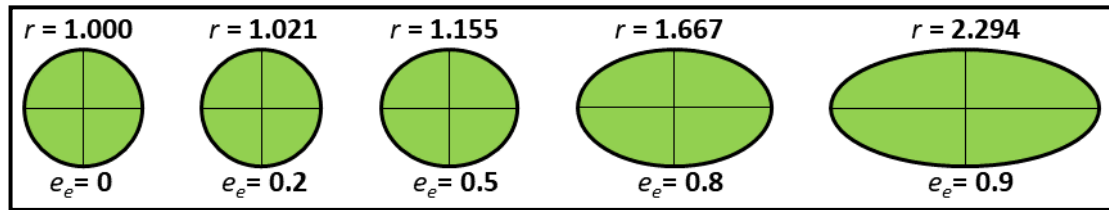


**Figure 6.8** – For a fixed value of the minor axis of a given ellipse, the more the eccentricity tends towards 1, the more the major axis, the axes ratio and the elongation of the ellipse will increase accordingly. Therefore, the eccentricity for fitting ellipses was used to assess the shapes of both living and dead DS cells. Adapted from [296].

The Matlab code calculated  $c_e$  from the major and minor axes of the fitting ellipses through eq. 6.11 and afterwards computed the cells eccentricities through eq. 6.10.

The code also filtered the results in order to rule out all the “unfeasible” sizes and shapes. Firstly, as mentioned in the **Section 2.3.2**, the length of a DS cell ranges from 5 to 25  $\mu\text{m}$  [112], therefore the code disregarded all the major axes bigger than 25  $\mu\text{m}$  and smaller than 5  $\mu\text{m}$ , which could have been due to mostly impurities and cells that had managed to swim in and out of focus despite the chosen flow rate.

The code did not take into account cells whose eccentricity was bigger than 0.7 since they would be unfeasibly elongated, compared to the cells used in the study. These relatively big eccentricity values may have been due to impurities with irregular shapes (*e.g.* lysed cells or salty impurities) or cells that could not be seen properly (*e.g.* cells that had been interacting with the channel boundaries) and therefore were assigned elongated ellipsoids by ImageJ.

As can be seen in the **Figures 6.9**, the experimental investigations involving the living *Dunaliella* microalgae within the 7-1 ECR microgeometry demonstrated that the cells with their major axis between 10 and 20  $\mu\text{m}$  comprised 86.23% of the population, while in the experiments carried using the elongated geometry these accounted to 86.55% of the cells; therefore, for living cells a major axis of 15  $\mu\text{m}$  was considered to be representative (see **Figure 6.9 A and B**).

Similarly, it was observed that the dead *Dunaliella* cells (DDCs) with their major axis between 15 and 20  $\mu\text{m}$  represented 71.12% of the cells in the experiments involving the 7-1 ECR channel and 68.11% of those within the elongated geometry; consequently, for the dead cells an average major axis of 17.5  $\mu\text{m}$  was assigned (see **Figure 6.9 C and D**).

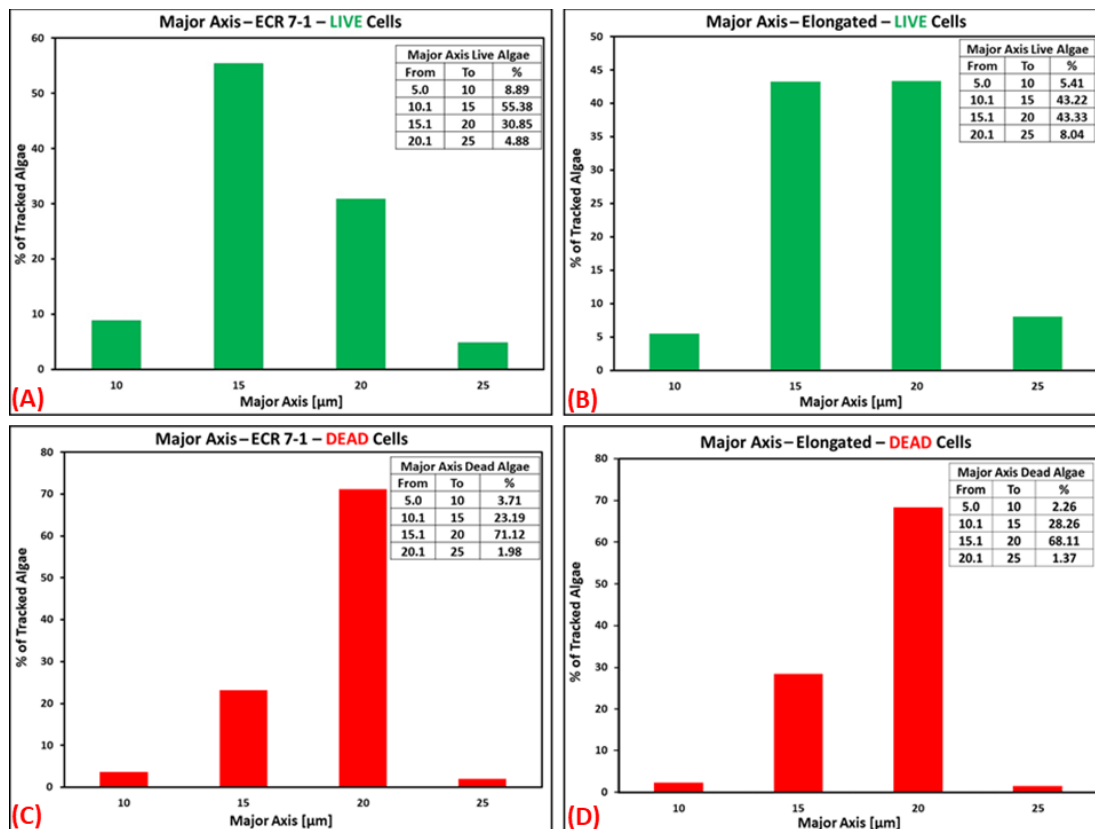


**Figure 6.9** – The major axes histograms concerning the living DS cells in the ECR 7-1 channel (A), in the elongated one (B) and those regarding the dead microalgae (C) and (D). Sizes and shapes of the microalgae were assessed through the 7-1 ECR and the elongated geometries since their inertial-induced effects allowed the cells to be visualise properly using a relatively low flow rate. The other geometries would have required higher flow rates in order to prevent the cells from swimming in and out of focus and interacting with the walls, making the tracking process more difficult.

As shown in the **Figure 6.10**, the living algae with eccentricity values between 0.2 and 0.6 accounted for 85.29% of the experimental observations involving the 7-1 ECR microgeometry and the 88.14% of those concerning the elongated geometry. Hence, the living cells were considered to have an average eccentricity of 0.4. Regarding the DDCs, it was found that the cells with an eccentricity varying from 0.2 to 0.5 comprised 83.07% of the cells observed in the 7-1 ECR geometry and the 84.61% in those using the elongated one; therefore, the average eccentricity of the DDCs was assumed as 0.35.

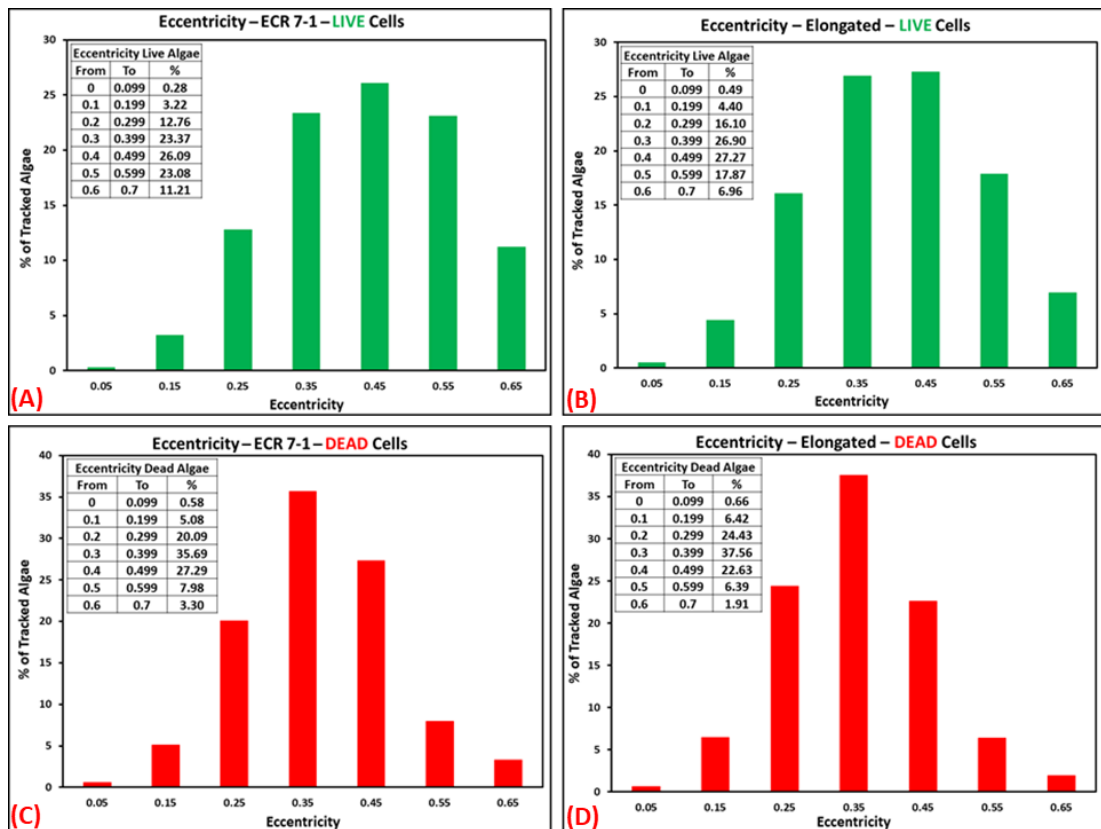


Figure 6.10 – Eccentricity histograms for living DS cells in the ERC 7-1 channel (A), in the elongated one (B) and those for dead microalgae (C) and (D). These results demonstrated that the killing procedure (see Section 5.3.1) did not significantly affect the original algal shape. The rounded shape of the dead algae can be explained considering that DS cells lack of a cell wall, often becoming spherical under unfavourable conditions. [249]

Hence, DDCs were found to be slightly bigger and more rounded than the living microalgae. However, since both living and dead cells were characterised by low axes ratios values, they were assumed to be circular or, in other words, that their major axis equalled the minor one (see Table 6.3).

Table 6.3 – Major axes, eccentricities and axes ratios of the employed DS cells.

Type of Cells	Major Axis [ $\mu\text{m}$ ]	Eccentricity	Axes Ratio
Living <i>Dunaliella</i> Cells	15	0.4	1.091
Dead <i>Dunaliella</i> Cells	17.5	0.35	1.068

However, the approach of considering all the cells during the experimental investigations to have the same dimension and shape may seem to be misleading since they tend to change over time during the various phases of growth, as emphasised in Section 6.4.1.

This is true in PBRs where the usual cultivation time (*i.e.* the residence time of the cells within the culture device) may last several days [288] and where stressing conditions are deliberately applied causing biological, dimensional and morphological changes to the cells which therefore cannot be modelled assuming an average size and shape. [21, 22] However, the average residence time spent by the cells in the channels used in these experiments was much shorter than the typical time-scales of the algal birth, death and adaptation processes (*i.e.* the ones that lead to morphological and dimensional changes) [55] and therefore the variations of size and shape were neglected during the experiments, this is further justified because the microalgae had not been stressed in any way.

Whilst microfluidic devices and the image analysis technique can be employed to periodically monitor a given culture and to determine how size and shape distributions of the organisms vary over time. In fact, the morphologies and dimensions of the cells can be assumed as constant, so if a sample of the culture is analysed, the results provide a “snapshot” of its corresponding size and shape distributions, providing that the technical analysis is carried out within an amount of time where dimensional and morphological changes of the organisms are not significant.

However, the approach could be used in parallel with the currently-employed PBRs optimisation procedures and quality controls methodologies; for example, potential early shear-induced damages on a given culture are currently detected indirectly by monitoring some biological feature of the cells (*e.g.* their viability, growth rates, *etc.*) through specific assessing techniques such as optical density, cells count, fluorescence microscopy and so on. [166] Nevertheless, when the culture is recirculated along a solar collector equipped with static mixers, the quantification of both the inertial-induced effects on the fluid dynamic behaviours of the organisms (see **Section 6.3.3**) and the variations of their sizes and shapes distributions would permit critical phases of the cultivation process to be identified, to better investigate possible distress of the cells and to adapt the processing conditions accordingly. More examples of potential advantages arising from exploitation of the typical PBRs design techniques, quality controls methodologies and microfluidic devices will be provided in **Section 7.3.1**.

The hypothesis of assuming the microchannels as “simplified PBRs” useful to study the fluid dynamic behaviours of the algae and consequently the attainable results presents some biological and engineering limits. These are mostly due to the culturing and experimental conditions used to grow and analyse the cells (see **Section 7.3**). Some of these limitations will be introduced in the next section that is concerned with the main constraints of the scale-up process for tubular PBRs, considering in detail the effects owing to the accumulation of dissolved oxygen along the PBR tubes [118, 139], which were disregarded during the experimental observations of this PhD (see **Section 7.3**).

## 6.5 The scaling-up of tubular photobioreactors

In order to understand the results discussed in this thesis, this section gives a general overview of the main “issues” related to the scale-up process for tubular PBRs, focusing particular attention on the constraints of cells fragility, the accumulation of dissolved oxygen along the tubes of larger PBRs, the need to ensure optimal dark/light cycle frequencies in scaled-up reactors and how these factors limit the maximum scalable length and diameter of PBR tubes, at given processing conditions.

As described in **Section 4.2**, the design of a tubular PBR requires some preliminary experimental investigations in order to observe and quantify some fundamental features concerning the cultivated cells and the PBRs performance (*e.g.* the biomass growth, its quality, temperature profiles along the reactor, *etc.*), which will eventually be employed to optimise the scale up process and to manufacture the final PBR. [118, 166]

Generally, the scaling up of a given tubular PBR involves both the solar loop and the recirculating device. Increasing pump size does not pose a constraint for any realistic size of the PBR but the scale up of continuous solar collectors presents some limitations. [139, 154] In principle, tubular PBRs can be scaled up by increasing either the length or the diameter of the tube but, in practise, they are both constrained mainly by the fragility of the cultured organisms, the accumulation of dissolved oxygen along the tube and the need of achieving optimal dark/light cycles frequencies, as better addressed in the next sub-sections. [139, 154]

### **The accumulation of dissolved oxygen**

The accumulation of dissolved oxygen (DO) represents one of the biggest constraints for the scale-up of horizontal tubular PBRs; in particular, the oxygen is produced and released by the cells as a by-product of the photosynthetic reaction (see **Section 1.3.1**) and it tends to coalesce and form DO pockets in the upper parts of the tubes whilst the culture flows from the aeration port to the degasser port. DO accumulations make it difficult to move both the culture and the gases between the upper and lower parts of the tubes (*i.e.* to achieve optimal gases mixing levels and dark/light cycles) and prevent the cells from exploiting the flashing light effect, decreasing the light utilization efficiency. [154, 232]

When the oxygen concentration in the culture is above air saturation (*i.e.* when the DO concentration exceeds its counterpart in equilibrium with the oxygen partial pressure in the atmosphere), the photosynthetic reaction will be shifted to the left, hampering the biomass production. [142] Thus, DO has an inhibitory threshold value  $C_{O_2,OUT}$  (*i.e.* the maximum allowable oxygen concentration that does not inhibit photosynthesis) which limits the maximum achievable length  $L_{t,max}$  of the PBR tubes as:

$$L_{t,max} = \frac{U_{L,max} \cdot (C_{O_2,OUT} - C_{O_2,IN})}{R_{O_2}} \quad (\text{eq. 6.16})$$

Where  $U_{L,max}$  is the maximum permissible culture velocity (which is limited by the sensitivity to shear of the cultured organisms),  $C_{O_2,IN}$  is the oxygen concentration at the aeration port of the PBR (it generally coincides with the air saturation value) and  $R_{O_2}$  is the volumetric rate of oxygen generation due to photosynthesis in the tube. [154] *Eq. 6.16* permits to obtain the maximum tube length which allows to maintain the level of oxygen below the critical value. [154]

### **Increasing the tube diameter and the ideal dark/light cycle frequencies**

Using narrow tubes guarantees higher illumination surface-to-volume ratios, shorter light paths, better dark/light cycles (DLCs) and therefore the achievable biomass volumetric productivities are usually higher than those in larger diameter tubes. However, employing small diameters implies also that longer tubes will be required, the number of passages of the culture through the solar collector will increase and higher dissolved gases concentrations and temperature gradients along the tubes will occur. [139]

Generally, under given conditions (*i.e.* solar irradiance, biomass concentration and algal pigment content), when the diameter of the PBR tube is increased, the depth at which the light intensity declines below the compensation intensity (*i.e.* the minimum intensity required for the photosynthetic process to occur, see **Section 5.2.1**) will not be affected, whereas the relative volumes of the dark zones would increase accordingly. [118, 154, 231] Therefore, on scaling up the productivity of the reactor would deteriorate, unless adequate mixing is provided to improve mass transfer rates and enhance the light utilisation efficiency by circulating the cells between the upper and lower parts of the tubes. [231]

Molina Grima *et al.* proposed a scale-up criterion based on the increase of the tube diameter, suggesting that geometrically-similar PBRs can have identical productivities as long as their DLCs frequencies are held constant and kept within 1 – 1.5 Hz [139, 232]; higher frequencies would be achieved by turbulently pumping the algal suspensions and potentially damaging the cells, while at lower frequencies, the recirculation would be too slow decreasing the algal growth rates (see **Section 2.7.3**). [118]

According to the criterion suggested, in order to ensure that frequencies of DLCs are kept within the ideal range, the linear flow velocities  $U_L$  at the two scales must conform to the following equation:

$$U_{L,L} = f_s^{9/7} \cdot U_{L,S} \quad (\text{eq. 6.17})$$

where the subscripts L and S refer to the larger and the smaller scales and  $f_s$  is the scale factor, defined as the ratio of the tube diameters  $d_t$  at the two scales:

$$f_s = \frac{d_{t,L}}{d_{t,S}} \quad (\text{eq. 6.18})$$

However, the culture velocity cannot be increased limitlessly since it is constrained by potential shear-induced damage to the cells and limited mechanical strength of the most economic plastic tubes, implying that the maximum scalable diameter will also be restricted accordingly. [232]

The experience gathered by many authors [118, 139, 232] indicates that, for a given tubular PBR, the maximum scalable diameter is encompassed within 5 and 10 cm while the maximum scalable length ranges between 80 and 120 m; these values allow an optimal compromise of the effects described to be found. [231]

## 6.6 Chapter Summary

In this chapter the possibility of exploiting microfluidic devices to periodically monitor a given algal culture while flowing through a tubular PBR equipped with static mixers, focusing particular attention on shear-induced damage to the cells and the variations in their size and shape distributions.

In fact, while cultivated and stressed, cultured organisms must be recirculated along the solar collector and, during these passages, they tend to change their sizes, shapes, biological compositions and sensitivity to shear. [21, 22, 240] Motionless mixers cause local increases of the culture velocity that may result in shear-induced damages, whose effects could also depend on the stage of the cultivation process (*e.g.* the susceptibility to shear of some algal cells depends on the specific phase of growth [236]); thus, the culture must routinely be checked in order to ensure that the processing conditions cannot cause any damage.

The first part of the chapter provided an example used to demonstrate that microfluidic devices and the targeted image analysis process can be exploited to assess the increases of the algal swimming velocities owing to static mixers at the various cultivation phases. The experiments looked at exploring the behaviours of both living and dead *Dunaliella* cells while flowing within a 40-micron-width interval that included the centreline and the contraction region of the 7-1 ECR channel, considering four different flow rates (*i.e.*  $1 \mu\text{l}\cdot\text{min}^{-1}$ ,  $2 \mu\text{l}\cdot\text{min}^{-1}$ ,  $5 \mu\text{l}\cdot\text{min}^{-1}$  and  $10 \mu\text{l}\cdot\text{min}^{-1}$ ) and assuming the microgeometry to behave as an inline static mixer. The results showed that this approach would permit the quantification of how the inertial effects can influence both the cells and the flow and to achieve more insight into the actual fluid dynamic experiences of the cells at the same experimental conditions, demonstrating that the higher the flow rate used, the more living and dead microalgae tend to behave similarly, the more the role of motility can be disregarded.

The second part of the chapter aimed at experimentally assessing the shape and size distributions of both the living and dead *Dunaliella* cells that were used in this PhD, computing the major axes, minor axes and eccentricities of the microalgae that had flowed at  $1 \mu\text{l}\cdot\text{min}^{-1}$  within the 7-1 ECR channel and the elongated geometries. Interestingly, the dead cells were found to be slightly bigger and more rounded than the living microalgae.

In conclusion, the results presented in this chapter indicate that microfluidic devices could be used for quality control purposes and to quantify both the inertial-induced effects on the fluid dynamic behaviours of the organisms and the variations of their sizes and shapes distributions during the whole biomass production process. This information can then be utilised to detect early shear-induced damage to the cells, identify the critical phases of the cultivation process and to adapt the operational conditions accordingly, as long as the suggested approach is used alongside the currently-employed PBRs optimisation procedures and quality control methodologies (see **Section 7.3.1**).

As addressed in the next chapter, the suggested approach and the attainable results present some biological and engineering constraints which are mostly due to the fact that culturing conditions in PBRs are completely different from the ones used during the experimental investigations and the limited residence times spent by the cells in the channels (see **Section 6.4.3**).

## – Chapter 7 –

# Studying photobioreactors through microfluidic devices: main limitations and future work

### 7.1 Chapter layout

This last chapter addresses the main limitations concerning the assumption that microchannels represent horizontal PBRs and their microgeometries represent static mixers. It also provides some suggestions for future research work.

The major constraints of the approach are mostly due to the fact that the culturing conditions in real PBRs are completely different from the ones used to grow and study the *Dunaliella* cells in the laboratory, in addition the average residence times of the algae in the channels during these experiments were much shorter than those typically spent by the cells within a given culture device [288]. Consequently, some of the typical “issues” that usually occur in real PBRs could not be considered during the experimental investigations, *i.e.* the algal suspensions were assumed to contain only a predominant species, gradients of gases and temperatures were not taken into account, biofouling phenomena were neglected and morphological and dimensional changes of the cells were disregarded.

Nevertheless, the effects of these limits on the utilisation of microfluidic devices to simulate PBRs depend on the stage of the biomass production process where the attainable results will be exploited (*i.e.* whether they will be employed for optimisation or quality controls purposes).

The chapter provides two examples to demonstrate that the simultaneous exploitation of the suggested approach and the currently-utilised PBR optimisation procedures can be used to plan more efficient laboratory-scale experiments and detect early shear-induced damages on the cells.

## 7.2: The most important results achieved during this research work: a recap

This section summarises the main objectives, hypotheses and results of this research to study the fluid dynamic behaviours of both living and dead *Dunaliella Salina* cells within various expansion-contraction microchannels and to investigate the possibility of exploiting microfluidic devices and the image analysis technique as complementary tools for PBRs optimisation, assuming the channels as “simplified PBRs” and their microgeometries as static mixers.

The experimental investigations were run under the assumption that the fluid dynamic experience of cells can be compared to that of cells cultured in real horizontal PBRs equipped with static mixers and that the various “processing conditions” were simulated by pumping suspended cells at different flow rates within the channels. This work was undertaken to acquire helpful experimental data directly from the microalgae, taking into account their intrinsic properties, to exploit them during the PBR design and operation and improving the viability of the whole biomass production process.

The same approach was employed to study the behaviour of dead *Dunaliella* cells dragged by the flow, considering them to behave as passive particles, comparing the differences between dead and living algal cells’ responses under the same experimental conditions, investigating the role of the motility in the algal behaviours and further demonstrating that living microalgae cannot be treated as passive particles.

Moreover, the experiments allowed the size and shape distributions of both living and dead cells to be quantified, to assess how the inertial effects induced by the employed flow rates and microgeometries affected the swimming velocity of the cells and also to demonstrate that the optimisation of the geometrical configuration of real culturing devices would also result in more homogeneous irradiance profiles within the algal cultures.

All the experimental observations carried out during this PhD, the most significant outcomes and their potential applications have been summed up in the **Table 7.1**.

**Table 7.1 – The experimental observations carried out during this PhD, the resulting outcomes and in what stages of the biomass production process they can be exploited, *i.e.* Screening Process (SP), Design Process (DP), Cultivation Process (CP), Quality Control (QC) and Downstream Processes (DSP).**

<b>Experiment</b>	<b>Main outcomes and their potential applications</b>	<b>Where they can be exploited</b>	<b>Key sections</b>
Cells swimming under stagnant conditions	Quantify the algal swimming trajectories and velocities within the channels, compare different algal species, characterise the algal responses at the single cell level, assess the cells viability.	SP, DP, CP, QC	<b>Section 4.7</b>
Cell-wall interactions	Quantify the algal swimming velocities close to the walls and characterise the algal responses at the single cell level.	SP, DP, CP	<b>Section 4.7.2</b>
Study the living cells behaviours while flowing through the straight channel at a certain flow rate	Quantify the algal dispersion, the cell-wall interactions, the algal swimming trajectories and velocities within the channels at different processing conditions.	SP, DP, CP, QC	<b>Section 4.8</b>
Study the living and dead cells behaviours while flowing through a given microfluidic geometry at a certain flow rate	Quantify the algal dispersion, the interaction of the cells with the walls, the algal swimming trajectories and velocities within the channels, simulate and compare the fluid dynamic behaviours of both living and dead cells in a horizontal PBR equipped with static mixers.	SP, DP, CP, QC	<b>Section 4.9</b> <b>Section 5.6</b>
Study how the inertial-induced effects influenced the light diffusion within the culture.	Assess how the light distribution in the culture can be enhanced at different processing conditions, quantify the inertial-induced cell depleted regions and therefore how the algal mitigation phenomena are inhibited.	SP, DP, CP	<b>Section 5.7</b>
Study the behaviours of the cells while flowing within a given microgeometry	Quantify the inertial-induced effects on the cells during the various cultivation phases and adapt the processing conditions accordingly.	SP, DP, CP, QC	<b>Section 6.3</b>
Targeted ImageJ analysis process	Analyse and quantify the fluid dynamic behaviours of the cells in crucial parts of the channels.	SP, DP, CP, QC	<b>Section 4.7.2</b> <b>Section 6.3</b>
Quantify the algal shape and size distributions	Assess how algal size and shape distributions change during the whole cultivation and stressing processes and adapt the processing conditions accordingly.	DP, CP, QC, DSP	<b>Section 6.4</b>

Most importantly, the approach was developed also meant to pave the way towards a new mentality whereby PBRs, their configurations and processing conditions will be set and adapted starting from the biological and fluid dynamic characteristics of the cultured microalgae (see **Table 4.2**). Successful design and operation of PBRs must rely on attaining a proper balance between engineering and algal intrinsic features that are dependent on the species being cultured. Current practice neglects the algal swimming properties as insignificant complications and the cells are treated as passive particles. [56]

Nonetheless, despite the promising results, the hypotheses of assuming the microfluidic devices behave as horizontal PBRs and their microgeometries as static mixers present some biological and engineering limits that will be discussed in the next section.

### **7.3 Limitations of the suggested approach and main implications for the results**

This section is concerned with the major constraints relating to the study of horizontal PBRs through microfluidic devices, showing that they were mostly due to the culturing and experimental conditions used to analyse the cells. It is also outlined the ways in which these limits can affect the attainable results depending on how they will be exploited (*i.e.* whether they will be employed for optimisation or quality control purposes).

The major limitations of the approach are mainly due to the culturing conditions in a real PBR being completely different from the ones used to grow the *Dunaliella* cells employed in this research work in the following ways: **1)** the experimental observations were carried out utilising dilute algal suspensions; **2)** the average residence times of the algae in the channels during the experiments were much shorter than those typically spent by the cells within a given culture device [288]; **3)** the results represented the fluid dynamic experiences of the cells just at the channels centreline (*i.e.* during the experiments, specimens had to be brought into focus, in order to observe the channels centreline).

As described in the **2<sup>nd</sup> Chapter**, in order to be optimally cultivated, a certain algal culture requires a growth medium, a source of inorganic carbon, usually carbon dioxide-enriched air, and light, needed for the photosynthetic process. [118, 139] Nevertheless, the cultivation of large-scale microalgal cultures implies the optimisation of several operational, environmental and design variables, in order to fulfil the growth requirements of the selected strain, to avoid algal accumulations and eliminate gradients of light, nutrients, gases and temperature within the reactor [118], which are currently addressed by turbulently pumping the suspensions, using either airlift circulators or various types of pumps. [10, 118]

On the other hand, the microalgae employed in this research were grown within borosilicate flasks, which were sealed using cotton wool balls and aluminium foil as breathable lids, were kept at room temperature and exposed to a source of light (*i.e.* a set of cool white fluorescent tubes), without being mixed (see **Section 3.2.3**). Moreover, these cultures had to be reprepared periodically, in order to be able to use fresh cells for the experiments

Therefore, some of the typical “issues” that usually occur in a given culture device could not be investigated during the study; in particular, the algal suspensions were assumed to contain only one predominant species (*i.e.* the cultures were considered as axenic), gradients in gas concentrations, temperature and biofouling phenomena were neglected and morphological and dimensional changes of the cells were disregarded.

#### **Gases concentration gradients were not considered**

In a given PBR, gradients in gas concentrations are due to the accumulations of carbon dioxide-enriched air and dissolved oxygen, which is released by the cells due to the photosynthesis. [118]

During the experimental investigations, gas concentration gradients were not taken into account because **1)** the algal suspensions were dilute and therefore the amounts of released oxygen and carbon dioxide within the cultures were negligible; **2)** the inorganic carbon source used to grow the cells was sodium bicarbonate (*i.e.* no carbon dioxide-enriched air was injected in the medium); **3)** the dissolved oxygen accumulations during the experiments were not consistent, owing to the short residence times of the cells in the channels.

However, in commercial PBRs, gas concentration gradients play a key role and must be prevented since they may inhibit the cellular growth, compromise the biomass formation, hamper the dark/light cycles and can even impact the PBR scale up process. [160, 232]

#### **Temperature gradients were not taken into account**

During the experimental investigations, the effects temperature gradients were not investigated because **1)** the light bulbs did not cause the temperatures of the cultures to increase; **2)** the temperature within the channels remained constant, due to short residence times of the cells.

In commercial closed PBRs, the temperature of a certain culture is governed by the sunlight regimen and tends to vary with the day-night cycles, the amplitude of which is affected by the seasons [251] *e.g.* culture temperatures can range from below 0°C to 45°C [157]; therefore, PBRs require some temperature control systems in order to guarantee an ideal thermic profile in the culture. [139, 251]

#### **The cultures were axenic**

The algal suspensions studied were assumed to be axenic, albeit this is not true in commercial PBRs (see **Section 5.2.3**) that may be subject to chemical and biological contaminations. In particular, chemical contaminations are due to some pollutants that may be absorbed by the culture medium or to some chemical flocculants, used for creating algal self-aggregations (see **Section 2.10.2**), while biological contaminations are caused by other fast-growing opportunistic species that may compete for light and nutrients against the cultured cells and even predate them, leading to their extinction. [138]

#### **The sizes and shapes of the living and dead cells were assumed as constant**

During the experiments, sizes and shapes of the living and dead cells were considered to be constant because: **1)** the short residence times of the organisms in the channels (see **Section 6.4.3**), considering also that the microalgae had not been stressed in any ways; **2)** the fact that biological contaminations were prevented (*i.e.* the cultures were grown axenically) avoiding the presence of other organisms with different shapes and sizes; **3)** the algal cultures were reprepared periodically, to inhibit the accumulation of dead and lysed cells (*i.e.* algae with irregular shapes); **4)** the killing procedure developed and used in this research allowed the cells to be killed without affecting their morphology consistently.

An algal culture is a dynamic system that includes cells at various stages of growth and stressing levels (*i.e.* different substrate concentrations), lysed and dead cells; therefore, sizes and shapes of the cultured microalgae are non-uniform and change over time, considering also that the final shapes of dead cells depend on the various causes of death (see **Section 5.2**). [235, 249, 250]

#### **Uniform algal concentrations were employed**

The formations of algal patchiness and accumulations in the channels were prevented by **1)** using dilute suspensions; **2)** adapting the experimental setup and procedure of the experiments involving the dead cells so as to inhibit their sedimentation and aggregation phenomena (see **Section 5.3**).

Interestingly, the ways how these constraints can influence the study of PBRs through microfluidic devices depend on what stages of the biomass production process the attainable results will be exploited. Specifically, as summarised in the **Table 7.1**, some of the experimental procedures and their related outcomes can be used either for optimising the design and processing conditions of a given PBR (*e.g.* compare the algal responses at different conditions, quantify cell-wall interactions, *etc.*) or for quality controls purposes (*e.g.* study cell viability, assess algal size and shape distributions, *etc.*); the main effects of the limits on these potential applications are discussed in the following sub-sections.

#### **Employing the suggested approach for optimisation purposes**

When microfluidic devices and the image analysis technique are employed for PBR design and optimisation purposes, the hypotheses of assuming that the fluid dynamic experience of the cells can be compared to the ones that actually occur in commercial culturing devices are only valid during the preliminary cultivation phases.

In particular, at the beginning of the cultivation process, the cells of a given algal culture are usually inoculated within the PBR and, since they must adapt themselves to the new growth conditions, are not able to reproduce (*i.e.* they go through the lag phase); after this stage, the log phase occurs where the algae start to multiply exponentially and their concentration begins to increase. [223]

Theoretically, during these growth stages, the cells could be studied through the approach developed in this thesis, providing that their concentration  $C_A$  lies within a certain interval  $C_{A,min} < C_A < C_{A,max}$ , the PBR is well-mixed (*i.e.* algal patchiness, biofouling phenomena and gas concentration gradients are neglectable), equipped with an efficient heat exchanger (*i.e.* the temperature gradients are low) and the cells are not stressed (*i.e.* their biological composition is constant).

In the above-defined algal concentration interval,  $C_{A,min}$  and  $C_{A,max}$  are respectively the minimum and maximum algal concentrations that can be tracked in a given microfluidic device. Hence, when  $C_A < C_{A,min}$ , the culture is too dilute to be analysed and it would be difficult to obtain significant statistical results, whereas when  $C_A > C_{A,max}$ , the algal concentration is too high and the achievable results would be misleading.  $C_{A,min}$  and  $C_{A,max}$  values depend mostly on the experimental conditions (*e.g.* the geometrical characteristics of the channels and their microgeometries, the flow rate(s), the magnification(s), *etc.*) and should be assessed case by case, whereas the rate at which these concentrations are reached during the cultivation process can be influenced by various engineering, biological and environmental factors (*e.g.* the total working volume of the reactor, the incident solar light, *etc.*).

#### **Employing the suggested approach for performing quality controls on the cells**

All the limiting factors mentioned in the previous sub-section do not constrain the exploitation of microfluidic devices and the image analysis technique for routine cells screenings, owing to the relative short average residence times of the cells within the channels that allow to neglect their dimensional, morphological and biological changes (see **Section 6.4.3**), albeit it is still necessary to control the cell concentration  $C_A > C_{A,min}$  in order to carry out the tracking process.

However, the approach should always be used in parallel with current PBRs optimisation procedures, independently of what stage of the biomass production process is considered. These concepts are analysed further in the next section which shows how the simultaneous use of the typical PBRs design techniques, quality controls methodologies and microfluidic devices could allow more realistic results to be obtained.

### 7.3.1 Employing the research approach in parallel with other procedures: two practical examples

This section provides two examples to demonstrate how the exploitation of the suggested approach represents a valuable addition to PBRs optimisation when used in parallel with current techniques. In particular, the examples outline how studying the flow of the cultured organisms through microchannels can be used to efficiently detect early shear-induced damages to the cells in small laboratory-scale experiments

As described in the **Section 4.2**, the design of a PBR requires some laboratory-scale experiments which currently comprise **1)** the screening process which aims to identify the most appropriate microalgal strains to culture; **2)** the pre-cultivation of the cultures under well-controlled conditions that simulate the solar irradiance of the final PBR location, to avoid excessive environmental shock to the organisms during their inoculation in the PBR [222]; **3)** some CFD simulations to verify the performance of the pilot-scale reactor that is usually required in the next stage of the design process. [118, 166]

At this stage, all the required information and the biological features of the cells are usually obtained from data available in the literature [166]. This data may have been gathered from cells cultivated under different conditions to the ones of the final plant location, leading to deceptive results. [166] Using the microfluidic devices and the image analysis technique reported in this thesis would permit more realistic information from the cells (*e.g.* their actual shapes, sizes, tendency for biofouling, *etc.*) to be available to supplement the CFD simulations and the pilot-scale experiments.

Furthermore, once the algal cultures have pigmented sufficiently and the lab-scale optimisation processes have been performed, the cells will be inoculated in the pilot-scale reactor where further experimental investigations may be run through daily quality controls (QCs), in order to quantify how the processing conditions affect the reactor performance, to maximise the biomass production and to optimise the scale up process of the final PBR. [118, 166]

Interestingly, QCs relating to pilot-scale reactors focus on optimising the scale up process while those in commercial scale PBRs focus attention on biomass production and the wellbeing of the culture.

QCs must always check some fundamental biological and engineering features (*e.g.* dissolved oxygen concentration, temperature profiles, the presence of potential contaminant organisms, *etc.*), algal growth rate, quality and quantity of the obtained biomass and so on. QCs must also confirm that the processing conditions do not give rise to turbulent fields which may damage the cells or impact upon their viability, biochemical composition, morphology, *etc.* (*i.e.* not causing shear-induced “reversible” effects on the organisms), noting that cell fragility tends to change during the various stages of growth and stressing. [139, 198]

Currently QCs methods depend on the cultured algal strain, traditional methodologies which are routinely to test the cells and detect signs of damage to the cultured organisms are optical density, cells counts (used to determine the algal growth rate), fluorescence microscopy (where specific fluorescence dyes are exploited to reveal potential contaminants and substrates of interest, *e.g.* the fluorescent dye Nile red is used to localise and quantify lipids within the cells [166]) and visual techniques.

These procedures involve of placing the cells on a glass slide, typically under a cover slip, and observing the induced deformations or the reduced motility of the cells. [235, 240] However, under these conditions, the microorganisms are confined within an artificial environment with higher pressures, temperatures and lower oxygen concentrations than those of the culture owing to the rapid medium evaporation, consequently they cannot be studied over a long period of time and this may lead to misleading results. [297] Using the proposed microfluidic devices permit the cells to be observed longer, in more natural conditions, avoiding pressure and temperature changes [297] and therefore they have the potential to become a valuable tool for routine cell screening, considering all the other beneficial results that can be achieved (see **Table 7.1**).

These examples can also be thought as possible suggestions for future applications and research work which, along with the ones provided in the next section, could help to further understand the potential beneficial advantages of using microfluidic devices for optimisation and quality controls purposes.

## 7.4 Further suggestions for future research work

### Studying the behaviours of stressed cells

Future work should be aimed to develop a stressing procedure for the *Dunaliella* cells in order to investigate the fluid dynamic behaviours of the stressed cells and compare their responses to those of living and dead non-stressed algae, which would also allow simulation of different phases of the cultivation process.

Generally, the industrially-employed stressing techniques are specific to the cultured species and the desired substrate(s), *e.g.* oily algae are usually cultivated under sulphur-deprived or nitrogen-deprived media to maximise the production of lipids [10, 131] or are exposed to high salinity or high light intensities to trigger the accumulation of  $\beta$ -carotene. [249] Therefore, stressing the cells would imply modification of their growing conditions, for example, the procedure for preparing the culture medium (see **Appendix 3.1**) could be modified by either reducing or increasing the quantities of some required chemicals or completely removing them from the original “recipe”.

### The processing conditions as a prevention instrument

It could also be useful to investigate whether the processing conditions can be exploited as a prevention tool to inhibit potential detrimental effects due to opportunistic organisms.

This may be achieved by leaving a sample of the culture medium in the open air under stagnant conditions and checking it periodically to find out what kinds of organisms can grow and thrive within it. The container should be sealed using micropore filter paper. This would avoid potential chemical contaminations of the medium caused by environmental coarse dust particles, but would not prevent potential microorganisms from being carried along with fine dust and impurities particles through the filter pores.

If incoming species are observed, their potential interactions with DS cells should be investigated (*e.g.* symbiotic interactions may occur, organisms that may be fast-growing competitors, *etc.*), assessing also possible predator-prey scenarios. Where appropriate, they could be cultured and their fluid dynamic behaviours studied (*i.e.* their tendency for biofouling, for clumping, *etc.*) to evaluate whether the processing conditions may be adapted to prevent damaging effects on the desired culture.

This procedure could be repeated considering using both “normal” and the “modified” growing mediums in order to determine if different opportunistic organisms may be growing during different phases of the cultivation process and therefore if the processing conditions must be adapted accordingly.

#### **Further experiments concerning the algal plume-induced effects**

In **Sections 4.9.4** and **5.6**, results concerning the algal plume-induced effects on the behaviours of both living and dead DS cells were discussed, giving particular attention to their dispersion along the channel and their interactions with the walls and outlining that their influence tended to decrease with different fading velocities that depended on the microfluidic geometry and flow rate.

In some of the cases considered, the portion of the channels affected by the inertial effects were longer than the observable zone; consequently, it would be helpful to quantify how the “length” of a certain algal plume varies as a function of the processing conditions. In fact, this would allow some preliminary investigations to optimise the geometrical configuration of a given PBR where straight parts are interchanged with static mixers, in order to define an optimal spacing distance between two mixers (see **Section 4.9.4**).

All these suggestions for further research and all the experiments carried out in this research work could be run involving other species of swimming and non-swimming microalgae (*e.g. Chlorella, Chlamydomonas, etc.*), in order to shed further light on their behaviours under different fluid dynamic conditions and to investigate the utilisation of microfluidic devices as complementary instruments for the PBR optimisation process.

## 7.5 Final conclusions

The main objectives of this PhD were to investigate experimentally the viability of exploiting microfluidic devices and image analysis as complementary tools for PBR optimisation processes and to pave the way towards a new approach whereby PBRs, their configurations and processing conditions will be set and adapted starting from culture-specific characteristics.

The results reported in this thesis demonstrate that microchannels can be employed to study the role of flows on the motility of aquatic microorganisms, allowing the experimental conditions to be carefully controlled, to obtain statistically significant data in a cost efficient, less time-consuming way and using low volumes of algal cultures. Therefore, the suggested approach has great potential and can represent a new inexpensive and effective methodology for the development of PBRs, from algal cells screening to quality controls on the cultures.

Nonetheless, despite the promising results, the hypotheses of assuming microfluidic devices behave as horizontal PBRs presents some biological and engineering limitations and consequently, in order for such approach to be exploited, multidisciplinary collaborations between academia and industry would be required, which would allow critical bottlenecks of the whole biomass production process to be identified to address the future research activities accordingly.

## **Appendix 3.1 Preparation of the culture medium and its physical properties**

### **A 3.1.1 The preparation procedure**

In this research work, DS cells were cultured using the Hejazi and Wijffels modified culture medium (HWMCM), which is a standard medium used for algae growth. [185]

Since the preparation of the HWMCM involves some hazardous chemicals and potentially dangerous pieces of equipment (*e.g.* glass, electrical devices, *etc.*), both the related risk assessment and control of substances hazardous to health (COSHH) assessment should be carefully read, before starting to work.

Firstly, the following pieces of equipment are needed: a 2-litre glass beaker, a spatula, a 50-ml beaker, 1-litre bottle, disposable plastic containers for weighting the chemicals, an antibacterial disinfectant, a pair of lab gloves, a 200- $\mu$ l micropipette, two 3-ml plastic Pasteur pipettes and a pH meter.

In order to prepare 1 litre of HWMCM, the following procedure was used:

A litre of distilled water must be poured into the 2-litre glass beaker, 87.6600 g of sodium chloride must be weighted in the 50-ml beaker and added to the water. Using the spatula, the solution has to be mixed to ensure complete dissolution.

Next, the following chemicals must be weighed and added to the solution: 0.4200 g of sodium nitrate, 1.2324 g of magnesium sulfate heptahydrate, 0.0746 g of potassium chloride, 0.0441 g of calcium chloride dihydrate, 0.8400 g of sodium bicarbonate, 12.1440 g of Tris(hydroxymethyl)aminomethane (THAM).

At this point,  $100 \pm 0.5$   $\mu$ l of a trace elements solution, called f/2 medium and purchased from CCPA [190, 191], must be added through the micropipette. Furthermore,  $2.5 \pm 0.25$  ml of a 0.15 M boric acid solution must be added using the plastic pipette. The solution must be agitated until the components have dissolved to yield a clear solution. [298]

Following the procedure described in the risk and COSHH assessments, the pH of the solution must be lowered to around 7.5, using a 1 M hydrochloric acid solution.

After the pH has been adjusted, the solution must be poured into the 1-litre bottle, autoclaved and sterilised at 121°C for 30 minutes, to prevent opportunistic species from contaminating the medium and to compete against the algae.

In order to avoid precipitation issues [185],  $1 \pm 0.25$  ml of a 0.1 M monosodium phosphate solution has to be added to the medium after it has cooled down at room temperature, working in the fume hood. Nevertheless, before doing that, the fume hood surface must be sterilised, through an antibacterial disinfectant.

The medium must be kept in the fridge, where it can maintain its chemical properties for a few months.

### A 3.1.2 The physical properties

The physical properties of the HWMCM (*i.e.* its density and viscosity) were measured. The density was measured using a density bottle (10-ml density bottle with a mass of 12.7062 g, Jaytec glass) and an analytical balance (AV 64C Adventure Pro Semi-micro Analytical inCal Balance Scale, Ohaus GmbH), at room temperature (*i.e.*  $\sim 20^\circ\text{C}$ ).

In order to reduce errors, the measurements were repeated four times, obtaining the following values:

Table A3.1.1 – The measured density values regarding the culture medium.

Measurement	HWMCM and density bottle mass [g]	HWMCM volume [cm <sup>3</sup> ]	HWMCM density [g·cm <sup>-3</sup> ]
1	23.1375	10	1.0431
2	23.1372	10	1.0431
3	23.1370	10	1.0431
4	23.1367	10	1.4030

Therefore, the density value  $\rho_m$  of the culture medium can be assumed as  $1043.1 \text{ kg}\cdot\text{m}^{-3}$ .

The viscosity of the HWMCM has been measured by performing three sweep tests through a rotational rheometer (DHR-2 rotational rheometer, TA instruments), obtaining the following results:

Table A3.1.2 – The results of the first sweep test.

Stress [Pa]	Shear rate [s <sup>-1</sup> ]	Viscosity [Pa·s]	Step time [s]	Temperature [°C]	Normal Stress [Pa]
6.29 x 10 <sup>-3</sup>	1.00 x 10 <sup>-1</sup>	6.29 x 10 <sup>-2</sup>	181.14	19.90	-4.11
7.86 x 10 <sup>-3</sup>	1.58 x 10 <sup>-1</sup>	4.96 x 10 <sup>-2</sup>	362.26	20.00	-8.30
6.35 x 10 <sup>-3</sup>	2.52 x 10 <sup>-1</sup>	2.53 x 10 <sup>-2</sup>	543.34	20.00	-11.70
3.06 x 10 <sup>-3</sup>	3.98 x 10 <sup>-1</sup>	7.70 x 10 <sup>-3</sup>	724.40	20.00	-8.43
6.80 x 10 <sup>-3</sup>	6.31 x 10 <sup>-1</sup>	1.08 x 10 <sup>-2</sup>	905.48	19.99	-8.13
1.72 x 10 <sup>-3</sup>	1.00	1.72 x 10 <sup>-3</sup>	1086.55	20.00	-20.64
3.98 x 10 <sup>-3</sup>	1.59	2.51 x 10 <sup>-3</sup>	1267.62	20.00	-22.66
4.33 x 10 <sup>-3</sup>	2.51	1.73 x 10 <sup>-3</sup>	1448.70	20.01	-27.50
6.05 x 10 <sup>-3</sup>	3.98	1.52 x 10 <sup>-3</sup>	1629.76	20.00	-30.16
8.15 x 10 <sup>-3</sup>	6.31	1.29 x 10 <sup>-3</sup>	1810.83	19.99	-33.02
1.28 x 10 <sup>-2</sup>	10.00	1.28 x 10 <sup>-3</sup>	1991.89	19.99	-35.08
2.06 x 10 <sup>-2</sup>	15.85	1.30 x 10 <sup>-3</sup>	2112.93	19.99	-38.34
3.14 x 10 <sup>-2</sup>	25.12	1.25 x 10 <sup>-3</sup>	2233.99	20.00	-41.57
4.89 x 10 <sup>-2</sup>	39.82	1.23 x 10 <sup>-3</sup>	2355.04	20.00	-43.85
7.68 x 10 <sup>-2</sup>	63.10	1.22 x 10 <sup>-3</sup>	2476.09	20.00	-48.15
1.21 x 10 <sup>-1</sup>	100.00	1.21 x 10 <sup>-3</sup>	2597.15	20.00	-52.07
1.90 x 10 <sup>-1</sup>	158.90	1.20 x 10 <sup>-3</sup>	2718.23	20.00	-56.69
2.87 x 10 <sup>-1</sup>	251.19	1.14 x 10 <sup>-3</sup>	2839.33	19.97	-65.54
4.55 x 10 <sup>-1</sup>	398.11	1.14 x 10 <sup>-3</sup>	2990.45	20.01	-76.58
7.24 x 10 <sup>-1</sup>	630.96	1.15 x 10 <sup>-3</sup>	3141.52	20.00	-95.02
1.16777	999.99	1.17 x 10 <sup>-3</sup>	3262.56	19.99	-129.37

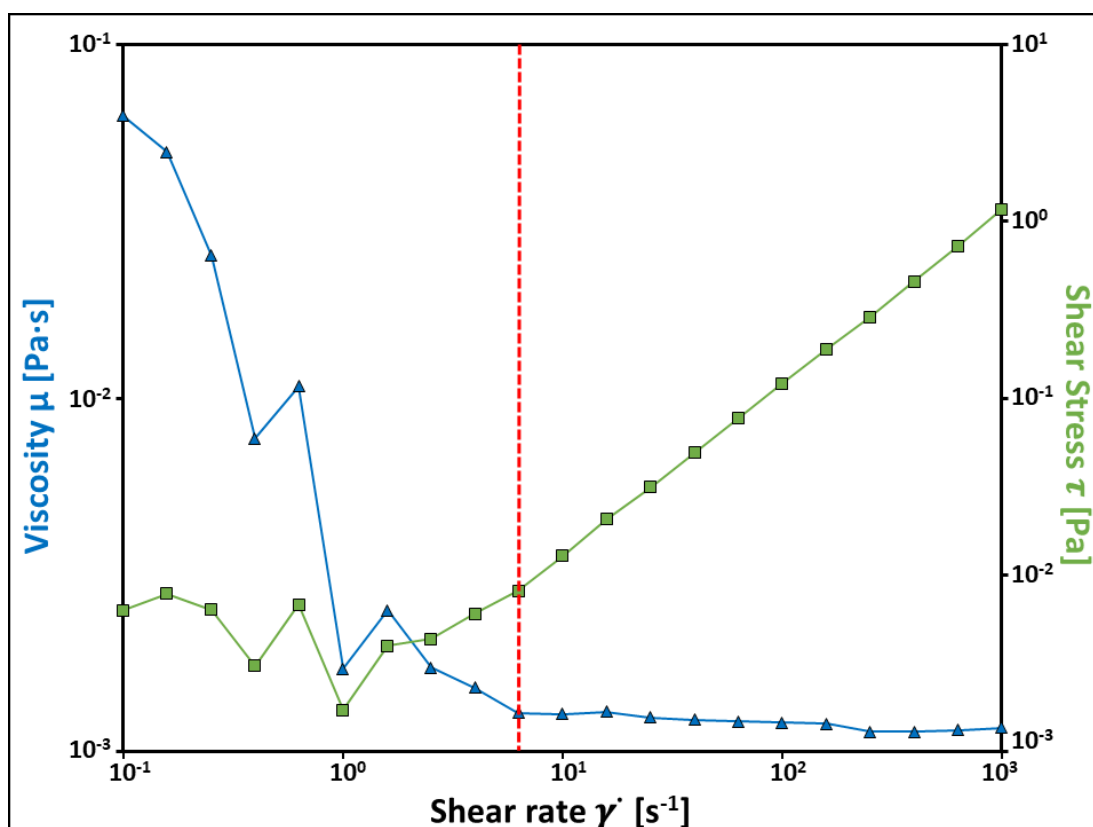


Figure A3.1.1 – Viscosity, shear rate and shear stress of the HWMCM, obtained during the first experiment. The medium showed a Newtonian behaviour when  $\dot{\gamma} \geq 6.31 \text{ s}^{-1}$  (see the red dashed line).

Table A3.1.3 – The results of the second sweep test.

Stress [Pa]	Shear rate [s <sup>-1</sup> ]	Viscosity [Pa·s]	Step time [s]	Temperature [°C]	Normal Stress [Pa]
1.23 x 10 <sup>-1</sup>	1.00 x 10 <sup>-1</sup>	1.23	181.10	19.99	-131.99
2.01 x 10 <sup>-1</sup>	1.58 x 10 <sup>-1</sup>	1.26	332.22	19.99	-179.60
1.90 x 10 <sup>-1</sup>	2.51 x 10 <sup>-1</sup>	7.58 x 10 <sup>-1</sup>	453.25	20.02	-190.10
1.35 x 10 <sup>-1</sup>	3.98 x 10 <sup>-1</sup>	3.39 x 10 <sup>-1</sup>	634.30	20.00	-181.15
1.17 x 10 <sup>-1</sup>	6.31 x 10 <sup>-1</sup>	1.85 x 10 <sup>-1</sup>	815.35	19.99	-176.78
1.11 x 10 <sup>-1</sup>	1.00	1.11 x 10 <sup>-1</sup>	996.39	20.00	-192.61
1.03 x 10 <sup>-1</sup>	1.58	6.52 x 10 <sup>-2</sup>	1177.41	20.00	-185.22
1.09 x 10 <sup>-1</sup>	2.52	4.33 x 10 <sup>-2</sup>	1358.46	20.01	-193.01
1.14 x 10 <sup>-1</sup>	3.98	2.88 x 10 <sup>-2</sup>	1539.51	19.99	-194.36
1.17 x 10 <sup>-1</sup>	6.31	1.85 x 10 <sup>-2</sup>	1690.54	20.01	-193.57
1.07 x 10 <sup>-1</sup>	10.00	1.07 x 10 <sup>-2</sup>	1871.56	19.99	-189.53
5.11 x 10 <sup>-2</sup>	15.85	3.22 x 10 <sup>-3</sup>	2052.61	19.99	-184.02
3.32 x 10 <sup>-2</sup>	25.11	1.32 x 10 <sup>-3</sup>	2233.66	19.99	-191.63
4.18 x 10 <sup>-2</sup>	39.81	1.05 x 10 <sup>-3</sup>	2354.69	19.99	-197.81
6.23 x 10 <sup>-2</sup>	63.10	9.87 x 10 <sup>-4</sup>	2475.73	20.00	-205.44
9.67 x 10 <sup>-2</sup>	100.00	9.67 x 10 <sup>-4</sup>	2596.76	20.00	-225.11
1.53 x 10 <sup>-1</sup>	158.49	9.64 x 10 <sup>-4</sup>	2717.80	20.01	-232.16
2.41 x 10 <sup>-1</sup>	251.19	9.62 x 10 <sup>-4</sup>	2868.83	19.99	-242.45
3.82 x 10 <sup>-1</sup>	398.11	9.61 x 10 <sup>-4</sup>	2989.89	19.99	-250.27
6.07 x 10 <sup>-1</sup>	630.96	9.62 x 10 <sup>-4</sup>	3140.92	20.00	-269.16
9.74 x 10 <sup>-1</sup>	999.99	9.74 x 10 <sup>-4</sup>	3261.96	20.00	-299.87

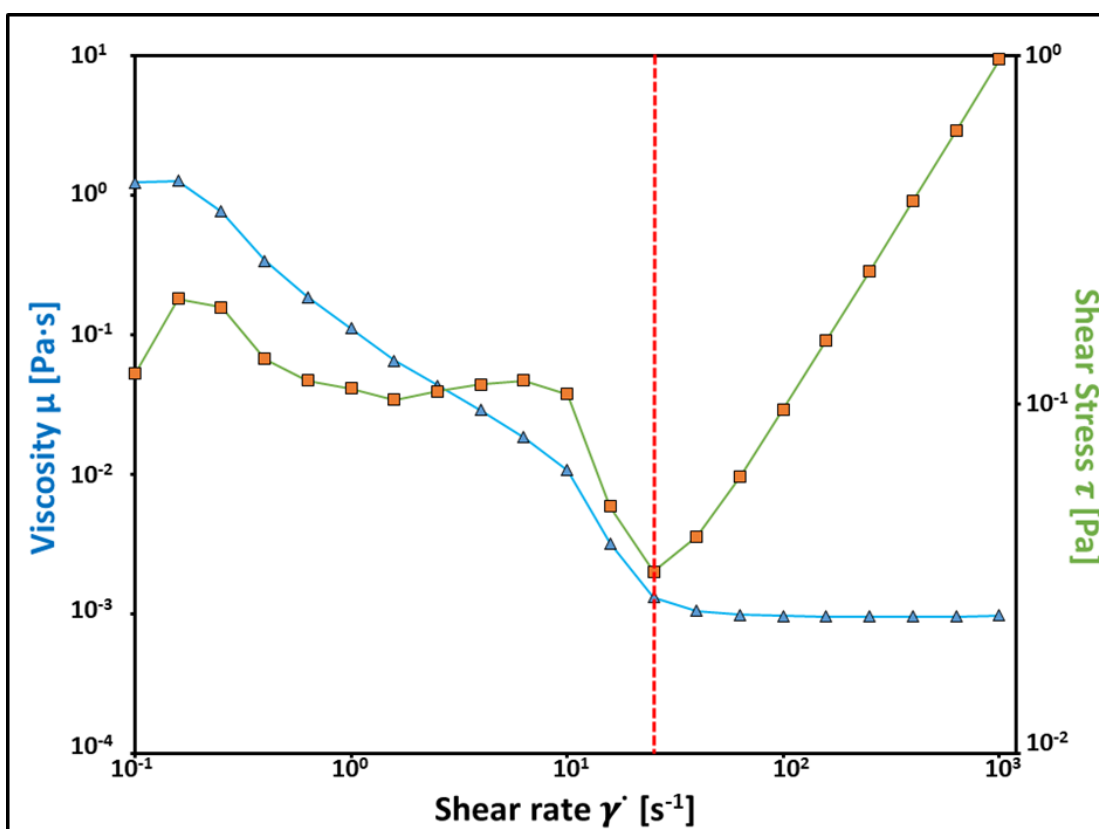


Figure A3.1.2 – Viscosity, shear rate and shear stress of the HWMCM, obtained during the second experiment. The medium showed a Newtonian behaviour when  $\dot{\gamma} \geq 25.12 \text{ s}^{-1}$  (see the red dashed line).

Table A3.1.4 – The results regarding the third sweep test.

Stress [Pa]	Shear rate [s <sup>-1</sup> ]	Viscosity [Pa·s]	Step time [s]	Temperature [°C]	Normal Stress [Pa]
-2.64 x 10 <sup>-3</sup>	9.99 x 10 <sup>-2</sup>	-0.26 x 10 <sup>-2</sup>	181.06	20.00	-10.66
7.05 x 10 <sup>-4</sup>	1.58 x 10 <sup>-1</sup>	4.45 x 10 <sup>-3</sup>	362.1	19.99	-43.74
3.32 x 10 <sup>-3</sup>	2.51 x 10 <sup>-1</sup>	0.13 x 10 <sup>-2</sup>	543.231	20.00	-70.42
3.51 x 10 <sup>-3</sup>	3.98 x 10 <sup>-1</sup>	8.82 x 10 <sup>-3</sup>	724.251	20.00	-109.84
2.41 x 10 <sup>-3</sup>	6.40 x 10 <sup>-1</sup>	3.82 x 10 <sup>-3</sup>	905.291	20.00	-134.26
1.20 x 10 <sup>-3</sup>	1.01	1.20 x 10 <sup>-3</sup>	1086.34	20.00	-185.86
5.02 x 10 <sup>-4</sup>	1.59	3.17 x 10 <sup>-4</sup>	1267.38	20.00	-206.22
2.07 x 10 <sup>-3</sup>	2.51	8.24 x 10 <sup>-4</sup>	1448.4	20.00	-241.20
2.72 x 10 <sup>-2</sup>	3.98	6.83 x 10 <sup>-3</sup>	1629.44	19.99	-264.37
7.73 x 10 <sup>-3</sup>	6.31	1.23 x 10 <sup>-3</sup>	1810.49	20.00	-291.40
1.28 x 10 <sup>-2</sup>	9.99	1.28 x 10 <sup>-3</sup>	1931.52	20.01	-313.13
1.90 x 10 <sup>-2</sup>	15.85	1.20 x 10 <sup>-3</sup>	2052.57	20.01	-319.45
3.12 x 10 <sup>-2</sup>	25.19	1.24 x 10 <sup>-3</sup>	2173.61	20.01	-317.35
4.89 x 10 <sup>-2</sup>	39.82	1.23 x 10 <sup>-3</sup>	2294.64	19.99	-310.97
7.72 x 10 <sup>-2</sup>	63.10	1.22 x 10 <sup>-3</sup>	2415.68	20.00	-307.80
1.22 x 10 <sup>-1</sup>	100.00	1.22 x 10 <sup>-3</sup>	2536.72	20.00	-306.15
1.94 x 10 <sup>-1</sup>	158.49	1.22 x 10 <sup>-3</sup>	2657.75	19.99	-305.93
3.06 x 10 <sup>-1</sup>	251.19	1.22 x 10 <sup>-3</sup>	2778.79	19.99	-304.99
4.81 x 10 <sup>-1</sup>	398.11	1.21 x 10 <sup>-3</sup>	2899.81	20.00	-308.39
7.57 x 10 <sup>-1</sup>	630.96	1.20 x 10 <sup>-3</sup>	3050.87	20.01	-321.42
1.19	999.99	1.19 x 10 <sup>-3</sup>	3171.91	20.00	-359.57

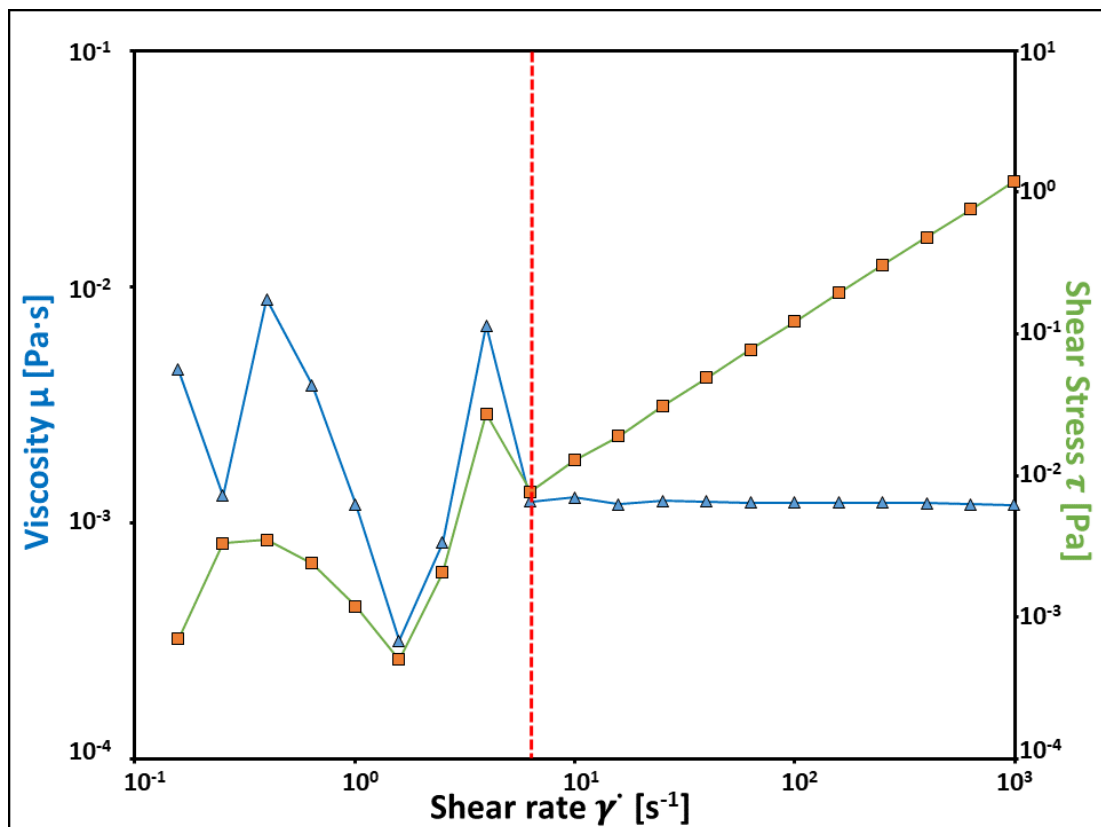


Figure A3.1.3 – Viscosity, shear rate and shear stress of the HWMCM, obtained during the third experiment. The medium showed a Newtonian behaviour when  $\dot{\gamma} \geq 6.31 \text{ s}^{-1}$  (see the red dashed line).

Observing the obtained results, it can be noticed that the viscosity values showed a strange trend when  $\dot{\gamma} < 6.31 \text{ s}^{-1}$  for the first and the third experiments (see **Figures A3.1.1** and **A3.1.3**), and when  $\dot{\gamma} < 25.12 \text{ s}^{-1}$  for the second experiment (see **Figure A3.1.2**).

This is due to the limits of the measuring range of the rheometer.

However, when  $\dot{\gamma} \geq 6.31 \text{ s}^{-1}$  (for the first and the third experiments) and  $\dot{\gamma} \geq 25.12 \text{ s}^{-1}$  (for the second experiment), the culture medium showed a Newtonian behaviour (see **Table A3.1.5**).

**Table A3.1.5** – The shear rate intervals that have been considered in calculating the average viscosity values. The red viscosity values have not been considered since, in that interval (*i.e.*  $6.31 \text{ s}^{-1} \leq \dot{\gamma} \leq 15.85 \text{ s}^{-1}$ ), the viscosity had shown a strange trend, during the second experiment.

Shear rate [s <sup>-1</sup> ]	Viscosity [Pa·s] 1 <sup>st</sup> experiment	Viscosity [Pa·s] 2 <sup>nd</sup> experiment	Viscosity [Pa·s] 3 <sup>rd</sup> experiment	Average viscosity [Pa·s]
6.31	$1.29 \times 10^{-3}$	<b><math>1.85 \times 10^{-2}</math></b>	$1.23 \times 10^{-3}$	$1.26 \times 10^{-3}$
10.00	$1.28 \times 10^{-3}$	<b><math>1.07 \times 10^{-2}</math></b>	$1.28 \times 10^{-3}$	$1.28 \times 10^{-3}$
15.85	$1.30 \times 10^{-3}$	<b><math>3.22 \times 10^{-3}</math></b>	$1.20 \times 10^{-3}$	$1.25 \times 10^{-3}$
25.12	$1.25 \times 10^{-3}$	$1.32 \times 10^{-3}$	$1.24 \times 10^{-3}$	$1.27 \times 10^{-3}$
39.82	$1.23 \times 10^{-3}$	$1.05 \times 10^{-3}$	$1.23 \times 10^{-3}$	$1.17 \times 10^{-3}$
63.10	$1.22 \times 10^{-3}$	$9.87 \times 10^{-4}$	$1.22 \times 10^{-3}$	$1.14 \times 10^{-3}$
100.00	$1.21 \times 10^{-3}$	$9.67 \times 10^{-4}$	$1.22 \times 10^{-3}$	$1.13 \times 10^{-3}$
158.90	$1.20 \times 10^{-3}$	$9.64 \times 10^{-4}$	$1.22 \times 10^{-3}$	$1.13 \times 10^{-3}$
251.19	$1.14 \times 10^{-3}$	$9.62 \times 10^{-4}$	$1.22 \times 10^{-3}$	$1.11 \times 10^{-3}$
398.11	$1.14 \times 10^{-3}$	$9.61 \times 10^{-4}$	$1.21 \times 10^{-3}$	$1.10 \times 10^{-3}$
630.96	$1.15 \times 10^{-3}$	$9.62 \times 10^{-4}$	$1.20 \times 10^{-3}$	$1.10 \times 10^{-3}$
999.99	$1.17 \times 10^{-3}$	$9.74 \times 10^{-4}$	$1.19 \times 10^{-3}$	$1.11 \times 10^{-3}$

Considering the average viscosity values, we can obtain an overall viscosity value of  $1.17 \times 10^{-3} \text{ Pa}\cdot\text{s}$ . Thus, the employed growing medium can be assumed to behave as a water-like medium, since its density  $\rho_m$  had been found to be  $1043.1 \text{ kg}\cdot\text{m}^{-3}$ , its viscosity  $\mu_m$   $1.17 \times 10^{-3} \text{ Pa}\cdot\text{s}$  and therefore its kinematic viscosity  $\nu_m$   $1.12 \times 10^{-6} \text{ m}^2\cdot\text{s}^{-1}$

## Appendix 3.2 Preparation of *Dunaliella Salina* suspensions

### A 3.2.1 The preparation procedure

The objective of this appendix is to describe the preparation of the DS cultures, using the Hejazi and Wijffels modified culture medium (HWMCM) (see **Appendix 3.1.1**). Since the preparation of the DS cultures involves some hazardous chemicals and potentially dangerous pieces of equipment (*e.g.* glass, electrical devices, *etc.*), both the related risk assessment and control of substances hazardous to health (COSHH) assessment should be carefully read, before starting to work.

In order to prepare the algal suspensions, the following items are needed: a suspension of living algae (for the inoculation), the growth medium, 4 borosilicate flasks, an antibacterial disinfectant, some cotton wool balls, some aluminium foil, a plastic disposable pipette, a fume hood, a pair of lab gloves, an autoclave, a test tube brush.

The used flasks must be rinsed with distilled water, using the test tube brush, and then carefully autoclaved and sterilised with the cotton wool balls at 121°C for 30 minutes, to avoid biological contaminations. Moreover, particular care must be taken during the preparation of the suspensions, *i.e.* lab gloves must be worn and all the working surfaces must be cleaned using antibacterial products.

Once the autoclaved flasks have cooled down, working in the fume hood, 50 ml of the fresh medium must be poured in each autoclaved flasks and  $2 \pm 0.25$  ml of the living algae suspensions must be inoculated, using the plastic pipette. [298] Afterwards, each conical flask must be sealed using the cotton wool balls and aluminium foil, to avoid any foreign contaminants entering the culture suspensions. The external surface of the flasks must be washed with tap water in order to remove some salts than may have deposited after the sterilising process. This must be done to ensure that the light path through the flasks is not affected.

The DS suspensions must be stored in the algal hut, in order to prevent DS cells from being affected by luminous pollution. Moreover, the suspensions must be exposed to two fluorescent lights, using a 12-hour light/dark cycles, at room temperature.

After 4-5 weeks, all the DS cultures that have not been utilised must be disposed of safely, as described in both the related risk and COSHH assessments.

### A 3.2.2 The density of the living *Dunaliella* cells

The density of the living DS cells was measured using a density bottle (10-ml density bottle with a mass of 12.7062 g, Jaytec glass) and an analytical balance (AV 64C Adventure Pro Semi-micro Analytical inCal Balance Scale, Ohaus GmbH), at room temperature (*i.e.* ~ 20°C).

In order to reduce errors, the measures have been repeated five times, obtaining the following values:

**Table A3.2.1 – The measured density values of the living cells suspensions.**

Measure	Algal suspension and density bottle mass [g]	Suspension volume [cm <sup>3</sup> ]	Algal density [g·cm <sup>-3</sup> ]
1	23.6277	10	1.0921
2	23.6274	10	1.0921
3	23.6266	10	1.0920
4	23.6272	10	1.0921
5	23.6262	10	1.0920

Therefore, the density value of the culture of living DS cells  $\rho_{LDC}$  was assumed as 1092.1 kg·m<sup>-3</sup>; as expected, the algal cells are about 5% denser than the medium in which they swim [2] ( $\rho_m = 1043.1$  kg·m<sup>-3</sup>, see **Appendix 3.1**).

## Appendix 5.1 Dead *Dunaliella* cells: the killing procedure and their density

### A 5.1.1 The killing procedure

The objective of this appendix is to describe the thermal killing procedure (TKP) which was developed for the DS cells (see **Section 5.3.1**); since the TKP involved potentially dangerous pieces of equipment (*e.g.* glass, electrical devices, *etc.*), both the related risk assessment and control of substances hazardous to health (COSHH) assessment should be carefully read, before starting to work.

The TKP requires the following items: a suspension of living algae, some 10-ml vials with their tops, distilled water, a 3-ml disposable syringe, the oven (in this PhD a Fed 53 (E2) model drying and heating oven, Binder GmHB was used [see **Figure 3.9 E**]), a stopwatch and a pair of thermal gloves.

Firstly the required temperature (*i.e.* 50°C) must be set in the oven and, while it is preheating, the vials must carefully be washed using the distilled water and afterwards  $1 \pm 0.05$  ml of algal suspension must be transferred in each vial using the syringe. [298] Once 50°C has been reached, the vials are placed inside the oven making sure that their tops are in place to avoid fluid spillages. After 8 minutes, the vials can be removed from the oven wearing the thermal gloves. Since the residence time is a critical parameter for the TKP (see **Section 5.3.1**), it was tracked using the stopwatch.

The TKP assumed that the heated volume of living cells was kept constant in each vial, therefore the number of vials that must be used depends on the final volume of DDCs suspension which is required.

When the vials have cooled down to room temperature, the dead cells can be used for experimental investigations.

## A 5.1.2 The density of the dead *Dunaliella* cells

Similarly to what had been done for the living DS cells, the density of the dead cells was assessed using a density bottle (10-ml density bottle with a mass of 12.7062 g, Jaytec glass) and an analytical scale (AV 64C Adventure Pro Semi-micro Analytical inCal Balance Scale, Ohaus GmbH), at room temperature (i.e.  $\sim 20^{\circ}\text{C}$ ).

In order to reduce errors, the measurements have been repeated five times, obtaining the follow values:

**Table A5.1.1 – The measured density values of the dead cells suspensions.**

Measurements	Algal suspension and density bottle mass [g]	Suspension volume [cm <sup>3</sup> ]	Algal density [g·cm <sup>-3</sup> ]
1	23.6180	10	1.0912
2	23.6179	10	1.0912
3	23.6175	10	1.0911
4	23.6172	10	1.0911
5	23.6182	10	1.0912

Therefore, the density value of the suspensions of dead DS cells  $\rho_{DDC}$  was taken to be 1091.2 kg·m<sup>-3</sup>. Since the measured density of the living cells was 1092.1 kg·m<sup>-3</sup>, the difference between the two densities is less than 1%, meaning that the killing procedure did not affect significantly the algal density. However, these similar density values could be due to the fact that dilute algal suspensions were employed during the experiments.

## References

1. Madigan, M.T., *et al.*, *Brock Biology of microorganisms 12th edn.* International Microbiology, 2008. **11**: p. 65-73.
2. Pedley, T. and J. Kessler, *Hydrodynamic phenomena in suspensions of swimming microorganisms.* Annual Review of Fluid Mechanics, 1992. **24**(1): p. 313-358.
3. Haw, M. and O.A. Croze, *Physics comes to life.* Physics World, 2012. **25**(2): p. 39-43.
4. Field, C.B., *et al.*, *Primary production of the biosphere: integrating terrestrial and oceanic components.* Science, 1998. **281**(5374): p. 237-240.
5. Kirchman, D.L., *Microbial ecology of the oceans.* Vol. 36. 2010: John Wiley & Sons.
6. Webpage. *National Science Foundation.* [cited 2017 January]; Available from: <http://www.nsf.gov/od/lpa/news/03/pr0384.htm>.
7. Webpage. *BBC News.* [cited 2017 January]; Available from: <http://news.bbc.co.uk/1/hi/sci/tech/827063.stm>.
8. O'Malley, S., *Bi-flagellate swimming dynamics.* PhD Thesis, University of Glasgow, Glasgow (UK), 2011.
9. Webpage. *Applications of Microorganisms in various fields.* [cited 2017 January]; Available from: <http://tinyurl.com/jasyrw2>.
10. Bees, M.A. and O.A. Croze, *Mathematics for streamlined biofuel production from unicellular algae.* Biofuels, 2014. **5**(1): p. 53-65.
11. Webpage. *Symbiotic Relationships.* [cited 2017 January]; Available from: <http://tinyurl.com/j34zor6>.
12. Woese, C.R. and G.E. Fox, *Phylogenetic structure of the prokaryotic domain: the primary kingdoms.* Proceedings of the National Academy of Sciences, 1977. **74**(11): p. 5088-5090.
13. VanDemark, P.J. and B.L. Batzing, *The microbes: An introduction to their nature and importance.* Benjamin/Cummings Publishing, Menlo Park, CA(USA). 1987.
14. Woese, C.R., O. Kandler, and M.L. Wheelis, *Towards a natural system of organisms: proposal for the domains Archaea, Bacteria, and Eucarya.* Proceedings of the National Academy of Sciences, 1990. **87**(12): p. 4576-4579.
15. Webpage. *Prokaryotic Organisms.* [cited 2017 January]; Available from: <http://tinyurl.com/jntabxr>.
16. Webpage. *Classification of Microorganisms.* [cited 2017 January]; Available from: <http://tinyurl.com/zozg93v>.
17. Altermann, W. and J. Kazmierczak, *Archean microfossils: a reappraisal of early life on Earth.* Research in Microbiology, 2003. **154**(9): p. 611-617.
18. Webpage. *Eukaryotic Cells.* [cited 2017 January]; Available from: <http://tinyurl.com/zwrl4e3>.
19. Gibson, R., R. Atkinson, and J. Gordon, *Inherent optical properties of non-spherical marine-like particles—from theory to observation.* Oceanography and Marine Biology: An Annual Review, 2007. **45**: p. 1-38.
20. Guasto, J.S., R. Rusconi, and R. Stocker, *Fluid mechanics of planktonic microorganisms.* Annual Review of Fluid Mechanics, 2012. **44**: p. 373-400.
21. Dusenbery, D.B., *Living at micro scale: the unexpected physics of being small.* 2009: Harvard University Press.
22. Young, K.D., *The selective value of bacterial shape.* Microbiology and Molecular Biology Reviews, 2006. **70**(3): p. 660-703.
23. Kiørboe, T., *A mechanistic approach to plankton ecology.* 2008: Princeton University Press.

24. Hetzer, A., I.R. McDonald, and H.W. Morgan, *Venenivibrio stagnispumantis* gen. nov., sp. nov., a thermophilic hydrogen-oxidizing bacterium isolated from Champagne Pool, Waiotapu, New Zealand. *International Journal of Systematic and Evolutionary Microbiology*, 2008. **58**(2): p. 398-403.
25. Lalithambika, S., et al., *Carbohydrate hydrolysis and transport in the extreme thermoacidophile Sulfolobus solfataricus*. *Applied and Environmental Microbiology*, 2012. **78**(22): p. 7931-7938.
26. Hogg, S., *Essential microbiology*. 2013: John Wiley & Sons.
27. Thurman, H.V. and E.A. Burton, *Introductory oceanography*. 1997: Prentice Hall New Jersey.
28. Bryant, D.A. and N.-U. Frigaard, *Prokaryotic photosynthesis and phototrophy illuminated*. *Trends in Microbiology*, 2006. **14**(11): p. 488-496.
29. Maity, J.P., et al., *Microalgae for third generation biofuel production, mitigation of greenhouse gas emissions and wastewater treatment: Present and future perspectives—A mini review*. *Energy*, 2014. **78**: p. 104-113.
30. Lauga, E. and T.R. Powers, *The hydrodynamics of swimming microorganisms*. *Reports on Progress in Physics*, 2009. **72**(9): p. 1-36.
31. Brumley, D.R., et al., *Metachronal waves in the flagellar beating of Volvox and their hydrodynamic origin*. *Journal of The Royal Society Interface*, 2015. **12**(108): p. 1-12.
32. Silflow, C.D. and P.A. Lefebvre, *Assembly and motility of eukaryotic cilia and flagella. Lessons from Chlamydomonas reinhardtii*. *Plant Physiology*, 2001. **127**(4): p. 1500-1507.
33. Pedersen, R.A., *Current topics in developmental biology*. Vol. 27. 1992: Academic Press.
34. Namba, K. and F. Vonderviszt, *Molecular architecture of bacterial flagellum*. *Quarterly Reviews of Biophysics*, 1997. **30**(01): p. 1-65.
35. Webpage. *Prokaryotic vs Eukaryotic Flagella*. [cited 2017 January]; Available from: <http://tinyurl.com/zjx39oe>.
36. Chengala, A., M. Hondzo *Microalgal Swimming in Fluid Environments: Experimental and Numerical Investigations*. PhD Thesis, Minnesota University, Minneapolis (USA), 2013.
37. Omoto, C.K., et al., *Rotation of the central pair microtubules in eukaryotic flagella*. *Molecular Biology of the Cell*, 1999. **10**(1): p. 1-4.
38. Webpage. *Flagella and Cilia*. [cited 2017 April]; Available from: <http://tinyurl.com/y9fvsayy>.
39. Webpage. *How Algae Move*. [cited 2017 January]; Available from: [http://www.eplantscience.com/index/algae/anatomy/how\\_algae\\_move.php](http://www.eplantscience.com/index/algae/anatomy/how_algae_move.php).
40. Villareal, T. and E. Carpenter, *Buoyancy regulation and the potential for vertical migration in the oceanic cyanobacterium Trichodesmium*. *Microbial Ecology*, 2003. **45**(1): p. 1-10.
41. Boyd, C. and D. Gradmann, *Impact of osmolytes on buoyancy of marine phytoplankton*. *Marine Biology*, 2002. **141**(4): p. 605-618.
42. O'Malley, S. and M.A. Bees, *The orientation of swimming biflagellates in shear flows*. *Bulletin of Mathematical Biology*, 2012. **74**(1): p. 232-255.
43. Garcia, X., S. Rafai, and P. Peyla, *Light control of the flow of phototactic microswimmer suspensions*. *Physical Review Letters*, 2013. **110**(13): p. 1-4.
44. Böhmer, M., et al., *Ca<sup>2+</sup> spikes in the flagellum control chemotactic behavior of sperm*. *The EMBO Journal*, 2005. **24**(15): p. 2741-2752.
45. Scott, T.M., et al., *Microbial source tracking: current methodology and future directions*. *Applied and Environmental Microbiology*, 2002. **68**(12): p. 5796-5803.

46. Azam, F., *et al.*, *The ecological role of water-column microbes in the sea*. Estuaries, 1983. **50**(2).
47. Bees, M. and N. Hill, *Wavelengths of bioconvection patterns*. Journal of Experimental Biology, 1997. **200**(10): p. 1515-1526.
48. Frankel, R.B., *et al.*, *Magneto-aerotaxis in marine coccoid bacteria*. Biophysical Journal, 1997. **73**(2): p. 994-1000.
49. Paster, E. and W.S. Ryu, *The thermal impulse response of Escherichia coli*. Proceedings of the National Academy of Sciences, 2008. **105**(14): p. 5373-5377.
50. Kessler, J., *Hydrodynamic focusing of motile algal cells*. Nature, 1985. **313**(5999): p. 218-220.
51. Williams, C. and M. Bees, *Photo-gyrotactic bioconvection*. Journal of Fluid Mechanics, 2011. **678**: p. 41-86.
52. Hope, A., M. Haw, *Particles in Oscillatory Flows: Jamming of Concentrated Particulate Suspensions and the Response of Swimming Algae*. PhD Thesis, University of Strathclyde, Glasgow (UK), 2014.
53. Stocker, R., *Microorganisms in vortices: a microfluidic setup*. Limnology and Oceanography: Methods, 2006. **4**(10): p. 392-398.
54. Oren, A., *Diversity of halophilic microorganisms: environments, phylogeny, physiology, and applications*. Journal of Industrial Microbiology and Biotechnology, 2002. **28**(1): p. 56-63.
55. Hill, N. and T. Pedley, *Bioconvection*. Fluid Dynamics Research, 2005. **37**(1): p. 1-20.
56. Croze, O.A., *et al.*, *Dispersion of swimming algae in laminar and turbulent channel flows: consequences for photobioreactors*. Journal of The Royal Society Interface, 2013. **10**(81): p. 1-14.
57. Purcell, E.M., *Life at low Reynolds number*. American Journal of Physics, 1977. **45**(1): p. 3-11.
58. Happel, J. and H. Brenner, *Low Reynolds number hydrodynamics: with special applications to particulate media*. Vol. 1. 2012: Springer Science & Business Media.
59. Nichols, R.L., *Viscosity of lava*. The Journal of Geology, 1939. **47**(3): p. 290-302.
60. Vogel, S., *Comparative biomechanics: life's physical world*. 2013: Princeton University Press.
61. Kundu, P. and L. Cohen, *Fluid mechanics*. Academic, Calif, 1990.
62. Stocker, R. *Lecture 13 - The perils of reversibility*. 1.961 Lecture Videos 2008 [cited 2017 March]; Available from: <http://tinyurl.com/ktlrjya>.
63. Pande, J. and N.-D. Indien, *Analytical and numerical study of microswimming using the 'bead-spring model'*. PhD Thesis, University of Erlangen-Nürnberg, (Erlangen, Germany), 2016.
64. Berg, H.C., *E. coli in Motion*. 2008: Springer Science & Business Media.
65. Brennen, C. and H. Winet, *Fluid mechanics of propulsion by cilia and flagella*. Annual Review of Fluid Mechanics, 1977. **9**(1): p. 339-398.
66. Pak, O.S. and E. Lauga, *Extensibility enables locomotion under isotropic drag*. Physics of Fluids, 2011. **23**(8): p. 1-4.
67. Berg, H.C. and D.A. Brown, *Chemotaxis in Escherichia coli analysed by three-dimensional tracking*. Nature, 1972. **239**(5374): p. 500-504.
68. Weibel, D.B., *et al.*, *Microoxen: Microorganisms to move microscale loads*. Proceedings of the National Academy of Sciences of the United States of America, 2005. **102**(34): p. 11963-11967.
69. Leal, L.G., *Advanced transport phenomena: fluid mechanics and convective transport processes*. 2007: Cambridge University Press.

70. Visser, A., *Hydromechanical signals in the plankton*. Marine Ecology-Progress Series, 2001. **222**: p. 1-24.
71. Berke, A.P., et al., *Hydrodynamic attraction of swimming microorganisms by surfaces*. Physical Review Letters, 2008. **101**(3): p. 1-4.
72. Clift, R., J.R. Grace, and M.E. Weber, *Bubbles, drops, and particles*. 2005: Courier Corporation.
73. Berlyand, L.V. *Self-Organization in Biological Systems*. 2013 [cited 2017 April]; Available from: <http://tinyurl.com/y8los7at>.
74. Tuson, H.H. and D.B. Weibel, *Bacteria–surface interactions*. Soft Matter, 2013. **9**(17): p. 4368-4380.
75. Duprat, C. and H.A. Shore, *Fluid-Structure Interactions in Low-Reynolds-Number Flows*. 2015: Royal Society of Chemistry.
76. Kantsler, V., et al., *Ciliary contact interactions dominate surface scattering of swimming eukaryotes*. Proceedings of the National Academy of Sciences, 2013. **110**(4): p. 1187-1192.
77. Pedley, T. and J. Kessler, *The orientation of spheroidal microorganisms swimming in a flow field*. Proceedings of the Royal Society of London B: Biological Sciences, 1987. **231**(1262): p. 47-70.
78. Kessler, J., *The external dynamics of swimming micro-organisms*. Progress In Phycological Research, 1986. **4**: p. 257-307.
79. Durham, W.M., J.O. Kessler, and R. Stocker, *Disruption of vertical motility by shear triggers formation of thin phytoplankton layers*. Science, 2009. **323**(5917): p. 1067-1070.
80. Heuschele, J. and E. Selander, *The chemical ecology of copepods*. Journal of Plankton Research, 2014. **36**(4): p. 895-913.
81. Berg, H.C., *Random walks in biology*. 1993: Princeton University Press.
82. Stocker, R. *Lecture 3 - Diffusion Around a Sphere*. 1.961 Lecture Videos 2008 [cited 2017 March]; Available from: <http://tinyurl.com/kyd65rn>.
83. Schmidt-Nielsen, K., *Scaling: why is animal size so important?* 1984: Cambridge University Press.
84. Vogel, S., *Life's devices: the physical world of animals and plants*. 1988: Princeton University Press.
85. Karp-Boss, L., E. Boss, and P. Jumars, *Nutrient fluxes to planktonic osmotrophs in the presence of fluid motion*. Oceanography and Marine Biology, 1996. **34**: p. 71-108.
86. Acrivos, A. and T.D. Taylor, *Heat and mass transfer from single spheres in Stokes flow*. The Physics of Fluids, 1962. **5**(4): p. 387-394.
87. Brenner, H., *Forced convection heat and mass transfer at small Peclet numbers from a particle of arbitrary shape*. Chemical Engineering Science, 1963. **18**(2): p. 109-122.
88. Graham, L.E. and L.W. Wilcox, *Algae*. 2000: Prentice Hall.
89. Azam, S.M.G.G., et al., *A study on epyphytic algae growing on charophytes*. Journal of Environment, Science and Technology, 2016. **2**(1): p. 1-12.
90. Garbary, D., et al., *Epizoic algae from freshwater turtles in Nova Scotia*. Journal of Freshwater Ecology, 2007. **22**(4): p. 677-685.
91. Castenholz, R.W., *Thermophilic blue-green algae and the thermal environment*. Bacteriological Reviews, 1969. **33**(4): p. 476-504.
92. Duval, B., K. Shetty, and W.H. Thomas, *Phenolic compounds and antioxidant properties in the snow alga Chlamydomonas nivalis after exposure to UV light*. Journal of Applied Phycology, 1999. **11**(6): p. 559-566.

93. Fazeli, M., *et al.*, *Effects of salinity on  $\beta$ -carotene production by Dunaliella tertiolecta DCCBC26 isolated from the Urmia salt lake, north of Iran*. *Bioresource Technology*, 2006. **97**(18): p. 2453-2456.
94. Thakur, A. and S. Bassi, *A Textbook of Botany: Diversity of Microbes and Cryptogams*. S. Chand & Company Ltd, New Delhi, 2008.
95. Carlsson, A.S., *Micro-and macro-algae: utility for industrial applications: outputs from the EPOBIO project*. 2007: CPL Press.
96. Bold, H.C. and M. Wynne, *Introduction to the algae: structure and reproduction*. 1978: Prentice Hall.
97. Manuel, M.E., *The cultivation of Chlorella sp.* *Plant Physiology*, 1944. **19**(2): p. 359-369.
98. Harris, E.H., *The Chlamydomonas sourcebook: a comprehensive guide to biology and laboratory use*. 2013: Elsevier.
99. Krammer, K., *Diatoms of Europe: Diatoms of the European Inland Waters and Comparable Habitats. Vol. 5. sensu lato*. ARG Gantner-Verlag KG: Ruggell, Liechtenstein, 2009.
100. Wang, D.-Z., *Neurotoxins from marine dinoflagellates: a brief review*. *Marine Drugs*, 2008. **6**(2): p. 349-371.
101. Raja, R., S. Hemaiswarya, and R. Rengasamy, *Exploitation of Dunaliella for  $\beta$ -carotene production*. *Applied Microbiology and Biotechnology*, 2007. **74**(3): p. 517-523.
102. Fassett, R.G. and J.S. Coombes, *Astaxanthin, oxidative stress, inflammation and cardiovascular disease*. *Future Cardiology*, 2009. **5**(4): p. 333-342.
103. Tasić, M.B., *et al.*, *Botryococcus braunii for biodiesel production*. *Renewable and Sustainable Energy Reviews*, 2016. **64**: p. 260-270.
104. Pulz, O. and W. Gross, *Valuable products from biotechnology of microalgae*. *Applied Microbiology and Biotechnology*, 2004. **65**(6): p. 635-648.
105. Oren, A., *A hundred years of Dunaliella research: 1905–2005*. *Saline Systems*, 2005. **1**(1): p. 1-14.
106. Borowitzka, M.A. and C.J. Siva, *The taxonomy of the genus Dunaliella (Chlorophyta, Dunaliellales) with emphasis on the marine and halophilic species*. *Journal of Applied Phycology*, 2007. **19**(5): p. 567-590.
107. Tran, D., *et al.*, *Identification of Dunaliella viridis using its markers*. *International Journal of Applied*, 2013. **3**(4): p. 118-126.
108. Ginzburg, M., *Dunaliella: a green alga adapted to salt*. *Advances in Botanical Research*, 1988. **14**: p. 93-183.
109. Bees, M. *Crystal Lakes (pty)*. [cited 2017 April]; Available from: <https://tinyurl.com/y2mf4wnn>.
110. Ramos, A.A., *et al.*, *The unicellular green alga Dunaliella salina Teod. as a model for abiotic stress tolerance: genetic advances and future perspectives*. *Algae*, 2011. **26**(1): p. 3-20.
111. Shariati, M. and M.R. Hadi, *Microalgal biotechnology and bioenergy in Dunaliella*. 2011: INTECH Open Access Publisher.
112. Hosseini Tafreshi, A. and M. Shariati, *Dunaliella biotechnology: methods and applications*. *Journal of Applied Microbiology*, 2009. **107**(1): p. 14-35.
113. Borowitzka, M.A. *The mass culture of Dunaliella salina*. in *Regional Workshop on the Culture and Utilization of Seaweeds, Cebu City (Philippines), 27-31 Aug 1990*.
114. Shaish, A., A. Ben-Amotz, and M. Avron, [41] *Biosynthesis of  $\beta$ -carotene in Dunaliella*. *Methods in enzymology*, 1992. **213**: p. 439-444.

115. Brown, A. and L.J. Borowitzka, *Halotolerance of Dunaliella*. Biochemistry and Physiology of Protozoa, 1979. **1**: p. 139-190.
116. Ben-Amotz, A., J.r.E. Polle, and D. Subba Rao, *The alga Dunaliella*. 2009: Science Publishers.
117. Ruffer, U. and W. Nultsch, *High-speed cinematographic analysis of the movement of Chlamydomonas*. Cytoskeleton, 1985. **5**(3): p. 251-263.
118. Posten, C., *Design principles of photo-bioreactors for cultivation of microalgae*. Engineering in Life Sciences, 2009. **9**(3): p. 165-177.
119. Aasen, A., K. Eimhjellen, and S. Liaaen-Jensen, *An extreme source of beta-carotene*. Acta Chemica Scandinavica, 1969. **23**(7): p. 2544-5.
120. Leach, G., G. Oliveira, and R. Morais, *Production of a carotenoid-rich product by alginate entrapment and fluid-bed drying of Dunaliella salina*. Journal of the Science of Food and Agriculture, 1998. **76**: p. 298-302.
121. Mokady, S., *Nutritional, toxicological and therapeutic aspects*. Dunaliella: Physiology, Biochemistry, and Biotechnology, 1992: p. 217-229.
122. Chen, B.J. and C. Chi, *Process development and evaluation for algal glycerol production*. Biotechnology and Bioengineering, 1981. **23**(6): p. 1267-1287.
123. Talbot, P. and J. De la Noüe, *Tertiary treatment of wastewater with Phormidium bohneri (Schmidle) under various light and temperature conditions*. Water Research, 1993. **27**(1): p. 153-159.
124. Foster, S., D. Thomson, and W. Maher, *Uptake and metabolism of arsenate by anoxic cultures of the microalgae Dunaliella tertiolecta and Phaeodactylum tricorutum*. Marine Chemistry, 2008. **108**(3): p. 172-183.
125. Dönmez, G. and Z. Aksu, *Removal of chromium (VI) from saline wastewaters by Dunaliella species*. Process Biochemistry, 2002. **38**(5): p. 751-762.
126. Santin-Montanya, I., et al., *Optimal growth of Dunaliella primolecta in axenic conditions to assay herbicides*. Chemosphere, 2007. **66**(7): p. 1315-1322.
127. Chen, J., J. Jiang, and Q. Lin, *Technical Note: Toxicity Tests of Typical Mutagenic Phenols on Dunaliella salina*. Transactions of the ASABE, 2007. **50**(2): p. 685-688.
128. Davis, J.L., *Chlamydomonas Reinhardtii Exposure to Phenol and Genetic Response*. University of Tennessee Honors Thesis Projects, 2005: p. 1-14.
129. Rosenberg, J.N., G.A. Oyler, and M.J. Betenbaugh, *Paving the Road to Algal Biofuels with the Development of a Genetic Infrastructure*. Biofuel's Engineering Process Technology, 2011: p. 267-292.
130. Hirsch, R.L., R.M. Bezdek, and R.M. Wendling, *Peaking of world oil production: impacts, mitigation, & risk management*. 2005, National Energy Technology Laboratory (NETL), Pittsburgh, PA, Morgantown, WV, and Albany, OR. p. 1-3.
131. Sheehan, J., et al., *Look back at the US department of energy's aquatic species program: biodiesel from algae; close-out report*. 1998, National Renewable Energy Lab., Golden, CO.(US). p. 1-4.
132. Miao, X., Q. Wu, and C. Yang, *Fast pyrolysis of microalgae to produce renewable fuels*. Journal of Analytical and Applied Pyrolysis, 2004. **71**(2): p. 855-863.
133. Gouveia, L. and A.C. Oliveira, *Microalgae as a raw material for biofuels production*. Journal of Industrial Microbiology & Biotechnology, 2009. **36**(2): p. 269-274.
134. Fukuda, H., A. Kondo, and H. Noda, *Biodiesel fuel production by transesterification of oils*. Journal of Bioscience and Bioengineering, 2001. **92**(5): p. 405-416.
135. Meher, L., D.V. Sagar, and S. Naik, *Technical aspects of biodiesel production by transesterification—a review*. Renewable and Sustainable Energy Reviews, 2006. **10**(3): p. 248-268.

136. Webpage. *Chemical Conversion*. [cited 2017 April]; Available from: <http://tinyurl.com/ya4e37vq>.
137. Pires, J., et al., *Carbon dioxide capture from flue gases using microalgae: engineering aspects and biorefinery concept*. *Renewable and Sustainable Energy Reviews*, 2012. **16**(5): p. 3043-3053.
138. Stein, J.R., *Handbook of phycological methods: culture methods and growth measurements*. Vol. 1. 1979: CUP Archive.
139. Torzillo, G. and G.C. Zittelli, *Tubular Photobioreactors*, in *Algal Biorefineries 2015*, Springer. p. 187-212.
140. Zhu, Y.-H. and J.-G. Jiang, *Continuous cultivation of Dunaliella salina in photobioreactor for the production of  $\beta$ -carotene*. *European Food Research and Technology*, 2008. **227**(3): p. 953-959.
141. Moazami, N., et al., *Large-scale biodiesel production using microalgae biomass of Nannochloropsis*. *Biomass and Bioenergy*, 2012. **39**: p. 449-453.
142. Carvalho, A.P., L.A. Meireles, and F.X. Malcata, *Microalgal reactors: a review of enclosed system designs and performances*. *Biotechnology Progress*, 2006. **22**(6): p. 1490-1506.
143. Sforza, E., M. Enzo, and A. Bertucco, *Design of microalgal biomass production in a continuous photobioreactor: an integrated experimental and modeling approach*. *Chemical Engineering Research and Design*, 2014. **92**(6): p. 1153-1162.
144. Richmond, A. and Z. Cheng-Wu, *Optimization of a flat plate glass reactor for mass production of Nannochloropsis sp. outdoors*. *Journal of Biotechnology*, 2001. **85**(3): p. 259-269.
145. Boussiba, S., et al., *Lipid and biomass production by the halotolerant microalga Nannochloropsis salina*. *Biomass*, 1987. **12**(1): p. 37-47.
146. Iqbal, M., et al., *A flat-sided photobioreactor for culturing microalgae*. *Aquacultural Engineering*, 1993. **12**(3): p. 183-190.
147. Sun, Y., et al., *Enhancement of microalgae production by embedding hollow light guides to a flat-plate photobioreactor*. *Bioresource Technology*, 2016. **207**: p. 31-38.
148. Ugwu, C.U. and H. Aoyagi, *Microalgal culture systems: an insight into their designs, operation and applications*. *Biotechnology*, 2012. **11**(3): p. 127-132.
149. Babu, A.G., et al., *Cultivation of an indigenous Chlorella sorokiniana with phytohormones for biomass and lipid production under N-limitation*. *Algal Research*, 2017. **23**: p. 178-185.
150. Ogonna, J.C., T. Soejima, and H. Tanaka, *An integrated solar and artificial light system for internal illumination of photobioreactors*. *Journal of Biotechnology*, 1999. **70**(1): p. 289-297.
151. Ding, Y.-D., et al., *Effect of CO<sub>2</sub> bubbles behaviors on microalgal cells distribution and growth in bubble column photobioreactor*. *International Journal of Hydrogen Energy*, 2016. **41**(8): p. 4879-4887.
152. Fernández, F.A., et al., *Airlift-driven external-loop tubular photobioreactors for outdoor production of microalgae: assessment of design and performance*. *Chemical Engineering Science*, 2001. **56**(8): p. 2721-2732.
153. Surendhiran, D. and M. Vijay, *Microalgal biodiesel-a comprehensive review on the potential and alternative biofuel*. *Research Journal of Chemical Sciences*, 2012. **2231**: p. 71-82.
154. Molina, E., et al., *Tubular photobioreactor design for algal cultures*. *Journal of Biotechnology*, 2001. **92**(2): p. 113-131.

155. Morweiser, M., *et al.*, *Developments and perspectives of photobioreactors for biofuel production*. Applied Microbiology and Biotechnology, 2010. **87**(4): p. 1291-1301.
156. Grima, E.M., *et al.*, *Photobioreactors: light regime, mass transfer, and scaleup*. Journal of Biotechnology, 1999. **70**(1): p. 231-247.
157. Torzillo, G., *et al.*, *Production of Spirulina biomass in closed photobioreactors*. Biomass, 1986. **11**(1): p. 61-74.
158. Weyer, K.M., *et al.*, *Theoretical maximum algal oil production*. Bioenergy Research, 2010. **3**(2): p. 204-213.
159. Webpage. *BIOL 1406*. [cited 2017 April]; Available from: <http://tinyurl.com/y7lt6j76>.
160. Long, S., S. Humphries, and P.G. Falkowski, *Photoinhibition of photosynthesis in nature*. Annual Review of Plant Biology, 1994. **45**(1): p. 633-662.
161. Tredici, M.R. and G.C. Zittelli, *Efficiency of sunlight utilization: tubular versus flat photobioreactors*. Biotechnology and Bioengineering, 1998. **57**(2): p. 187-197.
162. Pruvost, J., J.-F. Cornet, and J. Legrand, *Hydrodynamics influence on light conversion in photobioreactors: an energetically consistent analysis*. Chemical Engineering Science, 2008. **63**(14): p. 3679-3694.
163. Richmond, A., *CRC Handbook of microalgal mass culture*. 1986: CRC press.
164. Granum, E. and S.M. Mykkestad, *A photobioreactor with pH control: demonstration by growth of the marine diatom Skeletonema costatum*. Journal of Plankton Research, 2002. **24**(6): p. 557-563.
165. Raven, J. and M. MICHELIS, *Acid-base regulation during nitrate assimilation in Hydrodictyon africanum*. Plant, Cell & Environment, 1979. **2**(3): p. 245-257.
166. *Lisbon Microalgae Biotechnology 2nd Advanced Course (LIMBAC)*. in Lisbon. 2016.
167. Bees, M.A. and O.A. Croze, *Dispersion of biased swimming micro-organisms in a fluid flowing through a tube*. Proceedings of the Royal Society 2010. **466**(2119): p. 2057-2077.
168. Bearon, R., M. Bees, and O. Croze, *Biased swimming cells do not disperse in pipes as tracers: a population model based on microscale behaviour*. Physics of Fluids, 2012. **24**(12): p. 1-20.
169. Taylor, G.I., *Dispersion of soluble matter in solvent flowing slowly through a tube*. Proc. R. Soc. Lond. A, 1953. **219**(1137): p. 186-203.
170. Aris, R., *On the dispersion of a solute in a fluid flowing through a tube*. Proc. R. Soc. Lond. A, 1956. **235**(1200): p. 67-77.
171. Taylor, G., *The dispersion of matter in turbulent flow through a pipe*. Proceedings of the Royal Society, 1954. **223**(1155): p. 446-468.
172. Fischer, H.B., *Longitudinal dispersion and turbulent mixing in open-channel flow*. Annual Review of Fluid Mechanics, 1973. **5**(1): p. 59-78.
173. Probstein, R.F., *Physicochemical hydrodynamics: an introduction*. 2005: John Wiley & Sons.
174. Croze, O.A., R.N. Bearon, and M.A. Bees, *Gyrotactic swimmer dispersion in pipe flow: testing the theory*. Journal of Fluid Mechanics, 2017. **816**: p. 481-506.
175. Ben-Amotz, A. and M. Avron, *The biotechnology of mass culturing Dunaliella for products of commercial interest*. Algal and Cyanobacterial Biotechnology, 1989: p. 91-114.
176. Grima, E.M., *et al.*, *Recovery of microalgal biomass and metabolites: process options and economics*. Biotechnology Advances, 2003. **20**(7): p. 491-515.

177. Berberoğlu, H. and L. Pilon, *Maximizing the solar to H<sub>2</sub> energy conversion efficiency of outdoor photobioreactors using mixed cultures*. International Journal of Hydrogen Energy, 2010. **35**(2): p. 500-510.
178. Proctor, V.W., *Studies of algal antibiosis using Haematococcus and Chlamydomonas*. Limnology and Oceanography, 1957. **2**(2): p. 125-139.
179. Baas-Becking, L., *Salt effects on swarms of Dunaliella viridis Teod*. The Journal of General Physiology, 1931. **14**(6): p. 765-779.
180. Lerche, W., *Untersuchungen über Entwicklung und Fortpflanzung in der Gattung Dunaliella; Mit 5 Abb. im Text u. 3 Taf.* 1937, Lippert.
181. Borowitzka, M., *Algal growth media and sources of algal cultures*. 1988, Cambridge University Press.
182. Gibor, A., *The culture of brine algae*. The Biological Bulletin, 1956. **111**(2): p. 223-229.
183. Van Auken, O.W. and I.B. McNULTY, *The effect of environmental factors on the growth of a halophylic species of algae*. The Biological Bulletin, 1973. **145**(1): p. 210-222.
184. Sathasivam, R. and N. Juntawong, *Modified medium for enhanced growth of Dunaliella strains*. Int J Curr Sci, 2013. **5**: p. 67-73.
185. Hejazi, M. and R. Wijffels, *Effect of light intensity on  $\beta$ -carotene production and extraction by Dunaliella salina in two-phase bioreactors*. Biomolecular Engineering, 2003. **20**(4): p. 171-175.
186. McLachlan, J., *The culture of Dunaliella tertiolecta Butcher—a euryhaline organism*. Canadian Journal of Microbiology, 1960. **6**(3): p. 367-379.
187. Webpage. *Grading Systems of Salt*. [cited 2019 July (while doing the corrections)]; Available from: <https://tinyurl.com/y564tmmy>.
188. Milko, E., *Study of the requirements of two Dunaliella species in mineral and organic components of the medium*. Moscow University, Vestnik. Biologia, 1962. **6**: p. 21-23.
189. Siegel, B., et al., *Brine organisms and the question of habitat-specific adaptation*. Origins of Life, 1984. **14**(1-4): p. 757-770.
190. CCPA. *Culture Collection of Algae and Protozoa*. [cited 2017 May]; Available from: <https://www.ccap.ac.uk/>.
191. CCPA. *f/2 Medium Recipe*. [cited 2019 July (while doing the corrections)]; Available from: <https://tinyurl.com/y57vvszy>.
192. GRAS [Online Webpage]. [cited 2016 October]; Available from: <http://tinyurl.com/nqmu5r7>.
193. Saleh-Lakha, S. and J.T. Trevors, *Perspective: microfluidic applications in microbiology*. Journal of Microbiological Methods, 2010. **82**(1): p. 108-111.
194. Ahmed, T., T.S. Shimizu, and R. Stocker, *Microfluidics for bacterial chemotaxis*. Integrative Biology, 2010. **2**(11-12): p. 604-629.
195. McDonald, J.C. and G.M. Whitesides, *Poly (dimethylsiloxane) as a material for fabricating microfluidic devices*. Accounts of Chemical Research, 2002. **35**(7): p. 491-499.
196. De Sousa, P.C.S., M.A. Moreira Alves, and M.S.N.d.F. Oliveira, *Entry flow of viscoelastic fluids at macro-and micro-scale, PhD Thesis, Universidade do Porto (Porto, Portugal)*. 2010.
197. Permselect. *Silicone (PDMS) Chemical Compatibility*. [cited 2017 June]; Available from: <http://tinyurl.com/y9pw5cgs>.
198. Flickinger, M. and S. Drew, *Fermentation, biocatalysis and bioseparation: shear sensitivity*. Encyclopedia of Bioprocess Technology, 1999. **1**: p. 2369-2396.

199. JPhoto. *JD Photo Tools Website*. [cited 2017 June]; Available from: <http://www.id-photodata.co.uk/>.
200. Petty, H.R., *Fluorescence microscopy: established and emerging methods, experimental strategies, and applications in immunology*. Microscopy Research and Technique, 2007. **70**(8): p. 687-709.
201. Antony, P.P.M.A., et al., *Light microscopy applications in systems biology: opportunities and challenges*. Cell Communication and Signaling, 2013. **11**(1): p. 1-19.
202. Musharraf, S.G., et al., *Biodiesel production from microalgal isolates of southern Pakistan and quantification of FAMES by GC-MS/MS analysis*. Chemistry Central Journal, 2012. **6**(1): p. 1-10.
203. Webpage. *Olympus IX71/IX81 Microscopes brochure*. [cited 2017 June]; Available from: <http://www.olympusmicro.com/brochures/pdfs/ix71.pdf>.
204. Zeiss. *Education in Microscopy and Digital Imaging*. [cited 2017 May]; Available from: <http://zeiss-campus.magnet.fsu.edu/articles/basics/index.html>.
205. Nikon. *MicroscopyU: The source for microscopy education*. [cited 2017 May]; Available from: <https://www.microscopyu.com/>.
206. Olympus. *Microscopy Resource Center*. [cited 2017 June]; Available from: <http://www.olympusmicro.com/index.html>.
207. Oliveira, M.S.N., et al., *Viscous flow through microfabricated hyperbolic contractions*. Experiments in Fluids, 2007. **43**(2-3): p. 437-451.
208. Webpage. *Cokin A003 Red Filter*. [cited 2017 June]; Available from: <http://tinyurl.com/yd4xwtju>.
209. Apparatus, H. *Syringe Selection Guide*. [cited 2017 May]; Available from: <http://tinyurl.com/y7koedtk>.
210. Hope, A., et al., *Resonant alignment of microswimmer trajectories in oscillatory shear flows*. Physical Review Fluids, 2016. **1**(5): p. 1-6.
211. ParkCameras. *Cokin A003 Red*. [cited 2017 May]; Available from: <http://tinyurl.com/ycqsljrq>.
212. Olympus. *XM10 Monochrome camera*. [cited 2017 May]; Available from: <http://tinyurl.com/ybmnmslx>.
213. Miura, K., *Basics of image processing and analysis*. Centre for Molecular & Cellular Imaging EMBL Heidelberg, 2006.
214. Webpage. *Exposure Times*. [cited 2017 August]; Available from: <http://tinyurl.com/ycjzt6ah>.
215. ImageJ. *ImageJ Download*. [cited 2017 June]; Available from: <https://imagej.nih.gov/ij/download.html>.
216. Hartig, S.M., *Basic image analysis and manipulation in ImageJ*. Current Protocols in Molecular Biology, 2013: p. 1-12.
217. Webpage. *ImageJ: Image Processing and Analysis in Java*. [cited 2017 November]; Available from: <https://imagej.nih.gov/ij/index.html>.
218. Webpage. *ImageJ: an open platform for scientific image analysis*. [cited 2017 November]; Available from: <https://imagej.net/Welcome>.
219. Webpage. *Olympus CellSens User Manual*. [cited 2017 November]; Available from: <https://tinyurl.com/yahwudbm>.
220. Pedersen, J.S. *C. elegans motility analysis in ImageJ - A practical approach*. [cited 2017 June]; Available from: <http://www.phage.dk/plugins/wrmtrck.html>.
221. Sternberg, S.R., *Biomedical image processing*. Computer, 1983. **16**(1): p. 22-34.

222. Degen, J., *et al.*, *A novel airlift photobioreactor with baffles for improved light utilization through the flashing light effect*. *Journal of Biotechnology*, 2001. **92**(2): p. 89-94.
223. Flickinger, M. and S. Drew, *Fermentation, biocatalysis and bioseparation: microalgae mass culture methods*. *Encyclopedia of Bioprocess Technology*, 1999. **1**: p. 1754-1770.
224. Huang, J., *et al.*, *Novel flat-plate photobioreactors for microalgae cultivation with special mixers to promote mixing along the light gradient*. *Bioresource Technology*, 2014. **159**: p. 8-16.
225. Cheng, W., J. Huang, and J. Chen, *Computational fluid dynamics simulation of mixing characteristics and light regime in tubular photobioreactors with novel static mixers*. *Journal of Chemical Technology and Biotechnology*, 2016. **91**(2): p. 327-335.
226. Thakur, R., *et al.*, *Static mixers in the process industries—a review*. *Chemical Engineering Research and Design*, 2003. **81**(7): p. 787-826.
227. Flickinger, M. and S. Drew, *Fermentation, biocatalysis and bioseparation: stating mixing in fermentation process*. *Encyclopedia of Bioprocess Technology*, 1999. **1**: p. 2476-2491.
228. Ugwu, C., J. Ogbonna, and H. Tanaka, *Improvement of mass transfer characteristics and productivities of inclined tubular photobioreactors by installation of internal static mixers*. *Applied Microbiology and Biotechnology*, 2002. **58**(5): p. 600-607.
229. Miron, A.S., *et al.*, *Comparative evaluation of compact photobioreactors for large-scale monoculture of microalgae*. *Journal of Biotechnology*, 1999. **70**(1): p. 249-270.
230. Ugwu, C., J. Ogbonna, and H. Tanaka, *Light/dark cyclic movement of algal culture (*Synechocystis aquatilis*) in outdoor inclined tubular photobioreactor equipped with static mixers for efficient production of biomass*. *Biotechnology Letters*, 2005. **27**(2): p. 75-78.
231. Ugwu, C., J. Ogbonna, and H. Tanaka, *Design of static mixers for inclined tubular photobioreactors*. *Journal of Applied Phycology*, 2003. **15**(2): p. 217-223.
232. Molina, E., *et al.*, *Scale-up of tubular photobioreactors*. *Journal of Applied Phycology*, 2000. **12**(3-5): p. 355-368.
233. Pirt, S.J., *et al.*, *A tubular bioreactor for photosynthetic production of biomass from carbon dioxide: design and performance*. *Journal of Chemical Technology and Biotechnology*. *Biotechnology*, 1983. **33**(1): p. 35-58.
234. Hoek, C., D. Mann, and H.M. Jahns, *Algae: an introduction to phycology*. 1995: Cambridge University Press.
235. Kokkinos, D., *et al.*, *Deformation and rupture of *Dunaliella salina* at high shear rates without the use of thickeners*. *Biorheology*, 2016. **53**(1): p. 1-11.
236. Gudin, C. and D. Chaumont, *Cell fragility—the key problem of microalgae mass production in closed photobioreactors*. *Bioresource Technology*, 1991. **38**(2-3): p. 145-151.
237. Webpage. *Mass Transport Processes*. [cited 2017 April]; Available from: <http://tinyurl.com/y9byx3gn>.
238. Stocker, R. *Lecture 15- Drag and terminal velocity*. 1.961 Lecture Videos 2008 [cited 2017 March]; Available from: <http://tinyurl.com/l7w3b2j>.
239. Mathijssen, A.J., *et al.*, *Hotspots of boundary accumulation: dynamics and statistics of micro-swimmers in flowing films*. *Journal of The Royal Society Interface*, 2016. **13**(115): p. 1-11.
240. Jaouen, P., L. Vandanjon, and F. Quéméneur, *The shear stress of microalgal cell suspensions (*Tetraselmis suecica*) in tangential flow filtration systems: the role of pumps*. *Bioresource Technology*, 1999. **68**(2): p. 149-154.

241. Bruus, H., *Lecture notes, Theoretical microfluidics*. DTU (MIC), 2004.
242. Barnes, H.A., J.F. Hutton, and K. Walters, *An introduction to rheology*. Vol. 3. 1989: Elsevier.
243. Sousa, P., *et al.*, *Laminar flow in three-dimensional square–square expansions*. *Journal of Non-Newtonian Fluid Mechanics*, 2011. **166**(17): p. 1033-1048.
244. Sousa, P., *et al.*, *Effect of the contraction ratio upon viscoelastic fluid flow in three-dimensional square–square contractions*. *Chemical Engineering Science*, 2011. **66**(5): p. 998-1009.
245. Vrentas, J. and J. Duda, *Flow of a Newtonian fluid through a sudden contraction*. *Applied Scientific Research*, 1973. **28**(1): p. 241-260.
246. Ahmad, T. and I. Hassan, *Experimental analysis of microchannel entrance length characteristics using microparticle image velocimetry*. *Journal of Fluids Engineering*, 2010. **132**(4): p. 1-13.
247. Galvis, E., S. Yarusevych, and J. Culham, *Incompressible laminar developing flow in microchannels*. *Journal of Fluids Engineering*, 2012. **134**(1): p. 1-4.
248. Green Don, W., *Perry's Chemical Engineers' Handbook*. 2008, McGraw-Hill.
249. Borowitzka, M.A. *The mass culture of Dunaliella salina*. in *Regional Workshop on the Culture and Utilization of Seaweeds, Cebu City (Philippines)*, . 27-31 Aug 1990.
250. Shaish, A., A. Ben-Amotz, and M. Avron, *Biosynthesis of  $\beta$ -carotene in Dunaliella*. *Methods in Enzymology*, 1992. **213**: p. 439-444.
251. Chisti, Y., *Large-scale production of algal biomass: raceway ponds*, in *Algae Biotechnology*. 2016, Springer. p. 21-40.
252. Chisti, Y., *Raceways-based production of algal crude oil*. *Green*, 2013. **3**(3-4): p. 195-216.
253. Slocombe, S.P. and J.R. Benemann, *Microalgal Production for Biomass and High-value Products*. 2016: CRC Press.
254. Fuentes, J.L., *et al.*, *Impact of microalgae-bacteria interactions on the production of algal biomass and associated compounds*. *Marine Drugs*, 2016. **14**(5): p. 1-16.
255. Fulbright, S.P., *Crop protection in industrial algae farming: detecting weedy algae and characterizing bacterial communities*. PhD Thesis, Colorado State University, Fort Collins (Colorado, USA), 2015.
256. Sevilla, J. and E.M. Grima, *A model for light distribution and average solar irradiance inside outdoor tubular photobioreactors for the microalgal mass culture*. *Biotechnol Bioeng*, 1997. **55**: p. 701-14.
257. Wegmann, K., A. Ben-Amotz, and M. Avron, *Effect of temperature on glycerol retention in the halotolerant algae Dunaliella and Asteromonas*. *Plant Physiology*, 1980. **66**(6): p. 1196-1197.
258. Davison, I.R., *Environmental effects on algal photosynthesis: temperature*. *Journal of Phycology*, 1991. **27**(1): p. 2-8.
259. Richmond, A., *Large scale microalgal culture and applications*. *Progress in Phycological Research*, 1990. **7**: p. 269-330.
260. Teplitski, M. and S. Rajamani, *Signal and nutrient exchange in the interactions between soil algae and bacteria*, in *Biocommunication in Soil Microorganisms*. 2011, Springer. p. 413-426.
261. Edmundson, S.J. and M.H. Huesemann, *The dark side of algae cultivation: Characterizing night biomass loss in three photosynthetic algae, Chlorella sorokiniana, Nannochloropsis salina and Picochlorum sp.* *Algal Research*, 2015. **12**: p. 470-476.
262. Matas, J.-P., J.F. Morris, and É. Guazzelli, *Inertial migration of rigid spherical particles in Poiseuille flow*. *Journal of Fluid Mechanics*, 2004. **515**: p. 171-195.

263. Di Carlo, D., *et al.*, *Continuous inertial focusing, ordering, and separation of particles in microchannels*. Proceedings of the National Academy of Sciences, 2007. **104**(48): p. 18892-18897.
264. Tavakol, M., *et al.*, *Dispersion and deposition of ellipsoidal particles in a fully developed laminar pipe flow using non-creeping formulations for hydrodynamic forces and torques*. International Journal of Multiphase Flow, 2015. **75**: p. 54-67.
265. Byron, M.L., Variano Evan, A., *The rotation and translation of non-spherical particles in homogeneous isotropic turbulence*. PhD Thesis, University of California, Berkeley (USA), 2015.
266. Zhang, J., *et al.*, *Fundamentals and applications of inertial microfluidics: a review*. Lab on a Chip, 2016. **16**(1): p. 1-39.
267. Geislinger, T.M. and T. Franke, *Hydrodynamic lift of vesicles and red blood cells in flow—from Fåhræus & Lindqvist to microfluidic cell sorting*. Advances in Colloid and Interface Science, 2014. **208**: p. 161-176.
268. Segré, G. and A. Silberberg, *Behaviour of macroscopic rigid spheres in Poiseuille flow Part 2. Experimental results and interpretation*. Journal of Fluid Mechanics, 1962. **14**(1): p. 136-157.
269. Zhou, J. and I. Papautsky, *Fundamentals of inertial focusing in microchannels*. Lab on a Chip, 2013. **13**(6): p. 1121-1132.
270. Jeffery, G.B., *The motion of ellipsoidal particles immersed in a viscous fluid*. Proceedings of The Royal Society of London Series A, 1922. **102**(715): p. 161-179.
271. Stokes, G.G., *On the effect of the internal friction of fluids on the motion of pendulums*. Vol. 9. 1851: Pitt Press Cambridge.
272. Zastawny, M., *et al.*, *Derivation of drag and lift force and torque coefficients for non-spherical particles in flows*. International Journal of Multiphase Flow, 2012. **39**: p. 227-239.
273. Karnis, A., H. Goldsmith, and S. Mason, *Axial migration of particles in Poiseuille flow*. Nature, 1963. **200**(4902): p. 159-160.
274. Qi, D., *et al.*, *Lateral migration and orientation of elliptical particles in Poiseuille flows*. Journal of Statistical Physics, 2002. **107**(1-2): p. 101-120.
275. Rubinow, S. and J.B. Keller, *The transverse force on a spinning sphere moving in a viscous fluid*. Journal of Fluid Mechanics, 1961. **11**(3): p. 447-459.
276. Saffman, P., *The lift on a small sphere in a slow shear flow*. Journal of Fluid Mechanics, 1965. **22**(2): p. 385-400.
277. Jeffrey, R.C. and J. Pearson, *Particle motion in laminar vertical tube flow*. Journal of Fluid Mechanics, 1965. **22**(4): p. 721-735.
278. Ho, B. and L. Leal, *Inertial migration of rigid spheres in two-dimensional unidirectional flows*. Journal of Fluid Mechanics, 1974. **65**(2): p. 365-400.
279. Briggs, L.J., *Effect of spin and speed on the lateral deflection (curve) of a baseball; and the Magnus effect for smooth spheres*. American Journal of Physics, 1959. **27**(8): p. 589-596.
280. Webpage. *Dynamic Lift And Magnus Effect: Applications*. [cited 2018 February]; Available from: <https://byjus.com/physics/dynamic-lift/>.
281. Lee, M.G., S. Choi, and J.-K. Park, *Inertial separation in a contraction–expansion array microchannel*. Journal of Chromatography A, 2011. **1218**(27): p. 4138-4143.
282. Syed, M.S., *et al.*, *Selective separation of microalgae cells using inertial microfluidics*. Bioresource Technology, 2018. **252**: p. 91-99.
283. Li, M., *et al.*, *Shape-based separation of microalga Euglena gracilis using inertial microfluidics*. Scientific Reports, 2017. **7**(1): p. 1-8.

284. Park, J.-S., S.-H. Song, and H.-I. Jung, *Continuous focusing of microparticles using inertial lift force and vorticity via multi-orifice microfluidic channels*. *Lab on a Chip*, 2009. **9**(7): p. 939-948.
285. Cornet, J.-F., et al., *A simplified monodimensional approach for modeling coupling between radiant light transfer and growth kinetics in photobioreactors*. *Chemical Engineering Science*, 1995. **50**(9): p. 1489-1500.
286. Rabe, A. and R. Benoit, *Mean light intensity—a useful concept in correlating growth rates of dense cultures of microalgae*. *Biotechnology and Bioengineering*, 1962. **4**(4): p. 377-390.
287. Michels, M.H., et al., *Effects of shear stress on the microalgae *Chaetoceros muelleri**. *Bioprocess and biosystems engineering*, 2010. **33**(8): p. 921-927.
288. Hejazi, M., et al., *Effect of mixing rate on  $\beta$ -carotene production and extraction by *dunaliella salina* in two-phase bioreactors*. *Biotechnology and Bioengineering*, 2003. **84**(5): p. 591-596.
289. Dalley, S. and J.P. Oleson, *Sennacherib, Archimedes, and the water screw: the context of invention in the ancient world*. *Technology and Culture*, 2003. **44**(1): p. 1-26.
290. Vandanon, L., et al., *Effects of shear on two microalgae species. Contribution of pumps and valves in tangential flow filtration systems*. *Biotechnology and Bioengineering*, 1999. **63**(1): p. 1-9.
291. Xu, Y., et al., *Effects of centrifugal stress on cell disruption and glycerol leakage from *Dunaliella salina**. *Microalgae Biotechnology*, 2015. **1**(1): p. 20-27.
292. Grover, J.P., *Influence of cell shape and size on algal competitive ability*. *Journal of Phycology*, 1989. **25**(2): p. 402-405.
293. Wayama, M., et al., *Three-dimensional ultrastructural study of oil and astaxanthin accumulation during encystment in the green alga *Haematococcus pluvialis**. *PloS One*, 2013. **8**(1): p. 1-9.
294. Concas, A., M. Pisu, and G. Cao, *Novel simulation model of the solar collector of BIOCOIL photobioreactors for CO<sub>2</sub> sequestration with microalgae*. *Chemical Engineering Journal*, 2010. **157**(2): p. 297-303.
295. Webpage. *Wolfram Mathworld: Ellipse*. [cited 2018 March]; Available from: <http://mathworld.wolfram.com/Ellipse.html>.
296. Webpage. *Orbital Eccentricity*. [cited 2018 March]; Available from: <https://tinyurl.com/yavcbn2a>.
297. Goldstein, D. *Inverted microscopes*. [cited 2017 June]; Available from: <http://tinyurl.com/v49m3wr>.
298. Webpage. *Measurements and Errors*. [cited 2019 July (while doing the corrections)]; Available from: <https://tinyurl.com/y6s4dumz>.